Functional materials for destabilizing and stabilizing emulsions and underlying interfacial interaction mechanisms

by

Xiaohui Mao

A thesis submitted in partial fulfillment of the requirements for the degree of

Doctor of Philosophy

in
Chemical Engineering

Department of Chemical and Materials Engineering
University of Alberta

Abstract

Oil related issues such as oil/water emulsions are critical challenging issues in a wide range of engineering processes and have caused negative effects to economy, environment, and ecology. To deal with these issues, functional materials targeting at oil spills, emulsion destabilization have been widely explored, and the relative interaction mechanisms have been extensively studied from many aspects. However, despite much effort devoted to this area, the developed materials remain many limitations. For example, the traditional materials for breaking the asphaltenes stabilized emulsions are usually amphiphilic polymers that may further stabilize the emulsion at high dosage. In the oil spill treatment and destabilization of surfactant stabilized emulsions, the developed materials are usually functionalized by polymers via complicated methods. The material synthesized via a simple strategy using small molecules has rarely been reported. Besides, the understanding of underlying mechanisms needs to be improved, especially in the aspect of direct force measurement of interactions between emulsified droplets in emulsion, which plays an important role in predicting and altering the stability of emulsions.

In this project, a novel functional material with superhydrophilic polyelectrolyte has been developed to destabilize asphaltenes-stabilized emulsion, and the scalable materials functionalized with small molecules have been synthesized via a simple and facile method for oil absorption, oil/water separation and demulsification. The atomic force microscope (AFM) is employed to study the interactions between water/oil droplet and as-prepared materials, and the interactions between two water or oil droplets with interfacially active particles to elucidate the destabilization and stabilization mechanisms of emulsion.

In the first work, novel core-shell microspheres consisting of magnetic core and superhydrophilic zwitterionic polyelectrolyte shell have been developed to break asphaltenes stabilized water-in-oil

(W/O) emulsion and to release water from the emulsion with the assistance of external magnetic field. In the study of interactions and mechanism, AFM force measurement reveals strong attraction between the polyelectrolyte and water droplet surrounded by interfacially absorbed asphaltenes in oil. Besides, the addition of as-synthesized core-shell microspheres increase the water-oil interfacial tension (IFT). Also, the result of quartz crystal microbalance with dissipation (QCMD) test shows that asphaltenes can adsorb on the polyelectrolyte, which indicates the microsphere may absorb and rupture the asphaltenes film around emulsified water droplets to facilitate destabilization of emulsions.

In the second work, fiber-based hydrophobic and oleophilic materials are synthesized via a facile and scalable method using a small molecule, γ-mercaptopropyldi(trimethylsiloxy)methylsilane (MD(SH)M). The MD(SH)M-functionalized materials can effectively absorb five types of oil spills from water, separate water from the mixture with high-density/low-density oil and destabilize asphaltenes/surfactants stabilized emulsions. The mechanism is studied using adhesion force measurement and AFM force measurement and is found to be related to the hydrophobicity and oleophilicity of as-prepread materials, as well as the hydrophobic interaction between MD(SH)M and oil droplets in aqueous phase.

In the third work, the Pickering emulsions formed by oil/water mixture under pH 2, 4, 9 and 11 with bilayer oleic acid coated Fe_3O_4 nanoparticles (Fe_3O_4@2OA NPs) are characterized using microscope imaging, zeta potential, IFT and AFM force measurement. W/O emulsion is formed at low pHs (i.e., pH 2 and 4), and its stabilization mechanism is mainly governed by the formation of steric barrier of the confined particle layer (with Fe_3O_4@2OA NPs and aggregates). At high pHs (i.e., pH 9 and 11), oil-in-water (O/W) emulsion is formed, and its stabilization mechanism is mainly due to relatively low IFT, strong electrostatic repulsion from negatively charged carboxyl

groups, and steric repulsion from the confined nanoparticles and their aggregates. Increasing the maximum loading force and dwelling time enhances the confinement of Fe_3O_4@2OA particles and aggregates at oil/water interface.

In the fourth work, the small molecule MD(SH)M is used to prepare slippery surface that is independent of complex micro-/nano-scale surface structures and conventional infused lubricant oils. The as-prepared MD(SH)M surfaces allow facile transport of bubbles in aqueous media and water drops in oil, as well as facilitate the self-assembly of nanoparticles from their aqueous suspensions. The MD(SH)M slippery surfaces have lower surface energy and contact angle hysteresis as compared to conventional lubricant liquid-infused slippery surfaces, which allows the three-phase contact line to move more freely and accounts for the higher moving velocity of bubbles/drops under the same test condition.

In all, this project has developed novel superhydrophilic demulsifier for asphaltenes stabilized emulsion and paved a new way to separate oil and water using small molecules. The useful methodology developed in this work can be readily applied to study the interactions in other emulsion systems to elucidate the destabilization and stabilization mechanism. Our work points out a new path using polyelectrolytes and suitable small molecules to effectively solve the oil/water emulsion issues and provides useful insights into the interaction forces of Pickering emulsions stabilized by stimuli-responsive interface-active particles, which has great significance and potential applications in many engineering processes.

Preface

Chapter 3 of this thesis has been published as Xiaohui Mao, Lu Gong, Lei Xie, Hui Qian, Xiaogang Wang, Hongbo Zeng, "Novel Fe_3O_4 based superhydrophilic core-shell microspheres for breaking asphaltenes-stabilized water-in-oil emulsion," Chemical Engineering Journal 358 (2019): 869-877. I was responsible for the design of research, experimental and manuscript composition under the supervision of Dr. Hongbo Zeng. Dr. Lu Gong was responsible for the force measurement in the experiment and corresponding manuscript composition. Dr. Lei Xie was responsible for part of the design of research and manuscript composition. Hui Qian assisted with analyses of experiment data. Dr. Xiaogang Wang was involved in manuscript composition. Dr. H. Zeng was the supervisory author and was involved in concept formation and manuscript composition.

Chapter 4 of this thesis has been submitted to Journal of Colloid and Interface Science and is currently under review as Xiaohui Mao, Ziqian Zhao, Diling Yang, Chenyu Qiao, Jinglin Tan, Qi Liu, Tian Tang, Hao Zhang, Hongbo Zeng, "Bio-inspired, facile and scalable surface functionalization approach with small molecules for multitasking oil decontamination". I was responsible for the design of research, experimental and manuscript composition under the supervision of Dr. Hongbo Zeng. Ziqian Zhao was responsible for part of the characterization in experiment and manuscript composition. Diling Yang, Chenyu Qiao and Dr. Jinglin Tan assisted to interpret the data, discussed the results and commented on the manuscript. Dr. Qi Liu, Dr. Tian Tang, Dr. Hao Zhang commented on the manuscript. Dr. H. Zeng was the supervisory author and was involved in concept formation and manuscript composition.

Chapter 5 of this thesis has been submitted to The Journal of Physical Chemistry C and is currently under review, as Xiaohui Mao, Diling Yang, Lei Xie, Qi Liu, Tian Tang, Hao Zhang, Hongbo Zeng, "Probing the interactions between Pickering emulsion droplets stabilized with pH-

responsive nanoparticles". I was responsible for the design of research, experimental and manuscript composition under the supervision of Dr. Hongbo Zeng and Dr. Lei Xie. Diling Yang and Dr. Lei Xie assisted with experiment and manuscript composition. Dr. Qi Liu, Dr. Tian Tang, Dr. Hao Zhang commented on the manuscript. Dr. Lei Xie and Dr. H. Zeng both supervised this work and were involved in concept formation and manuscript composition.

Chapter 6 of this thesis has been published as Xiaohui Mao, Jinglin Tan, Lei Xie, Jingyi Wang, Hongbo Zeng, "Novel multifunctional solid slippery surfaces with self-assembled fluorine-free small molecules" Chemical Engineering Journal 404 (2021): 127064. I was responsible for the design of research, experimental and manuscript composition under the supervision of Dr. Hongbo Zeng and Dr. Jinglin Tan. Dr. Jinglin Tan assisted with the experiment. Dr. Lei Xie contributed to manuscript composition. Dr. Jingyi Wang assisted with part of the experiment and manuscript composition. Dr. Jinglin Tan and Dr. H. Zeng both supervised this work and were involved in concept formation and manuscript composition.

Chapters 1, 2, and 7 are originally written by Xiaohui Mao, and have never been published before.

Acknowledgement

I would like to express my sincere gratitude to Dr. Hongbo Zeng for the supervision and insightful guidance through the whole period of my PhD study. Dr. Zeng always gives me helpful suggestions and feasible plans when I have difficulties in research or in life. Though Dr. Zeng is very busy with many things as an outstanding professor and research chair, he is always patient with my questions and explains the solution to me until I fully understand. He respects my opinions in the discussion and gently points out the places that I still need to improve. With Dr. Zeng's help, I have improved a lot in many aspects in the past five years. Now when I look back, I realized how simple my question was and if I were him, I probably would not be that patient to explain such a simple question. I really appreciate Dr. Zeng for treating my problems patiently and seriously and giving me helpful guidance from my side of view. Dr. Zeng never pushes me in the work and always inspires me with his enthusiasm and dedication for scientific research, which encourages me to become a principal investigator in the future. Dr. Zeng is not only an excellent researcher but also a great teacher and supervisor. I would like to thank Dr. Zeng from the bottom of my heart for giving me such a wonder journey and making me a better person.

I would like to thank all my group members, especially Dr. Chen Shi, Dr. Jingyi Wang, Dr. Lu Gong, and Dr. Jing Liu for their generous help and assistance during my study. Special thanks to Dr. Lei Xie for all the help and valuable advice during my PhD study.

I would like to thank my friends, Dr. Jun Li, Dr. Xiaoyu Sun, Dr. Kuixin Cui, Dr. Jing Liu, and Dr. Qianhui Zhao, for bringing lots of joy in my life and helping me out in the difficult times.

In addition, I gratefully acknowledge the financial support from the Natural Sciences and Engineering Research Council of Canada (NSERC), the Canada Foundation for Innovation (CFI),

the Future Energy Systems under the Canada First Research Excellence Fund and the Canada Research Chairs Program.

Last but not least, I would like to thank my parent, especially my mom for the unconditional love and insightful guidance in my whole life. I would like to thank my husband Weida Bu for the love and support, and great effort you made for our family. I would like to express the deepest love to my sweet one year old baby boy, Albert, for giving me the chance to be your mom, bringing me lots of joy and motivating me to become better and better.

Table of Content

List of Tables

List of Figures

List of Abbreviations

AFM	Atomic force microscope
QCMD	Quartz Crystal Microbalance with Dissipation
FTIR	Fourier Transform Infrared Spectroscopy
SEM	Scanning Electron Microscopy
EDS	Energy-dispersive X-ray Spectrometry
TEM	Transmission electron microscopy
VDW	Van der Waals
EDL	Electric double layer
IFT	Interfacial tension
ITFDA	Integrated thin film drainage apparatus
XPS	X-ray photoelectron spectroscopy
XRD	X-ray Diffraction
W/O	Water-in-oil
O/W	Oil-in-water
W/O/W	Water-in-oil-in-water
PDMS	Polydimethylsiloxane

EO	Polyethylene oxide
PO	Polypropylene oxide
A	Hamaker constant
F	Force
D_0	Decay length of hydrophobic interaction
Δf	Frequency shift
T	Temperature

Chapter 1 Introduction

1.1 Oil contamination

The oil contamination, such as oily wastewater generated in food, textile and petrochemical fields[1], oil spill accident during oil production and transportation[2], and corrosion and fouling issues caused by oil-water emulsions[3] has aroused great concern in recent decades due to a huge negative impact on environment and ecosystems that human life relies on. The hazardous oily component in wastewater can pollute the soil and groundwater resources and endanger living creatures and human beings[4]. The oily wastewater from food industry contains fats, grease, flesh, and blood, which requires high biochemical oxygen demand and chemical oxygen demand to degrade[5]. The wastewater from textile industry contains a large amount of unconsumed dyes and surfactants[6], and wastewater from petrochemical industry contains high content of organics including phenols, light hydrocarbons, polycyclic aromatic hydrocarbons[7]. Besides oily wastewater, oil spill is also a critical worldwide oil contamination issue. Hundreds of oil spill accidents have happened all over the world in the past century which heavily pollute the ocean and threat marine lives. The first recorded oil spill accident can be traced back to as early as a century ago in November 1903, Petriana, Australia[8]. Among hundreds of oil spill accidents, one of the biggest accidents in history is the "Deepwater Horizon" oil spill in the Gulf of Mexico in 2010. In the accident, millions of barrels of crude oil were spilled into the ocean which brought deadly impact on marine lives and local ecology[9,10]. In addition, the problems caused by oil becomes more challenging in the presence of artificial or natural stabilizers (e.g., span80, asphaltenes) where stable and complex water-oil emulsions are formed.

1.1.1 Formation of emulsion

The emulsion is usually formed with two immiscible liquids, such as water and oil, in the presence of interfacially active components. The type of emulsions includes water-in-oil emulsion (W/O), oil-in-water emulsion (O/W) and complex emulsions, such as water-in-oil-in-water (W/O/W) emulsion[11]. The W/O emulsion refers to micro-/nanoscale emulsified water drops suspended in continuous oil phase (Figure 1.1)[12]. Similarly, in O/W emulsion, water serves as a continuous phase and the emulsified oil drops are suspended, as illustrated in Figure 1.1. The suspended drop in continuous phase (e.g., water) in complex emulsion (e.g., W/O/W) is not a single-phase liquid drop but a mixture of two immiscible liquids (e.g., W/O)[13]. The stabilizers of emulsion include artificial stabilizers (e.g., surfactants, particles) and natural stabilizers (e.g., asphaltenes, resins). Artificial stabilizers such as the surfactants have affinity to both water and oil and are prone to stay at oil/water interface to lower the interfacial tension, and thus stabilize the emulsion[14]. The surfactants can be divided into non-ionic surfactant (e.g., polyethylene oxide-co-polypropylene oxide block polymers)[15], cationic surfactant (e.g., cetyltrimethylammonium bromide), anionic surfactant (e.g., sodium dodecyl sulfate)[16] and zwitterionic surfactant (e.g., octadecyl dimethyl betaine)[17] according to their surface charges. Usually, the surfactant preferring water phase tends to stabilize O/W emulsion while the surfactant preferring oil phase tends to stabilize W/O emulsion[18].

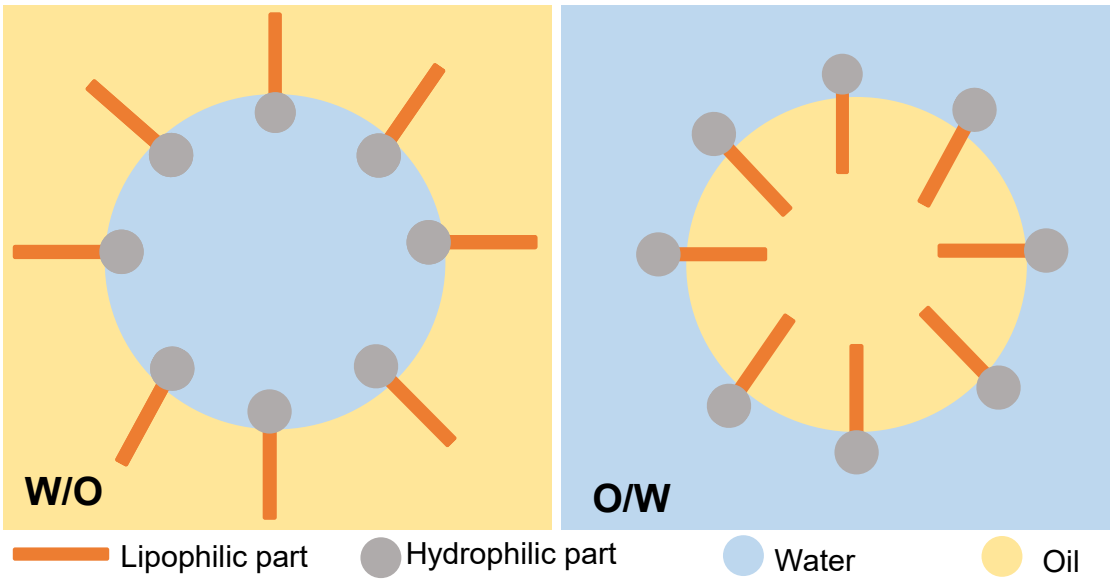

Figure 1.1 Schematic of formation of water-in-oil (W/O) and oil-in-water (O/W) emulsions[19].

The emulsion stabilized with particles is called Pickering emulsion following Pickering's pioneering work in 1907[20]. The particles adsorbed at oil/water interface prevent the coalescence of emulsified droplets and stabilize the emulsion as steric barrier[21]. The stability of Pickering emulsion is related to the energy of removing the particle from oil/water interface to either oil or water phase and the energy can be calculated using the oil/water interfacial tension and the contact angle of particle at interface[22]. The type of Pickering emulsion can be predicted by evaluating the contact angle of particle at oil/water or air/water interface. The particles with contact angle less than 90° tend to form O/W emulsion while those with contact angle greater than 90° tend to form W/O emulsion, as illustrated in Figure 1.2 Numerous types of particles (e.g., clays, hydroxyapatite) have been used by researchers to form Pickering emulsions in the past century. Silica particle is one of the most frequently used particles because the silica particles can be easily obtained and modified to study the factors (e.g., hydrophobicity, pH, salinity) affecting Pickering emulsion's

stability[23,24]. Besides, the particles responding to external stimuli have also attracted great research interest, and the stabilization, destabilization, phase inversion or reactions of Pickering emulsions can be easily achieved by controlling the external stimuli, such as magnetic, pH, and temperature[21]. For example, external magnetic field was employed to drive the Fe_3O_4 particle stabilized droplets closer so that the reactants contained in the emulsified droplets would get contact and react under UV radiation[25]. The particles coated with double layer oleic acid could respond to the change of pH to switch between W/O and O/W type Pickering emulsions[26]. Also, the effect of temperature on the stability of Pickering emulsion was studied using thermal responsive particles[27].

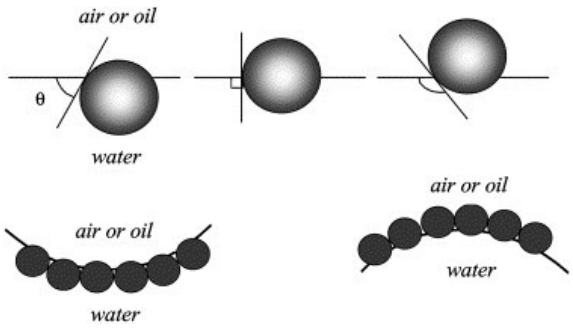

Figure 1.2 (Upper) Position of a small spherical particle at a planar fluid–water interface for a contact angle (measured through the aqueous phase) less than 90° (left), equal to 90° (centre) and greater than 90° (right). (Lower) Corresponding probable positioning of particles at a curved fluid–water interface. For $\theta<90°$, solid-stabilised aqueous foams or o/w emulsions may form (left). For $\theta>90°$, solid-stabilised aerosols or w/o emulsions may form (right)[22].

1.1.2 Asphaltenes behavior in stabilizing emulsion

The asphaltenes are the natural component in crude oil defined by the solubility, viz., the asphaltenes are soluble in aromatic solvent (e.g., toluene) but insoluble in aliphatic solvent (e.g., heptane). The asphaltenes consist of many aromatic rings with short peripheral aliphatic chains and some heteroatoms such as sulfur, nitrogen and oxygen[28]. The asphaltenes start to aggregate

above a critical concentration (~100 mg/L) in good solvent (e.g., toluene) and the number of asphaltenes molecules in one aggregation is usually less than ten[29]. This aggregation with several asphaltenes molecules is called asphaltenes nano-aggregates, of which the structure is described as a disk with radius of 3.2 nm and height of 0.67 nm[30]. When the concentration increases to a few g/L in good solvent, the asphaltenes would form large aggregates. The shape of large aggregates could be disks or vesicles with radius less than 10 nm[31,32]. The formation of asphaltenes aggregates is not only related to the concentration but also the solvent quality and temperature. When the good solvent is mixed with alkanes (e.g., heptane) or the temperature is decreased, the large aggregates tend to be generated in the solution[33,34]. The thickness of the oil-water interfacial layer with asphaltenes (3 g/L) is studied and measured to be ~7 nm, which is similar to the size of asphaltenes large aggregates in good solvent[35,36]. According to the size, it is deduced that the asphaltenes aggregates would adsorb on oil-water interface to stabilize the emulsion[29]. The adsorbed asphaltenes form a rigid "skin-like" layer at the interface after a certain aging time to prevent the coalescence of droplets in the emulsion[37–39]. It is reported that the emulsions are more stable with longer aging time in the emulsion stability test[40,41]. Freer and Radke studied the aged asphaltenes interfacial film using interfacial dilatational rheology and the result was fitted to two combined models to show that most of the asphaltenes at oil-water interface were irreversibly adsorbed[42]. In the irreversibly adsorbed asphaltenes, about less than 2% of asphaltenes are interfacially active and mainly contribute to the emulsion stability[43]. The remaining more than 98% asphaltenes almost have no negative effect on emulsion stability if removed from the water/oil interface[44,45]. In addition, the effects of pH and salinity on the stability of asphaltenes emulsion are also investigated. It is found that the asphaltenes are charged at either low or high pH to increase the interfacial activity and form stable emulsion. And the interfacial tensions (IFT) at oil-water

interface with three different concentrations of asphaltenes (i.e., 0.01%, 0.1%, 1%) all show the highest value at neutral pH (pH 7). The IFT decreases when pH either decreases from 7 to 2 or increases from 7 to 12, showing the asphaltenes emulsion is stable at low and high pH. The water resolved from the as-prepared W/O emulsion with asphaltenes at different pH reveals the same conclusion as IFT result that the emulsion is stable under low and high pH and the least amount of water is resolved at pH 2 and pH 12[46]. The increase of salinity or the addition of divalent ions (e.g., Ca^{2+}) usually destabilizes the asphaltenes emulsion as the electric or electrostatic repulsion between ionized groups at interface are screened[47–49].

1.2 Functional materials for destabilizing emulsions

Over the past decades, a variety of materials have been developed and applied to break emulsions stabilized by either surfactant or asphaltenes. The developed functional materials could be a functional chemical compound or a substrate modified with a functional compound. The demulsification ability of a functional material is highly related to the special wetting phenomenon (e.g., hydrophilic, oleophilic) which is determined by the property of functional compound as well as the substrate. The functional compounds may possess different wettability of water and oil, such as hydrophilic/oleophobic compound (e.g., cellulose)[50], hydrophobic/oleophilic compound (e.g., polydimethylsiloxane (PDMS))[51], hydrophobic/oleophobic compound (e.g., polytetrafluoroethylene)[52]. The wettability of functional material can also be affected by the structure of substrates. As illustrated in Figure 1.3, when the roughness of hydrophobic surfaces increases, the hydrophobicity could be enhanced as compared to the original surface[53]. The water drop (Figure 1.3 (middle one)) on rough surface has greater contact angle than that of the water drop on flat surface (Figure 1.3 (left one)). And if some air bubbles are trapped in the structured rough surface (Figure 1.3 (right one)), the contact angle could be further increased to more than

150°[54]. In this case, besides the intrinsic wetting property of functional compound, the roughness of surfaces also plays an important role in altering the wettability of desired functional materials. In addition, other properties of substrate also affect the demulsification performance, such as magnetic property and high surface to volume ratio. The magnetic substance such as magnetic particles can respond to the external magnetic field which provides additional magnetic force to assist the break of emulsions[55]. The fiber-based porous substrate is an excellent candidate for highly efficient demulsification due to the advantages of high specific surface area, controllable pore sizes and ease of chemical modification[10]. The details of magnetic particles and fiber-based materials will be discussed in the following two subsections.

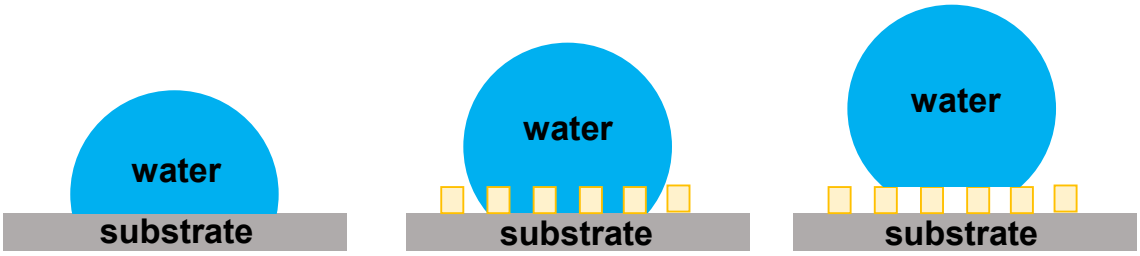

Figure 1.3 (Left) water drop on a hydrophobic substrate with smooth surface; (middle) water drop on a hydrophobic substrate with rough surface; (right) water drop on a hydrophobic substrate with trapped air bubbles in the rough surface.

Generally, the functional materials for destabilizing surfactant stabilized emulsions are either hydrophilic/oleophobic or hydrophobic/oleophilic, and the demulsification is achieved mainly through the distinctly different affinity to oil and water. The hydrophilic/oleophobic functional material is usually suitable for the demulsification of O/W emulsion as the bulk water phase would easily penetrate the functional material while the emulsified oil droplets are held to realize the separation. For example, the superhydrophilic and underwater superoleophobic poly(vinylidene

fluoride) membrane was applied to separate the sodium dodecyl sulfate stabilized O/W emulsion[56]. The multiwall carbon nanotube decorated poly(vinylidene fluoride) membrane with superhydrophilic property efficiently separates the sodium dodecyl sulfate stabilized O/W emulsion at high flux[57]. Likewise, the hydrophobic/oleophilic functional material is suitable for the separation of W/O emulsion as the bulk oil phase flows through the functional material and emulsified water drop is retained. For example, the PDMS-co-polymethylhydrosiloxane modified glass fiber has superhydrophobic and superoleophilic property and is used to demulsify span 80 stabilized W/O emulsion[58]. In sometimes cases, the hydrophobic/oleophilic functional material can destabilize both W/O and O/W emulsions. For instance, Liu et al. synthesized a magnetic PDMS functionalized sponge that could destabilize W/O emulsion stabilized by span 80 and O/W emulsion stabilized by sodium dodecyl sulfate. In the experiment, the sponge is capped in a vertical glass tube and the W/O emulsion was poured into the tube to allow the bulk oil phase to penetrate through the functionalized sponge. The water droplets are kept in the sponge to realize the separation of W/O emulsion. In the demulsification of O/W emulsion, the functionalized sponge is immersed in the emulsion to absorb the oil droplets from bulk water phase[51]. Overall, the separation of either W/O or O/W emulsion is achieved via the different affinity to water or oil so that the functional material can be wetted by one phase (i.e., water/oil) but not be wetted by the other phase (i.e., oil/water).

Unlike the demulsifiers for surfactant stabilized emulsions, the common functional materials to break asphaltenes stabilized emulsions are amphiphilic. It is found that the amphiphilic material would actively adsorb at interface, thinning and penetrating the interfacial rigid asphaltenes film to facilitate the coalescence of emulsified droplets. One of the most used material is polypropylene oxide (PO)-polyethylene oxide (EO) block polymers. The PO-EO block polymers are interfacially

active and tend to adsorb at oil/water interface to compete with the asphaltenes. The PO-EO block polymers with different structures have been extensively studied. The demulsification performance is found to be related to the structure of block polymer where the branched structure has the best performance, followed by star structure and linear structure[59–61]. In addition, the demulsification performance is also related to the hydrophilic-lipophilic balance (HLB) value. The EO block in PO-EO polymer represents the hydrophilic part and the PO block represents the lipophilic part. The HLB value of PO-EO block polymer would change with the change of chain length of EO or PO. When the HLB value falls into the range between 8 and 14, the PO-EO block polymers work as demulsifiers. Otherwise, the PO-EO block polymers with HLB lower than 8 or higher than 14 may further stabilize the W/O and O/W emulsion instead of breaking the emulsions[62–65]. Besides traditional PO-EO block polymers, the PDMS based block copolymers with PDMS unit as the core and EO moieties as terminals (EO-PDMS-EO) is another commonly used demulsifier with satisfying demulsification performance[66]. Other materials like the ethyl cellulose[67], triethylenetetramine and diethylenetruamine with amine groups as terminals are also good candidates for destabilizing asphaltenes emulsions[68,69].

1.2.1 Materials based on magnetic nanoparticles

The functional materials based on magnetic nanoparticles attract lots of interest in emulsion treatment area due to the swift response to external magnetic field, large specific surface area, and the ease of recycle from the emulsion. The functional magnetic nanoparticles have great application potentials in a wide range of areas including wastewater treatment, petrochemical engineering and oil and gas industry (Figure 1.4), which all contain oil spill, oil/water separation and demulsification processes [70]. For example, the synthesized Fe_3O_4 nanoparticles are coated with polydopamine as middle layer and then functionalized by 1H,1H,2H,2H-perfluorodecanethiol to

form superhydrophobic magnetic nanoparticles for collection of oil spills under external magnetic field[71]. Besides, magnetic particles synthesized via solvothermal method was treated by surface-initiated atom transfer radical polymerization of dimethylaminoethyl methacrylate to break O/W emulsion[72]. Magnetic Janus particles with convex hydrophilic surface and concave oleophilic surface were synthesized for fast and effective separation of oil droplets from O/W emulsion[73].

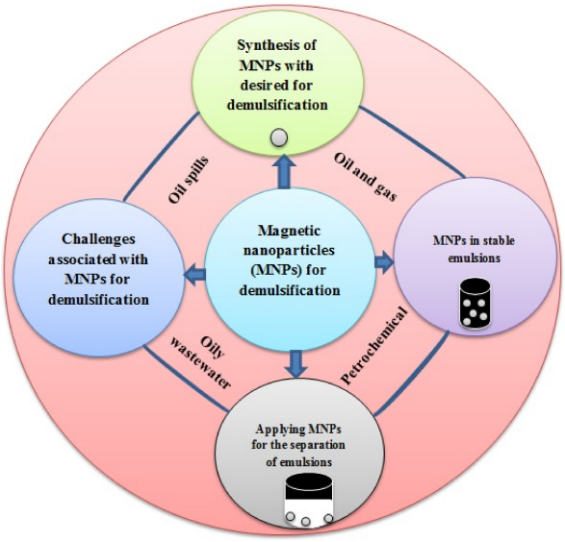

Figure 1.4 Applications of functional magnetic nanoparticles[70].

1.2.2 Fiber-based materials

The fiber-based materials with advantages of high specific surface area, porous structure and the ease of surface modification are good candidates to develop functional materials with controllable wettability and have been extensively studied in the past decades. The fiber-based materials can be generally divided into two categories: the inorganic fibers and the organic fibers[10]. Three types of inorganic fibers (i.e., metallic mesh, carbon nanotube membrane, inorganic oxide fiber) and organic fibers (i.e., fabric fiber, electrospinning fiber, natural fiber) are discussed below respectively.

The easy manufacturing, strong mechanical property and adjustable pore size have made metallic meshes such as stainless steel mesh a widely used substrate for the materials in oil/water separation. For example, a polytetrafluoroethylene coated stainless steel mesh with superhydrophobic and superoleophilic property is prepared for the oil/water separation[74]. The carbon nanotube membrane as a substrate has the unique characteristics of ultrathin film layer and strong mechanical property. For example, an ultrathin single wall carbon nanotube membrane is reported to effectively separate emulsified oil/water mixture[75]. The inorganic oxide fibers are commonly used in commercial applications, especially those under extreme situations such as corrosive or high temperature situation due to the high chemical and thermal stability. For example, nano-sized ZrO_2 is used to coat commercial Al_2O_3 membrane to separate the stable O/W emulsion[76].

The fabric fibers are usually flexible and scalable materials with satisfying mechanical strength and suitable porous structure for the oil/water separation[10]. For example, polyaniline and fluorinated alkyl silane are incorporated to the cotton fabric to prepare a material with super-hydrophobicity for the highly efficient oil/water separation[77]. The benefit of electrospinning is that the fibers with different lengths and different materials can be combined easily to synthesize the fiber membrane with desired needs, such as great tensile strength, large surface area and various pore sizes. For example, electrospinning fibers with superwetting property are developed to separate oil/water mixture as well as O/W emulsions under the driving force of gravity[78]. The natural fibers such as wood fibers and cellulose fibers have the benefits of non-toxic, biodegradable and abundant source. For example, the surface chemistry and roughness of wood fiber are modified to obtain a super-hydrophobic natural fiber material with high tensile strength and high relative humidity condition[79].

1.3 Functional materials for stabilizing emulsions

Though the formation of emulsion discussed above is very undesired and great efforts have been made to break the emulsion, a stable emulsion is sometimes needed in pharmaceutical, food, cosmetics industries and other engineering processes[80,81]. For example, the encapsulation of drug in a bio-compatible material, the production of diary product, candies, cereal-based products, soups, and the manufacture of facial lotions and creams are all related to the techniques of stabilizing emulsions. As discussed in section 1.1.1, the formation of emulsion needs two immiscible liquids (e.g., oil and water) and interfacially active components. The stability of emulsion is found to be related to the interfacial rheology and interfacial tension property[82,83]. The interfacial rheology reflects the adsorption kinetics of interfacially active component at interface and the viscoelasticity of interfacial films which is related to interfacial mechanical property and is used to deduce the emulsion stability[84]. The adsorption of surfactant could change the interfacial tension to stabilize emulsion. Usually, higher concentration of surfactants may lead to a lower interfacial tension that indicates a higher stability of emulsion[85]. The interfacial tension may not be affected by the concentration of particles in Pickering emulsion as the stabilization mechanism is via the steric hinderance rather than lowering interfacial tension. The stability of Pickering emulsion depends on properties of particles including surface wettability, particle size, particle shape, particle concentration and so on[86]. Various functional particles such as bare particles, particles chemically bonded with polymers, or particles physically blended with polymers, have been developed to stabilize the emulsion. For example, bare chitosan or chitosan-based materials are commonly used to stabilize Pickering emulsion. The chitosan colloidal particles used to stabilize Pickering emulsion can be formed by self-aggregation of chitosan at alkaline pH as the amino groups is deprotonated[87]. The chitosan-based particles are synthesized through the attraction

between positively charge amino groups of chitosan and negatively charged groups of polyanion or polyelectrolyte[88]. Another way to prepare chitosan-based particles is to functionalize chitosan with hydrophobic segment to alter the affinity to oil and water, and thus to further stabilize the Pickering emulsion[89].

1.4 Study of interaction mechanisms

There are many techniques to study the interaction mechanism in emulsion such as IFT[90], quartz crystal microbalance with dissipation (QCMD)[91], integrated thin film drainage apparatus (ITFDA)[92], surface force apparatus (SFA)[93], and atomic force microscopy (AFM)[94]. As a well-developed nanoscale technique, AFM has attracted great interest in recent years in the application of directly measuring the interactions between an emulsified droplet and another object (i.e., droplet, substrate), which plays an important role in understanding the mechanism of oil/water separation and emulsion treatment. For example, the interaction between oil drop containing asphaltenes and hydrophobic/hydrophilic substrate in aqueous solution was studied to investigate the influence of the substrate wettability on the stability of emulsified asphaltenes oil droplets. The results greatly help with the understanding of the mechanism related to oil fouling, corrosion, and oil/water separation[95]. Besides, the interaction between two oil droplets with interfacially mobilized asphaltenes in water was measured using AFM force measurement to understand the interaction mechanism in O/W emulsion stabilized by asphaltenes[94]. The AFM force measurement is a powerful and useful technology to quantify the interaction forces among the species (i.e., emulsified droplets, interfacially active components, bulk phase) in emulsion at nanoscale, which provide new understanding of emulsion systems and useful information for many engineering processes.

1.5 Objectives

The oil related issues, either the oil absorption, break of emulsion or stabilization of emulsion are critical problems in many science and engineering fields. Despite the rapid development of various functional materials for emulsion treatment, the synthesis of most materials usually requires complex process and involves amphiphilic polymers and materials for demulsification of asphaltenes stabilized emulsions. Unfortunately, these amphiphilic materials have the potential to further stabilize the emulsion. Thus, the development of a facile and simple method to synthesize functional materials is necessary and the novel materials to destabilize emulsion with asphaltenes are needed. In addition, though there are many particle materials for stabilizing Pickering emulsion, the stimuli-responsive Pickering emulsion is not yet well studied especially in the aspect of stabilization mechanism and arrangement of particles at water/oil interface. Besides, the direct and quantified measurement of interactions in emulsion at nanoscale is of great importance in understanding the mechanism and providing guidance to develop functional materials to interfere the interactions in emulsions and alter the stability. The major objective of this project is to develop novel functional materials to solve oil contamination, including oil spills and oil/water mixtures (i.e., emulsion stabilized by asphaltenes or surfactants), as well as to unravel the underlying interactions between droplets in the presence of interfacially active components using the state-of-the-art nanomechanical techniques such as AFM force measurement. The specific objectives are listed as follows.

(1). Develop novel superhydrophilic magnetic spherical particles using zwitterionic polyelectrolyte to break asphaltenes stabilized W/O emulsion and investigate interfacial interactions using AFM force measurement, as well as elucidate the destabilization mechanism.

(2). Develop simple and scalable fiber-based materials using a novel small molecule to realize oil/water separation, oil absorption and demulsification of surfactant or asphaltenes stabilized W/O emulsions and elucidate the interaction mechanism using AFM force measurement and ITFDA.

(3). Unravel the interfacial interactions in pH-responsive Pickering emulsions stabilized by double oleic acid layer coated nanoparticles using AFM force measurement, and propose the model of particles arrangement at interface.

(4). Investigate the slippery behavior of a novel small molecule (the same small molecule in objective No. 2) functionalized surface at water/oil and water/gas interface.

1.6 Structure of thesis

Chapter 1 introduces the current challenges of oil related issues and the development of functional materials to destabilize or stabilize the emulsions. The mechanism of emulsion formation and stabilization, and the nanomechanical techniques to study the interactions in emulsions at nanoscale are also introduced. The objectives of this project are clarified.

Chapter 2 describes the characterizations and techniques used in this project including working principles of AFM force measurements and QCM-D measurements, the setup and operation procedure of ITFDA, procedures of measuring contact angle and IFT, and other surface characterizations such as transmission electron microscopy (TEM), and X-ray diffraction (XRD).

Chapter 3 synthesizes a superhydrophilic magnetic microsphere to destabilize the asphaltenes stabilized W/O emulsion at room temperature. The property of synthesized microsphere are characterized and the interactions between asphaltenes and superhydrophilic polyelectrolyte at oil/water interface are studied using techniques including XRD, TEM, AFM force measurement, QCMD, and IFT, for better understanding of the destabilization mechanism.

Chapter 4 synthesizes hydrophobic fiber-based scalable materials using a novel small molecule for oil/water separation, oil absorption and demulsification of surfactant/asphaltenes stabilized emulsions. The surface properties of synthesized materials, the interactions between oil/water droplet and synthesized materials, and the hydrophobic interaction between an air bubble and novel small molecule coated surface in water are characterized using techniques including SEM, ITFDA and AFM force measurement for better understanding of the destabilization mechanism.

Chapter 5 demonstrates the stabilization mechanism and interfacial interactions of a pH-responsive Pickering emulsion stabilized by double oleic acid layer coated nanoparticles using techniques including AFM force measurement, IFT and optical imaging. Two models of nanoparticles arrangement around emulsified droplets at oil/water interface are proposed and the effects of force load and dwell time are studied.

Chapter 6 synthesizes a slippery surface using a liquid-like small molecule (the same small molecule used in Chapter 4) and studies the slippery behavior of sliding air bubble in water, water droplet in air and water droplet in oil. The forces related to the air bubble/droplet transportation is theoretically analyzed and the surface properties including surface tension and surface morphology is studied using techniques including AFM imaging and contact angle for better understanding of the slippery behavior.

Chapter 7 presents the major conclusion and the future work of this thesis.

References

1. Xue, Z., Cao, Y., Liu, N., Feng, L. & Jiang, L. Special wettable materials for oil/water separation. *Journal of Materials Chemistry A* vol. 2 2445–2460 (2014).

2. Nordvik, A. B., Simmons, J. L., Bitting, K. R., Lewis, A. & Strøm-Kristiansen, T. Oil and water separation in marine oil spill clean-up operations. *Spill Sci. Technol. Bull.* **3**, 107–122 (1996).

3. Yang, F. *et al.* Asphaltene Subfractions Responsible for Stabilizing Water-in-Crude Oil Emulsions. Part 2: Molecular Representations and Molecular Dynamics Simulations. *Energy & Fuels* **29**, 4783–4794 (2015).

4. Jamaly, S., Giwa, A. & Hasan, S. W. Recent improvements in oily wastewater treatment: Progress, challenges, and future opportunities. *Journal of Environmental Sciences (China)* vol. 37 15–30 (2015).

5. Barrera-Díaz, C., Roa-Morales, G., Ávila-Córdoba, L., Pavón-Silva, T. & Bilyeu, B. Electrochemical Treatment Applied to Food-Processing Industrial Wastewater. *Ind. Eng. Chem. Res.* **45**, 34–38 (2006).

6. Hachem, C., Bocquillon, F., Zahraa, O. & Bouchy, M. Decolourization of textile industry wastewater by the photocatalytic degradation process. *Dye. Pigment.* **49**, 117–125 (2001).

7. Asatekin, A. & Mayes, A. M. Oil industry wastewater treatment with fouling resistant membranes containing amphiphilic comb copolymers. *Environ. Sci. Technol.* **43**, 4487–4492 (2009).

8. Hearn, M. Contesting ‘the Ballarat cry’: Interpreting the unstable narrative of trade and race

in the 1903 federal election. *Hist. Aust.* **15**, 693–710 (2018).

9. Schrope, M. Oil spill: Deep wounds. *Nature* vol. 472 152–154 (2011).

10. Yue, X., Li, Z., Zhang, T., Yang, D. & Qiu, F. Design and fabrication of superwetting fiber-based membranes for oil/water separation applications. *Chemical Engineering Journal* vol. 364 292–309 (2019).

11. Moradi, M., Alvarado, V. & Huzurbazar, S. Effect of salinity on water-in-crude oil emulsion: Evaluation through drop-size distribution proxy. *Energy and Fuels* **25**, 260–268 (2011).

12. Tadros, T. F. *Emulsion Formation and Stability*. *Emulsion Formation and Stability* vol. 13 (2013).

13. Goubault, C. *et al.* Shear rupturing of complex fluids: Application to the preparation of quasi-monodisperse water-in-oil-in-water double emulsions. *Langmuir* **17**, 5184–5188 (2001).

14. Da Rocha, S. R. P., Harrison, K. L. & Johnston, K. P. Effect of Surfactants on the Interfacial Tension and Emulsion Formation between Water and Carbon Dioxide. *Langmuir* **15**, 419–428 (1999).

15. Barnes, T. J. & Prestidge, C. A. PEO-PPO-PEO block copolymers at the emulsion droplet-water interface. *Langmuir* **16**, 4116–4121 (2000).

16. Xin, X. *et al.* Influence of CTAB and SDS on the properties of oil-in-water nano-emulsion with paraffin and span 20/Tween 20. *Colloids Surfaces A Physicochem. Eng. Asp.* **418**, 60–67 (2013).

17. Meneghetti, P. & Qutubuddin, S. Synthesis of Poly(methyl methacrylate) Nanocomposites via Emulsion Polymerization Using a Zwitterionic Surfactant. *Langmuir* **20**, 3424–3430 (2004).

18. Opawale, F. O. & Burgess, D. J. Influence of interfacial properties of lipophilic surfactants on water- in-oil emulsion stability. *J. Colloid Interface Sci.* **197**, 142–150 (1998).

19. Khan, B. A. *et al.* Basics of pharmaceutical emulsions: A review. *African Journal of Pharmacy and Pharmacology* vol. 5 2715–2725 (2011).

20. Pickering, S. U. CXCVI-Emulsions. *J. Chem. Soc. Trans.* **91**, 2001–2021 (1907).

21. Yang, Y. *et al.* An overview of pickering emulsions: Solid-particle materials, classification, morphology, and applications. *Frontiers in Pharmacology* vol. 8 287 (2017).

22. Binks, B. P. Particles as surfactants - Similarities and differences. *Curr. Opin. Colloid Interface Sci.* **7**, 21–41 (2002).

23. Binks, B. P. & Lumsdon, S. O. Stability of oil-in-water emulsions stabilised by silica particles. *Phys. Chem. Chem. Phys.* **1**, 3007–3016 (1999).

24. Binks, B. P. & Clint, J. H. Solid wettability from surface energy components: Relevance to pickering emulsions. *Langmuir* **18**, 1270–1273 (2002).

25. Xie, C. Y. *et al.* Light and Magnetic Dual-Responsive Pickering Emulsion Micro-Reactors. *Langmuir* **33**, 14139–14148 (2017).

26. Lan, Q. *et al.* Synthesis of bilayer oleic acid-coated Fe3O4nanoparticles and their application in pH-responsive Pickering emulsions. *J. Colloid Interface Sci.* **310**, 260–269

(2007).

27. Saigal, T., Dong, H., Matyjaszewski, K. & Tilton, R. D. Pickering emulsions stabilized by nanoparticles with thermally responsive grafted polymer brushes. *Langmuir* **26**, 15200–15209 (2010).

28. Mullins, O. C. The asphaltenes. *Annu. Rev. Anal. Chem.* **4**, 393–418 (2011).

29. Langevin, D. & Argillier, J. F. Interfacial behavior of asphaltenes. *Advances in Colloid and Interface Science* vol. 233 83–93 (2016).

30. Eyssautier, J. *et al.* Insight into asphaltene nanoaggregate structure inferred by small angle neutron and X-ray scattering. *J. Phys. Chem. B* **115**, 6827–6837 (2011).

31. Porte, G., Zhou, H. & Lazzeri, V. Reversible description of asphaltene colloidal association and precipitation. *Langmuir* **19**, 40–47 (2003).

32. Gawrys, K. L. & Kilpatrick, P. K. Asphaltenic aggregates are polydisperse oblate cylinders. *J. Colloid Interface Sci.* **288**, 325–334 (2005).

33. Fenistein, D. *et al.* Viscosimetric and neutron scattering study of asphaltene aggregates in mixed toluene/heptane solvents. *Langmuir* **14**, 1013–1020 (1998).

34. Roux, J. N., Broseta, D. & Demé, B. SANS study of asphaltene aggregation: Concentration and solvent quality effects. *Langmuir* **17**, 5085–5092 (2001).

35. Alvarez, G., Jestin, J., Argillier, J. F. & Langevin, D. Small-angle neutron scattering study of crude oil emulsions: Structure of the oil - Water interfaces. *Langmuir* **25**, 3985–3990 (2009).

36. Jestin, J., Simon, S., Zupancic, L. & Barré, L. A small angle neutron scattering study of the adsorbed asphaltene layer in water-in-hydrocarbon emulsions: Structural description related to stability. *Langmuir* **23**, 10471–10478 (2007).

37. Strassner, J. E. Effect of pH on Interfacial Films and Stability of Crude Oil-Water Emulsions. *J. Pet. Technol.* **20**, 303–312 (1968).

38. Yarranton, H. W., Sztukowski, D. M. & Urrutia, P. Effect of interfacial rheology on model emulsion coalescence. I. Interfacial rheology. *J. Colloid Interface Sci.* **310**, 246–252 (2007).

39. Yarranton, H. W., Sztukowski, D. M. & Urrutia, P. Effect of interfacial rheology on model emulsion coalescence. I. Interfacial rheology. *J. Colloid Interface Sci.* **310**, 246–252 (2007).

40. Yeung, A., Moran, K., Masliyah, J. & Czarnecki, J. Shear-induced coalescence of emulsified oil drops. *J. Colloid Interface Sci.* **265**, 439–443 (2003).

41. Zhang, L., Shi, C., Lu, Q., Liu, Q. & Zeng, H. Probing Molecular Interactions of Asphaltenes in Heptol Using a Surface Forces Apparatus: Implications on Stability of Water-in-Oil Emulsions. *Langmuir* **32**, 4886–4895 (2016).

42. Freer, E. M. & Radke, C. J. Relaxation of asphaltenes at the toluene/water interface: Diffusion exchange and surface rearrangement. *J. Adhes.* **80**, 481–496 (2004).

43. Yang, F. *et al.* Asphaltene subfractions responsible for stabilizing water-in-crude oil emulsions. Part 1: Interfacial behaviors. *Energy and Fuels* **28**, 6897–6904 (2014).

44. Chaverot, P., Cagna, A., Glita, S. & Rondelez, F. Interfacial tension of bitumen - Water interfaces. Part 1: Influence of endogenous surfactants at acidic pH. *Energy and Fuels* **22**, 790–798 (2008).

45. Xu, Y., Dabros, T., Hamza, H. & Shefantook, W. Destabilization of water in bitumen emulsion by washing with water. *Pet. Sci. Technol.* **17**, 1051–1070 (1999).

46. Poteau, S., Argillier, J. F., Langevin, D., Pincet, F. & Perez, E. Influence of pH on stability and dynamic properties of asphaltenes and other amphiphilic molecules at the oil-water interface. *Energy and Fuels* **19**, 1337–1341 (2005).

47. Moradi, M., Alvarado, V. & Huzurbazar, S. Effect of salinity on water-in-crude oil emulsion: Evaluation through drop-size distribution proxy. *Energy and Fuels* **25**, 260–268 (2011).

48. Borges, B., Rondón, M., Sereno, O. & Asuaje, J. Breaking of water-in-crude-oil emulsions. 3. influence of salinity and water-oil ratio on demulsifier action. in *Energy and Fuels* vol. 23 1568–1574 (2009).

49. Shi, C. *et al.* Interaction Mechanism of Oil-in-Water Emulsions with Asphaltenes Determined Using Droplet Probe AFM. *Langmuir* **32**, 2302–2310 (2016).

50. Rohrbach, K. *et al.* A cellulose based hydrophilic, oleophobic hydrated filter for water/oil separation. *Chem. Commun.* **50**, 13296–13299 (2014).

51. Liu, Y., Wang, X. & Feng, S. Nonflammable and Magnetic Sponge Decorated with Polydimethylsiloxane Brush for Multitasking and Highly Efficient Oil–Water Separation. *Adv. Funct. Mater.* **29**, 1902488 (2019).

52. Feng, S., Zhong, Z., Zhang, F., Wang, Y. & Xing, W. Amphiphobic Polytetrafluoroethylene Membranes for Efficient Organic Aerosol Removal. *ACS Appl. Mater. Interfaces* **8**, 8773–8781 (2016).

53. Murakami, D., Jinnai, H. & Takahara, A. Wetting transition from the cassie-baxter state to the wenzel state on textured polymer surfaces. *Langmuir* **30**, 2061–2067 (2014).

54. Liu, M., Wang, S., Wei, Z., Song, Y. & Jiang, L. Bioinspired design of a superoleophobic and low adhesive water/solid interface. *Adv. Mater.* **21**, 665–669 (2009).

55. Liang, C., He, X., Liu, Q. & Xu, Z. Adsorption-Based Synthesis of Magnetically Responsive and Interfacially Active Composite Nanoparticles for Dewatering of Water-in-Diluted Bitumen Emulsions. *Energy and Fuels* **32**, 8078–8089 (2018).

56. Yuan, T., Meng, J., Hao, T., Wang, Z. & Zhang, Y. A scalable method toward superhydrophilic and underwater superoleophobic PVDF membranes for effective oil/water emulsion separation. *ACS Appl. Mater. Interfaces* **7**, 14896–14904 (2015).

57. Yang, X. *et al.* Bio-inspired method for preparation of multiwall carbon nanotubes decorated superhydrophilic poly(vinylidene fluoride) membrane for oil/water emulsion separation. *Chem. Eng. J.* **321**, 245–256 (2017).

58. Li, X., Cao, M., Shan, H., Handan Tezel, F. & Li, B. Facile and scalable fabrication of superhydrophobic and superoleophilic PDMS-co-PMHS coating on porous substrates for highly effective oil/water separation. *Chem. Eng. J.* **358**, 1101–1113 (2019).

59. Wang, D. *et al.* Stabilization mechanism and chemical demulsification of water-in-oil and oil-in-water emulsions in petroleum industry: A review. *Fuel* vol. 286 119390 (2021).

60. Mansur, C. R. E., Barboza, S. P., González, G. & Lucas, E. F. PLURONIC x TETRONIC polyols: Study of their properties and performance in the destabilization of emulsions formed in the petroleum industry. *J. Colloid Interface Sci.* **271**, 232–240 (2004).

61. Mansur, C. R. E., Lechuga, F. C., Mauro, A. C., González, G. & Lucas, E. F. Behavior of mixtures of nonionic polyoxide-based surfactants and their application in the destabilization of oil emulsions. *J. Appl. Polym. Sci.* **106**, 2947–2954 (2007).

62. Bhattacharyya, B. R., Nikolov, A. D. & Wasan, D. T. Demulsification of Water in Oil Emulsions Using Water Soluble Demulsifiers. *J. Dispers. Sci. Technol.* **13**, 121–133 (1992).

63. Al-Sabagh, A. M., Nasser, N. M., El-Sukkary, M. M. A., Eissa, A. M. F. & Abd El-Hamid, T. M. Demulsification Efficiency of Some New Stearate Esters of Ethoxylated and Propoxylated 1,8-Diamino-Octane for Water in Crude Oil Emulsions. *J. Dispers. Sci. Technol.* **34**, 1409–1420 (2013).

64. Wu, J., Xu, Y., Dabros, T. & Hamza, H. Effect of Demulsifier Properties on Destabilization of Water-in-Oil Emulsion. *Energy and Fuels* **17**, 1554–1559 (2003).

65. Fan, Y., Simon, S. & Sjöblom, J. Chemical destabilization of crude oil emulsions: Effect of nonionic surfactants as emulsion inhibitors. *Energy and Fuels* **23**, 4575–4583 (2009).

66. Daniel-David, D. *et al.* Elastic properties of crude oil/water interface in presence of polymeric emulsion breakers. *Colloids Surfaces A Physicochem. Eng. Asp.* **270**–**271**, 257–262 (2005).

67. Feng, X. *et al.* Effect of hydroxyl content and molecular weight of biodegradable ethylcellulose on demulsification of water-in-diluted bitumen emulsions. *Ind. Eng. Chem. Res.* **50**, 6347–6354 (2011).

68. Zhang, Z., Xu, G., Wang, F., Dong, S. & Chen, Y. Demulsification by amphiphilic dendrimer copolymers. *J. Colloid Interface Sci.* **282**, 1–4 (2005).

69. Xu, Y. *et al.* Breaking water-in-bitumen emulsions using polyoxyalkylated DETA demulsifier. *Can. J. Chem. Eng.* **82**, 829–835 (2004).

70. Adewunmi, A. A., Kamal, M. S. & Solling, T. I. Application of magnetic nanoparticles in demulsification: A review on synthesis, performance, recyclability, and challenges. *Journal of Petroleum Science and Engineering* vol. 196 107680 (2021).

71. Zhang, L., Li, L. & Dang, Z. M. Bio-inspired durable, superhydrophobic magnetic particles for oil/water separation. *J. Colloid Interface Sci.* **463**, 266–271 (2016).

72. Wang, X., Shi, Y., Graff, R. W., Lee, D. & Gao, H. Developing recyclable pH-responsive magnetic nanoparticles for oil-water separation. *Polymer (Guildf).* **72**, 361–367 (2015).

73. Song, Y. *et al.* Hydrophilic/Oleophilic Magnetic Janus Particles for the Rapid and Efficient Oil–Water Separation. *Adv. Funct. Mater.* **28**, 1802493 (2018).

74. Feng, L. *et al.* A Super-Hydrophobic and Super-Oleophilic Coating Mesh Film for the Separation of Oil and Water. *Angew. Chemie* **116**, 2046–2048 (2004).

75. Shi, Z. *et al.* Ultrafast Separation of Emulsified Oil/Water Mixtures by Ultrathin Free-Standing Single-Walled Carbon Nanotube Network Films. *Adv. Mater.* **25**, 2422–2427 (2013).

76. Zhou, J. E., Chang, Q., Wang, Y., Wang, J. & Meng, G. Separation of stable oil-water emulsion by the hydrophilic nano-sized ZrO2 modified Al2O3 microfiltration membrane. *Sep. Purif. Technol.* **75**, 243–248 (2010).

77. Zhou, X. *et al.* Robust and durable superhydrophobic cotton fabrics for oil/water separation. *ACS Appl. Mater. Interfaces* **5**, 7208–7214 (2013).

78. Serhan, M. *et al.* Total iron measurement in human serum with a smartphone. in *AIChE Annual Meeting, Conference Proceedings* vols 2019-Novem 1–3 (2019).

79. Yang, H. & Deng, Y. Preparation and physical properties of superhydrophobic papers. *J. Colloid Interface Sci.* **325**, 588–593 (2008).

80. Kim, J. W., Lee, D., Shum, H. C. & Weitz, D. A. Colloid surfactants for emulsion stabilization. *Adv. Mater.* **20**, 3239–3243 (2008).

81. Tavernier, I., Wijaya, W., Van der Meeren, P., Dewettinck, K. & Patel, A. R. Food-grade particles for emulsion stabilization. *Trends in Food Science and Technology* vol. 50 159–174 (2016).

82. Boyd, J., Parkinson, C. & Sherman, P. Factors affecting emulsion stability, and the HLB concept. *J. Colloid Interface Sci.* **41**, 359–370 (1972).

83. Kumar, N. & Mandal, A. Surfactant Stabilized Oil-in-Water Nanoemulsion: Stability, Interfacial Tension, and Rheology Study for Enhanced Oil Recovery Application. *Energy and Fuels* **32**, 6452–6466 (2018).

84. Wei, Y., Xie, Y., Cai, Z., Guo, Y. & Zhang, H. Interfacial rheology, emulsifying property and emulsion stability of glyceryl monooleate-modified corn fiber gum. *Food Chem.* **343**, 128416 (2021).

85. Da Rocha, S. R. P., Harrison, K. L. & Johnston, K. P. Effect of Surfactants on the Interfacial Tension and Emulsion Formation between Water and Carbon Dioxide. *Langmuir* **15**, 419–428 (1999).

86. Vignati, E., Piazza, R. & Lockhart, T. P. Pickering emulsions: Interfacial tension, colloidal

layer morphology, and trapped-particle motion. *Langmuir* **19**, 6650–6656 (2003).

87. Sharkawy, A., Barreiro, M. F. & Rodrigues, A. E. Chitosan-based Pickering emulsions and their applications: A review. *Carbohydrate Polymers* vol. 250 116885 (2020).

88. Li, M. F. *et al.* The formation of zein-chitosan complex coacervated particles: Relationship to encapsulation and controlled release properties. *Int. J. Biol. Macromol.* **116**, 1232–1239 (2018).

89. Atarian, M., Rajaei, A., Tabatabaei, M., Mohsenifar, A. & Bodaghi, H. Formulation of Pickering sunflower oil-in-water emulsion stabilized by chitosan-stearic acid nanogel and studying its oxidative stability. *Carbohydr. Polym.* **210**, 47–55 (2019).

90. Jian, C., Liu, Q., Zeng, H. & Tang, T. A Molecular Dynamics Study of the Effect of Asphaltenes on Toluene/Water Interfacial Tension: Surfactant or Solute? *Energy and Fuels* **32**, 3225–3231 (2018).

91. Liu, J. *et al.* Destabilization of fine solids suspended in oil media through wettability modification and water-assisted agglomeration. *Fuel* **254**, 115623 (2019).

92. Niu, Z. *et al.* Interfacial properties pertinent to W/O and O/W emulsion systems prepared using polyaromatic compounds. *Colloids Surfaces A Physicochem. Eng. Asp.* **575**, 283–291 (2019).

93. Natarajan, A. *et al.* Understanding molecular interactions of asphaltenes in organic solvents using a surface force apparatus. *J. Phys. Chem. C* **115**, 16043–16051 (2011).

94. Shi, C. *et al.* Interaction Mechanism of Oil-in-Water Emulsions with Asphaltenes Determined Using Droplet Probe AFM. *Langmuir* **32**, 2302–2310 (2016).

95. Shi, C., Xie, L., Zhang, L., Lu, X. & Zeng, H. Probing the interaction mechanism between oil droplets with asphaltenes and solid surfaces using AFM. *J. Colloid Interface Sci.* **558**, 173–181 (2019).

Chapter 2 Experimental Methodologies

2.1 AFM force measurement

The AFM (atomic force microscope) force measurement is a powerful tool to study the interaction force at nanoscale between two surfaces across a medium[1–3]. As shown in Figure 2.1, the AFM mainly consists of a laser source, a cantilever with tip, sample stage, scanner, and photodiode. The scanner is composed by three piezo components to manage the horizontal (x and y direction) and vertical (z direction) movement of sample. In the force measurement, the cantilever is placed at a certain place above the sample. Then the cantilever is driven to approach the sample at a fixed speed until a pre-set deflection of cantilever is reached, after which the cantilever is driven back to the original position. The laser is focused on the end of cantilever and reflected to a photo detector. The deflection of cantilever leads to the change of laser signal which is detected and monitored by photo detector. In this case, the deflection of cantilever caused by interaction force between the sample and the tip is monitored. Then the interaction force is obtained by converting the deflection of cantilever using Hooke's law. After measurement, the curve of force versus the relative separation distance between tip and sample can be plotted. AFM cannot measure the absolute separation distance between tip and sample and the zero point of relative separation distance can be selected arbitrarily, such as at the maximum deflection of cantilever[4]. The tip and sample can be functionalized with functional materials if needed and the measurement can be done in air or across a fluid media. Besides cantilever with tip, a tipless cantilever glued with silica microsphere or tipless cantilever pre-treated to pick up a water droplet/oil droplet/air bubble can also be applied in AFM force measurement based on the specific needs.

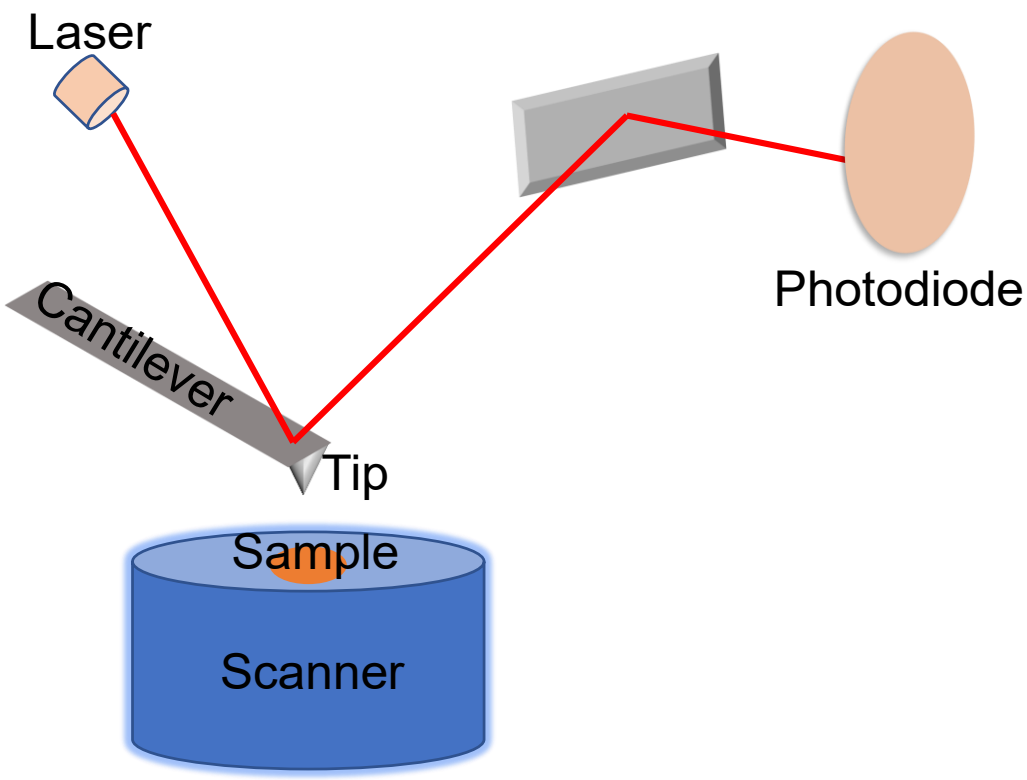

Figure 2.1 Schematic setup of AFM.

2.2 QCMD measurement

The QCMD (quartz crystal microbalance with dissipation) is a very useful nanoscale tool to measure the real-time interactions and thin film formations. The QCMD sensor is a thin quartz crystal sandwiched between a pair of electrodes and works as a microbalance in the experiment. When a thin and rigid film is adsorbed on the sensor in experiment, the frequency will decrease, and the change of frequency is proportional to the mass of adhered thin film. The relationship between mass and frequency can be expressed by Sauerbrey equation $\Delta m = -\frac{C\Delta f}{n}$, where Δm is adsorbed mass, Δf is the frequency shift, n is the order of harmonic overtones of the crystal sensor and n equals to 1,3,5,7,9,11, C =17.7 ng/(Hz·cm^2) for 5 MHz crystal sensor.

2.3 Contact angle and IFT measurement

The contact angle and IFT (interfacial tension) measurement are both critical techniques in experiments for surface property and interfacial property. The contact angle and IFT are measured using a goniometer/tensiometer, the setup of which is simply illustrated in Figure 2.2. In the contact angle measurement, the substrate is placed on sample stage and a sessile drop is generated on the substrate. Then the image is captured by the camera to measure contact angle using software when the contact line between sessile drop and substrate is defined. In the measurement of IFT, the needle is immersed in a quartz cell placed on the sample stage and filled with liquid/air. A pendant drop is generated at the tip of needle and the shape of pendant drop is monitored by camera. The interfacial tension is automatically obtained in the software by analyzing the pendent drop shape and the properties (e.g., density) of the bulk liquid/air and pendant drop.

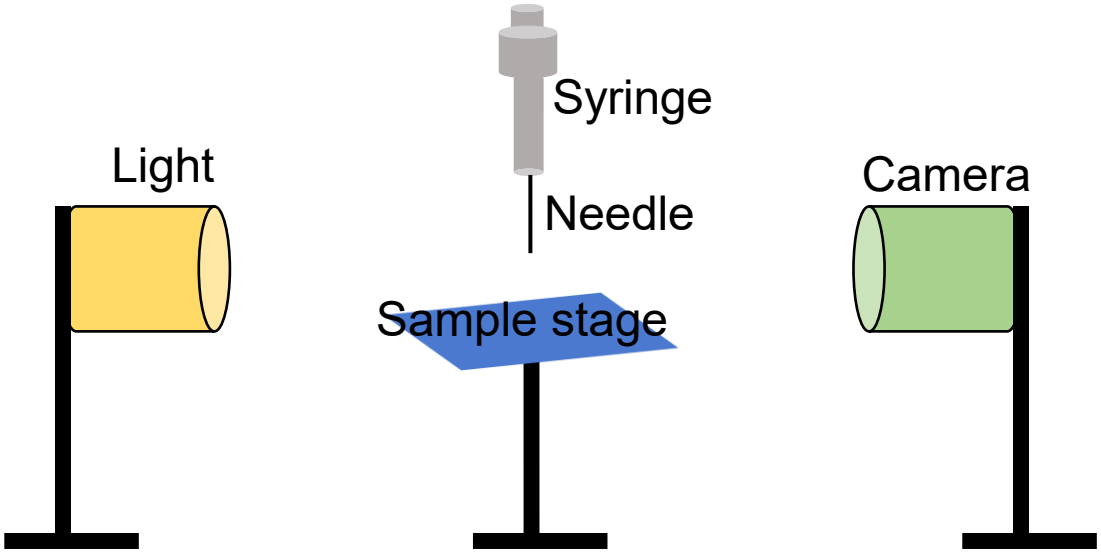

Figure 2.2 Schematic setup of goniometer/tensiometer.

2.4 ITFDA

The ITFDA, integrated thin film drainage apparatus, is a technique to analyze the interaction force between a drop and a sample substrate at microscale. As presented in Figure 2.3, the ITFDA consists of a glass cell, actuator, capillary tube, sample stage and bimorph. A droplet is generated using a gastight syringe at one end of the glass capillary tube (inner radius 0.74±0.05 mm) and the movement toward/away from the sample is controlled by a motorized actuator. The sample is fixed on the round shape sample stage clamped at the free end of bimorph cantilever. The bimorph consists of two piezoelectric slabs that is sandwiched together to form a bending type force transducer and covered in a fluorinated ethylene propylene sheath with the other end connected to a high impedance charge amplifier. The force exerted on sample stage leads to the deflection of bimorph to generate electrical charge. The relationship between exerted force and electric charge can be calibrated by applying known weights at sample stage. The interaction between drop and sample is recorded by a CCD camera. The glass cell can be filled with water/oil for under liquid measurement at room temperature.

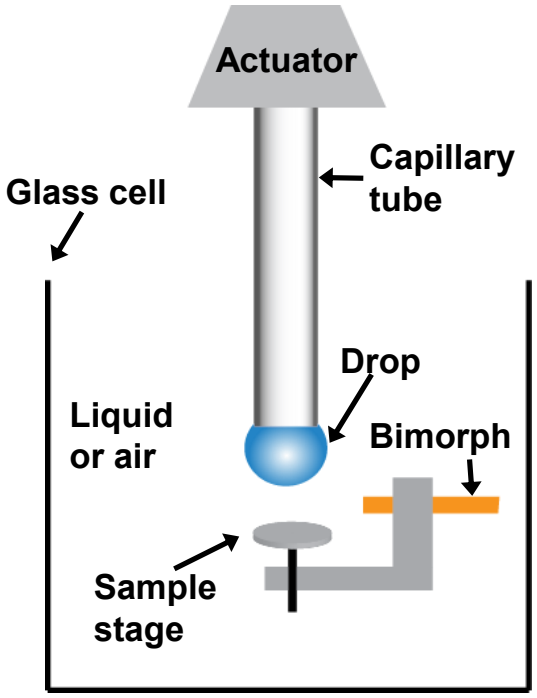

Figure 2.3 The schematic setup of ITFDA.

2.5 Other characterizations

In addition to the AFM, QCMD, ITFDA technique, other techniques such as zeta potential, X-ray diffraction (XRD), Transmission Electron Microscope (TEM) are also used in this project. Zeta potential is measured using a Zetasizer Nano ZSP (Malvern Instruments, UK). XRD is performed using a Rigaku Ultimate IV X-ray diffractometer with Cu Kα radiation (40 kV, 40 mA). The TEM images of samples are characterized using a JEOL 2200FS Transmission Electron Microscope. The attenuated total reflectance Fourier transform infrared (ATR-FTIR) spectrum of samples are measured on ATR-FTIR (Thermo Scientific Nicolet iS50). The field emission scanning electron microscope (FE-SEM) images and energy dispersive X-ray spectroscopy (EDS) were conducted on Zeiss Sigma SEM (Carl Zeiss, Germany). X-ray photoelectron spectroscopy (XPS) was analyzed on a PHI VersaProbe III (Φ ULVAC-PHI, Inc., Japan/USA) and a Kratos Axis spectrometer with monochromatized Al Kα. The C 1s peak at 284.6 eV is used to correct all XPS

spectra. The molecular weight and molecular weight distribution (PDI) are determined by gel permeation chromatography (GPC) (Viscotek model 250 dual detectors system), using 0.5 M sodium acetate and 0.5 M acetic acid as eluent. The cyclic voltammetry measurement is performed using a CHI 920c electrochemical workstation (CH Instruments Inc.) with a platinum wire (counter electrode), Ag/AgCl (1 M KCl) microelectrode (reference electrode, 0.222 V vs standard hydrogen electrode (SHE)). All potentials quoted are referred to the Ag/AgCl (1 M KCl) reference electrode. The thickness of sample is measured using a spectroscopic ellipsometer (Sopra GESP-5, France).

References

1. Xie, L. *et al.* Interaction Mechanisms between Air Bubble and Molybdenite Surface: Impact of Solution Salinity and Polymer Adsorption. *Langmuir* **33**, 2353–2361 (2017).

2. Shi, C. *et al.* Long-Range Hydrophilic Attraction between Water and Polyelectrolyte Surfaces in Oil. *Angew. Chemie - Int. Ed.* **55**, 15017–15021 (2016).

3. Shi, C. *et al.* Interaction Mechanism of Oil-in-Water Emulsions with Asphaltenes Determined Using Droplet Probe AFM. *Langmuir* **32**, 2302–2310 (2016).

4. Shi, C. *et al.* Measuring forces and spatiotemporal evolution of thin water films between an air bubble and solid surfaces of different hydrophobicity. *ACS Nano* **9**, 95–104 (2015).

Chapter 3 Novel Fe_3O_4 Based Superhydrophilic Core-shell Microspheres for Breaking Asphaltenes-stabilized Water-in-oil Emulsion

3.1 Introduction

Emulsions have been used in a broad range of biological and technical applications, such as food science[1-3], pharmaceutical[4-6] and oil industry[7-9]. When two immiscible liquids encounter each other under mixing, one liquid generally disperses as drops in the other liquid, where emulsions are generally formed[10-12]. For example, oil and water can form water-in-oil (W/O) emulsions, oil-in-water (O/W) emulsions and even multiple emulsions, such as water-in-oil-in-water (W/O/W) and vice versa[13]. Thermodynamically, emulsions are generally considered to be unstable as the dispersed drops can readily coalesce with each other due to the low energy barrier. To stabilize the emulsions, interface-active components, including amphiphilic polymers, Janus particles, proteins and surfactants, are commonly applied as emulsion stabilizers that can adsorb at the liquid/liquid interface, thereby elevating the energy barrier between emulsion drops and preventing the coalescence[14,15]. However, stable emulsions are undesirable in many engineering and environmental processes due to the challenges associated with the downstream processing in oil production (e.g., fouling, plugging and corrosion), oil-water separation and water treatment, thus demulsifiers are required to break the emulsions.

Over the past few decades, considerable effort has been devoted to developing effective demulsifiers, most of which focused on W/O emulsions such as water-in-diluted bitumen emulsion or water-in-crude oil emulsion, the most commonly encountered emulsions in production of conventional crude oil and oil sands[16–19]. Asphaltenes are generally considered to be the main stabilizers of emulsions in crude oil or bitumen, which is attributed to the heteroatoms (e.g., N, S, O) in polyaromatic cores and side chains of asphaltenes molecules[20–22]. Compared with bitumen,

asphaltenes can stabilize the W/O emulsion at a much lower concentration or form thicker organic liquid films when the concentrations are the same[23]. It has been found that the adsorption of asphaltenes is mostly irreversible due to the formation of a "skin-like" rigid film around water drops, and the drop size could be less than 5 μm to generate extremely stable emulsion[24]. The complex characters of asphaltenes have made the destabilization and removal of W/O emulsions to be one of the toughest challenges in the oil industry. Despite the significant progress achieved, studies on the demulsifiers for effectively breaking asphaltene-stabilized W/O emulsion are still limited[24–27]. Amphiphilic ethylene oxide (EO) and propylene oxide (PO) block polymer is one of the most commonly used commercial polymers to break the asphaltene-stabilized W/O emulsion, and the demulsification performance depends on the structure and relative ratio of EO and PO segments and polymer concentration[28]. The underlying demulsification mechanism was found to be attributed to the more interfacially active EO-PO polymers that compete with asphaltenes at the interface, penetrating and softening the interfacial asphaltenes film[29]. The traditional non-ionic emulsifiers are usually amphiphilic, which can affect the performance of demulsification and stabilize the emulsions if a high concentration is applied[29,30]. Thus, the development of a non-amphiphilic demulsifier, that can stay at the water-oil interface, may avoid the risk of emulsification by the amphiphilic demulsifiers.

Polyelectrolytes, well-known for their super-wettability, are promising candidates for water-oil separation as non-amphiphilic materials[31–34]. K. He *et al.* reported a zwitterionic poly(2-methacryloyloxylethyl phosphorylcholine) (PMPC) brush grafted surface which allows effective separation of oil-water mixture and the repellency of oil in either dry or water-wetted state[35]. Later, a long-range "hydrophilic" attraction was found between polyzwitterionic surface and water drop in oil media, originated from strong electrically induced dipole-dipole and ion-dipole

interactions[36]. Such strong attraction between polyzwitterions and water across oil could provide a facile strategy to demulsify the asphaltenes-stabilized W/O emulsions using microspheres coated with zwitterionic polyelectrolytes.

In this study, novel core-shell magnetic microspheres coated with superhydrophilic zwitterionic polyelectrolytes were synthesized by a facile method, which were used to break the asphaltene-stabilized water-in-toluene emulsion. Quartz crystal microbalance with dissipation (QCM-D) was conducted to investigate the adsorption of asphaltenes on polyelectrolyte surface in toluene. In addition, the water drop probe atomic force microscope (AFM) technique was employed to quantitatively measure the interaction forces between the water drop and polyelectrolyte surface in oil media in the presence of asphaltenes at the nanoscale. This work provides an insightful approach to synthesize new demulsifier materials and useful information regarding the interaction behaviors of water droplets with asphaltenes and superhydrophilic microspheres at the water/oil interface, with implications in breaking emulsions in a variety of environmental and engineering processes.

3.2 Material and methods

3.2.1 Materials

The C_7-asphaltenes (solid free) were extracted from Athabasca bitumen[37,38]. Iron(III) chloride hexahydrate ($FeCl_3 \cdot 6H_2O$), dopamine hydrochloride, sodium citrate (Na_3Cit), [2-(methacryloyloxy)ethyl]dimethyl-(3-sulfopropyl)ammonium hydroxide, 4-cyano-4-(phenylcarbonothioylthio)pentanoic acid and 4,4'-azobis(4-cyanovaleric acid) were obtained from Sigma-Aldrich. Ethylene glycol (EG), anhydrous sodium acetate (NaOAc), Tris(hydroxymethyl)aminomethane, sodium hydroxide (NaOH) and sodium borohydride ($NaBH_4$) were purchased from Fisher Scientific.

3.2.2 Preparation of poly{3-[dimethyl(2-methacryloyloxyethyl)ammonio] propanesulfonate} (PDMAPS)

The PDMAPS was prepared with a modified RAFT polymerization method[39]. The RAFT agent 4-cyano-4-(phenylcarbonothioylthio)pentanoic acid (0.4 mmol, 0.1120 g) was added into 100 mL 4 mM NaOH solution at 45 ℃ until fully dissolved. Then the monomer [2-(methacryloyloxy)ethyl]dimethyl-(3-sulfopropyl)ammonium hydroxide (20 mmol, 5.6000 g) and 4,4'-azobis(4-cyanovaleric acid) (0.08 mmol, 0.0224 g) were added. After purged with argon for 30 min to remove oxygen, the polymerization was conducted at 75 ℃ for 24 h. Thereafter, the polymer product was purified by dialysis against distilled water for 3 days. Pink powder polymer product was obtained after freeze-drying.

3.2.3 Preparation of Fe_3O_4@PDA-PDMAPS microsphere (FPPM)

The Fe_3O_4 microspheres and Fe_3O_4@PDA microspheres were prepared by following a previously reported method[40]. Then the prepared Fe_3O_4@PDA and PDMAPS were dissolved in Tris buffer solution (pH=8.5), stirring at room temperature for 24 h. The product was washed with distilled water and ethanol for three times. FPPM was obtained after drying under vacuum at room temperature.

3.2.4 Characterizations

X-ray diffraction (XRD) patterns were recorded on a Rigaku Ultimate IV X-ray diffractometer with Cu Kα radiation (40 kV, 40 mA). The morphologies of Fe_3O_4@PDA and FPPM were characterized by JEOL JEM 2100 Transmission Electron Microscope (TEM). All the other morphologies were characterized by JEOL 2200FS TEM. X-ray photoelectron spectroscopy (XPS) was analyzed on a Kratos Axis spectrometer with monochromatized Al Kα. The C 1s peak at 284.6 eV was used to correct all XPS spectra. The magnetic property was characterized on a

Quantum Design 9 T-PPMS magnetometer with an applied field between -10 000 and 10 000 at 300 K. The molecular weight and molecular weight distribution (PDI) were determined by gel permeation chromatography (GPC) (Viscotek model 250 dual detectors system), using 0.5 M sodium acetate and 0.5 M acetic acid as eluent.

3.2.5 Emulsion test

The W/O emulsion was prepared with 20 vol% distilled water and 80 vol% organic phase. The organic phase was 300 mg/L C_7-asphaltenes in toluene solution which was sonicated for 20 min to ensure complete dissolution before emulsion preparation. The distilled water was added to organic phase dropwise with an IKA T18 digital ultra-turrax homogenizer at 18 000 rpm for 8 min. The solution was set for 2 h after mixing. After settling, two phases were observed: continuous organic phase (supernatant) and a settled emulsion phase. The supernatant organic phase was removed except the layer very close to the interphase to avoid the trace removal of emulsion[41]. 15 mL of emulsion was prepared in each vial. 1 mL 3 mg/mL FPPM in toluene solution was added into one arbitrarily selected vial while 1 mL pure toluene was added into another one. The dispersion of FPPM in toluene is limited due to the hydrophilic polyelectrolyte outer layer. To facilitate the dispersion of the FPPM in oil phase, a low concentration (3 mg/mL) of FPPM in toluene was prepared and sonicated for 20 min. After sonication, the FPPM was well dispersed in toluene, which was immediately added into the emulsion. The two vials were hand-shaken for 1 min to mix the emulsion and added liquid. Then the emulsions were settled for 3 h before putting on a magnet. Pictures were taken before and after adding FPPM at 20, 40, 48 and 68 h. All the procedures were conducted under ambient temperature (23 °C).

3.2.6 AFM force measurement

PDMAPS was coated onto a gold wafer by following a method reported previously[35]. The interaction forces between PDMAPS coated gold surface and a water droplet in the asphaltene-in-toluene solution were measured using an MFP-3D AFM (Asylum Research, Santa Barbara, CA) mounted on an inverted microscope (Nikon Ti-U). For a typical test, the asphaltene-in-toluene solution was first injected in a fluid cell with a pre-hydrophobized glass substrate where the water droplets injected by a custom-made ultra-sharp glass pipet were spontaneously settled down and immobilized[42]. The water drops were aged for 10 min before the free asphaltenes in the solution were completely washed off by exchanging the solution with pure toluene. The water droplet was picked up by a custom-made silicon cantilever and placed above the PDMAPS coated wafer[43,44]. The force measurement was conducted by driving drop-anchored cantilever toward the PDMAPS coated gold surface until drop attachment occurred or until a certain deflection of cantilever was reached. To minimize the hydrodynamic effect, the driving velocity of water drop was kept at 1 μm/s. The spring constant of the cantilever was calibrated using Hutter's thermal method[45]. For each experiment, force curves of at least 5 water drops and two independently prepared PDMAPS substrates were measured and similar results were obtained. A schematic picture of the experimental setup was shown in Figure 3.1.

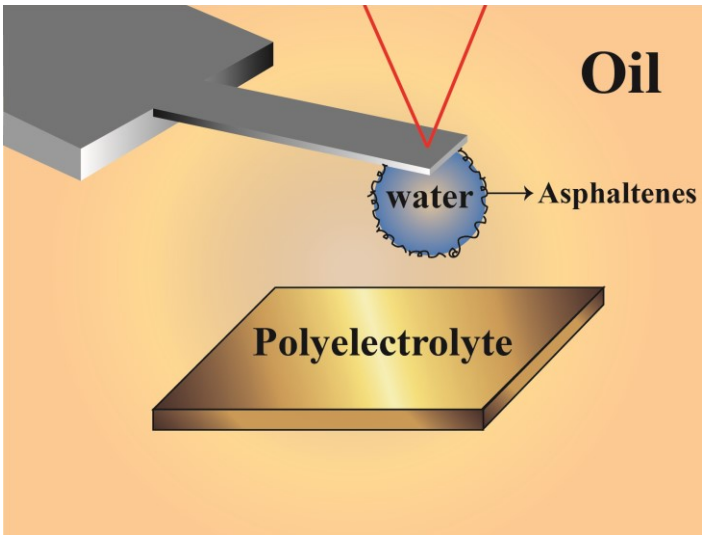

Figure 3.1 Schematic of AFM force measurement setup for measuring the interaction between a water drop and polyelectrolyte surface coated on gold wafer in oil (i.e., asphaltene-in-toluene solution).

3.2.7 Quartz crystal microbalance with dissipation monitoring (QCM-D) tests

The adsorption of asphaltenes on PDMAPS was monitored by a QCM-D E4 system (Q-sense, Sweden) employing a QCM-D sensor which is a thin piezoelectric crystal disk with gold electrodes on each side. The resonance frequency, *f*, and dissipation, D, will change simultaneously if the adsorption occurs on the sensor. Prior to each experiment, the PDMAPS was grafted onto the cleaned gold sensor using the same method in Section 2.6. A stable baseline was established by pumping background solution (pure toluene) into the QCM-D chamber. Then the asphaltene-in-toluene solution was pumped into the chamber at a flow rate of 0.35 mL/min for 50 mins when the frequency shift Δf became stable. The change of frequency (Δf) is related to the mass adsorbed (Δm) on the sensor surface by the Sauerbrey equation as follows,

$$\Delta m = -\frac{C \times \Delta f}{n} \tag{3.1}$$

where C is a constant as 17.7 ng $Hz^{-1}cm^{-2}$, Δf is frequency change in Hz, n is the overtone number which could be 1, 3, 5, 7, 9 or 13. In this work, n was chosen as 5 to show the typical data analysis.

3.2.8 Interfacial tension measurement

The interfacial tension (IFT) of asphaltene-in-toluene was measured in water using the pendant drop method using a standard tensiometer (ramè-hart, instrument Co., NJ, USA) at room temperature. In a typical measurement, the organic solution was loaded into a syringe with a U-shaped needle which was inserted in a quartz cell filled with distilled water. A pendant droplet was generated at the tip of the needle by a syringe pump. The droplet profile was captured by a high-speed charge-coupled device (CCD) camera every 1 s for 3600 s. All the experiments were performed on an anti-vibration table. IFT was measured using asphaltene-in-toluene solutions with asphaltene concentrations of 100, 200, 300, 400 and 500 mg/L with/without FPPM (1mg FPPM/15 mL asphaltene-in-toluene solution).

3.3 Results and discussion

3.3.1 Material characterizations

The molecular weight and polydispersity index (PDI) of synthesized PDMAPS were measured as 13.6 kDa and 1.35, respectively. The PDA was first coated on Fe_3O_4 (the grey color sphere) by dissolving the equal amount of PDA and Fe_3O_4 in Tris buffer (pH 8.5) for 24 h, after which the PDMAPS (red color) was deposited on the PDA layer (pale gold color), forming a core-shell structure (Figure 3.2)[46].

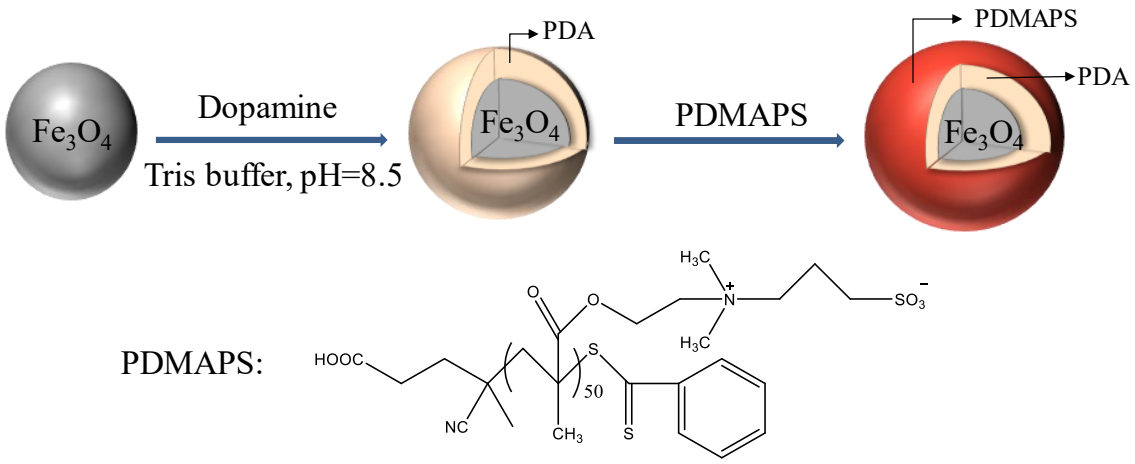

Figure 3.2 Schematic of synthesis route of Fe3O4@PDA-PDMAPS (FPPM) core-shell microspheres where dark grey sphere represents Fe3O4, rose gold and red color shells represent PDA and PDMAPS, respectively.

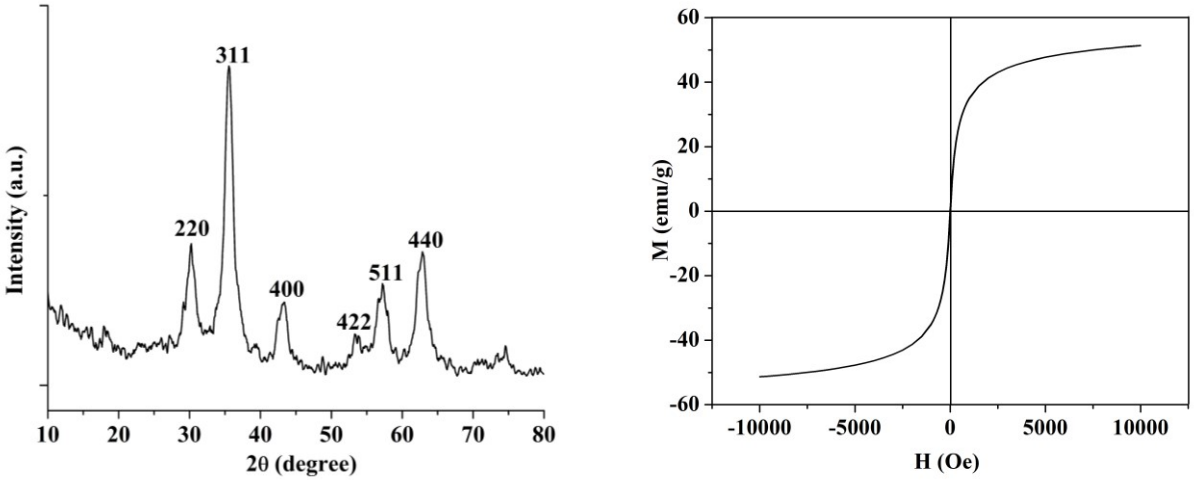

(a) (b)

Figure 3.3 (a) XRD spectrum of the Fe3O4 core; (b) Magnetic hysteresis loop of Fe3O4 core.

Figure 3a is the XRD result where all the peaks can be assigned to the typical pattern of Fe_3O_4 (JCPDS 19-0629), showing a crystalline structure. The saturation magnetization value (M_s) is

measured as 51 emu/g in the hysteresis loop (Figure 3.3b), which is sufficiently strong to collect the microspheres by a small magnet[40,47]. It should be noted that there is no hysteresis in the magnetization curve, suggesting the superparamagnetism of the Fe_3O_4 particles. The morphology of Fe_3O_4 core, Fe_3O_4@PDA and FPPM was characterized by TEM (Figure 3.4a-c), the average diameters of which were measured as 200 nm (Figure 3.4a), 212 nm (Figure 3.4b) and 216 nm (Figure 3.4c), respectively, indicating an average of ~10 nm PDA layer and ~4 nm PDMAPS layer. The synthesize core-shell particle is named as Fe_3O_4@PDA -PDMAPS Microsphere (FPPM) as the size is at sub-micron scale. The black line, green line and red line in Figure 3.4d show the XPS spectra for PDMAPS, Fe_3O_4@PDA and FPPM, respectively. The peak at 167 eV is assigned to S 2p which is a typical binding energy of S[48]. One obvious difference among the three spectra is that the S peak is present in the spectra of FPPM and PDMAPS while absent in the spectrum of Fe_3O_4@PDA. As PDMAPS is the only one of the three materials (Fe_3O_4, PDA and PDMAPS) containing S, the overlapped S peak in PDMAPS and FPPM spectra strongly suggests PDMAPS has been successfully coated around Fe_3O_4@PDA as outer layer. The S 2p peak could be deconvoluted into two peaks due to the S $2p_{3/2}$ and S $2p_{1/2}$ spin-orbit splitting[49]. It is worth mentioning that no peak can be assigned to Fe in the spectrum of Fe_3O_4@PDA, which is attributed to the well coated PDA shell. Since the detection depth of XPS is about 10 nm, to screen the Fe signal, the thickness of PDA layer should be at least ~10 nm, which agrees well with the TEM analysis.

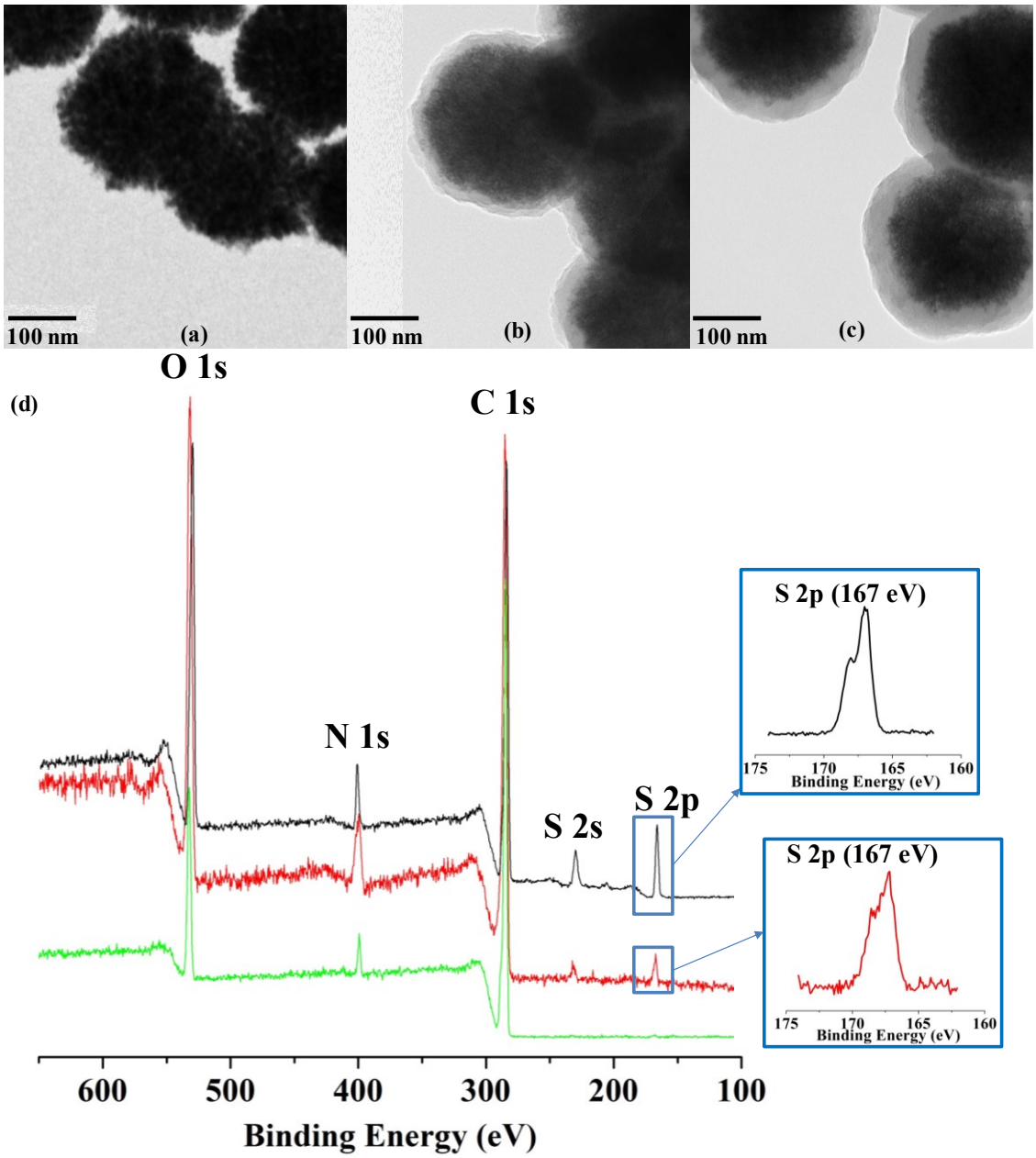

Figure 3.4 TEM images of (a) Fe3O4 core, (b) Fe3O4@PDA microspheres and (c) FPPM; (d) XPS spectra of PDMAPS polymer (black line), Fe3O4@PDA (green line) and FPPM (red line).

3.3.2 Performance of FPPM on W/O emulsion

To clarify the effect of FPPM on the destabilization of W/O emulsion in the presence of asphaltenes, a control experiment was conducted by adding 1 mL pure toluene into the emulsion

(vial B), as compared with the addition of 1 mL 3mg/mL FPPM in toluene (vial A). The destabilization performance was evaluated by monitoring the conditions of emulsion and the amount of released water. In Figure 3.5a, the two vials of emulsion were prepared under the same protocol, one of which was arbitrarily selected as the control experiment and labelled as B while the other one was labelled as A. The asphaltenes, known as the main factor contributing to the emulsion stability, can stabilize the W/O emulsion for a long time if no treatment is taken place. In many cases, physical treatments, such as high temperature or long time vigorous shaking, were employed together with the chemical treatment to facilitate the destabilization of emulsion[50–52]. In this work, to illustrate the influence of FPPM, all the above-mentioned treatments were not considered except 1 min hand-shaken to ensure the complete mixing of solutions. After the first 20 h, a considerable amount of free water was released at bottom left corner, and large water drops, mainly gathered at the bottom part, can be observed in vial A (Figure 3.5b). In comparison, no obvious change can be detected for the emulsion without FPPM (vial B), indicating the significant role of FPPM in destabilizing the emulsion. The samples at 0.8 cm from the bottom were taken for observation under optical microscopeafter 3 h. For emulsion samples from via A (Figure A.2a), coalesced water drops were observed, while the emulsion from vial B contained water drops with rigid round shape that stayed isolated from each other (Figure A.2b), which agrees well with the phenomenon described above (Figure 3.5b). The observed phenomena in Figure A.3 showed the changes of emulsion condition at micro level, suggesting the time of the initial appearance of free water was much earlier than 20 h. With longer time, large water drops started to appear in the top emulsion layer and more water was released. Meanwhile, the layer thickness of supernatant organic phase increased, attributed to the oil liberated from coalesced emulsion phase. At t=68 h, a thick water layer was formed at the bottom due to the continuous breaking of emulsions and

coalescence of water drops, which also led to shrinking of the emulsion layer and larger water drops. Overall, the emulsion kept coalescing, releasing free water after adding FPPM; while the reference emulsion remained almost unchanged without FPPM (Figure 3.5b-e).

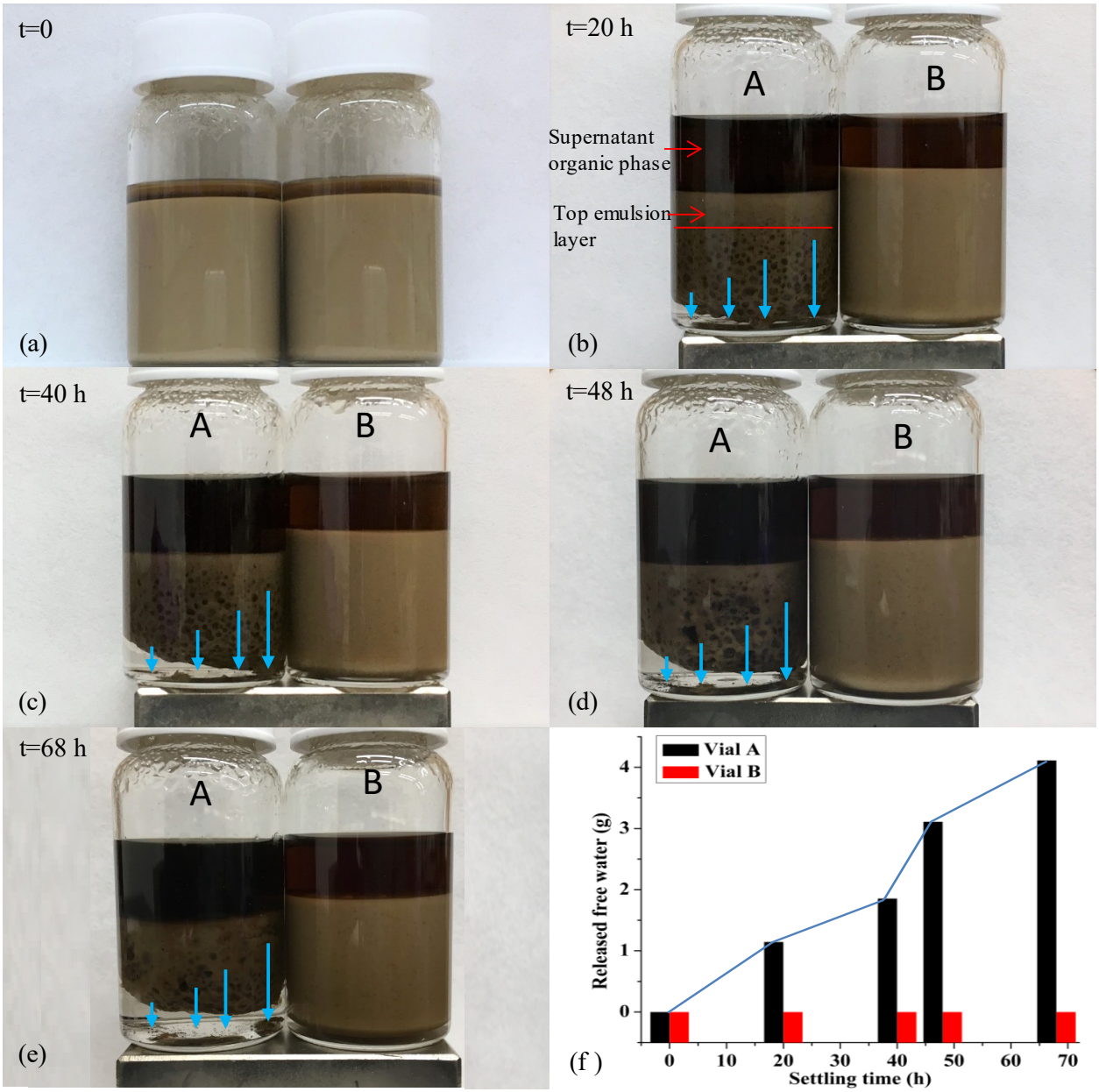

Figure 3.5 Images of (a) prepared water-in-oil emulsions in the presence of asphaltenes: after adding 1 mL 3 mg/mL FPPM in toluene solution (A) and 1 mL pure toluene (B). The emulsions were settled on magnet for (b) t=20 h, (c) 40 h, (d) 48 h, and (e) 68 h, respectively. The blue arrow

represents the direction of magnetic field. (f) The amount of released water with time (blue line: the trend of released water amount) for the two cases: Vial A with the addition of 1 mL 3 mg/mL FPPM in toluene solution, and Vial B (reference case) with the addition of 1 mL pure toluene.

The amount of released free water was weighed at different times (Figure 3.5f), showing a steady increase with time and a relatively sharp increase during 40-48 h. As shown in Figure 3.5b-d, more water drops were present at 40 h as compared to the case of 20 h, especially at the top part of emulsion, most of which coalesced and disappeared at 48 h, ultimately leading to a sharp increase of water amount. One phenomenon that is worth mentioning is the released water always initially appears in the position far from the center of the magnet, which can be attributed to the distribution of magnetic field. The vials were placed on the pole side of the magnet that exhibits the strongest magnetism among the external field, especially around the center of the pole. As shown in Figure 3.5a-e, the blue arrow represents the magnetic force and the length of arrows indicates the strength of magnetism. This strong magnetic force would drag more FPPM, as well as the trapped emulsion drops, to the pole center, which squeezes water to the side far from the center.

Another emulsion test was performed following the same procedure of vial A but without magnet (Figure A.3). After adding FPPM in toluene solution and handshaking, the color of emulsion turns darker than that of the initial state, indicating the uniform dispersion of black FPPM. At the first 20 h, the emulsion remained uniform and no change was observed. At 40 and 48 h, some tiny water drops appeared which can be observed clearly in the zoomed picture. With longer time, more water drops appeared (Figure A.3e), and the morphology of the emulsion was completely different from that at 20 h. After 96 h settling under gravity, a small amount of free water was released at both left and right corners, suggesting the formation of a thin water layer. Without the magnet, there

was no external force attracting the FPPM and trapped emulsion drops, and the generated water layer was spread evenly at the bottom. Comparing the demulsification performance in Figure A.3 and Figure 3.5, it is concluded that FPPM can destabilize the emulsion, and the absence of external magnetic filed would largely slow down the demulsification process and decrease the efficiency.

3.3.3 Force measurement between PDMAPS and emulsified water drop

To investigate the interaction between the FPPM outer layer and the emulsion drop, PDMAPS was coated on a gold wafer and the force measurement was conducted between PDMAPS surface and a water droplet in asphaltene-in-toluene solution. The morphology of the coated gold surface was imaged by AFM tapping mode (Figure A.1), which showed similar morphology as previously reported[36]. Figure 3.6a and 3.6b show the typical force curves of water droplets in asphaltene-in-toluene solution of 10 and 100 mg/L, respectively.

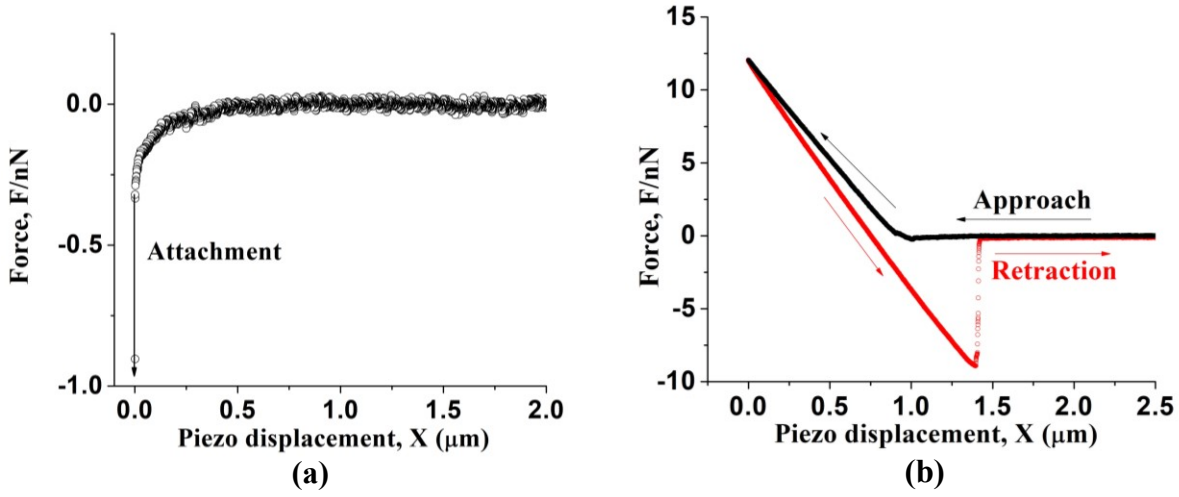

Figure 3.6 Force curve between PDMAPS coated gold surface and water droplet in toluene with asphaltenes concentration of (a) 10 mg/L, and (b) 100 mg/L. The arrow in (a) indicates the

attachment of water droplet on PDMAPS surface; the arrows in (b) indicate the movement of the droplet.

Figure 3.6a shows that with asphaltene concentration of 10 mg/L, the water droplet would attach to the PDMAPS surface when the water drop was driven to approach the surface. Prior to attachment, a strong attraction was measured at about 0.5 μm. Such long-range attractive interaction between the water drop and zwitterionic polyelectrolyte surface in toluene could be most likely attributed to the strong Debye and London interactions, consistent with our previous report[36]. When asphaltene concentration increased to 100 mg/L, no obvious jumping-in behavior (attachment) was observed during approaching and strong adhesion was detected during retraction. With increasing asphaltene concentration, the asphaltenes adsorbed at the oil-water interface could weaken the long-range attraction between water drop and zwitterionic polyelectrolyte. The adhesion measured during the retraction process in Figure 3.6b suggests that the PDMAPS and the protective asphaltenes layer adsorbed at oil−water interface remain limited adhesion even under high asphaltene concentration condition.

3.3.4 Change of interfacial property and adsorption of asphaltenes

The AFM force results above have shown the attraction between PDMAPS and water droplets in the emulsion phase, which could drive the migration and adsorption of FPPM to the oil-water interface. To confirm the change of interfacial property, the water-toluene IFT was measured at five different asphaltenes concentrations with/without FPPM (Figure 3.7). The grey bar and red bar represent the IFT at the water-oil in the presence of asphaltenes with/without FPPM, respectively. In the absence of FPPM, the IFT decreased gradually with the increase of concentration due to the adsorption of asphaltenes at the interface. The relationship between IFT and the logarithm of asphaltenes concentration can be fitted to linear with R^2 equals to 0.994,

which is consist with previous study[22]. With the addition of FPPM, the IFT increased at each concentration, suggesting the instability of water drop and the trend to coalesce.

In addition, it is worth mentioning that the changes of IFT before/after adding the same concentration of FPPM were different at different asphaltenes concentrations (Figure 3.7). At both low and high asphaltenes concentrations (i.e., 100 and 500 mg/L), the IFT had minimal changes while at the concentration of 300 mg/L the IFT had maximal increase, which was most likely attributed to their interaction mechanisms shown below. At a high asphaltenes concentration, the shielding effect is dominant and there would be high adsorption of asphaltenes on PDMAPS[53], which could weaken the interaction between FPPM and water, ultimately leading to a minor change of IFT. On the other hand, at a low asphaltenes concentration, the interaction between FPPM and water is comparatively strong, which may result in a diffusion of FPPM to the surrounding bulk water phase, thus causing a minor change of IFT as well. At the asphaltenes concentration of 300 mg/L, both the shielding effect and adsorption of asphaltenes would suitably stabilize FPPM onto the water-oil interface, consequently contributing to the major change of IFT.

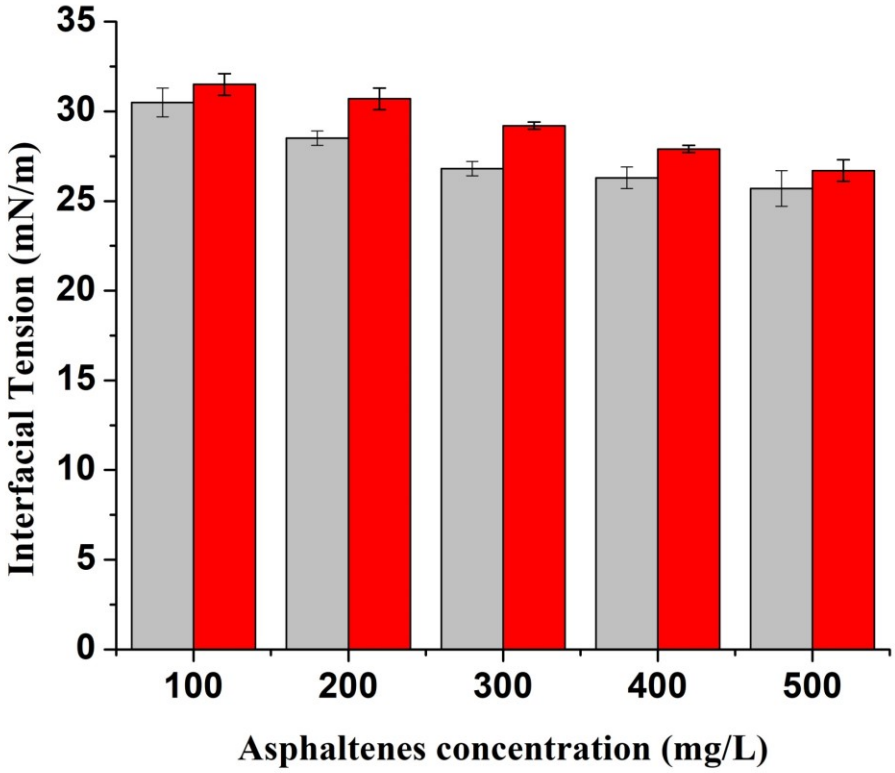

Figure 3.7 Water-oil interfacial tension with asphaltenes (grey) and water-oil interfacial tension with both asphaltenes and FPPM (red).

To investigate the adsorption behavior of asphaltenes on PDMAPS surface, QCM-D test was conducted on PDMAPS coated gold sensor using asphaltene-in-toluene solution as fluid phase. The asphaltenes concentration was set to be 50, 100, 300 and 400 mg/L, respectively, which was injected into the QCM-D chamber before the reach of a plateau (frequency change less than 0.2 Hz during 5 min). Figure 3.8a shows the frequency and dissipation changes at four different concentrations where both the frequency and dissipation changes increased with concentration and reached a plateau at the end. The changes of the four dissipations are all close to zero, meeting the condition of using Equation (3.1) to calculate the mass of adsorbed asphaltenes. In Figure 3.8b, similar to the trend of frequency (Figure 3.8a), the mass increased with both time and

concentration. At a typical concentration, the mass increased sharply in the first 500 second, and then accumulated slowly till the end. At a certain time (e.g., 1000 s), compared with the significant mass increase from 135 ng/cm^2 (at 50 mg/L) to 170 ng/cm^2 (at 100 mg/L), the mass increase for the concentration from 100 mg/L to 300 mg/L and from 300 mg/L to 400 mg/L became much smaller, which are from 170 to 180 ng/cm^2 and from 180 to 183 ng/cm^2 respectively. This decreased increment indicates the trend of reaching a saturated adsorption state of polyelectrolyte surface with increasing asphaltene concentration.

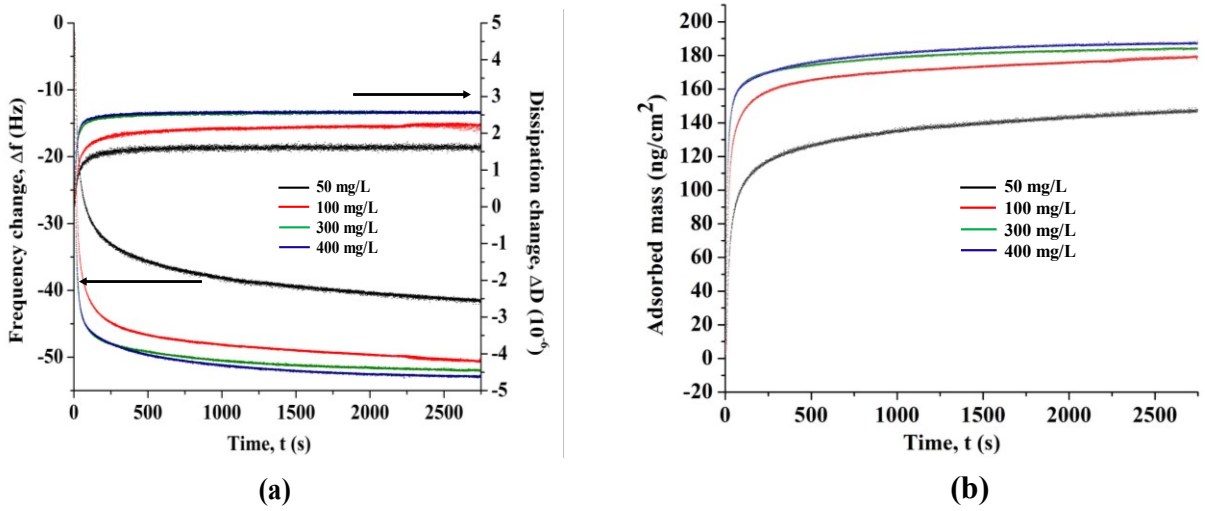

Figure 3.8 (a) Frequency and dissipation changes with time during the QCM-D test on PDMAPS coated gold sensor with asphaltene-in-toluene solution. (b) The mass of asphaltenes adsorbed on PDMAPS coated gold sensor determined using QCM-D.

It was reported that the outer PDMAPS layer of FPPM could desorb the asphaltenes when the asphaltenes-adsorbed PDMAPS was treated in water[53]. This unique adsorption and desorption behavior indicate the potential application of FPPM in recycle and reuse. To further prove the asphaltenes desorption property of FPPM, the FPPM was firstly immersed in the 300 mg/L solids-free C_7-asphaltenes-in-toluene solution for 24 h, and then extracted by magnet and dried under

vacuum, followed by the sonication in water for 20 min. The TEM images were taken after the extraction from asphaltene-in-toluene solution (Figure A.4 (a)-(c)) and after sonication (Figure A.4 (d)-(e)). From the TEM morphology, it was clear that the microspheres were covered and connected by thin films (e.g., the red circles part), which filled the space between sphere shape particles and changed the original round shape edges into irregular ones (Figure A.4 (a)-(b)). In the zoomed TEM image (Figure A.5 (c)), the overlapped layers showed the morphology of micelle shape (blue circle) which was similar as the previously reported morphology of asphaltenes[54]. After sonication in water, the edges of particles became round shape again and the layers connecting the particles disappeared (Figure A.4 (d)-(e)), suggesting the asphaltenes desorption behavior on FPPM.

3.3.5 Proposed interaction schematic

Based on the tests and analyses above, a possible interaction schematic is proposed. Figure 3.9a shows the schematic picture of emulsion test where FPPM in toluene solution was added to vial A while pure toluene was added to vial B. Figure 3.9b depicts the emulsion in vial A at micro level where the water drops have been fully or partially broken to form the irregular shape of water under the effect of FPPM. In the zoomed part of Figure 3.9b, because of the attraction to water, the FPPM partitions to the water-oil interface after adding into the bulk emulsion phase, increasing the interfacial energy. The “skin-like” asphaltenes protection layer around water droplet is known as one of the main reasons of stabilizing the W/O emulsion and difficult to break. As demonstrated by QCM-D tests, the FPPM can adsorb asphaltenes, which plays an important role in disrupting the asphaltenes protection layer. The ruptured asphaltenes layer highly increases the probability of water droplet coalescence and promotes the break of emulsions. In Figure 3.9a, the black arrow lines represent the magnetic induction and the area with more lines has a stronger magnetic field.

The vials were settling on either the north or south side of the magnet, the center point of which has the maximum numbers of magnetic induction lines, suggesting the strongest magnetic force. Therefore, the trapped water droplets together with the emulsion tend to be dragged to the center which squeezes the released free water to the side.

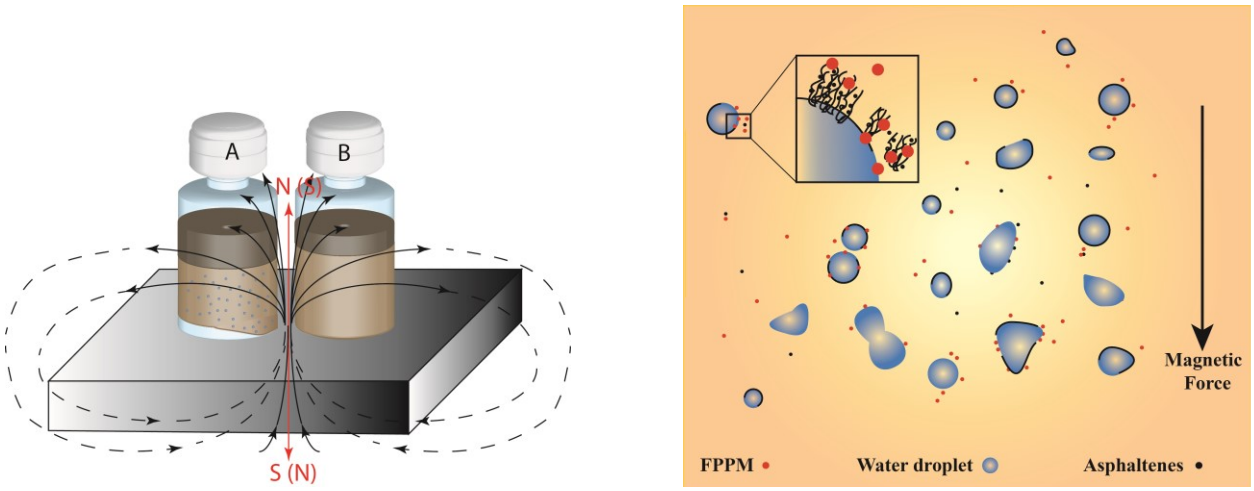

(a) (b)

Figure 3.9 (a) schematic of demulsification test; and (b) illustration of the interactions between water-in-oil emulsion drops with asphaltenes and FPPM under external magnetic field involved in the demulsification process in vial A of (a).

3.4 Conclusions

Removal of asphaltenes-stabilized W/O emulsion is a tough challenge in oil industry. In this work, a novel type of microspheres with core-shell structure (FPPM) was synthesized via a facile route, with magnetic core and superhydrophilic polyelectrolyte (PDMAPS) outer layer. The as-prepared microspheres could greatly facilitate the demulsification process of asphaltenes-stabilized W/O emulsion, especially under external magnetic field, where a considerable amount of free water could be released. A strong attraction between PDMAPS and water drop was measured in the

presence of asphaltenes using a drop probe AFM technique. Compared with the IFT at the water-oil interface, the IFT increased with the addition of FPPM under all the asphaltenes concentrations tested, indicating the emulsion drops were prone to coalescence. The asphaltenes have been found to adsorb on the polyelectrolyte surface by the QCM-D test, demonstrating the protective asphaltene layer at water-oil interfaces could be disrupted by FPPM. In addition, when the asphaltene-adsorbed FPPM was treated in water, the adsorbed asphaltenes on the polyelectrolyte shell can be released, which was verified by TEM imaging. This work provides useful insights into the design of novel demulsifier materials and their interaction mechanism with water-in-oil emulsions, with implications in a variety of engineering and environmental applications such as oil-water separation.

References

1. Dickinson, E. Stabilising emulsion-based colloidal structures with mixed food ingredients. *J. Sci. Food Agric.* **93**, 710–721 (2013).

2. Xu, D. *et al.* Influence of whey protein–beet pectin conjugate on the properties and digestibility of β-carotene emulsion during in vitro digestion. *Food Chem.* **156**, 374–379 (2014).

3. Asnaashari, M., Farhoosh, R. & Sharif, A. Antioxidant activity of gallic acid and methyl gallate in triacylglycerols of Kilka fish oil and its oil-in-water emulsion. *Food Chem.* **159**, 439–444 (2014).

4. Jeong, S. *et al.* Erratum to: Comparison of the Efficacy of Atopalm(®) Multi-Lamellar Emulsion Cream and Physiogel(®) Intensive Cream in Improving Epidermal Permeability Barrier in Sensitive Skin. *Dermatol. Ther. (Heidelb).* **6**, 57 (2016).

5. Sundar, S. *et al.* Efficacy and Safety of Amphotericin B Emulsion versus Liposomal Formulation in Indian Patients with Visceral Leishmaniasis: A Randomized, Open-Label Study. *PLoS Negl. Trop. Dis.* **8**, e3169 (2014).

6. Shao, K. *et al.* Emulsion PCR: A High Efficient Way of PCR Amplification of Random DNA Libraries in Aptamer Selection. *PLoS One* **6**, e24910 (2011).

7. Zhang, W. *et al.* A Solvothermal Route Decorated on Different Substrates: Controllable Separation of an Oil/Water Mixture to a Stabilized Nanoscale Emulsion. *Adv. Mater.* **27**, 7349–7355 (2015).

8. Liu, D. *et al.* Multifunctional Polymer/Porous Boron Nitride Nanosheet Membranes for

Superior Trapping Emulsified Oils and Organic Molecules. *Adv. Mater. Interfaces* **2**, 1500228 (2015).

9. Yang, H.-C. *et al.* Mussel-inspired modification of a polymer membrane for ultra-high water permeability and oil-in-water emulsion separation. *J. Mater. Chem. A* **2**, 10225–10230 (2014).

10. J. Ekott, E. & J. Akpabio, E. A Review of Water-in-Crude Oil Emulsion Stability, Destabilization and Interfacial Rheology. *J. Eng. Appl. Sci.* **5**, 447–452 (2010).

11. Gafonova, O. V. & Yarranton, H. W. The stabilization of water-in-hydrocarbon emulsions by asphaltenes and resins. *J. Colloid Interface Sci.* **241**, 469–478 (2001).

12. Lan, Q. *et al.* Synthesis of bilayer oleic acid-coated Fe3O4nanoparticles and their application in pH-responsive Pickering emulsions. *J. Colloid Interface Sci.* **310**, 260–269 (2007).

13. Hong, L., Sun, G., Cai, J. & Ngai, T. One-Step Formation of W/O/W Multiple Emulsions Stabilized by Single Amphiphilic Block Copolymers. *Langmuir* **28**, 2332–2336 (2012).

14. Li, Z., Ming, T., Wang, J. & Ngai, T. High Internal Phase Emulsions Stabilized Solely by Microgel Particles. *Angew. Chemie* **121**, 8642–8645 (2009).

15. Chevalier, Y. & Bolzinger, M. A. Emulsions stabilized with solid nanoparticles: Pickering emulsions. *Colloids Surfaces A Physicochem. Eng. Asp.* **439**, 23–34 (2013).

16. Yang, H.-C. *et al.* Mussel-inspired modification of a polymer membrane for ultra-high water permeability and oil-in-water emulsion separation. *J. Mater. Chem. A* **2**, 10225–10230 (2014).

17. An, Q. *et al.* A facile method to fabricate functionally integrated devices for oil/water separation. *Nanoscale* **7**, 4553–4558 (2015).

18. Cheng, M., Ju, G., Jiang, C., Zhang, Y. & Shi, F. Magnetically directed clean-up of underwater oil spills through a functionally integrated device. *J. Mater. Chem. A* **1**, 13411 (2013).

19. Ju, G., Cheng, M. & Shi, F. A pH-responsive smart surface for the continuous separation of oil/water/oil ternary mixtures. *NPG Asia Mater.* **6**, (2014).

20. Rondón, M. *et al.* Breaking of water-in-crude-oil emulsions. 2. Influence of asphaltene concentration and diluent nature on demulsifier action. *Energy and Fuels* **22**, 702–707 (2008).

21. Yan, Z., Elliott, J. A. W. & Masliyah, J. H. Roles of Various Bitumen Components in the Stability of Water-in-Diluted-Bitumen Emulsions. *J. Colloid Interface Sci.* **220**, 329–337 (1999).

22. Pradilla, D., Simon, S. & Sjöblom, J. Mixed interfaces of asphaltenes and model demulsifiers part I: Adsorption and desorption of single components. *Colloids Surfaces A Physicochem. Eng. Asp.* **466**, 45–56 (2015).

23. Tchoukov, P. *et al.* Role of asphaltenes in stabilizing thin liquid emulsion films. *Langmuir* **30**, 3024–3033 (2014).

24. Ortiz, D. P., Baydak, E. N. & Yarranton, H. W. Effect of surfactants on interfacial films and stability of water-in-oil emulsions stabilized by asphaltenes. *J. Colloid Interface Sci.* **351**, 542–555 (2010).

25. Razi, M., Rahimpour, M. R., Jahanmiri, A. & Azad, F. Effect of a Different Formulation of Demulsifiers on the Efficiency of Chemical Demulsification of Heavy Crude Oil. *J. Chem. Eng. Data* **56**, 2936–2945 (2011).

26. Poteau, S., Argillier, J. F., Langevin, D., Pincet, F. & Perez, E. Influence of pH on stability and dynamic properties of asphaltenes and other amphiphilic molecules at the oil-water interface. *Energy and Fuels* **19**, 1337–1341 (2005).

27. Fortuny, M. *et al.* Effect of Salinity, Temperature, Water Content, and pH on the Microwave Demulsification of Crude Oil Emulsions †. *Energy & Fuels* **21**, 1358–1364 (2007).

28. Wu, J., Xu, Y., Dabros, T. & Hamza, H. Effect of EO and PO positions in nonionic surfactants on surfactant properties and demulsification performance. *Colloids Surfaces A Physicochem. Eng. Asp.* **252**, 79–85 (2005).

29. Pensini, E. *et al.* Demulsification mechanism of asphaltene-stabilized water-in-oil emulsions by a polymeric ethylene oxide-propylene oxide demulsifier. *Energy and Fuels* **28**, 6760–6771 (2014).

30. Wu, J., Xu, Y., Dabros, T. & Hamza, H. Effect of Demulsifier Properties on Destabilization of Water-in-Oil Emulsion. *Energy and Fuels* **17**, 1554–1559 (2003).

31. Zhu, Y. *et al.* A novel zwitterionic polyelectrolyte grafted PVDF membrane for thoroughly separating oil from water with ultrahigh efficiency. *J. Mater. Chem. A* **1**, 5758–5765 (2013).

32. Kobayashi, M. *et al.* Wettability and Antifouling Behavior on the Surfaces of Superhydrophilic Polymer Brushes. *Langmuir* **28**, 7212–7222 (2012).

33. Honda, T. *et al.* Polymer coating glass to improve the protein antifouling effect. *Polym. J.*

50, 381–388 (2018).

34. Zhang, C. *et al.* CuSO4/H2O2-Induced Rapid Deposition of Polydopamine Coatings with High Uniformity and Enhanced Stability. *Angew. Chemie - Int. Ed.* **55**, 3054–3057 (2016).

35. He, K. *et al.* Cleaning of Oil Fouling with Water Enabled by Zwitterionic Polyelectrolyte Coatings: Overcoming the Imperative Challenge of Oil-Water Separation Membranes. *ACS Nano* **9**, 9188–9198 (2015).

36. Shi, C. *et al.* Long-Range Hydrophilic Attraction between Water and Polyelectrolyte Surfaces in Oil. *Angew. Chemie - Int. Ed.* **55**, 15017–15021 (2016).

37. Zhang, L. Y., Lawrence, S., Xu, Z. & Masliyah, J. H. Studies of Athabasca asphaltene Langmuir films at air-water interface. *J. Colloid Interface Sci.* **264**, 128–140 (2003).

38. Zhang, L., Shi, C., Lu, Q., Liu, Q. & Zeng, H. Probing Molecular Interactions of Asphaltenes in Heptol Using a Surface Forces Apparatus: Implications on Stability of Water-in-Oil Emulsions. *Langmuir* **32**, 4886–4895 (2016).

39. Donovan, M. S., Sumerlin, B. S., Lowe, A. B. & McCormick, C. L. Controlled/"Living" Polymerization of Sulfobetaine Monomers Directly in Aqueous Media via RAFT †. *Macromolecules* **35**, 8663–8666 (2002).

40. Xie, Y. *et al.* Highly Regenerable Mussel-Inspired Fe_3O_4 @Polydopamine-Ag Core–Shell Microspheres as Catalyst and Adsorbent for Methylene Blue Removal. *ACS Appl. Mater. Interfaces* **6**, 8845–8852 (2014).

41. Rocha, J. A. *et al.* Role of Aqueous Phase Chemistry, Interfacial Film Properties, and Surface Coverage in Stabilizing Water-in-Bitumen Emulsions. *Energy & Fuels* **30**, 5240–

5252 (2016).

42. Shi, C. *et al.* Surface Interaction of Water-in-Oil Emulsion Droplets with Interfacially Active Asphaltenes. *Langmuir* **33**, 1265–1274 (2017).

43. Yang, D. *et al.* Probing Anisotropic Surface Properties and Interaction Forces of Chrysotile Rods by Atomic Force Microscopy and Rheology. *Langmuir* **30**, 10809–10817 (2014).

44. Kristiansen, K., McGuiggan, P., Carver, G., Meinhart, C. & Israelachvili, J. 3D force and displacement sensor for SFA and AFM measurements. *Langmuir* **24**, 1541–1549 (2008).

45. Hutter, J. L. & Bechhoefer, J. Calibration of atomic-force microscope tips. *Rev. Sci. Instrum.* **64**, 1868–1873 (1993).

46. Liu, C.-Y. & Huang, C.-J. Functionalization of Polydopamine via the Aza-Michael Reaction for Antimicrobial Interfaces. *Langmuir* **32**, 5019–5028 (2016).

47. Xu, C. *et al.* Dopamine as a robust anchor to immobilize functional molecules on the iron oxide shell of magnetic nanoparticles. *J. Am. Chem. Soc.* **126**, 9938–9939 (2004).

48. Ma, T. *et al.* Fabrication of electro-neutral nanofiltration membranes at neutral pH with antifouling surface via interfacial polymerization from a novel zwitterionic amine monomer. *J. Memb. Sci.* **503**, 101–109 (2016).

49. Crispin, X. *et al.* Conductivity, morphology, interfacial chemistry, and stability of poly(3,4-ethylene dioxythiophene)-poly(styrene sulfonate): A photoelectron spectroscopy study. *J. Polym. Sci. Part B Polym. Phys.* **41**, 2561–2583 (2003).

50. Liang, C., Liu, Q. & Xu, Z. Dewatering Bitumen Emulsions Using Interfacially Active

Organic Composite Absorbent Particles. *Energy and Fuels* **30**, 5253–5258 (2016).

51. Feng, X., Xu, Z. & Masliyah, J. Biodegradable Polymer for Demulsification of Water-in-Bitumen Emulsions. *Energy & Fuels* **23**, 451–456 (2009).

52. Fortuny, M. *et al.* Effect of Salinity, Temperature, Water Content, and pH on the Microwave Demulsification of Crude Oil Emulsions †. *Energy & Fuels* **21**, 1358–1364 (2007).

53. Higaki, Y. *et al.* Adsorption and Desorption Behavior of Asphaltene on Polymer-Brush-Immobilized Surfaces. *ACS Appl. Mater. Interfaces* **6**, 20385–20389 (2014).

54. Pérez-Hernández, R. *et al.* Microstructural study of asphaltene precipitated with methylene chloride and n-hexane☆. *Fuel* **82**, 977–982 (2003).

Chapter 4 Bio-inspired, Facile and Scalable Surface Functionalization Approach with Small Molecules for Multitasking Oil Decontamination

4.1 Introduction

Oil contaminations have been challenging issues in many industries, such as gas and oil production[1,2] and textiles[3], and have aroused great attention all over the world due to the negative impacts on environment and sustainable development of economy. The oil spill accidents are representative examples, which could damage local environment and threaten wildlife over a long period of time[4]. The industrial oily wastewater usually contains many harmful and non-biodegradable organic compounds that could pollute local soil and fresh water sources, and would generally take years to degrade in nature[5,6]. It becomes more challenging that oily contaminants form stable emulsions in water [i.e., oil-in-water (O/W) emulsion, water-in-oil (W/O) emulsion, complex emulsion (e.g., W/O/W and O/W/O)] in the presence of artificial (e.g., surfactants, nanoparticles) or natural surface-active species (e.g., asphaltenes, resins)[7]. Surfactants usually stabilize emulsions by lowering water/oil interfacial tension while asphaltenes form a rigid skin-like layer at oil-water interface to stabilize the emulsion[8,9]. The different stabilization mechanisms of diverse stabilizers require effective strategies for efficient demulsification.

Over the past few decades, a variety of materials have been developed to target oil decontamination issues, among which fiber-based materials are commonly used as supporting substrate due to the high specific surface area, interconnected porous structure and wide range of pore sizes[10–12]. The fiber-based substrates include two major categories: inorganic fibers (e.g., metal mesh) and organic fibers (e.g., fabrics fiber), both of which have been applied in oil/water separation and

demulsification processes[10]. For example, stainless steel mesh was used as substrate and modified by zeolitic imidazolate framework-8 film for oi/water separation[11]. It was reported that cotton fiber modified with SiO_2 and octadecyltrichlorosilane was an excellent candidate for oil absorption and oil/water separation[13]. Stainless steel mesh after functionalization with poly-(N,N-dimethylaminoethyl methacrylate) and poly(divinylbenzene) was employed for the demulsification of sodium dodecyl sulfate stabilized W/O emulsions[12]. A superhydrophobic/superoleophilic cotton fiber-based material modified by poly(vinyl phenol) and 1,3-phenylene bisoxazoline was also synthesized to treat span 80-stabilized W/O emulsions[14]. Generally, fiber-based functional materials are fabricated through specific reactions between certain functional molecules and desired reactants on or pre-coated to fiber-based substrates[15,16], to which the functional coating layers grant the capability for oil contamination removal and water/oil separation. However, such an approach generally requires complex molecular design and pre-treatment of the substrates. It remains a great challenge to develop a facile and substrate-independent surface-functionalization approach for tailoring and regulating the fiber-based supporting materials.

Recently, surface functionalization via polydopamine (PDA) chemistry has attracted much research interest, which is a facile, versatile and scalable method to modify various types of substrates[17–23]. The PDA deposition is inspired by the mussel adhesive proteins that are rich in catecholic amino acid residue (i.e., 3,4-dihydroxyphenylalanine). PDA can be spontaneously formed by polymerization of dopamine monomers in alkaline solution and easily coat various substrates[24]. Moreover, PDA deposition layer has many chemical-reactive sites for diversified secondary functionalization, enabling it to serve as an intermediate layer to immobilize various functional compounds on target substrates.

The surface wettability of materials after the secondary functionalization dominates their oil/water separation and oil removal performance and is determined by the functional compounds used in secondary functionalization. Specifically, hydrophilic/oleophobic compounds are usually suitable for separating water from oil-water mixture; while hydrophobic/oleophilic compounds are usually suitable for separating oil from oil-water mixture[25,26]. The commonly used hydrophobic functional compounds fall into two categories: fluorinated compounds and non-fluorinated compounds. The fluorinated compounds are traditional candidates for oil/water separation because of their low surface energy and outstanding oil wetting property[27]. However, the rising environmental concern about fluoride pollution prompts researchers to pay more attention to non-fluorinated chemicals including inorganics (e.g., TiO_2[28], SiO_2[29], Al_2O_3[30]), small molecules and polymers[31,32]. Many polymers have been developed to functionalize porous substrates for oil/water separation, oil absorption and demulsificaion, such as poly(methyl methacrylate) for hexane/water separation[33], polydimethylsiloxane for oil absorption (both heavy and light oils) and treating emulsion stabilized by span 80[34,35], polyethyleneimine for demulsification of tween 80-stabilized emulsion[36], and polypropylene oxide-polyethylene oxide block polymers for demulsification of asphaltenes-stabilized emulsion[37]. The polymers used to break surfactants (e.g., span80, tween 80) stabilized emulsions can be either hydrophilic or oleophilic; while the polymers targeting demulsification of asphaltenes-stabilized emulsions are usually amphiphilic. Despite that much effort devoted to the development of polymers to address oil contamination issues, substrate-supported small molecules that can effectively break both surfactant- and asphaltenes-stabilized emulsions have rarely been reported[38].

In this work, we report a facile surface functionalization strategy for porous substrates using small non-fluorinated molecules for effective oil/water separation and treatment of surfactant-

/asphaltenes-stabilized emulsion. A small molecule, γ-mercaptopropyldi(trimethylsiloxy)methylsilane (MD(SH)M), has been applied to functionalize fiber-based substrates, successfully realizing oil/water separation, oil absorption and demulsification capabilities. The MD(SH)M is immobilized on commercial fiber-based substrates via PDA deposition approach. The as-prepared materials are used to separate mixtures of water and high-density/low-density oil, absorb oil from water, and break W/O emulsions stabilized by span 80 or asphaltenes. The interaction forces between as-prepared functionalized fiber-based materials and oil/water droplets are characterized using a modified integrated thin film drainage apparatus (ITFDA). The hydrophobic interaction between MD(SH)M self-assembled monolayer (SAM) and air bubbles in aqueous media is measured using atomic force microscope (AFM). This work provides a novel, facile and scalable method for functionalizing diverse substrates or fiber-based materials by using small non-fluorinated molecules, which has a great potential to address effective water-oil separation and oil contamination issues, and improves the fundamental understanding of the underlying interfacial interaction mechanisms.

4.2 Experimental section

4.2.1 Materials

The C7-asphaltenes (solid free) were extracted from Athabasca bitumen using a method reported previously39. Chloroform (ACS reagent, ≥99.8%), hexanes (ACS reagent, ≥98.5%), toluene (ACS reagent, ≥99.5%), petroleum ether (PE) (ACS reagent), n-dodecane (ACS reagent, ≥99%), 2-propanol (ACS reagent, ≥99.5%), hydrochloric acid (36%), tris(hydroxymethyl)aminomethane (THAM), fiber-free polyurethane (PU) sponge and hydrophilic polyvinylidene fluoride (PVDF) membrane with pore size 0.22 μm were purchased from Fisher Scientific, Canada. Dopamine hydrochloride, oil red O, (3-mercaptopropyl)methyldimethoxysilane (MPMDMS) and

hexamethyldisiloxane (HMDSO) were ordered from Sigma-Aldrich, Canada. The stainless-steel mesh (SSM) was purchased from Alfa Aesar. The cotton fiber (CF) was from cotton balls sold in local pharmacy store. Corn oil was bought from local superstore. All the materials were used as received.

4.2.2 Preparation of small molecule coated surfaces with various substrates

Selected substrates (i.e., CF, SSM, PVDF membrane, PU sponge) were first immersed in Tris buffer (10 mM, pH=8.5) containing 2 mg/mL dopamine hydrochloride for 24 h at room temperature to achieve PDA deposition, and then were thoroughly rinsed with water and ethanol and dried under vacuum40. The CF, SSM, PVDF membrane and PU sponge coated by PDA were denoted as CF@PDA, SSM@PDA, PVDF@PDA, and PU@PDA, respectively. The synthesis of the small molecule has been reported in our previous work41. Briefly, MPMDMS, HMDSO, and hydrochloric acid were mixed at 70°C in nitrogen atmosphere. After reacting for 4 h, the resultant organic phase was washed by Milli-Q water to remove acid and was separated from aqueous phase using a separatory funnel. The MD(SH)M was obtained by distilling the organic phase under reduced pressure. The PDA-coated substrate was immersed in 2-propanol with MD(SH)M (5 mg/mL) for 24 h at room temperature to immobilize MD(SH)M via Michael addition21. The CF@PDA, SSM@PDA, PVDF@PDA and PU@PDA with MD(SH)M functionalization were named as CF@PM, SSM@PM, PVDF@PM, and PU@PM, respectively. The synthesis process was illustrated in Figure 4.1.

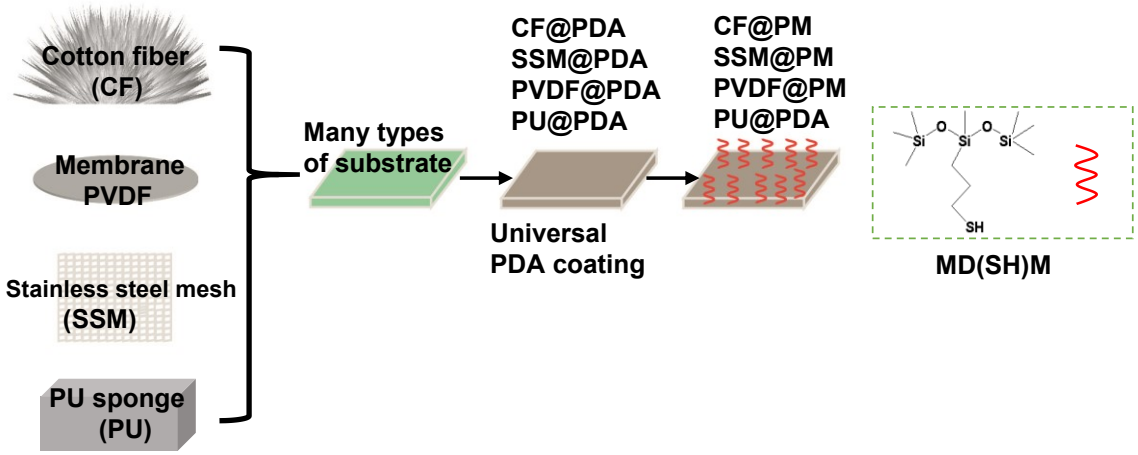

Figure 4.1 Schematic of synthesis route of functionalizing various substrates using MD(SH)M.

4.2.3 Oil/water separation and oil absorption

In the oil/water separation experiment, dodecane/water and chloroform/water mixtures were prepared and used as model mixture systems to test the oil/water separation performance of as-prepared materials. It is worth noting that the oil phase was dyed in red for ease of observation. The freshly prepared oil/water mixture was poured into a beaker covered by SSM@PM to separate oil and water under gravity force.

To evaluate the oil absorption capacity of as-prepared materials, the dry CF@PM was immersed in various types of oil, including hexanes, chloroform, toluene, PE and corn oil. The CF@PM was first immersed in oil (~50 mL) for 5 min to reach absorption saturation, and then the saturated CF@PM was lifted out of the oil and exposed in air for about 10 s to remove loosely attached oil under gravity. When there was no free oil on the surface of CF@PM, it was transferred and sealed in a glass vial and weighed. The weight gain (w) of CF@PM was used to evaluate the oil absorption capacity, which was expressed in Equation 1,

$$\text{Weight gain } (w) = \frac{m_1 - m_0}{m_0} \quad (1)$$

where m_0 and m_1 are the weight of CF@PM before and after oil absorption, respectively.

The oil absorption capacity from water was also investigated for the as-prepared materials. Briefly, 2 mL oil was dyed in red and added to ~20 mL water. The dry CF@PM was held by a tweezer to absorb the oil from water, after which the oil was squeezed out from CF@PM for water content analysis. The water rejection rate (η_r) was used to determine the ability of absorbing oil from water, as expressed in Equation 2,

$$\text{Rejection } (\eta_r) = (1 - c) \times 100\% \quad (2)$$

where c is the water concentration (ppm) in the oil squeezed out from CF@PM (after absorption test in oil-water mixture) as compared with absorption from pure oil. It is noted that trace amount of water might be contained in the pristine oil reagent; thus, the value of c is calculated by using "the water concentration (ppm) in oil squeezed out from CF@PM" minus "the water concentration (ppm) in pure oil". The used CF@PM was washed in 2-propanol and dried with air for cyclic reuse. Each type of oil absorption test was repeated for at least three times.

4.2.4 Demulsification of W/O emulsion

The W/O emulsions were prepared by adding water into oil phase dropwise and mixing with an IKA T18 digital ultra-turrax homogenizer at 15 000 rpm for 5 min. The water/oil volume ratio was 1/99 for W/O emulsion stabilized by span 80 (1 mg/mL) and 10/90 for W/O emulsion stabilized by solid-free C_7-asphaltenes (300 mg/L). The span 80 (1mg/mL)/C_7-asphaltenes 300 mg/L) were dissolved in toluene as the oil phase for emulsion preparation. The demulsification experiments were conducted by adding the W/O emulsion into an in-house built apparatus consisting of a

vertical glass pipe with dry CF@PM stuffed at the bottom end. The emulsion flowed through the CF@PM under gravity force, and the liquid coming out from the end of glass pipe was collected for further analysis. The amount of emulsion added in each run was controlled as 1 mL. The demulsification performance of the CF@PM was evaluated by separation efficiency (η_s), which was calculated as below:

$$\text{Separation efficiency } (\eta_s) = (1 - \frac{c_l}{c_e}) \times 100\% \quad (3)$$

where c_e and c_l are the water concentrations in original W/O emulsion and the separated liquid phase collected at the end of glass pipe, respectively.

4.2.5 Interactions between water/oil droplets and as-prepared materials

The interaction forces between water/oil droplets and different materials were measured using a modified setup of integrated thin film drainage apparatus (ITFDA)[42]. Specifically, the interaction forces between a water droplet and bare CF in air, a water droplet and CF@PM in air, a water droplet and SSM@PM in oil, and an oil droplet and SSM@PM in water were quantified. As presented in Figure 4.2a, the water/oil droplet was generated using a gastight syringe at one end of the glass capillary tube (inner radius 0.74±0.05 mm) and moved toward/away from the surface of sample driven by a motorized actuator. The sample was fixed on the stage clamped at the free end of a bimorph cantilever. The force exerted on the sample would lead to the deflection of bimorph to generate electric feedback response, which could be translated to force between water/oil droplet and the sample surface using a calibrated relationship between exerted force and electric response of the bimorph cantilever. Besides, the whole interaction process between the droplet and sample was recorded by a CCD camera. The glass cell could be filled with water or oil for force measurements in liquid at room temperature. A typical measurement includes four

steps, as illustrated in Figure 4.2b. First, a droplet was generated at the end of glass capillary tube and held above the sample (Figure 4.2b(1)). Then the droplet approached the sample at a constant speed and stayed for a dwell time of 5 s after getting contact with the sample (Figure 4.2b(2)). The droplet was subsequently lifted to a position higher than original position to ensure the detachment from the sample (Figure 4.2b(3)), after which the droplet was driven back to the field of view (Figure 4.2b(4)). The approach and retraction velocity of droplet was fixed as 100 μm/s.

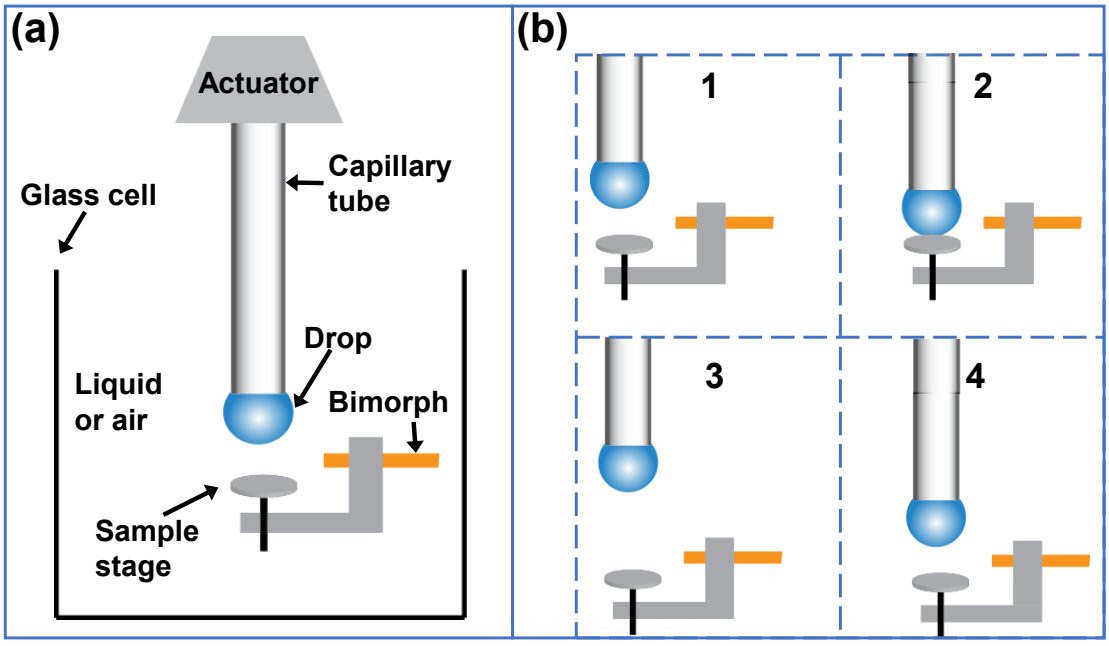

Figure 4.2 (a) Schematic configuration of the modified setup of integrated thin film drainage apparatus (ITFDA) for measuring the interaction forces between a liquid droplet and a substrate surface. (b) Typical experiment protocol: (1) droplet starting to approach sample stage; (2) droplet contacting with sample stage and staying for a certain time (dwell time); (3) droplet moving away from the sample stage to ensure the detachment of the droplet and sample; (4) droplet moving back to the field of view.

4.2.6 AFM force measurement and theoretical model

The MD(SH)M SAM surface were prepared by functionalizing flat gold wafer substrates in MD(SH)M in 2-propanol solution according to a method reported previously[41]. The interaction force between an air bubble and MD(SH)M SAM surface in 500 mM NaCl solution was measured by an MFP-3D AFM (Asylum Research, Santa Barbara, CA) mounted on an inverted microscope (Nikon Ti-U). The bottom glass of fluid cell was pre-treated by octyltrichlorosilane to enhance its affinity to air bubbles, which was generated by a custom-made ultra-sharp glass pipet. A tipless cantilever with gold patch at the end was treated by 1-dodecanethiol and employed to pick up one air bubble, which was then placed above the MD(SH)M SAM surface for force measurement[43]. The velocity of bubble approaching/retracting from the surface was set as 1 μm/s to suppress hydrodynamic effect. The spring constant of tipless cantilever was calibrated using Hutter's thermal method[44]. The measured force was analyzed using a theoretical model based on Reynolds lubrication theory coupled with augmented Young-Laplace equation shown as below[45,46],

$$\frac{\partial h}{\partial t} = \frac{1}{12\mu r}\frac{\partial}{\partial r}(rh^3\frac{\partial p}{\partial r}) \tag{4}$$

where h is the thickness of confined water film, t is the time, μ is the viscosity of water, r is the radical coordinate, and p is the relative hydrodynamic pressure. The boundary condition at air/water interface is assumed as non-slippery according to recent reports[47–49].

The deformation of bubble during the interaction process can be described by augmented Young-Laplace equation as shown in Equation (5),

$$\frac{\gamma}{r}\frac{\partial}{\partial r}(r\frac{\partial h}{\partial r}) = \frac{2\gamma}{R} - p - \Pi \tag{5}$$

where γ is the air/water interfacial tension, R is the bubble radius, Π is the overall disjoining pressure arising from surface forces such as van der Waals (VDW) force, electric double layer (EDL) force and hydrophobic interaction (HB). Since the EDL force is significantly screened in 500 mM NaCl, VDW force and hydrophobic interaction dominate the disjoining pressure in this case, which can be described in Equation (6) and (7), respectively,

$$\Pi_{vdw} = -\frac{A_H}{6\pi h^3} \tag{6}$$

where A_H is the Hamaker constant of air/water/gold system calculated using Lifshitz theory. As the thickness of MD(SH)M SAM is less than 1 nm[41], the VDW interaction is dominated by the air/water/gold interaction, and the contribution of MD(SH)M SAM to the overall VDW force can be neglected[43,50].

$$\Pi_{HB} = -\frac{C_0}{D_0}\exp(-\frac{h}{D_0}), \qquad C_0 = \gamma(1-\cos\theta) \tag{7}$$

where C_0 is a constant (mJ/m^2) related to the wettability and interfacial tension of the surface, θ is the static water contact angle on MD(SH)M SAM and D_0 is the decay length of hydrophobic interaction.

The overall interaction between an air bubble and MD(SH)M SAM surface, $F(t)$, is calculated by integrating $p(r, t)$ and $\Pi(r, t)$ according to Derjaguin approximation[42,43,49–51].

$$F(t) = 2\pi\int_0^\infty [p(r,t) + \Pi(h(r,t))]rdr \tag{8}$$

4.2.7 Material characterizations

Field emission scanning electron microscope (FE-SEM) imaging and energy dispersive X-ray spectroscopy (EDS) were conducted on a Zeiss Sigma SEM (Carl Zeiss, Germany) to characterize

the surface morphology and elemental distribution of as-prepared materials. The chemical composition of bare CF and CF@PM were investigated using the attenuated total reflectance Fourier transform infrared (ATR-FTIR) spectroscopy (Thermo Scientific Nicolet iS50). The water concentration (ppm) in pure oil and in oil samples squeezed out from CF@PM was measured using Karl-Fischer titration (C20 Coulometric KF Titrator, Mettler Toledo, Switzerland). The water contact angles on different materials were measured using a goniometer (ramè-hart, instrument Co., NJ, USA). The surface chemical composition of different materials was quantified by X-ray photoelectron spectroscopy (XPS) on a PHI VersaProbe III (Φ ULVAC-PHI, Inc., Japan/USA), and the XPS spectra was corrected by the C 1s peak at 284.6 eV.

4.3 Results and discussion

4.3.1 Preparation and characterization of MD(SH)M functionalized materials

The MD(SH)M can be immobilized on various types of substrates through the universal PDA coating as an intermediate layer. The SEM images of bare and functionalized CF and SSM are shown in Figure 4.3. The SSM weaved by stainless steel wires has a pore size of about 100 μm (Figure 4.3a). After PDA deposition, some aggregates are generated on the surface of stainless wires with the size varying from a few microns to sub-microns (Figure 4.3b). The pore size of SSM is not significantly affected by these aggregates, and the surface morphology of SSM barely changes after functionalization of MD(SH)M (Figure 4.3c). Similarly, the SEM images of bare CF show smooth fiber surface with width of about 8 μm (Figure 4.3d). In contrast, the CF@PDA has many aggregates spreading pervasively on all the fibers (Figure 4.3e), suggesting that the deposition of PDA causes evident changes in morphology and increases surface roughness. As the coating of MD(SH)M does not exhibit obvious morphology changes in SEM images (Figure 4.3f),

the EDS elemental mapping is employed to characterize the distribution of elements contained in MD(SH)M. As shown in Figure 4.4a, the bare CF has strong signal of C (red color), O (purple color) but almost no signal of Si, which is one of the main elements in MD(SH)M. The signal of C is a bit strong in the pore area because the fiber is very thin and close to the background carbon tape so that the C contained in the tape is detected as well. In comparison, besides C and O, the Si signal shows up in the mapping of CF@PM, implying the successful functionalization of MD(SH)M on fibers (Figure 4.4b). In the FTIR analysis, a new peak at 798 cm^{-1} appears in the spectra of CF@PM as compared with that of bare CF, which corresponds to the stretching vibration of Si-C bond (Figure 4.4c) [16]. In the XPS analysis, the bare CF contains a high concentration of C and O, and a very low concentration of Si, which agrees well with the EDS result that the signals of C and O are strong but that of Si can barely be observed. The signal of N is noticed and the signals of Si and O in the XPS spectra of CF@PM are much stronger than that of bare CF, which is attributed to the PDA and MD(SH)M deposition. These results show the small molecule MD(SH)M are scalable with various types of substrates through the universal PDA deposition as an intermediate layer.

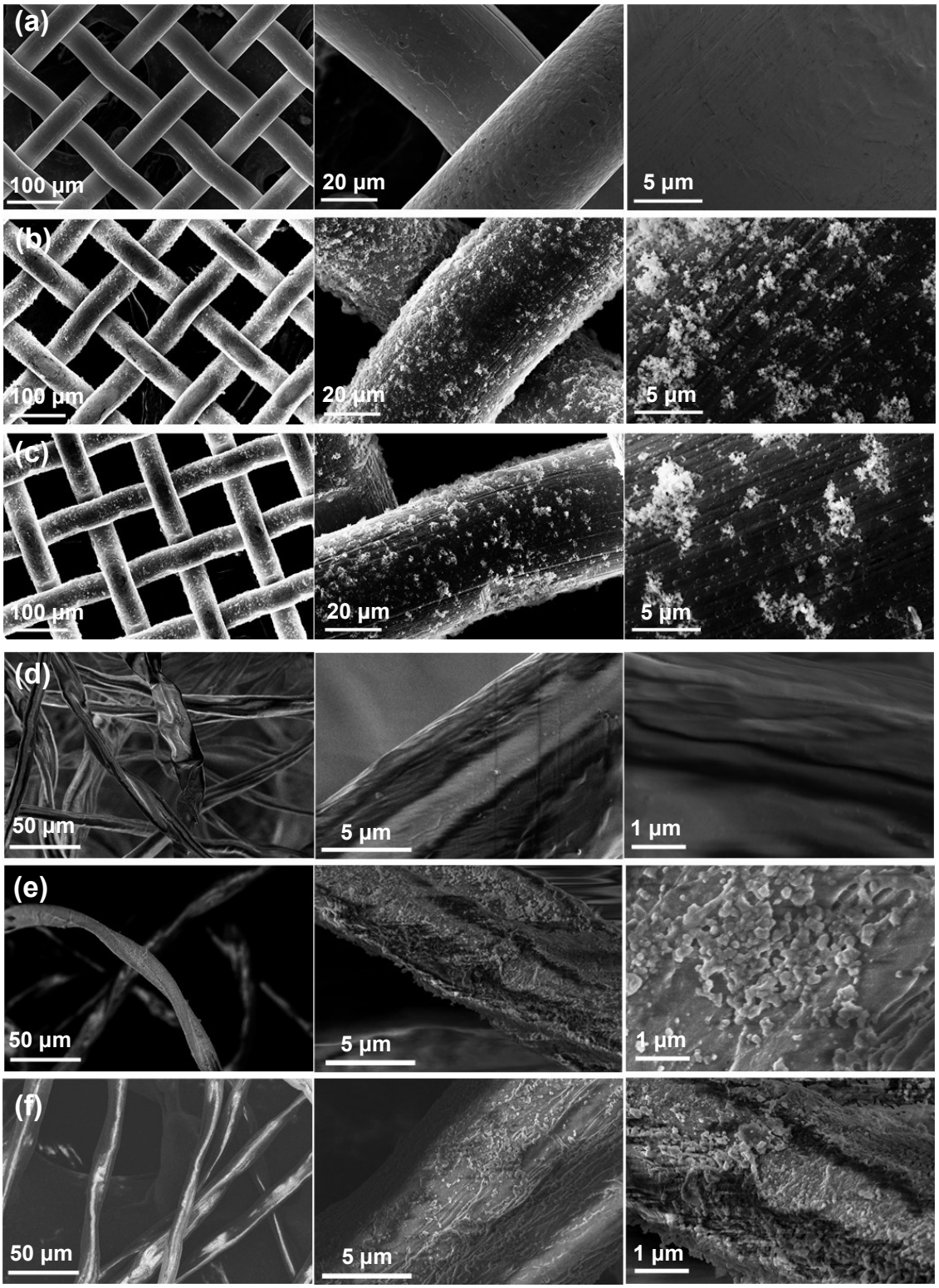
(a)
100 µm
20 µm
5 µm
(b)
100 µm
20 µm
5 µm
(c)
100 µm
20 µm
5 µm
(d)
50 µm
5 µm
1 µm
(e)
50 µm
5 µm
1 µm
(f)
50 µm
5 µm
1 µm

Figure 4.3 SEM images of (a) SSM; (b) SSM@PDA; (c) SSM@PM; (d) bare CF; (e) CF@PDA; (f) CF@PM.

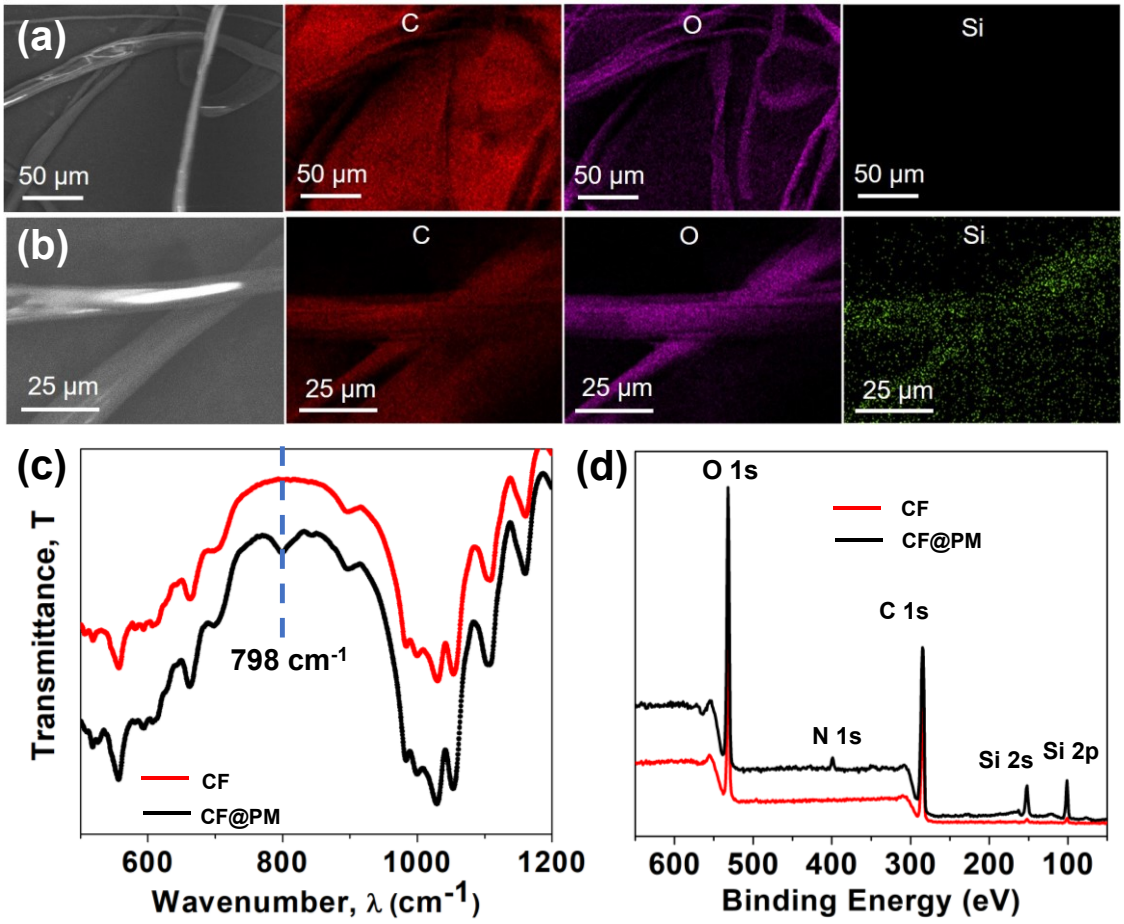

Figure 4.4 SEM-EDS mapping of (a) bare CF and (b) CF@PM; (c) FTIR spectra of bare CF and CF@PM; (d) XPS spectra of bare CF and CF@PM.

4.3.2 Wettability of MD(SH)M functionalized surfaces

The surface wettability of materials plays an important role in many engineering processes (e.g., oil/water separation). The wettability of MD(SH)M functionalized materials were evaluated by measuring the contact angle of water and oil (i.e., toluene) droplet on them. It is worth noting that

the oil is dyed in red to be distinguished from the water droplet. As shown in Figure 4.5, the MD(SH)M functionalized surfaces all exhibit hydrophobicity and oleophilicity in air. The water droplet on SSM@PM surface is stable with a contact angle of ~135°, while the oil droplet spread on the SSM@PM forming a large oil stain (Figure 4.5a). The water droplet on CF@PM can maintain a spherical shape with contact angle of ~160°, while the oil droplet is completely absorbed by CF@PM in air (Figure 4.5b). The hydrophilic PVDF membrane shows a water contact angle of ~105° and oil contact angle of ~0° after MD(SH)M functionalization (Figure 4.5c). Similarly, the water contact angle of PU@PM is ~131°, and the absorbed oil can be squeezed out from PU sponge to leave a red stain on paper.

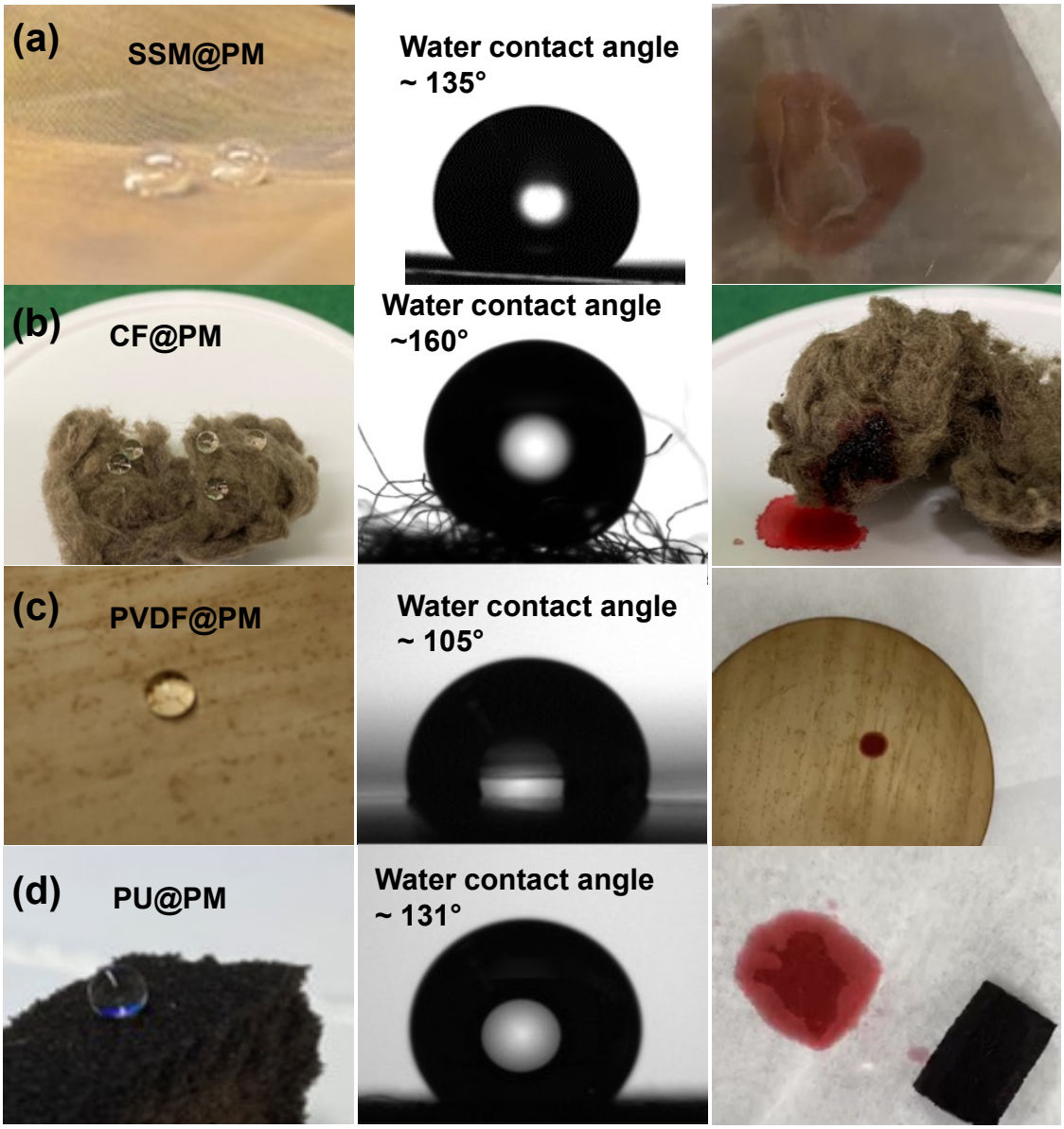

Figure 4.5 Images of water droplet, and toluene droplet (dyed in red) on (a) SSM@PM, (b) CF@PM, (c) PVDF@PM, and (d) PU@PM.

To better understand the change of surface properties after functionalization using MD(SH)M, the interaction forces between a water droplet and CF@PM in air (red curve) were studied by ITFDA and compared with that of water droplet-bare CF (black curve) system, as illustrated in Figure

4.6a. The force value is the net force exerted on sample where the positive and negative signals represent repulsive and attractive forces, respectively. The tiny fluctuations in force curves are due to the interferences of pieces of fibers inside cotton. The force curve of water droplet-bare CF system can be divided into four stages: (1) the water droplet starts to approach the bare CF from original position and negligible net force is measured; (2) the water droplet gets contact with bare CF where an attractive force is generated and increases with time; (3) the attractive force rapidly changes to repulsion as water droplet is about to withdraw from the tube; (4) almost all the water in water droplet is absorbed by CF and the water droplet detaches from the glass tube, resulting in a constant force exerted on the sample. The corresponding snapshots for each stage are shown in Figure 4.6b and the water droplet has a spherical shape before interacting with bare CF (stage 1, 1.1 s). Weak attraction of about 0.02~0.03 mN is measured at the very beginning of stage 2 (5.7 s) when water droplet starts to contact with a few pieces of fluffy fibers on bare CF. The shape of water droplet remains spherical at 5.7 s under weak attraction, after which the droplet is dragged to cylindrical shape at 9.0 s due to the strong attraction arising from the increased contact area between water droplet and bare CF. As water droplet is being absorbed by bare CF during dwell time, the cylindrical droplet turns to a concave bridge at 13.6 s and the increased attractive force arises from the formation of capillary neck. With the increase of time, some water has been absorbed by bare CF to exert a force due to its gravity on the sample and partially balance the attractive capillary force, resulting in a smaller net attraction (15.3 s) as compared to the maximum attractive force. The capillary neck becomes thinner and thinner with the retraction of glass capillary tube and breaks at about 16.4 s, while the attractive force drastically decreases and turns to positive value because of the increased mass from absorbed water. Then the water is completely absorbed by bare CF (stage 4, 17.7 s), and the signal reflects a constant gravity force (~0.08 mN)

of the absorbed water exerted on the sample. The force measurement shows a strong attraction between water and bare CF.

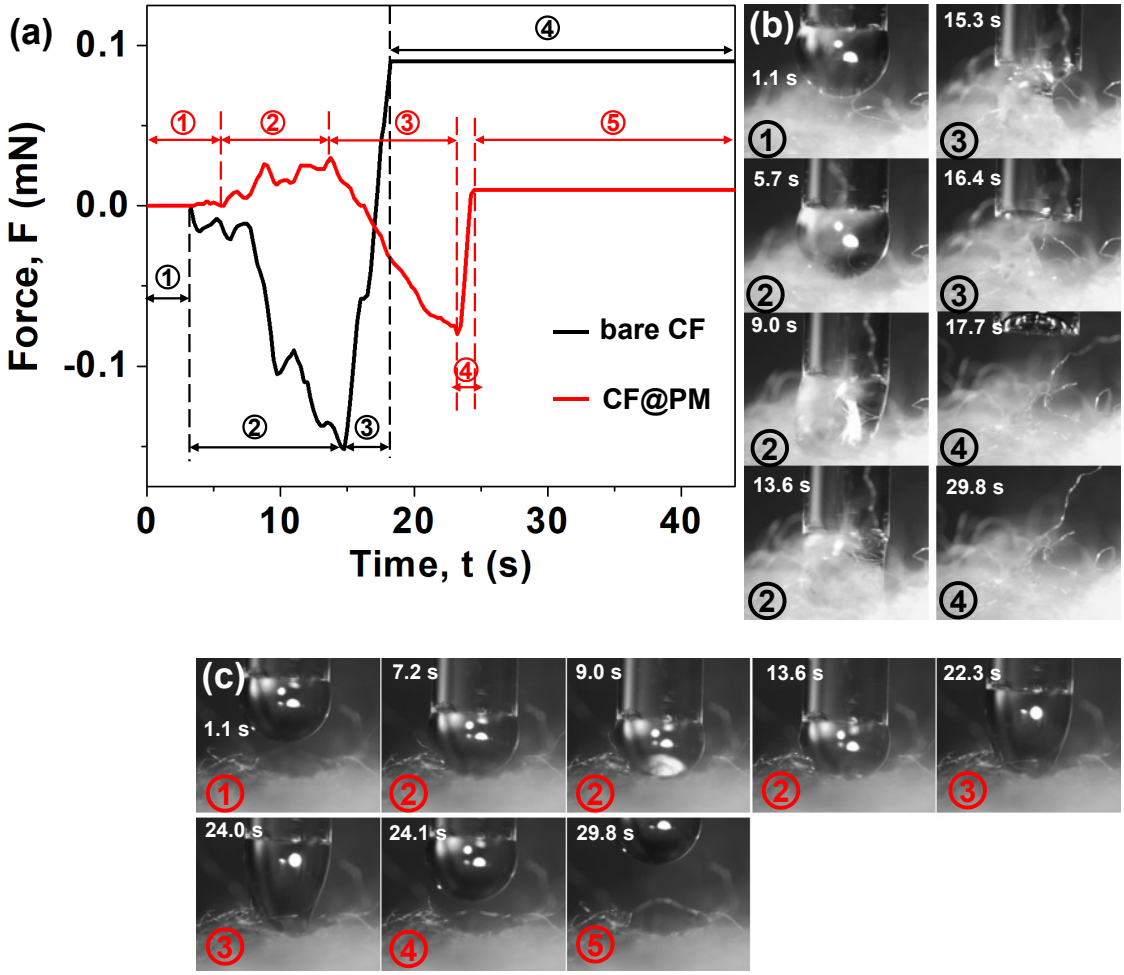

Figure 4.6 (a) Typical force curve as a function of time between a water droplet and bare CF (black curve)/CF@PM (red curve) in air. The black and red force curves overlap at stage 1 (from 0 to ~3 s). (b) The snapshots in corresponding to the regime labeled with the same number in black force curve in panel (a). (c) The snapshots in corresponding to the regime labeled with the same number in red force curve in panel (a).

The interaction between water droplet and MD(SH)M functionalized CF can be divided into five stages and the corresponding snapshots are shown in Figure 4.6c. Same as the force curve of bare CF, the interaction force at stage 1 is negligible when the water droplet moves toward CF@PM. As the water droplet starts to get in contact with CF@PM (7.2 s and 9.0 s), a repulsive force is observed at stage 2, suggesting the resistance of water after MD(SH)M functionalization, which is distinctly different from the trend of bare CF. The water droplet can maintain a spherical shape during the contact with CF@PM (13.6 s), and the repulsive force increases with the increased contact area between water droplet and CF@PM. The force turns to attraction (~ 0.8 mN) at stage 3 and the water droplet is dragged to a cone shape due to the affinity to CF@PM (22.3 s, 24.0 s). The water droplet eventually detaches from CF@PM with the elevation of glass capillary tube (stage 4), during which the force rapidly changes back to almost zero, indicating there is almost no water absorbed by CF@PM (stage 5). The shape of spherical water droplet barely changes after interacting with CF@PM, as demonstrated in the snapshots at 24.1 s and 29.8 s. Though there is limited adhesion measured during the separation of water and CF@PM, which was mainly attributed to the attractive intermolecular interaction (e.g., VDW) at their contact interface, the force measurement reveals that the wetting phenomenon by water is greatly resisted with functionalization of MD(SH)M.

4.3.3 Oil/water separation

The oil/water separation performance of SSM@PM is tested using mixture of water and low-density oil (i.e., dodecane)/high-density oil (i.e., chloroform) and water (Figure 4.7). The SSM@PM is bent to a bowl-like shape and placed on top of a beaker prior to the separation experiment. The oil phase is dyed in red to be distinguished from water. It is noted that SSM@PM

does not need to be pre-wetted prior to the experiment. In the separation of low-density oil and water, the oil/water mixture is gradually poured on SSM@PM. Dodecane penetrates SSM@PM smoothly and flows into the beaker, while water is held steadily on top (Figure 4.7a). In the separation of high-density oil and water, water contacts with the mesh first and is held on top. Some water spills on the paper due to limited volume capacity of hand-made mesh bowl. The chloroform can expel water layer to penetrate through SSM@PM to realize oil/water separation (Figure 4.7b). The excellent capability in oil/water separation of SSM@PM can be attributed to its special wettability of water and oil after MD(SH)M functionalization, and the underlying mechanisms will be further studied using ITFDA and AFM force measurements.

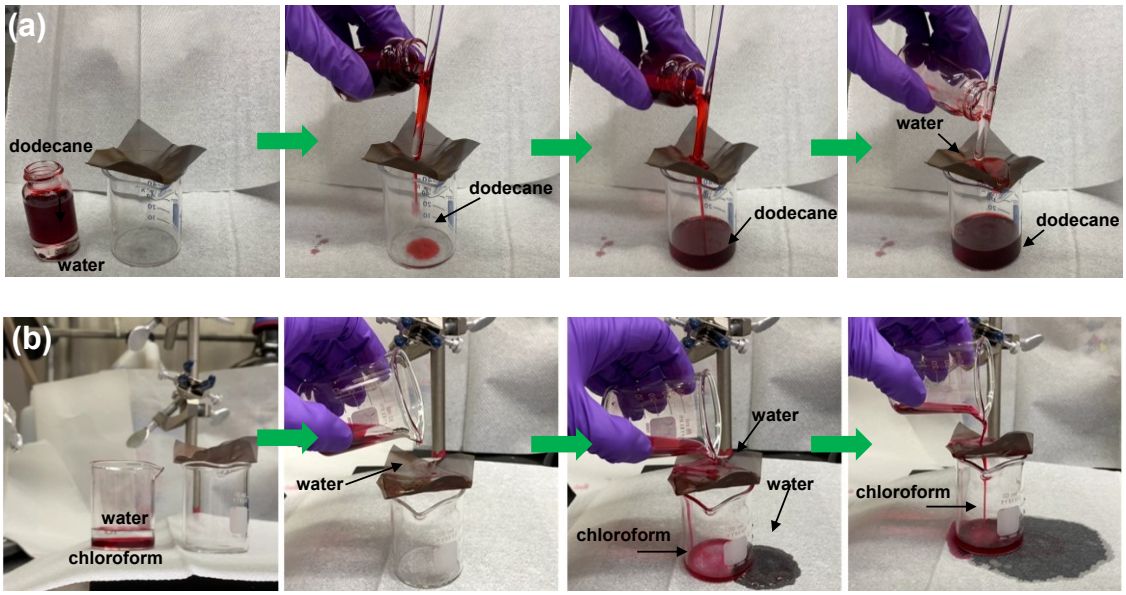

Figure 4.7 Separation of water and (a) dodecane, (b) chloroform using SSM@PM. The oil phase is dyed in red.

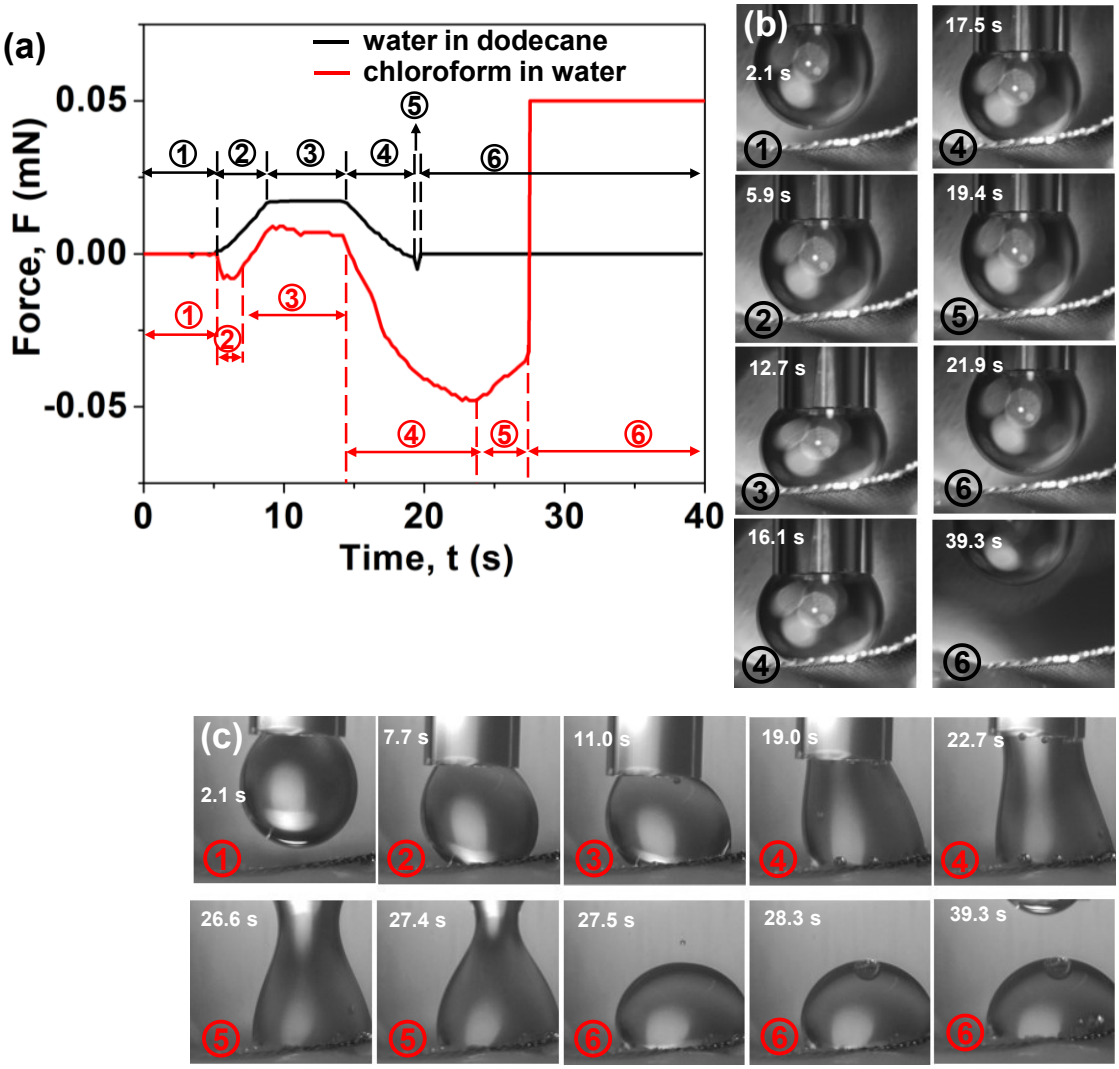

Figure 4.8 (a) the force curves as a function of time between a water droplet and SSM@PM in dodecane (black curve), and between a chloroform droplet and SSM@PM in water (red curve). The black and red force curves overlap at stage 1 (from 0 to ~5 s) and red force curve is shown in front. (b) the snapshots in corresponding to the region labeled with the same number in black force curve in panel (a). (c) the screenshots in corresponding to the region labeled with the same number in red force curve in panel (a).

The force curve as a function of time between a water droplet and SSM@PM in dodecane is shown in Figure 4.8a (black curve) and the corresponding snapshots are shown in Figure 4.8b. No interaction is observed at stage 1 when water droplet is approaching SSM@PM. As water droplet starts to get contact with SSM@PM, the force becomes positive indicating there is a repulsion between SSM@PM and water in dodecane (stage 2, 5.9 s). The capillary tube is driven to move closer to the sample at stage 2, which results in an increase of contact area between water droplet and SSM@PM as well as the increased repulsive force. The water droplet greatly deforms at stage 3 in response to the strong repulsion (~0.02 mN) from SSM@PM, as shown in the snapshot of 12.7 s. The repulsion decreases during the retraction of water droplet (stage 4) and a weak attraction of about 0.005 mN is detected when the water droplet completely detaches from SSM@PM (stage 5). However, the deformation of water droplet can barely be observed in the snapshot (19.4 s) because the attraction is very weak. Then the force goes back to zero suggesting that there is no water residue left on SSM@PM (stage 6, 21.9 s and 39.3 s). The force measurement exhibits strong repulsion between SSM@PM and water in the oil phase and well explains why water can be held steadily on dodecane wetted SSM@PM in oil/water separation.

The force curve and corresponding snapshots of the interaction between chloroform droplet and SSM@PM in water are shown in Figure 4.8a (red curve) and 4.8c, respectively. Different from the force curve of water-dodecane-SSM@PM system, an attractive force is detected right after stage 1 (2.1 s). The attractive force induces chloroform droplet to attach to SSM@PM and deforms the droplet to an elliptical shape (7.7 s). The attractive force gradually turns to repulsion (stage 3) arising from the hinderance of expelling water film confined between the chloroform droplet and SSM@PM (11.0 s). The droplet changes to cylindrical shape in the beginning of retraction process (stage 4, 19.0 s), and then gradually turns into concave bridge with neck (22.7 s) with the elevation

of capillary tube, during which the force turns to attraction and increases quickly. The attraction becomes smaller as the neck grows thinner at stage 5 (26.6 s). At 27.4 s, the capillary neck breaks to leave a chloroform droplet on SSM@PM (stage 6, 27. 5 s), and the interaction force changes from ~ -0.038 mN to ~0.05 mN within 0.1 s. The tiny fluctuations in force curve may arise from the motion of small bubbles lifted from SSM@PM in the measurement. The bubbles lifted after the rupture of capillary neck move to the top of the chloroform droplet on SSM@PM to generate a relatively large bubble (28.3 s, 39.3 s). The constant positive force value (~0.05 mN) arises from the gravity force of chloroform droplet left on the SSM@PM. The force measurement demonstrates a strong attraction between SSM@PM and chloroform droplet in water that helps to expel the water film confined between them, so that the chloroform droplet jumps into contact with and adheres to SSM@PM. As one side of SSM@PM is exposed to air in oil/water separation, the chloroform can easily penetrate SSM@PM to achieve oil/water separation.

4.3.4 Bubble-MD(SH)M interaction

The force profile between an air bubble and MD(SH)M SAM surface in 500 mM NaCl solution is measured using AFM to investigate the hydrophobic interaction, as illustrated in Figure 4.9. In Figure 4.9a, a weak repulsion of ~5.5 nN arising mainly from VDW force appears during approach, after which a sudden "jump-in" behavior occurs, implying the bubble attaches onto the surface. The surface force in 500 mM NaCl solution mainly consists of VDW force and hydrophobic interaction as the EDL force is significantly suppressed. As illustrated in the force curve, the hydrophobic interaction overcomes repulsive VDW force to rupture the water film and induce bubble attachment. The experimental data (red circle) can be well fitted by the aforementioned model based on the Reynolds lubrication theory and augmented Young-Laplace equation (black curve) using the C_0 of 89.2 mJ/m^2, which is calculated based on the data (i.e., contact angle and

interfacial tension) reported previously[41]. The decay length D_0 is determined to be 1.50 ± 0.05 nm from the theoretical calculation, showing a strong hydrophobic interaction between air bubble and MD(SH)M SAM surface[43,52]. The critical central separation just before bubble attachment is calculated to be 13.7 nm, as shown in Figure 4.9b. The "pimple" droplet shape reveals that the center of bubble is severely pulled to the SAM surface because of the hydrophobic interaction. It can be estimated in the calculated disjoining pressure profiles that the overall disjoining pressure turns attractive at separation distance of ~17 nm due to the hydrophobic attraction and increases drastically until 13.7 nm where the bubble attachment occurs (Figure 4.9c). The hydrophobic interaction endows MD(SH)M functionalized materials with strong attraction to oil in aqueous phase.

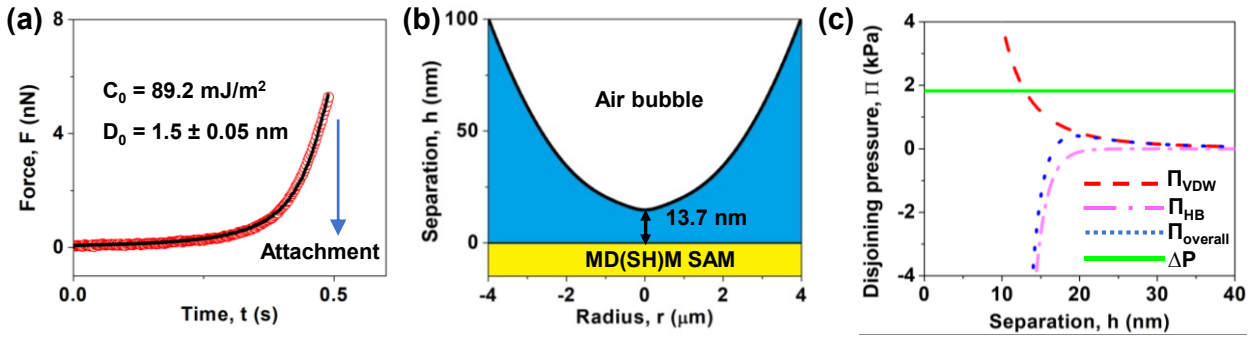

Figure 4.9 (a) Force profile between an air bubble and MD(SH)M SAM surface in 500 mM NaCl, red circle and black line represent measured force data and theoretically fitted result, respectively. (b) The calculated bubble profile before attachment. (c) The disjoining pressure profiles due to the various surface forces (e.g., VDW, HB).

4.3.5 Oil absorption

As illustrated above, the MD(SH)M functionalized materials have strong affinity to oil in both air and liquid phase, which makes them a good candidate for oil absorption as well as demulsification.

CF is chosen as the substrate for oil absorption tests because of the high specific surface area and the good capacity of liquid absorption. The gained weights of CF@PM after absorbing five types of oil, hexane, chloroform, toluene, PE and corn oil are shown in Figure 4.10a, which are 11.0, 16.1, 12.4, 5.9 and 14.0 times larger than the original weight of CF@PM, respectively. The weight gain follows the trend of density that chloroform has the highest density (1.48 g/mL), while hexane (0.65 g/mL) and PE (0.65 g/mL) have the lowest density. The weight gain after absorbing PE is relatively small because of its high volatility. Some absorbed PE evaporates during the 10 s waiting time before transferring CF@PM to glass vial.

The CF@PM is also used to absorb spilled oil from water, as illustrated in Figure 4.10b, where toluene is dyed in red and used as the model oil. The CF@PM is held by a tweezer to move around to absorb spilled oil. After absorption, the red toluene oil cannot be observed in the beaker, and the performance is evaluated by calculating the water rejection rate. As shown in Figure 4.10c, only trace amount of water is absorbed by CF@PM while absorbing five types of spilled oil, showing a good water repellency in oil absorption. The water rejection rate of chloroform is a bit lower than that of hexane, toluene and PE, which may be attributed to the small amount of water adhered to the superficial layer of CF@PM in the immersion in water. The chloroform spill can be effectively absorbed by CF@PM from the bottom of beaker even though a small amount of water has adhered to CF@PM, which is mainly contributed to the strong hydrophobic interaction. The water rejection of corn oil is low because some organic acid components in corn oil can form hydrogen bonding with water and result in a relatively higher water content in the absorbed oil. The recycle and reuse of CF@PM in oil absorption is tested using toluene as spilled oil, and the results are exhibited in Figure 4.10d-e. Despite some minor fluctuations, generally the water concentrations stay low (a few hundred ppm) and slightly increases from ~450 ppm to ~600 ppm

in 10 cycles (Figure 4.10d). The water rejection rate is nearly 100% for all the cycles, showing a good recyclability of CF@PM in absorbing oil from water (Figure 4.10e).

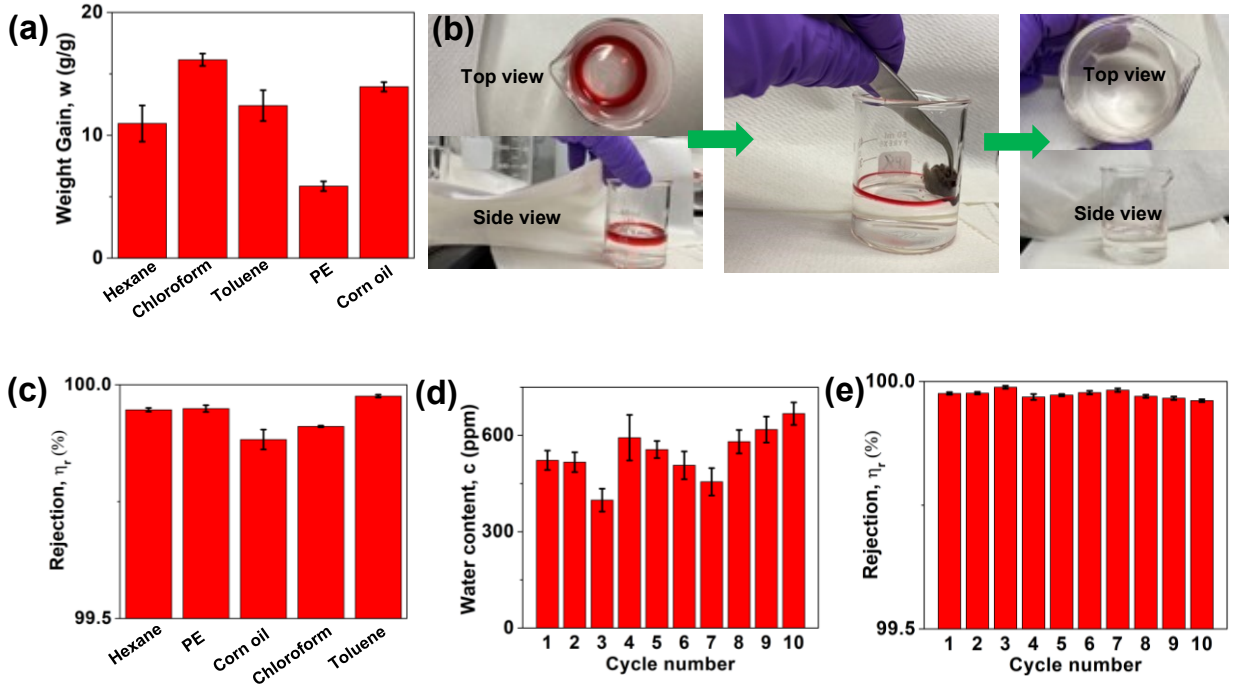

Figure 4.10 (a) The weight gain of CF@PM after absorbing different types of oil. (b) The experiment of absorbing toluene (dyed in red) from water in a beaker using CF@PM. (c) The water rejection rate of absorbing different types of oil from water using CF@PM. (d) The water concentration in the toluene squeezed out from CF@PM after oil absorption in 1-10 cycles. (e) the water rejection rate of absorbing toluene from water in 1-10 cycles.

4.3.6 Demulsification of span 80 or asphaltenes stabilized W/O emulsions

The demulsification of surfactant or asphaltenes stabilized W/O emulsions is conducted using a custom-made apparatus, and the CF@PM does not need to be pre-wetted by oil before use. As illustrated in Figure 4.11a, the span 80-stabilized emulsion turns from milky white to a clear solution after filtering through CF@PM under gravity. Besides, the emulsified spherical water

droplets disappear after filtration as shown in the microscope images (Figure 4.11b). The water content in the demulsified solution of first run greatly decreases to ~380 ppm as compared with that of original emulsion (1 vol.%). The water content stays around ~350 ppm in the following 9 runs (Figure 4.11c). The separation efficiency for first 10 runs is all above 95%, suggesting CF@PM could efficiently break span80-stabilized W/O emulsion with satisfying capacity. In the demulsification of asphaltenes-stabilized W/O emulsion (Figure 4.12a), the turbid emulsion becomes clear organic solution after filtration. The pattern on background paper (inset in Figure 4.12a) cannot be observed through the turbid emulsion but is very clear through the filtered organic solution. The emulsified water droplets cannot be observed in the microscope image after filtration (Figure 4.12b), revealing the successful demulsification of asphaltenes-stabilized emulsion. The amount of filtered solution in the first run is less than that of original emulsion because some of the oil is absorbed by dry CF@PM. The demulsified solutions in 1 to 3 runs are optically clear to show the background letters (Figure 4.12c). Such excellent demulsification performance is mainly attributed to the strong affinity to oil as well as the resistance to water of MD(SH)M functionalized materials. The bulk oil phase in emulsion would be absorbed quickly by CF@PM and flow to the vial, while the emulsified water droplets would be inhibited, achieving the successful oil/water phase separation.

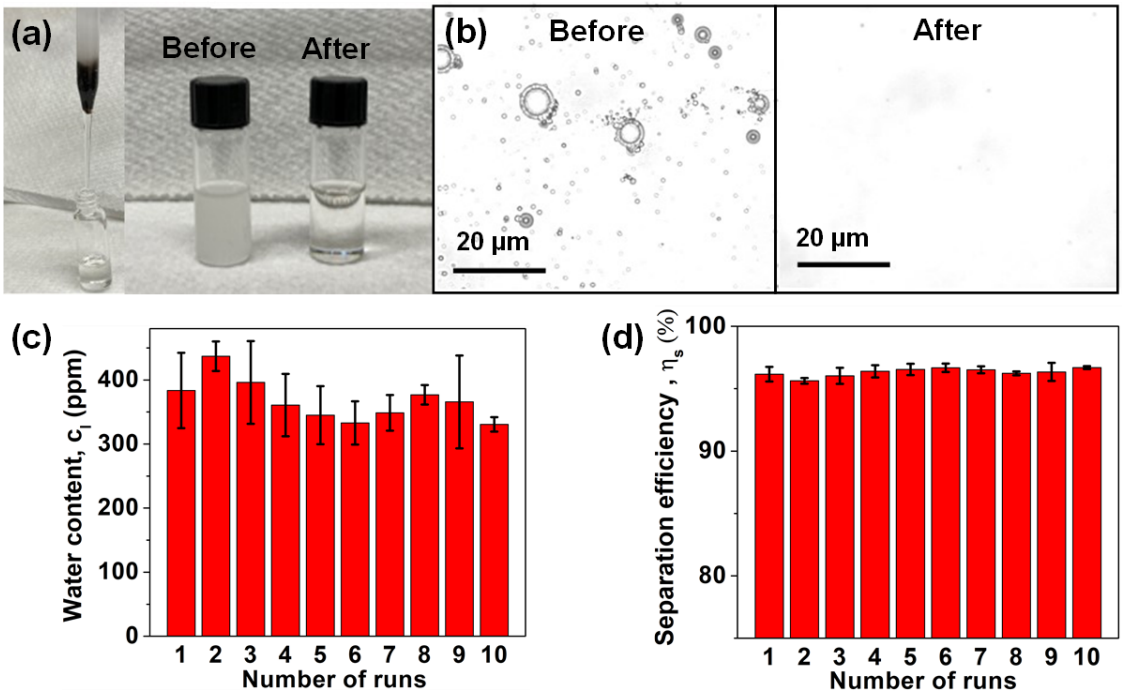

Figure 4.11 (a) Breaking water-in-toluene emulsion stabilized by span 80 using CF@PM. (b) Microscope images of emulsion before and after filtration. (c) The water concentration in oil phase after demulsification in 1-10 runs. (d) Separation efficiency of breaking span 80-stabilized W/O emulsion in 1-10 runs.

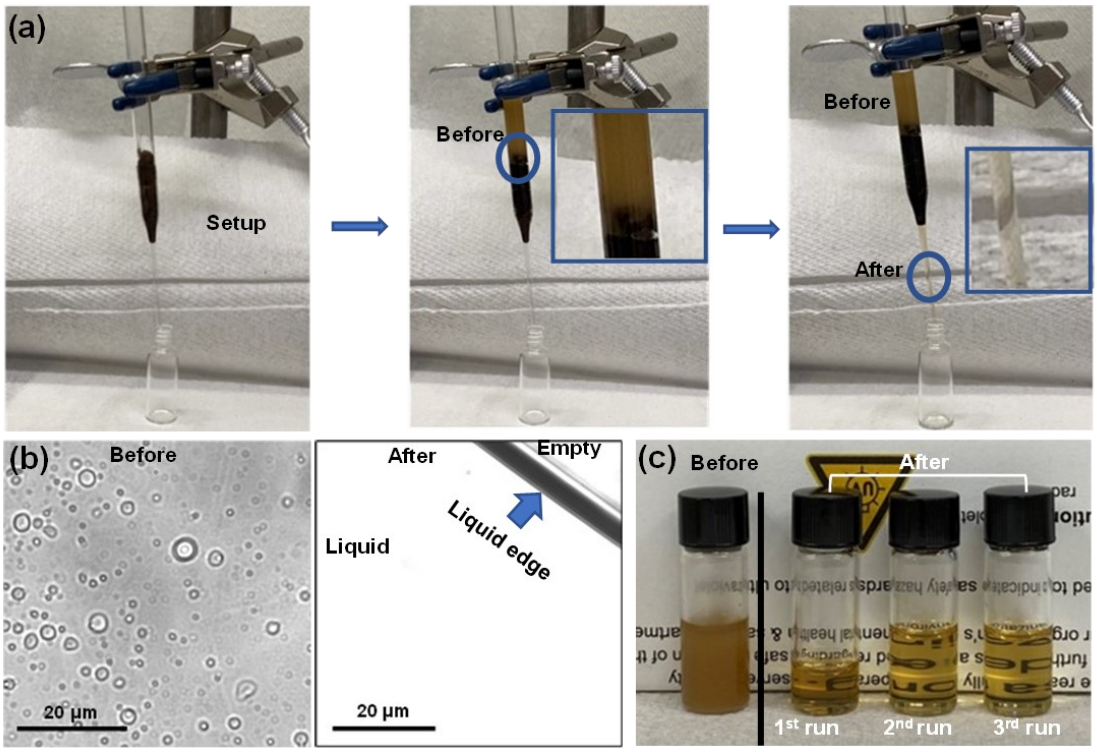

Figure 4.12 (a) Breaking asphaltenes (300 mg/L) stabilized W/O emulsion using CF@PM. The inset shows the zoomed region highlighted by blue circle. (b) Microscope images of emulsion before and after filtration. (c) The bottle test of emulsion before and after filtration, the volume of emulsion before filtration in each run is 1 mL.

4.4 Conclusions

In this work, we report a facile, universal, and scalable method to functionalize fiber-based substrates (e.g., SSM and CF) using a hydrophobic/oleophilic small molecule MD(SH)M for applications in oil/water separation, oil absorption and demulsification. Using the universal PDA coating as intermediate layer, this method can readily modify various commercially available substrates, which is of great importance in applications in engineering, food, and environmental fields. The results of XPS, ATR-FTIR and SEM-EDS characterizations demonstrate that the MD(SH)M coatings has been successfully and facilely immobilized on various surfaces with PDA

as the intermediate layer. The contact angle measurement in air on four MD(SH)M functionalized materials (i.e., CF@PM, SSM@PM, PVDF@PM, PU@PM) indicates that the MD(SH)M coating endows the as-prepared materials with very low oil contact angle (~0°) and high water contact angle (up to ~160°). This hydrophobic property of as-prepared material is further studied in force measurement with a water droplet in air that the CF@PM shows resistance to water droplet while the bare CF exhibits strong attraction to absorb water droplet. The SSM@PM is selected as the model material to conduct oil/water separation experiments and exhibits excellent separation ability for mixtures of water and low-density/high-density oil. The fundamental interaction mechanisms underlying the oil/water separation performance of MD(SH)M functionalized materials have been investigated using ITFDA and bubble probe AFM techniques. It is found that MD(SH)M coating layer possesses strong affinity to oil droplet under water but shows almost no adhesion to water droplet in oil. Surface force measurements between an air bubble and MD(SH)M SAM in 500 mM NaCl demonstrate that hydrophobic interaction contributes significantly to its excellent oil affinity in water, with a decay length of 1.50 nm. In addition, the oil absorption and demulsification tests show that CF@PM is capable of effectively absorbing five types of spilled oil from water with water rejection rate higher than 99.5%, maintaining high water rejection capability even after 10 cyclic uses. The CF@PM also shows excellent performance in treating W/O emulsions stabilized by surfactants or asphaltenes, with the separation efficiency higher than 95% in cyclic demulsification tests. Our work provides a facile and scalable method to functionalize a broad range of substrates by depositing suitable small molecules, with useful applications in various oil decontamination processes such as oil/water separation, oil absorption and demulsification.

References

1. Meng, Q. Rethink potential risks of toxic emissions from natural gas and oil mining. *Environ. Pollut.* **240**, 848–857 (2018).

2. Yan, B. *et al.* Rapid Dewatering and Consolidation of Concentrated Colloidal Suspensions: Mature Fine Tailings via Self-Healing Composite Hydrogel. *ACS Appl. Mater. Interfaces* **11**, 21610–21618 (2019).

3. Sivaram, N. M., Gopal, P. M. & Barik, D. Toxic waste from textile industries. in *Energy from Toxic Organic Waste for Heat and Power Generation* 43–54 (Elsevier, 2018). doi:10.1016/B978-0-08-102528-4.00004-3.

4. Aurell, J. & Gullett, B. K. Aerostat sampling of PCDD/PCDF emissions from the Gulf oil spill in situ burns. *Environ. Sci. Technol.* **44**, 9431–9437 (2010).

5. Gao, H., Zhao, S., Cheng, X., Wang, X. & Zheng, L. Removal of anionic azo dyes from aqueous solution using magnetic polymer multi-wall carbon nanotube nanocomposite as adsorbent. *Chem. Eng. J.* **223**, 84–90 (2013).

6. Cammarota, M. C. & Freire, D. M. G. A review on hydrolytic enzymes in the treatment of wastewater with high oil and grease content. *Bioresource Technology* vol. 97 2195–2210 (2006).

7. Shi, C., Xie, L., Zhang, L., Lu, X. & Zeng, H. Probing the interaction mechanism between oil droplets with asphaltenes and solid surfaces using AFM. *J. Colloid Interface Sci.* **558**, 173–181 (2019).

8. Jian, C., Liu, Q., Zeng, H. & Tang, T. A Molecular Dynamics Study of the Effect of

Asphaltenes on Toluene/Water Interfacial Tension: Surfactant or Solute? *Energy and Fuels* **32**, 3225–3231 (2018).

9. Ali, M. F. & Alqam, M. H. Role of asphaltenes, resins and other solids in the stabilization of water in oil emulsions and its effects on oil production in Saudi oil fields. *Fuel* **79**, 1309–1316 (2000).

10. Yue, X., Li, Z., Zhang, T., Yang, D. & Qiu, F. Design and fabrication of superwetting fiber-based membranes for oil/water separation applications. *Chemical Engineering Journal* vol. 364 292–309 (2019).

11. Ma, Q. *et al.* Zeolitic imidazolate framework-8 film coated stainless steel meshes for highly efficient oil/water separation. *Chem. Commun.* **54**, 5530–5533 (2018).

12. Cai, Y. *et al.* A facile method to fabricate a double-layer stainless steel mesh for effective separation of water-in-oil emulsions with high flux. *J. Mater. Chem. A* **4**, 18815–18821 (2016).

13. Lv, N., Wang, X., Peng, S., Luo, L. & Zhou, R. Superhydrophobic/superoleophilic cotton-oil absorbent: Preparation and its application in oil/water separation. *RSC Adv.* **8**, 30257–30264 (2018).

14. Daksa Ejeta, D. *et al.* Preparation of superhydrophobic and superoleophilic cotton-based material for extremely high flux water-in-oil emulsion separation. *Chem. Eng. J.* **402**, 126289 (2020).

15. Deng, Y. *et al.* Facile one-step preparation of robust hydrophobic cotton fabrics by covalent bonding polyhedral oligomeric silsesquioxane for ultrafast oil/water separation. *Chem. Eng.*

J. **379**, 122391 (2020).

16. Li, X., Cao, M., Shan, H., Handan Tezel, F. & Li, B. Facile and scalable fabrication of superhydrophobic and superoleophilic PDMS-co-PMHS coating on porous substrates for highly effective oil/water separation. *Chem. Eng. J.* **358**, 1101–1113 (2019).

17. Jin, K. *et al.* Design and fabrication of Gecko-inspired adhesives. *Langmuir* **28**, 5737–5742 (2012).

18. Jiang, J., Zhu, L., Zhu, L., Zhu, B. & Xu, Y. Surface characteristics of a self-polymerized dopamine coating deposited on hydrophobic polymer films. *Langmuir* **27**, 14180–14187 (2011).

19. Yang, S. *et al.* Robust, stretchable and photothermal self-healing polyurethane elastomer based on furan-modified polydopamine nanoparticles. *Polymer (Guildf).* **190**, 122219 (2020).

20. Shang, B., Wang, Y., Peng, B. & Deng, Z. Bioinspired polydopamine particles-assisted construction of superhydrophobic surfaces for oil/water separation. *J. Colloid Interface Sci.* **482**, 240–251 (2016).

21. Zhang, J. *et al.* Scalable polyzwitterion-polydopamine coating for regenerable oil/water separation and underwater self-cleaning of stubborn heavy oil fouling without pre-hydration. *Chem. Commun.* **54**, 9734–9737 (2018).

22. Han, L. *et al.* Universal Mussel-Inspired Ultrastable Surface-Anchoring Strategy via Adaptive Synergy of Catechol and Cations. *ACS Appl. Mater. Interfaces* **10**, 2166–2173 (2018).

23. Yu, Y., Shapter, J. G., Popelka-Filcoff, R., Bennett, J. W. & Ellis, A. V. Copper removal using bio-inspired polydopamine coated natural zeolites. *J. Hazard. Mater.* **273**, 174–182 (2014).

24. Malollari, K. G. *et al.* Mechanical Enhancement of Bioinspired Polydopamine Nanocoatings. (2019) doi:10.1021/acsami.9b15740.

25. Deng, W., Fan, T. & Li, Y. In situ biomineralization-constructed superhydrophilic and underwater superoleophobic PVDF-TiO2 membranes for superior antifouling separation of oil-in-water emulsions. *J. Memb. Sci.* **622**, 119030 (2021).

26. Liu, H. *et al.* Robust translucent superhydrophobic PDMS/PMMA film by facile one-step spray for self-cleaning and efficient emulsion separation. *Chem. Eng. J.* **330**, 26–35 (2017).

27. Zhou, X. *et al.* Robust and durable superhydrophobic cotton fabrics for oil/water separation. *ACS Appl. Mater. Interfaces* **5**, 7208–7214 (2013).

28. Feng, X., Zhai, J. & Jiang, L. The fabrication and switchable superhydrophobicity of TiO2 nanorod films. *Angew. Chemie - Int. Ed.* **44**, 5115–5118 (2005).

29. Wu, Z., Lee, D., Rubner, M. F. & Cohen, R. E. Structural color in porous, superhydrophilic, and self-cleaning SiO 2/TiO2́ bragg stacks. *Small* **3**, 1445–1451 (2007).

30. Kim, Y. *et al.* Robust superhydrophilic/hydrophobic surface based on self-aggregated Al 2O 3 nanowires by single-step anodization and self-assembly method. *ACS Appl. Mater. Interfaces* **4**, 5074–5078 (2012).

31. Luo, Z. Y. *et al.* Superhydrophilic Nickel Nanoparticles with Core-Shell Structure to Decorate Copper Mesh for Efficient Oil/Water Separation. *J. Phys. Chem. C* **120**, 12685–

12692 (2016).

32. Prystupa, J. Fluorine - A current literature review. An NRC and ATSDR based review of safety standards for exposure to fluorine and fluorides. *Toxicology Mechanisms and Methods* vol. 21 103–170 (2011).

33. Li, J. J., Zhou, Y. N. & Luo, Z. H. Smart Fiber Membrane for pH-Induced Oil/Water Separation. *ACS Appl. Mater. Interfaces* **7**, 19643–19650 (2015).

34. Liu, Y., Wang, X. & Feng, S. Nonflammable and Magnetic Sponge Decorated with Polydimethylsiloxane Brush for Multitasking and Highly Efficient Oil–Water Separation. *Adv. Funct. Mater.* **29**, 1902488 (2019).

35. Jin, Y. *et al.* Superhydrophobic and superoleophilic polydimethylsiloxane-coated cotton for oil-water separation process: An evidence of the relationship between its loading capacity and oil absorption ability. *J. Hazard. Mater.* **300**, 175–181 (2015).

36. Yang, H.-C. *et al.* Mussel-inspired Modification of Polymer Membrane for Ultrahigh Water Permeability and Oil-in-Water Emulsion Separation. *J. Name* **00**, (2013).

37. Ortiz, D. P., Baydak, E. N. & Yarranton, H. W. Effect of surfactants on interfacial films and stability of water-in-oil emulsions stabilized by asphaltenes. *J. Colloid Interface Sci.* **351**, 542–555 (2010).

38. Jiang, L., Tang, Z., Park-Lee, K. J., Hess, D. W. & Breedveld, V. Fabrication of non-fluorinated hydrophilic-oleophobic stainless steel mesh for oil-water separation. *Sep. Purif. Technol.* **184**, 394–403 (2017).

39. Mao, X. *et al.* Novel Fe3O4 based superhydrophilic core-shell microspheres for breaking

asphaltenes-stabilized water-in-oil emulsion. *Chem. Eng. J.* **358**, 869–877 (2019).

40. Xie, Y. *et al.* Highly Regenerable Mussel-Inspired Fe $_3$ O $_4$ @Polydopamine-Ag Core–Shell Microspheres as Catalyst and Adsorbent for Methylene Blue Removal. *ACS Appl. Mater. Interfaces* **6**, 8845–8852 (2014).

41. Mao, X., Tan, J., Xie, L., Wang, J. & Zeng, H. Novel multifunctional solid slippery surfaces with self-assembled fluorine-free small molecules. *Chem. Eng. J.* **404**, 127064 (2021).

42. Shi, C. *et al.* Interaction between Air Bubbles and Superhydrophobic Surfaces in Aqueous Solutions. *Langmuir* **31**, 7317–7327 (2015).

43. Liu, J. *et al.* Probing effects of molecular-level heterogeneity of surface hydrophobicity on hydrophobic interactions in air/water/solid systems. *J. Colloid Interface Sci.* **557**, 438–449 (2019).

44. Xie, L. *et al.* Interaction Mechanisms between Air Bubble and Molybdenite Surface: Impact of Solution Salinity and Polymer Adsorption. *Langmuir* **33**, 2353–2361 (2017).

45. Shi, C., Chan, D. Y. C., Liu, Q. & Zeng, H. Probing the hydrophobic interaction between air bubbles and partially hydrophobic surfaces using atomic force microscopy. *J. Phys. Chem. C* **118**, 25000–25008 (2014).

46. Shi, C. *et al.* Measuring forces and spatiotemporal evolution of thin water films between an air bubble and solid surfaces of different hydrophobicity. *ACS Nano* **9**, 95–104 (2015).

47. Vakarelski, I. U. *et al.* Dynamic interactions between microbubbles in water. *Proc. Natl. Acad. Sci. U. S. A.* **107**, 11177–11182 (2010).

48. Tabor, R. F., Manica, R., Chan, D. Y. C., Grieser, F. & Dagastine, R. R. Repulsive Van der Waals forces in soft matter: Why bubbles do not stick to walls. *Phys. Rev. Lett.* **106**, (2011).

49. Cui, X., Shi, C., Xie, L., Liu, J. & Zeng, H. Probing Interactions between Air Bubble and Hydrophobic Polymer Surface: Impact of Solution Salinity and Interfacial Nanobubbles. *Langmuir* **32**, 11236–11244 (2016).

50. Cui, X. *et al.* Modulation of Hydrophobic Interaction by Mediating Surface Nanoscale Structure and Chemistry, not Monotonically by Hydrophobicity. *Angew. Chemie* **130**, 12079–12084 (2018).

51. Xie, L., Cui, X., Gong, L., Chen, J. & Zeng, H. Recent Advances in the Quantification and Modulation of Hydrophobic Interactions for Interfacial Applications. *Langmuir* (2020) doi:10.1021/acs.langmuir.9b03573.

52. Cui, X. *et al.* Modulation of Hydrophobic Interaction by Mediating Surface Nanoscale Structure and Chemistry, not Monotonically by Hydrophobicity. *Angew. Chemie Int. Ed.* **57**, 11903–11908 (2018).

Chapter 5 Probing the Interactions Between Pickering Emulsion Droplets Stabilized with pH-Responsive Nanoparticles

5.1 Introduction

Emulsions play an important role in a wide range of chemical and industrial fields, such as oil industry[1–4], food engineering[5,6], pharmaceuticals[7] and cosmetics[8]. Emulsions are usually formed by mixing two or more immiscible liquids (e.g., oil and water) with interfacially active materials, such as surfactants[9], asphaltenes[10–12], and nano/micro particles[13]. The emulsions stabilized with particles are commonly called Pickering emulsions, which have been studied for more than a century following Pickering's pioneering work in 1907[14]. It is generally accepted that the particles with partial wettability in both aqueous and organic phases can adsorb to the oil/water interface. Pickering emulsions stabilized with hydrophilic particles tend to form oil-in-water (O/W) emulsions, while those with hydrophobic particles tend to form water-in-oil (W/O) emulsions. Over the past few decades, broad applications have been developed based on Pickering emulsions[4], such as preparation of Janus microgels[15], synthesis of hybrid microspheres[16], and formation of switchable emulsions[17].

Recently, stimuli-responsive Pickering emulsions have attracted great research interest due to their switchable property in response to external stimuli, such as pH[18,19], magnetic field[20] and temperature [21]. The pH-responsive Pickering emulsions are usually produced based on the particles bearing polar functional groups (e.g., carboxyl group) that respond to pH changes. Therefore, the alteration of surface wettability and surface charge by tuning pH could trigger the switch between phase separation and stable emulsions, or transition between different types of emulsions[22]. The stabilization mechanism of Pickering emulsion has been studied from many aspects, such as contact angle, interfacial tension, partitioning behavior, and especially the arrangement of particles

at interface[23,24]. It has been reported by Binks and co-workers that Pickering emulsion droplets can be stabilized by particles through two possible mechanisms, viz., steric repulsion due to the dense particle monolayer covering the oil/water interface of droplets, and steric barrier from a compact particle monolayer confined between contacted emulsion droplets (so-called bridging stabilization)[24,25]. Lee et al. observed the microstructure of faceted droplets bridged via monolayers of particles in a gel-like emulsion using confocal microscopy[26]. French et al. developed a model O/W system to study the factors affecting the bridging behaviors such as particle wettability, shear rate, and particle volume fraction[27]. French and co-workers also reported that particles adsorbed on two droplets could exchange with each other during the bridging process, which further enabled the formation of stable Pickering emulsion[28]. Despite the considerable research progress achieved through experimental characterization (e.g., microscopic imaging) and theoretical analysis, the experimental quantification of the interaction forces between two Pickering emulsion droplets has been rarely reported, particularly at the nanoscale. More importantly, unraveling how the pH stimuli modulates the interaction forces in W/O and O/W Pickering emulsions is still not available. Experimentally quantifying the surface forces of Pickering emulsions is of both fundamental and practical significance to reveal their interaction mechanisms and facilitate the development of pH-responsive Pickering emulsions[29–32].

Recently, the drop probe atomic force microscope (AFM) technique has been applied to quantify the interactions in emulsions at nanoscale, such as the interactions between two water droplets in oil with interface-active species (e.g., asphaltenes)[33–37]. In a typical measurement, a drop probe can be generated by anchoring a liquid droplet on a tipless AFM cantilever, which is placed above another droplet, lowered to make the head-on collision, and then driven to measure the interaction force. The measured force data can be well analyzed using a theoretical model based on Reynolds

lubrication theory and the augmented Young-Laplace equation to precisely reconstruct the combinatory effects arising from different surface forces (e.g., van der Waals, electric double layer forces) and hydrodynamic interaction[37–41]. These theoretical calculations have been also experimentally validated using AFM coupled with reflection interference contrast microscopy (RICM)[42,43]. These force measurements provide useful information on surface deformation, intermolecular forces and adhesion of droplets, which plays a critical role in determining the behaviors (e.g., stability) of bulk emulsions and their interaction mechanisms at nanoscale.

In this work, bilayer oleic acid-coated Fe_3O_4 nanoparticles (Fe_3O_4@2OA NPs) were synthesized for stabilizing oil/water emulsions. The pH-responsive Fe_3O_4@2OA NPs are able to switch the emulsions from W/O type in acidic condition to O/W type in basic condition. For the *first* time, the interaction forces between two Pickering emulsion droplets (i.e., pH-responsive O/W or W/O droplets with Fe_3O_4@2OA NPs) were measured using the drop probe AFM technique to study their stabilization mechanism. More specifically, force measurements were conducted between two water droplets at low pH (i.e., pH 2 and 4) in oil and between two oil droplets in alkaline water (i.e., pH 9 and 11) in the presence of Fe_3O_4@2OA NPs. The force profiles were analyzed using the theoretical model based on the Reynolds lubrication theory and augmented Young-Laplace equation by including the effect of disjoining pressure. The adsorption mechanisms of Fe_3O_4@2OA NPs to oil/water interfaces were proposed and their contributions to the stability of Pickering emulsions were discussed based on the surface force results and interfacial tension measurements.

5.2 Materials and methods

5.2.1 Materials

The chemicals including n-Dodecane, oleic acid (OA), iron(III) chloride hexahydrate ($FeCl_3 \cdot 6H_2O$), iron(II) chloride tetrahydrate ($FeCl_2 \cdot 4H_2O$), hydrochloric acid (HCl) (~37%) and trichloro(octadecyl)silane (OTS) were purchased from Sigma Aldrich. Ammonium hydroxide (NH_4OH) (30%) and sodium hydroxide (NaOH) were purchased from Fisher Scientific. All the chemicals were used as received.

5.2.2 Preparation of Fe_3O_4@2OA NPs and Pickering emulsions

The Fe_3O_4@2OA NPs were prepared according to a previously reported method, where $FeCl_3 \cdot 6H_2O$ and $FeCl_2 \cdot 4H_2O$ were mixed at 80 °C in aqueous solution, followed by the addition of NH_4OH and OA [44]. The 0.1 wt% Fe_3O_4@2OA NPs in aqueous suspensions with different pH conditions were prepared by adding HCl or NaOH to adjust pH to 2, 4, 9 and 11, respectively. Then the aqueous suspension containing Fe_3O_4@2OA NPs was mixed with equal volume of dodecane using an IKA T18 digital ultra-turrax homogenizer at 10,000 rpm for 5 min. The as-prepared emulsions were denoted according to the pH condition, emulsion2, emulsion4, emulsion9 and emulsion11, respectively. The microscopy images of the as-prepared emulsions were obtained using an optical microscope.

5.2.3 Sample characterizations

Zeta potentials of Fe_3O_4@2OA NPs in aqueous suspensions at pH 2, 4, 9, and 11 were measured using a Zetasizer Nano ZSP (Malvern Instruments, UK). The dodecane/water interfacial tension (IFT) in the presence of Fe_3O_4@2OA NPs was measured by a goniometer/tensiometer (ramè-hart, instrument Co., NJ, USA) using the pendant drop method at room temperature (21.5 ºC). The aqueous droplet at a certain pH containing Fe_3O_4@2OA NPs was generated at the tip of a needle

in the quartz cell filled with dodecane. The drop profile was captured by a charge-coupled device (CCD) camera every 1 s for a total of 1500 s. X-ray diffraction (XRD) spectrum of Fe_3O_4@2OA NPs was recorded on a Rigaku Ultimate IV X-ray diffractometer with Cu Kα radiation (40 kV, 40 mA). The morphology of Fe_3O_4@2OA NPs was characterized using a JEOL 2200FS Transmission Electron Microscope (TEM). The attenuated total reflectance Fourier transform infrared (ATR-FTIR) spectrum of Fe_3O_4@2OA NPs was measured on ATR-FTIR (Thermo Scientific Nicolet iS50).

5.2.4 AFM force measurements

The forces between two water droplets in oil (i.e., dodecane) or two oil (i.e., dodecane) droplets in aqueous solution (i.e., 1 mM NaCl) with/without Fe_3O_4@2OA NPs were measured using an MFP-3D AFM (Asylum Research, Santa Barbara, CA) mounted with an inverted microscope (Nikon Ti-U). The experimental configurations for the surface force measurements with/without Fe_3O_4@2OA NPs are shown in **Figure 5.1**. Prior to the force measurement, the water droplets were injected into AFM fluid cell using a custom-made ultra-sharp glass pipet, and the injected water droplets were then spontaneously settled and immobilized on a pre-hydrophobized glass substrate by gravity force [45]. For water droplets (pH 2 or 4) containing Fe_3O_4@2OA NPs, 15-min aging was applied to allow Fe_3O_4@2OA NPs to adsorb onto water/oil interface, after which a large amount of pure dodecane was applied to exchange with the bulk oil phase. For the force measurements between two oil droplets in aqueous solution, the oil droplets were generated and immobilized on the substrate of AFM fluid cell using a previously reported controlled dewetting method [46,47]. Similarly, 15-min aging was applied to allow Fe_3O_4@2OA NPs in the bulk aqueous phase (i.e., pH 9 or 11) to adsorb onto oil/water interface before washing off the free Fe_3O_4@2OA NPs by exchanging the bulk phase with 1 mM NaCl of the same pH. In all force measurements, a

custom-made tipless cantilever with gold patch at the end was pre-treated to pick up one water/oil droplet, generating a drop-probe, which was placed above another water/oil droplet to ensure a head-on contact[37,46]. To suppress hydrodynamic effect, the driving velocity of droplet probe was kept at very low values (e.g., 1 μm/s or less). The spring constant of the cantilever was calibrated using Hutter's thermal method[48].

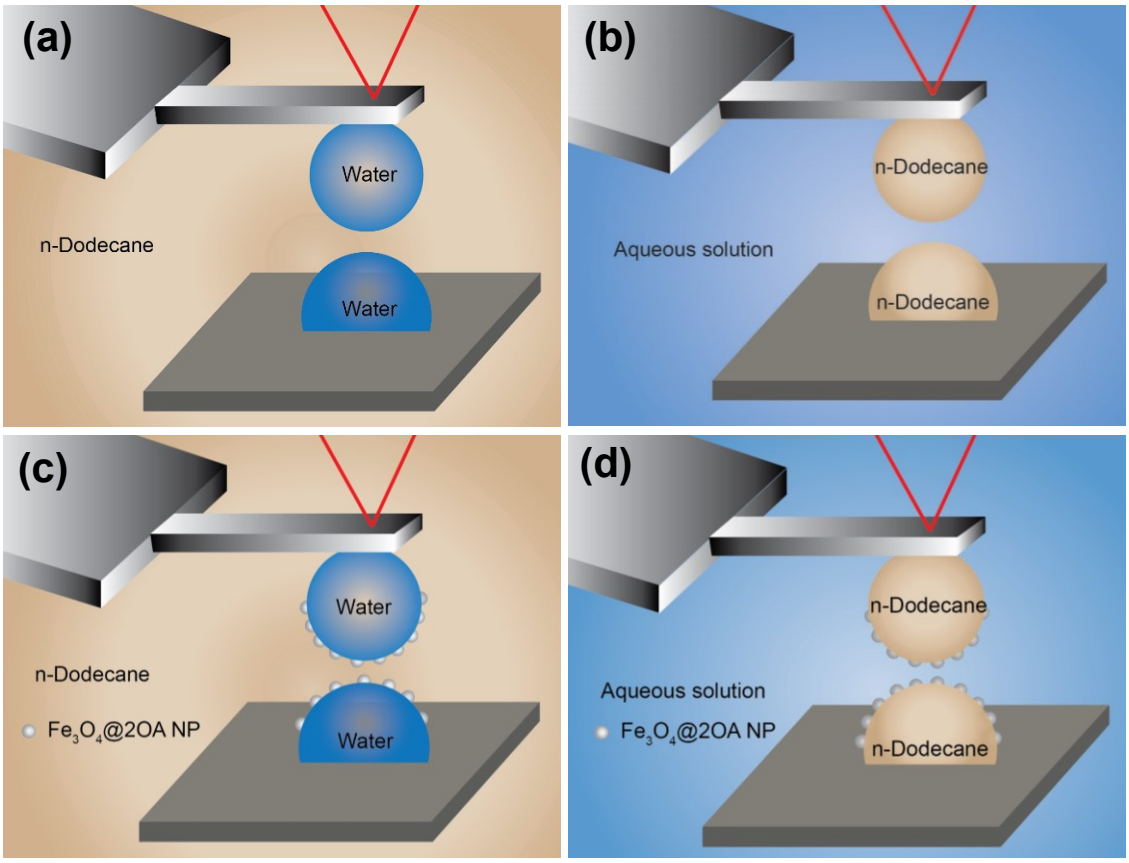

Figure 5.1 Schematic of four experimental configurations for force measurements using AFM for (a) two water droplets in oil; (b) two oil droplets in aqueous solution; (c) two water droplets (pH 2 or 4) in oil with Fe3O4 nanoparticles coated with bilayer oleic acid (Fe_3O_4@2OA NPs); and (d) two oil droplets in aqueous solution (pH 9 or 11) with Fe_3O_4@2OA NPs.

5.2.5 Theoretical model

The measured forces between two water droplets in oil or two oil droplets in aqueous solution without Fe_3O_4@2OA NPs were analyzed using a theoretical model based on the Reynolds lubrication theory and augmented Young-Laplace equation [45,49,50]. The deformation of droplets due to Laplace pressure, hydrodynamic pressure p, and disjoining pressure Π can be described by the augmented Young-Laplace equation:

$$\frac{\gamma}{2r}\frac{\partial}{\partial r}\left(r\frac{\partial h(r,t)}{\partial r}\right)=\frac{2\gamma}{R_0}-p(r,t)-\Pi \tag{5.1}$$

where γ is the interfacial tension, R_0 is the harmonic mean of the two droplet radii R_1 and R_2, r is the position expressed by radical coordinate, $p(r,t)$ is the hydrodynamic pressure, $h(r,t)$ is the separation between two drops at position r, and t is the time. The disjoining pressure Π generally arises from surface forces such as van der Waals (VDW) and electrostatic double layer (EDL) interactions. The disjoining pressure due to VDW and EDL interactions between two drops can be described by Equations (5.2) and (5.3), respectively [40,41,45,49–52].

$$\Pi_{VDW}[h(r,t)]=-\frac{A_H}{6\pi h^3(r,t)} \tag{5.2}$$

$$\Pi_{EDL}[h(r,t)]=64k_BT\rho_\infty\tanh^2\left(\frac{e\varphi}{4k_BT}\right)\exp[-\kappa h(r,t)] \tag{5.3}$$

where A_H is the Hamaker constant, κ is the inverse of Debye length, φ is the surface potential of water/oil interface, ρ_∞ is the number density of ions in water, and e is the fundamental charge. For aqueous solutions with 1:1 salt, the Debye length κ^{-1} can be calculated as

$$\kappa^{-1} = (2\rho_{\infty}e^2 / \varepsilon_0 \varepsilon k_B T)^{-1/2} \tag{5.4}$$

where ε_0 is the vacuum permittivity and ε is the dielectric constant of the medium. The overall interaction force $F(t)$ between two droplets can be calculated by integrating $p(r,t)$ and $\Pi(h(r,t))$ based on the Derjaguin approximation as shown below.

$$F(t) = 2\pi \int_0^{\infty} [p(r,t) + \Pi(h(r,t))] r dr \tag{5.5}$$

The drainage process of confined thin water/oil film between the oil/water drops is described by the Reynolds lubrication equation:

$$\frac{\partial h(r,t)}{\partial t} = \frac{1}{12\mu r} \frac{\partial}{\partial r} (r h^3(r,t) \frac{\partial p(r,t)}{\partial r}) \tag{5.6}$$

where μ is viscosity of bulk fluid phase. Immobile boundary condition is assumed at the oil/water interface, which is consistent with recent reports [38,40,53].

5.3 Results and discussion

5.3.1 Preparation and characterization of Fe_3O_4@2OA NPs

The morphology of Fe_3O_4@2OA NPs characterized by TEM is shown in Figure 5.2a-b. The as-prepared Fe_3O_4@2OA NPs are small spherical particles with mean diameter of ~10 nm. The peaks in the XRD spectrum of Fe_3O_4@2OA NPs (Figure 5.2c) can be assigned to the typical pattern of Fe_3O_4 (JCPDS 19-0629), revealing the crystalline structure of Fe_3O_4 core. Figure 5.2d shows the ATR-FTIR spectrum of Fe_3O_4@2OA NPs where the peaks at 550 cm^{-1} and 1625 cm^{-1} are assigned

to the Fe_3O_4 core, corresponding to the vibration of Fe-O bond and the hydroxy group on Fe_3O_4 surface [54]. Peaks at 2852 cm^{-1}, 2922 cm^{-1} and 1405 cm^{-1} represent asymmetric stretch of -CH_2, symmetric stretch of -CH_2, and vibration of -CH_3, respectively, attributing to the aliphatic chain of OA [55]. The -COO stretch at 1520 cm^{-1} and C-O stretch at 1050 cm^{-1} come from the carboxyl groups of OA bonded to the Fe_3O_4 core [56]. The peak shown at 1710 cm^{-1} corresponds to the stretch of C=O in second OA layer, suggesting the successful preparation of double OA layers [44,57]. Besides, zeta potentials of Fe_3O_4@2OA NPs in aqueous suspensions at pH 2, 4, 9, and 11 are shown in Figure 5.2e, which decrease with the increasing pH. The as-prepared Fe_3O_4@2OA NPs can be well dispersed in either organic solvent (i.e., dodecane) or aqueous phase at high pH (i.e., pH 11) because of the long aliphatic chains on OA layers or the negatively charged carboxyl groups on second OA layer (Figure 5.2f). In aqueous solution at low pH (i.e., pH 4), Fe_3O_4@2OA NPs tend to precipitate to the bottom because the carboxyl groups are uncharged and the hydrophobic interactions among the long aliphatic chains contribute to the aggregation. The above results demonstrate the successful preparation of pH-responsive Fe_3O_4@2OA NPs.

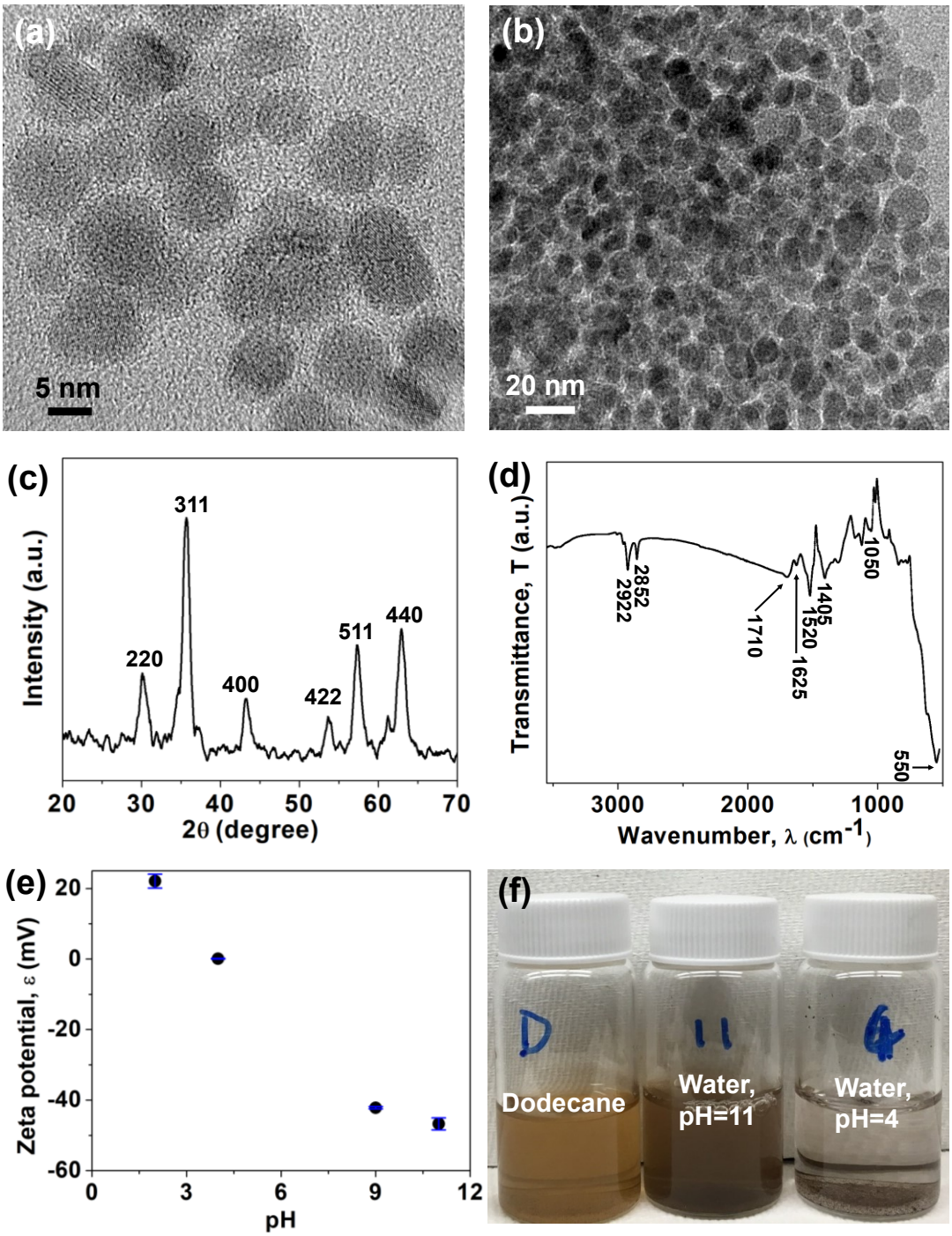

Figure 5.2 (a-b) Morphology of Fe3O4@2OA NPs characterized by Transmission Electron Microscope (TEM); (c) X-ray diffraction (XRD) spectrum of Fe3O4@2OA NPs; (d) attenuated total reflectance Fourier transform infrared (ATR-FTIR) spectrum of Fe3O4@2OA NPs; (e) zeta

potentials of Fe_3O_4@2OA NPs in aqueous suspension at pH 2, 4, 9 and 11; (f) Fe_3O_4@2OA NPs (0.01 wt%) dispersed in dodecane, and aqueous phase at pH 11 and pH 4.

5.3.2 Preparation of Pickering emulsions with Fe_3O_4@2OA NPs

The bulk Pickering emulsion was prepared by mixing equal volume of dodecane and aqueous solution containing Fe_3O_4@2OA NPs at pH 2, 4, 9 and 11, respectively. W/O emulsion is formed when aqueous solution is at pH 2 and 4 (denoted as emulsion2 and emulsion4, respectively); while O/W emulsion is formed when aqueous solution is at pH 9 and 11 (denoted as emulsion9 and emulsion11, respectively), agreeing with the results reported previously [30]. Emulsion2 tends to gradually coalesce after forming Pickering emulsion, which is more readily destabilized compared with emulsion4, emulsion9 and emulsion11. The optical microscopic images of formed Pickering emulsions are shown in Figure 5.3. The emulsion2 exhibits larger drops than other three emulsions, and some aggregated solids and coalesced water drops can be observed in Figure 5.3a, indicating partial water drop coalescence. In contrast, the drops in emulsion4, emulsion9 and emulsion11 are spherical with diameter ranging from 10 to 40 μm and no obvious coalescence is observed.

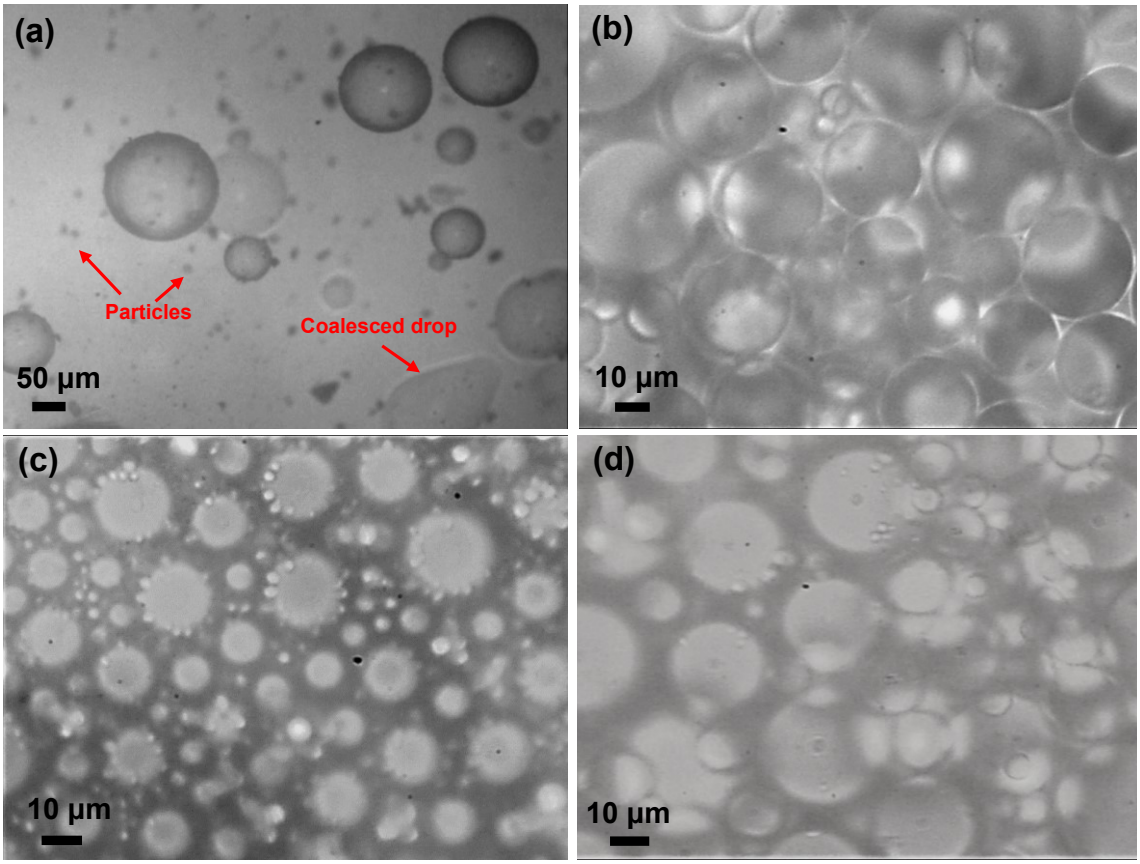

Figure 5.3 Optical microscopic image of formed (a) emulsion2; (b) emulsion4; (c) emulsion9 and (d) emulsion11.

The interfacial tension at water/dodecane interface with Fe_3O_4@2OA NPs under different pHs is shown in Figure 5.4. At pH 2, the IFT starts from ~50.4 mN/m and decreases to ~44.5 mN/m at 500 s, which then decreases more slowly until a plateau of ~43.5 mN/s is reached at 1250-1500 s (Figure 5.4a). Similarly, the IFT at pH 4 starts at ~50.0 mN/m and decreases to ~45.4 mN/m at 500 s, ending at the same IFT value (i.e., ~43.5 mN/s) at pH 2. Overall, the IFT values change with time at pH 2 and pH 4 in a very similar trend; but the emulsion2 is unstable while emulsion4 is more stable, suggesting the reduced IFT is not the factor responsible for the difference in the stability of W/O emulsions at pH 2 and 4. Unlike pH 2 and 4, the IFT at pH 9 (Figure 5.4b) starts

at ~54.0 mN/m and rapidly drops to ~48.8 mN/s within 250 s, which then keeps decreasing slowly to ~46.2 mN/m at 1500 s without reaching a plateau. The IFT at pH 11 exhibits a similar trend as that at pH 9, decreasing from ~51.5 mN/m at 0 s to ~42.2 mN/m at 1500 s, indicating Fe_3O_4@2OA NPs are more stable at water/dodecane interface at pH 11.

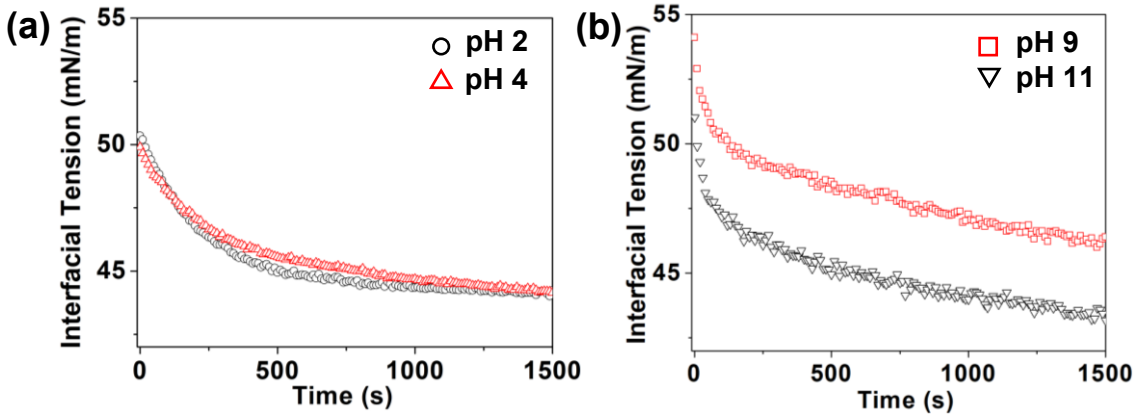

Figure 5.4 Interfacial tension between dodecane and water with Fe3O4@2OA NPs at (a) pH 2 (black circle) and pH 4 (red triangle), and (b) pH 9 (red square) and pH 11 (black inverted triangle).

5.3.3 Interactions between two water droplets in oil and two oil droplets in water

To quantitatively determine the influence of interfacial nanoparticles on the interactions of Pickering emulsions, the forces acting between two water droplets in oil and two oil droplets in water without nanoparticles were measured at first (Figure 5.5). The approaching and retracting velocity of droplet is fixed at 1 μm/s to suppress the hydrodynamic effect. All experimental data (black open circles) can be well fitted by the aforementioned theoretical model and the fitted data are shown as red solid dots. Here, the x-axis, "piezo displacement", refers to the relative displacement between bottom center point on upper droplet and top center point on lower droplet, and the zero point is set at the point where maximum force load (~38 nN) is reached or droplet coalescence happens. The arrows indicate the moving direction of upper droplet. Positive value

and negative value of measured force indicate repulsive and attractive interactions, respectively. The force between two water droplets interacting in oil is shown in Figure 5.5a where a small repulsion is measured due to weak hydrodynamic repulsion when the upper droplet approaches the lower one. A jump-in behavior is noticed when the repulsive force reaches ~0.15 nN, indicating that the upper water droplet is in contact with lower water droplet and then coalesces into a larger water droplet. The coalescence of two water droplets can also be observed using inverted microscope. The VDW force is the only surface force available for two pristine water droplets interacting in oil, and the positive Hamaker constant for water-dodecane-water system suggests an attractive VDW force. When attractive VDW force overcomes weak hydrodynamic repulsion, the coalescence of two water droplets happens. The force result in Figure 5.5a agrees well with other reported force measurements that water droplets without interfacially active materials tend to coalesce in oil[43,58].

Figure 5.5b shows the interaction forces between two oil droplets in water. The repulsion gradually increases due to hydrodynamic and EDL repulsion when the upper oil droplet approaches the lower one, and the measured repulsion gradually decreases during retraction until a weak attraction is reached, which is attributed to the "hydrodynamic suction" effect[59]. No coalescence is observed from either the force curve or microscope imaging during force measurement, suggesting that the two oil droplets are stable against each other and a stable water film is maintained between them. The surface force mainly consists of VDW and EDL force, where the VDW force is attractive while EDL force is repulsive. According to the DLVO theory, the Debye length is ~9.6 nm in 1 mM NaCl solution. The strong EDL repulsion overcomes VDW attraction and prevents the coalescence of two oil droplets. By fitting the experimental data with the theoretical model, the

surface potential is determined to be -38 mV, which is consistent with the reported experimental values[60,61].

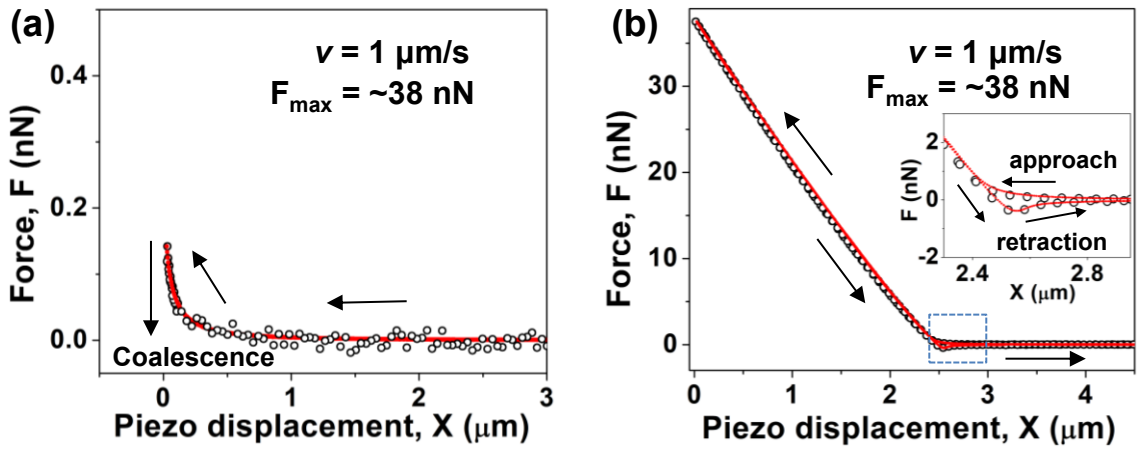

Figure 5.5 Interaction force profiles between (a) two water droplets in oil and (b) two oil droplets in 1 mM NaCl aqueous solution at pH 7 (the inset: enlarged regime in blue dash square). Black open circles are experimental data and red solid lines are fitted theoretical values. The velocity is 1 μm/s and the maximum load is fixed at ~38 nN. The arrow indicates the moving direction of upper droplet. The harmonic mean of the droplets' radii are 75 and 90 μm for (a) and (b), respectively.

5.3.4 Interactions between two water droplets in oil and two oil droplets in water with Fe_3O_4@2OA NPs

The measured force curves between two water droplets in oil and two oil droplets in 1 mM NaCl aqueous solution with Fe_3O_4@2OA NPs are shown in Figures 5.6a-b and Figures 5.6c-d, respectively. Clearly, no droplet coalescence can be observed from either force curve (Figure 5.6a-b) or inverted optical microscope images during the interaction of the emulsified water droplets in oil, which is different from the case without Fe_3O_4@2OA NPs (Figure 5.5a). The additional repulsive force that inhibits the droplet coalescence during the approach of water droplets arises

from the steric effect caused by Fe_3O_4@2OA NPs adsorbed at the water/oil interfaces. When the water droplets get separated, a jump-out behavior with an attractive force is detected, indicating the interfacial adhesion exists between the two water droplets. The adhesion is most likely attributed to the bridging effect of Fe_3O_4@2OA NPs at water/oil interfaces. It has been reported that a portion of particles at water/oil interface of one droplet will be shared by another droplet in the confined region when the two droplets enter into contact, thereby forming a confined particle monolayer and bridging the two droplets together[26–28]. During the separation of the two droplets, the confined particles will be redistributed to the water/oil interfaces of these two droplets, during which the exchange of particles could occur[28]. The confined particles at the contact region can behave as a robust barrier to effectively prevent the coalescence of droplets and such a bridging interaction also leads to the interfacial adhesion during separation. It is noted that many tiny force steps are observed before jump-out (detachment) in the retraction curve (inset of Figures 5.6a-b), and these weak step-like adhesion behaviors are most likely due to the loss of bridging at the edge of the contact zone and redistribution of confined Fe_3O_4@2OA NPs close to the edge region on the water/oil interfaces. Such interfacial particle bridging behaviors are similar to the fusion and adhesion behaviors when two bilayers are interacting with each other[62,63], and the small adhesive steps associated with detachment in Figure 5.6a-b are similar to the "stick-slip" phenomena observed during separation in the contact mechanics tests of polymer surfaces[64,65]. The approach and retraction force curves in Figures 5.6a-b do not overlap, and the adhesion hysteresis is mostly caused by the change of droplet shape during force measurements as well as the steric repulsion and interfacial adhesion associated with the re-arrangement of interfacial nanoparticles under confinement. The above interaction phenomena are observed for the cases at both pH 2 and 4. The normalized interfacial adhesion (maximum adhesion force/radius of droplet) at pH 2 is measured

to be ~0.056 mN/m (Figure 5.6a), which is larger than that at pH 4 (~0.014 mN/m) in Figure 5.6b, thereby contributing to the more evident adhesive hysteresis and more unstable emulsion at pH 2.

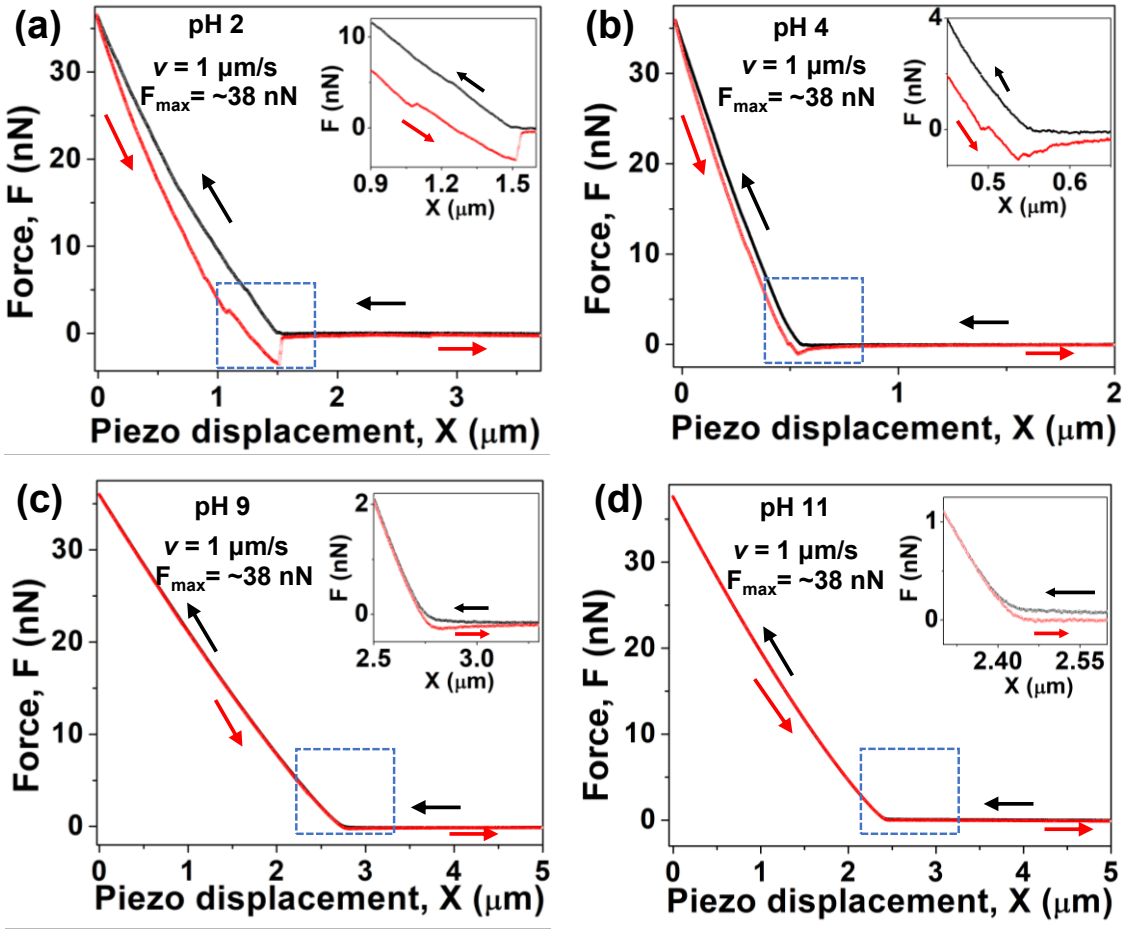

Figure 5.6 Interaction force profiles between two water droplets at (a) pH 2 and (b) pH 4 in oil with Fe3O4@2OA NPs. Interaction force profiles between two oil droplets in 1 mM NaCl at (c) pH 9 and (d) pH 11 with Fe3O4@2OA NPs. The inset is zoomed regime in blue dash square. Each force curve consists of both approach (black curve, indicated by black arrow) and retraction (red curve, indicated by red arrow) process. The maximum load applied is fixed at ~38 nN. The harmonic mean of the droplets' radii are 65, 55, 50 and 50 μm for (a), (b), (c) and (d), respectively.

The force curves measured between two oil droplets in 1 mM NaCl aqueous solutions at pH 9 and 11 with Fe_3O_4@2OA NPs are shown in Figures 5.6c and 5.6d, respectively. Similar to the force curve without Fe_3O_4@2OA NPs (Figure 5.5b), the two oil droplets are stable against each other during the complete approach-retraction cycle. It is worth noting that no force step or jump-out behavior is observed in the measurement between two oil droplets interacting in water at either pH 9 or 11, suggesting there exists a stable water film between two oil droplets and no confined bridging monolayer is formed. Compared to the force curve in Figure 5.5b, the "hydrodynamic suction effect" in the presence of Fe_3O_4@2OA NPs at pH 9 is less evident as indicated in the inset of Figure 5.6c, which most likely arises from the interfacial adsorption of nanoparticles that produces the relatively rigid structure of oil droplets. Interestingly, the "hydrodynamic suction effect" is completely suppressed at pH 11, indicating that more nanoparticles are adsorbed to the oil/water interface, resulting in denser distribution of nanoparticles and thus allowing the droplet to perform as a solid-like microsphere, which is consistent with the considerably reduced IFT at pH 11 shown in Figure 5.4b. Since each droplet is surrounded by a layer of particles at oil/water interface, the steric repulsion keeps the two oil droplets apart and maintains a thin water film in between. Therefore, the droplet is not deformed considerably, and a very low force hysteresis is observed. The above quantitative force results indicate the distinct arrangement and behaviors of pH-responsive Fe_3O_4@2OA NPs at the oil/water interface during the interactions of emulsion droplets under acidic or basic conditions. Under acidic environment, the particles around two droplets would form a confined monolayer to bridge the droplets in W/O emulsions. While under basic condition, the particles form a dense and rigid layer on each droplet that prevents the drainage of confined thin water film due to the strong steric repulsion among the O/W emulsions.

5.3.5 Effect of loading force on the interactions

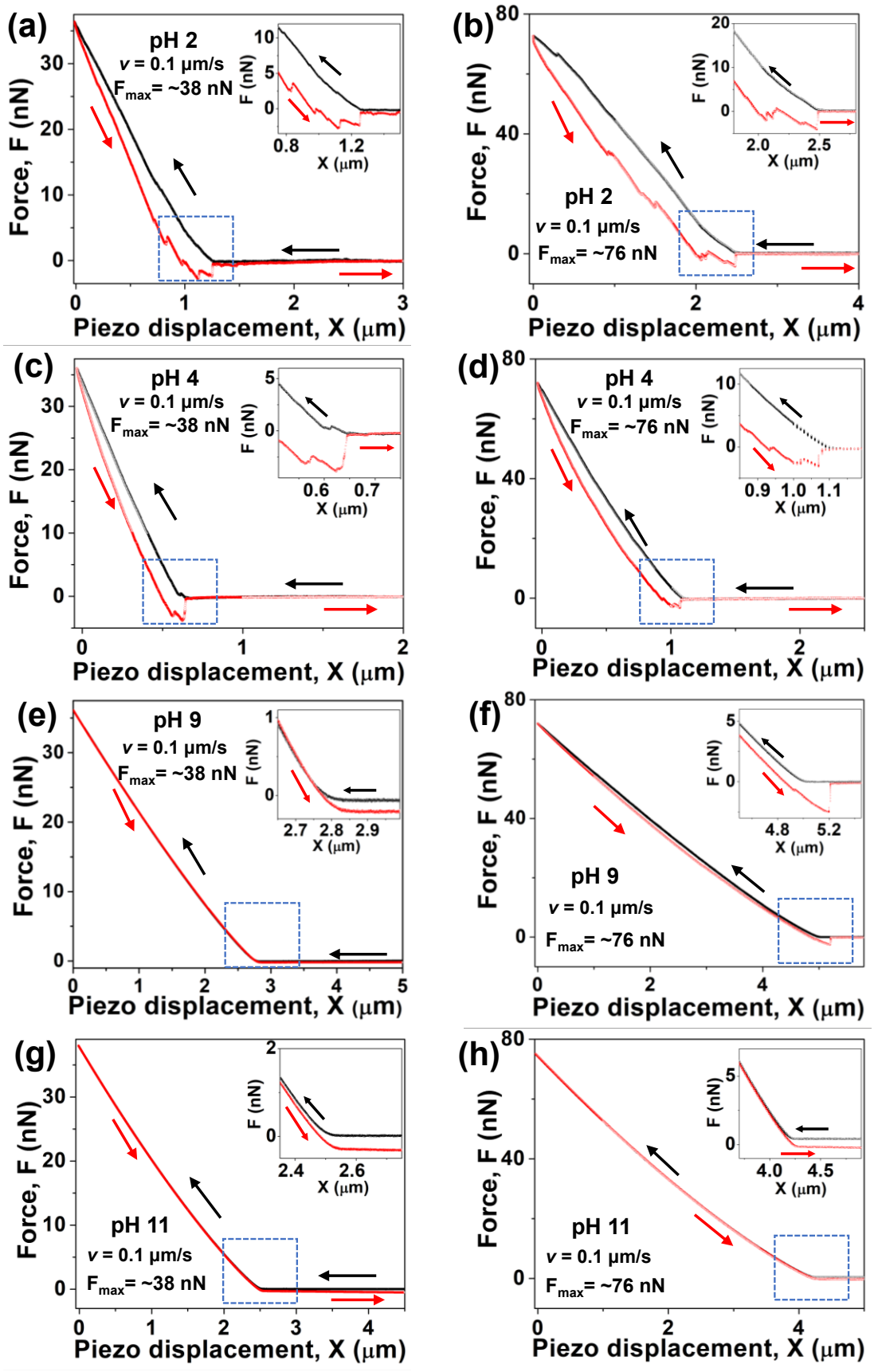
(a)
pH 2
v = 0.1 μm/s
F_max = ~38 nN
Force, F (nN)
Piezo displacement, X (μm)
F (nN)
X (μm)
(b)
pH 2
v = 0.1 μm/s
F_max = ~76 nN
Force, F (nN)
Piezo displacement, X (μm)
F (nN)
X (μm)
(c)
pH 4
v = 0.1 μm/s
F_max = ~38 nN
Force, F (nN)
Piezo displacement, X (μm)
F (nN)
X (μm)
(d)
pH 4
v = 0.1 μm/s
F_max = ~76 nN
Force, F (nN)
Piezo displacement, X (μm)
F (nN)
X (μm)
(e)
pH 9
v = 0.1 μm/s
F_max = ~38 nN
Force, F (nN)
Piezo displacement, X (μm)
F (nN)
X (μm)
(f)
pH 9
v = 0.1 μm/s
F_max = ~76 nN
Force, F (nN)
Piezo displacement, X (μm)
F (nN)
X (μm)
(g)
pH 11
v = 0.1 μm/s
F_max = ~38 nN
Force, F (nN)
Piezo displacement, X (μm)
F (nN)
X (μm)
(h)
pH 11
v = 0.1 μm/s
F_max = ~76 nN
Force, F (nN)
Piezo displacement, X (μm)
F (nN)
X (μm)

Figure 5.7 Interaction force profiles between two water droplets at (a-b) pH 2 and (c-d) pH 4 in oil with Fe3O4@2OA NPs. Interaction force profiles between two dodecane droplets in 1 mM NaCl aqueous solutions at (e-f) pH 9 and (g-h) pH 11 with Fe3O4@2OA NPs. The maximum loading force is fixed at ~38 nN for (a), (c), (e), (g), and ~76 nN for (b), (d), (f), (h). The inset is zoomed regime in blue dash square. Each force curve consists of both approach (black curve, indicated by black arrow) and retraction (red curve, indicated by red arrow) process. The harmonic mean of the droplets' radii are 65, 55, 50 and 50 μm for (a-b), (c-d), (e-f) and (g-h), respectively.

The maximum loading force applied can affect the interactions of emulsion droplets and behavior of particles at water/oil interface, which play an important role in mediating the surface interaction and emulsion stability. Under all the pH conditions, the approaching and retracting velocity is kept at 0.1 μm/s to further suppress the hydrodynamic effect (Figure 5.7). The maximum loading force is firstly fixed at ~38 nN (Figure 5.7a, 5.7c, 5.7e, 5.7g), the same as the maximum load force in Figure 5.6. Then the maximum loading force is increased to ~76 nN to investigate the effect of loading force (Figure 5.7b, 5.7d, 5.7f, 5.7h).

At pH 2, more force steps appear at velocity of 0.1 μm/s (Figure 5.7a) compared with the force curve under 1 μm/s, indicating that the "stick-slip" phenomena are more prominent under a low hydrodynamic condition [66]. Similarly, the force steps mainly appear in the blue dash square regime where two water droplets are about to detach. At a maximum load of ~76 nN (Figure 5.7b), the number of force steps obviously increases, and the force steps appear even at the piezo displacement of ~0.9 μm and ~1.5 μm, suggesting that more particles could be confined between two contacted emulsion droplets under larger loading force (i.e., strong confinement). The approach and retraction force curves are widely separated from each other, and the large hysteresis is due to more confined interfacial particles and particle aggregates serving as bridges, their

rearrangement and deformation of water droplet associated with the loading-unloading processes. The force measurement result agrees well with microscopic image of unstable bulk emulsion2. At pH 4 (Figures 5.7c and 5.7d), the force profiles under both low and high load forces are similar regarding the force steps and adhesion hysteresis, indicating that the droplet is stable against high loading force, which is consistent with the stable bulk emulsion4 based on microscopic observation.

For two oil droplets interacting in 1 mM NaCl at pH 9, the hydrodynamic suction effect can barely be observed at velocity of 0.1 μm/s (Figure 5.7e), and the approach and retraction curves almost overlap under a maximum loading force of ~38 nN. However, as shown in Figure 5.7f, a jump-out behavior with force steps appears at the high load force of ~76 nN, suggesting that the particles confined form a steric layer at contact region. The confined particle layer becomes more compact and forms adhesive bridges under stronger loading force condition. The hysteresis of approach-retraction force curves appears at the ~76 nN case is mostly due to the adhesion induced by the confined particles between the two drops. The force curve at pH 11 is not obviously affected by either hydrodynamic effect or force load (Figure 5.7g and 5.7h), and no adhesion or hysteresis is detected, indicating that a stable thin water film can be maintained between the two droplets with strong repulsion.

5.3.6 Effect of dwelling time on the interactions

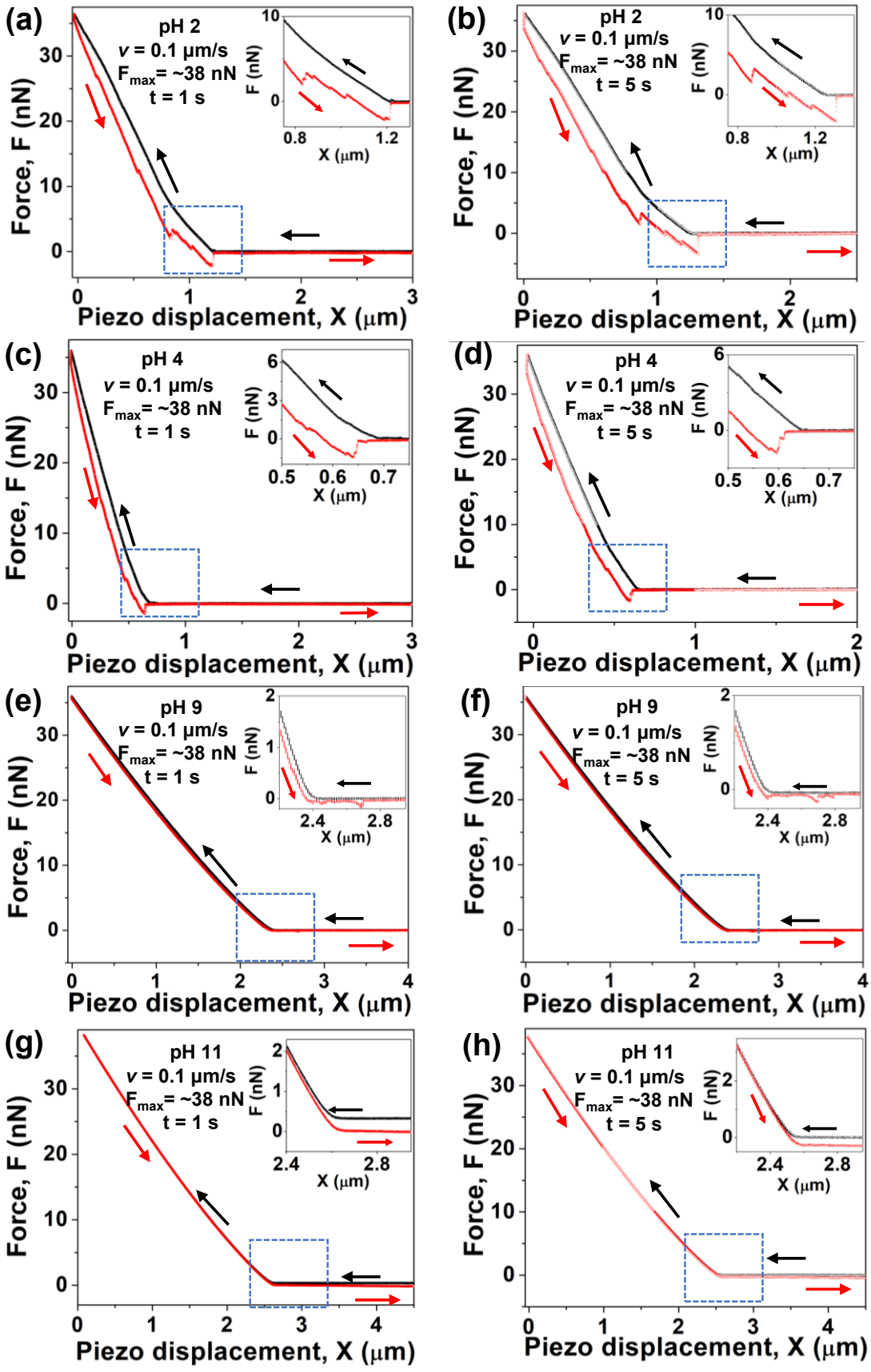
(a)
pH 2
v = 0.1 μm/s
F_max = ~38 nN
t = 1 s
Force, F (nN)
Piezo displacement, X (μm)
F (nN)
X (μm)
(b)
pH 2
v = 0.1 μm/s
F_max = ~38 nN
t = 5 s
Force, F (nN)
Piezo displacement, X (μm)
F (nN)
X (μm)
(c)
pH 4
v = 0.1 μm/s
F_max = ~38 nN
t = 1 s
Force, F (nN)
Piezo displacement, X (μm)
F (nN)
X (μm)
(d)
pH 4
v = 0.1 μm/s
F_max = ~38 nN
t = 5 s
Force, F (nN)
Piezo displacement, X (μm)
F (nN)
X (μm)
(e)
pH 9
v = 0.1 μm/s
F_max = ~38 nN
t = 1 s
Force, F (nN)
Piezo displacement, X (μm)
F (nN)
X (μm)
(f)
pH 9
v = 0.1 μm/s
F_max = ~38 nN
t = 5 s
Force, F (nN)
Piezo displacement, X (μm)
F (nN)
X (μm)
(g)
pH 11
v = 0.1 μm/s
F_max = ~38 nN
t = 1 s
Force, F (nN)
Piezo displacement, X (μm)
F (nN)
X (μm)
(h)
pH 11
v = 0.1 μm/s
F_max = ~38 nN
t = 5 s
Force, F (nN)
Piezo displacement, X (μm)
F (nN)
X (μm)

Figure 5.8 Interaction force profiles between two water droplets with different dwelling time (t) at (a) pH 2, t=1 s, (b) pH 2, t=5 s, (c) pH 4, t=1 s, and (d) pH 4, t=5 s in oil with Fe3O4@2OA NPs. Interaction force profiles between two dodecane droplets in 1 mM NaCl with different dwelling time at (e) pH 9, t=1 s, (f) pH 9, t=5 s, (g) pH 11, t=1 s, and (h) pH 11, t=5 s with Fe_3O_4@2OA NPs. The inset is zoomed regime in blue dash square. Each force curve consists of both approach (black curve, indicated by black arrow) and retraction (red curve, indicated by red arrow) process. The arrow indicates the moving direction of upper droplet. The harmonic mean of the droplets' radii are 65, 55, 50 and 50 μm for (a-b), (c-d), (e-f) and (g-h), respectively.

The effect of dwelling time is investigated by keeping the emulsion droplets under the maximum loading force (~38 nN) for a certain time (i.e., 1 s or 5 s) during the interaction (Figure 5.8). Compared with Figure 5.6a, force steps appear from the very beginning of separation (i.e., high repulsive load) rather than only at the end of separation (i.e., low repulsive load or attractive load) at the dwelling time of 1s (Figure 5.8a), suggesting that more Fe_3O_4@2OA NPs are under strong confinement which results in a stronger bridging particle layer. With the dwelling time increasing to 5 s, the number of force steps increases as shown in Figure 5.8b because the NPs have more time to migrate to the contacted interfaces. Unlike the force curve at pH 2, the dwelling time of 1 s and 5 s (Figure 5.8c and 5.8d) does not change the force curve considerably at pH 4, indicating that the Fe_3O_4@2OA NPs are able to migrate rapidly to form the confined particle layer, which contributes to the relatively more stable emulsion. At pH 9, it can be seen from the inset in Figure 5.8e and 5.8f that several tiny force steps occur when a dwelling time (i.e., 1s, 5 s) is applied. Interestingly, the force steps sometimes even occur in the adhesive force regime (Figure 5.8e and 5.8f), which is similar to the polymer bridging behavior commonly measured between solid

colloids. Such a behavior is different from the force steps aforementioned for water-water interaction in oil, which is partially attributed to the enhanced hydrogen bonding interaction of carboxyl groups covered on NPs located on the opposing oil droplets after contact for certain time. At pH 11, the effect of dwelling time on the force curve is not observed (Figure 5.8g and 5.8h), which might be due to the complete deprotonation of carboxyl groups under such basic condition with strong repulsion between the two drops, leading to a stable confined thin water film.

5.3.7 Interaction mechanism

The interaction mechanism between two water droplets in oil or two oil droplets in aqueous solution with Fe_3O_4@2OA NPs at water/oil interface is proposed based on the force measurements, IFT tests and microscopic imaging results. As W/O emulsion is formed at low pHs (i.e., pH 2 and 4), the interactions between two water droplets in oil have been measured. In the force measurement, two pristine water droplets coalesce in oil in the absence of Fe_3O_4@2OA NPs, while water droplets are stable against each other with the addition of Fe_3O_4@2OA NPs. It is reported that when aqueous phase is acidic, Fe_3O_4@2OA NPs tend to partition to oil phase, where the second layer of oleic acid is partially dissociated, thereby leading to the formation of partially bilayer-monolayered Janus coating [30]. In this case, the Fe_3O_4@2OA NPs form a confined layer at the contact of two water droplets and act as a steric barrier at water/oil interface due to the partial wettability to both water and oil phase (as illustrated in Figure 5.9). The stabilization mechanism is mainly governed by the formation of steric barrier of the confined particles layer (with Fe_3O_4@2OA NPs and aggregates as illustrated in Figure 5.9) instead of lowering interfacial tension [23], which contributes to the observation that the emulsions at pH 2 and pH 4 have similar IFT values but different stabilities. It is noted that the emulsion stability is related to the energy of

particle attachment/detachment from the oil/water interface, which can be approximately expressed as $E = \pi r^2 \gamma_{ow}(1+\cos\theta)^2$ for particles with diameter at nanometer scale, where E is the energy required to remove particle from interface to oil phase, r is particle radius, γ_{ow} is oil/water interfacial tension, and θ is water contact angle of particle [24]. The water contact angle of Fe_3O_4@2OA NPs at pH 2 (~120°) is higher than that at pH 4 (~100°) [30], so the Fe_3O_4@2OA NPs at pH 2 are easier to remove from the oil/water interface, which could induce an unstable Pickering emulsion as demonstrated by force measurement and microscopic imaging.

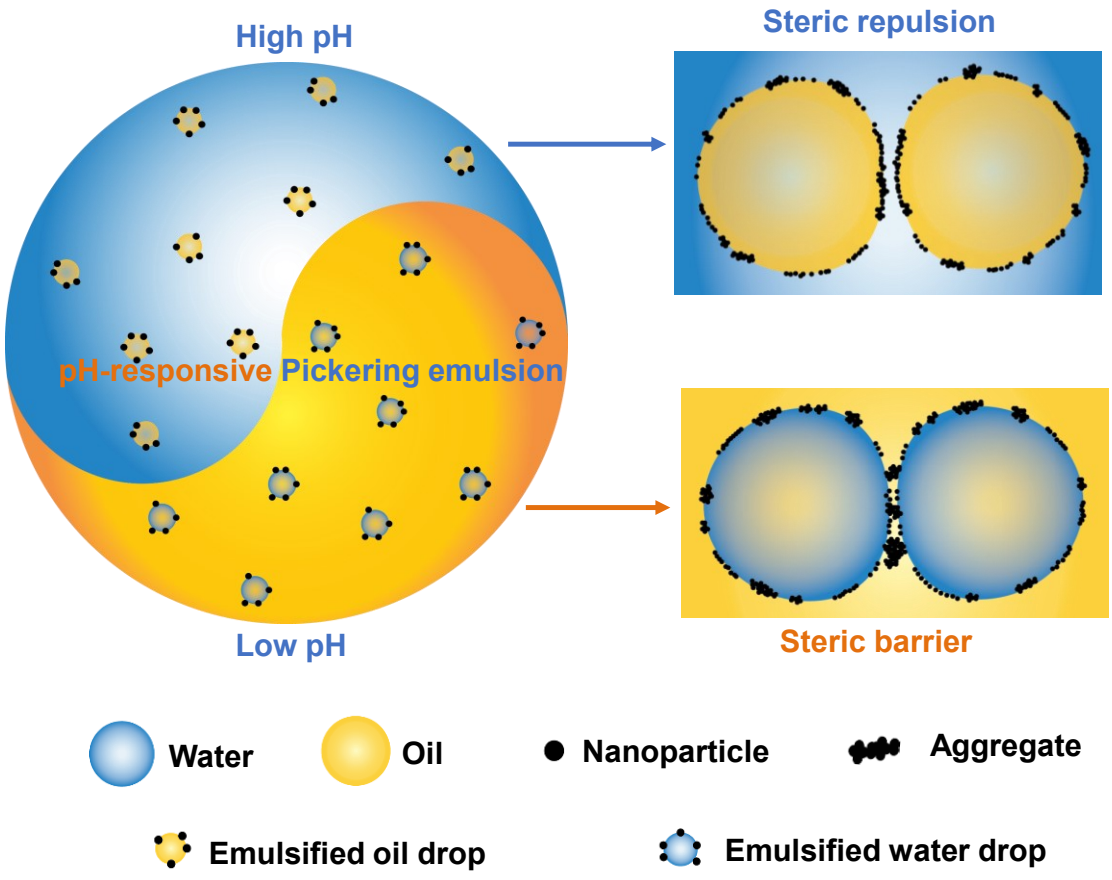

Figure 5.9 Schematic of interactions between emulsion droplets in the presence of Fe3O4@2OA nanoparticles under low pH (i.e., pH 2, pH 4) and high pH (i.e., pH 9, pH 11) conditions.

At high pHs (i.e., pH 9 and 11), O/W emulsion is formed since Fe_3O_4@2OA NPs with the charged $-COO^-$ groups on the second oleic layer tend to stay in aqueous phase[30]. The force measured between two oil droplets in 1 mM NaCl at basic conditions shows no adhesion and a stable thin water layer is confined between two oil droplets. As the carboxyl groups on the second oleic layer is charged, part of the Fe_3O_4@2OA NPs has preference to stay in water. Meanwhile, part of the Fe_3O_4@2OA NPs prefers staying in oil due to the long aliphatic chain of OA. In this case, the Fe_3O_4@2OA NPs act similarly to surfactants, which can lower IFT of oil/water interface as shown in Figure 5.4b. The stabilization mechanism of O/W emulsion drops under the basic condition is mainly due to relatively low IFT, strong electrostatic repulsion due to negatively charged carboxyl groups, and steric repulsion from the confined particles and their aggregates[30], leading to a stable confined thin water film between the oil drops, as illustrated in Figure 5.9.

According to the force measurements, increasing the maximum loading force or dwelling time will strengthen the confinement and particle-particle interaction of the confined Fe_3O_4@2OA NPs, thus affecting the emulsion drop interaction. Such a proposed stabilization mechanism for O/W and W/O Pickering emulsions in the presence of Fe_3O_4@2OA NPs is consistent with previous report on Pickering emulsions with microscopic particles[25].

5.4 Conclusions

In this work, we have investigated the stabilization mechanisms of W/O and O/W Pickering emulsions with pH-responsive Fe_3O_4@2OA NPs using microscope imaging, IFT tests and AFM force measurements. In the AFM force measurement, the interaction forces between two water droplets in oil as well as two oil droplets in water without/with interfacially active Fe_3O_4@2OA

NPs under different pH conditions are directly quantified at nanoscale. The measured forces of pristine water droplets in oil or oil droplets in water without Fe_3O_4@2OA NPs can be well described by a theoretical model based on Reynolds lubrication theory and augmented Young-Laplace equation. For force measurements of emulsions with Fe_3O_4@2OA NPs, water droplets are stable against each other in oil under acidic condition (i.e., pH 2 and pH 4) with adhesion detected during separation. In this case, particles are confined and form a steric barrier to prevent droplet coalescence, and these confined particles and aggregates also cause a bridging attraction during the separation of the drops. Under basic condition (i.e., pH 9 and pH 11), no adhesion is detected between two oil droplets, indicating the presence of a confined thin water film. For this case, the oil droplets are mainly stabilized due to relatively lower IFT, strong electrostatic repulsion due to negatively charged carboxyl groups, and steric repulsion from the confined particles and their aggregates. Increasing the maximum loading force and dwelling time enhance the confinement of particles and particle aggregates at oil/water interface and thus influence the interactions of the emulsion droplets.

The arrangement of particles in Pickering emulsion has been studied previously by many researchers[24,27,28,67,68] via theoretical simulation or experimental analyses such as low temperature field emission scanning electron microscopy. The experimental analyses mainly focus on the observation of particle arrangement at oil/water interface, based on which the stabilization mechanism is proposed[25,26]. Many previous studies focused on single emulsion system, such as water-in-cyclohexane Pickering emulsion with silica particles, and toluene-in-water Pickering emulsion with PS particles[67]. The direct measurement of interaction forces between emulsified droplets in Pickering emulsions at nanoscale is rarely reported. Pickering emulsions under external stimuli have many potential applications, but the interactions of such emulsions and particle

arrangement have been barely investigated. In this work we have employed a drop probe AFM technique to directly quantify the interaction forces between emulsified droplets in a pH-responsive Pickering emulsion, that can form either W/O or O/W emulsion with Fe_3O_4@2OA NPs under different pH conditions. This work has elucidated the interaction forces and stabilization mechanisms of W/O and O/W Pickering emulsions with pH-responsive particles and the arrangement of interfacially active particles. The methodologies established in this work can be readily extended to investigate the interaction mechanisms of other Pickering emulsion systems. In future studies, high-resolution imaging may be coupled with force measurements to provide a more complete picture on the interaction behaviors of Pickering emulsions under various stimuli (e.g., pH, temperature).

References

1. Mao, X. *et al.* Novel Fe 3 O 4 based superhydrophilic core-shell microspheres for breaking asphaltenes-stabilized water-in-oil emulsion. *Chem. Eng. J.* **358**, 869–877 (2019).
2. Yang, H.-C. *et al.* Mussel-inspired modification of a polymer membrane for ultra-high water permeability and oil-in-water emulsion separation. *J. Mater. Chem. A* **2**, 10225–10230 (2014).
3. Cheng, M. *et al.* A functionally integrated device for effective and facile oil spill cleanup. *Langmuir* **27**, 7371–7375 (2011).
4. Hu, Z., Marway, H. S., Kasem, H., Pelton, R. & Cranston, E. D. Dried and Redispersible Cellulose Nanocrystal Pickering Emulsions. *ACS Macro Lett.* **5**, 185–189 (2016).
5. Dickinson, E. Stabilising emulsion-based colloidal structures with mixed food ingredients. *J. Sci. Food Agric.* **93**, 710–721 (2013).
6. Xu, D. *et al.* Influence of whey protein–beet pectin conjugate on the properties and digestibility of β-carotene emulsion during in vitro digestion. *Food Chem.* **156**, 374–379 (2014).
7. Huang, C. *et al.* Preparation of a reversed-phase/anion-exchange mixed-mode spherical sorbent by Pickering emulsion polymerization for highly selective solid-phase extraction of acidic pharmaceuticals from wastewater. *J. Chromatogr. A* **1521**, 1–9 (2017).
8. Jeong, S. *et al.* Erratum to: Comparison of the Efficacy of Atopalm(®) Multi-Lamellar Emulsion Cream and Physiogel(®) Intensive Cream in Improving Epidermal Permeability Barrier in Sensitive Skin. *Dermatol. Ther. (Heidelb).* **6**, 57 (2016).
9. Xin, X. *et al.* Influence of CTAB and SDS on the properties of oil-in-water nano-emulsion with paraffin and span 20/Tween 20. *Colloids Surfaces A Physicochem. Eng. Asp.* **418**, 60–67 (2013).
10. Shi, C. *et al.* Surface Interaction of Water-in-Oil Emulsion Droplets with Interfacially Active Asphaltenes. *Langmuir* **33**, 1265–1274 (2017).
11. Yarranton, H. W. Asphaltene Self-Association. *J. Dispers. Sci. Technol.* **26**, 5–8 (2005).
12. Jian, C. *et al.* Reduction of Water/Oil Interfacial Tension by Model Asphaltenes: The Governing Role of Surface Concentration. *J. Phys. Chem. B* **120**, 5646–5654 (2016).
13. Song, P., Mao, X., Ren, Y., Zeng, H. & Lu, Q. Buckling Effect of Sole Zeolitic Imidazolate Framework-8 Nanoparticles Adsorbed at the Water/Oil Interface. *Langmuir* **36**, 2322–2329

(2020).

14. Pickering, S. U. CXCVI-Emulsions. *J. Chem. Soc. Trans.* **91**, 2001–2021 (1907).
15. Suzuki, D., Tsuji, S. & Kawaguchi, H. Janus microgels prepared by surfactant-free pickering emulsion-based modification and their self-assembly. *J. Am. Chem. Soc.* **129**, 8088–8089 (2007).
16. Chen, T., Colver, P. J. & Bon, S. A. F. Organic–Inorganic Hybrid Hollow Spheres Prepared from TiO2-Stabilized Pickering Emulsion Polymerization. *Adv. Mater.* **19**, 2286–2289 (2007).
17. Li, J. & Stöver, H. D. H. Doubly pH-responsive pickering emulsion. *Langmuir* **24**, 13237–13240 (2008).
18. Li, J. & Stöver, H. D. H. Doubly pH-responsive pickering emulsion. *Langmuir* **24**, 13237–13240 (2008).
19. Ngai, T., Behrens, S. H. & Auweter, H. Novel emulsions stabilized by pH and temperature sensitive microgels. *Chem. Commun.* 331–333 (2005) doi:10.1039/b412330a.
20. Lam, S., Blanco, E., Smoukov, S. K., Velikov, K. P. & Velev, O. D. Magnetically responsive pickering foams. *J. Am. Chem. Soc.* **133**, 13856–13859 (2011).
21. Saigal, T., Dong, H., Matyjaszewski, K. & Tilton, R. D. Pickering emulsions stabilized by nanoparticles with thermally responsive grafted polymer brushes. *Langmuir* **26**, 15200–15209 (2010).
22. Liu, K., Jiang, J., Cui, Z. & Binks, B. P. PH-Responsive Pickering Emulsions Stabilized by Silica Nanoparticles in Combination with a Conventional Zwitterionic Surfactant. *Langmuir* **33**, 2296–2305 (2017).
23. Vignati, E., Piazza, R. & Lockhart, T. P. Pickering emulsions: Interfacial tension, colloidal layer morphology, and trapped-particle motion. *Langmuir* **19**, 6650–6656 (2003).
24. Binks, B. P. Particles as surfactants - Similarities and differences. *Curr. Opin. Colloid Interface Sci.* **7**, 21–41 (2002).
25. Horozov, T. S. & Binks, B. P. Particle-Stabilized Emulsions: A Bilayer or a Bridging Monolayer? *Angew. Chemie* **118**, 787–790 (2006).
26. Lee, M. N., Chan, H. K. & Mohraz, A. Characteristics of pickering emulsion gels formed by droplet bridging. *Langmuir* **28**, 3085–3091 (2012).
27. French, D. J., Taylor, P., Fowler, J. & Clegg, P. S. Making and breaking bridges in a

Pickering emulsion. *J. Colloid Interface Sci.* **441**, 30–38 (2015).

28. French, D. J. *et al.* The secret life of Pickering emulsions: particle exchange revealed using two colours of particle. *Sci. Rep.* **6**, 1–9 (2016).
29. Yang, K., Peng, H., Wen, Y. & Li, N. Re-examination of characteristic FTIR spectrum of secondary layer in bilayer oleic acid-coated Fe3O4 nanoparticles. *Appl. Surf. Sci.* **256**, 3093–3097 (2010).
30. Lan, Q. *et al.* Synthesis of bilayer oleic acid-coated Fe3O4nanoparticles and their application in pH-responsive Pickering emulsions. *J. Colloid Interface Sci.* **310**, 260–269 (2007).
31. Ingram, D. R. *et al.* Superparamagnetic nanoclusters coated with oleic acid bilayers for stabilization of emulsions of water and oil at low concentration. *J. Colloid Interface Sci.* **351**, 225–232 (2010).
32. Sadeghpour, A., Pirolt, F. & Glatter, O. Submicrometer-Sized Pickering Emulsions Stabilized by Silica Nanoparticles with Adsorbed Oleic Acid. *Langmuir* **29**, 6004–6012 (2013).
33. Xie, L., Cui, X., Gong, L., Chen, J. & Zeng, H. Recent Advances in the Quantification and Modulation of Hydrophobic Interactions for Interfacial Applications. *Langmuir* **36**, 2985–3003 (2020).
34. Xie, L. *et al.* Interfacial behavior and interaction mechanism of pentol/water interface stabilized with asphaltenes. *J. Colloid Interface Sci.* **553**, 341–349 (2019).
35. Liu, J. *et al.* Destabilization of fine solids suspended in oil media through wettability modification and water-assisted agglomeration. *Fuel* **254**, 115623 (2019).
36. Cui, X. *et al.* Modulation of Hydrophobic Interaction by Mediating Surface Nanoscale Structure and Chemistry, not Monotonically by Hydrophobicity. *Angew. Chemie Int. Ed.* **57**, 11903–11908 (2018).
37. Shi, C. *et al.* Surface Interaction of Water-in-Oil Emulsion Droplets with Interfacially Active Asphaltenes. *Langmuir* **33**, 1265–1274 (2017).
38. Chan, D. Y. C., Klaseboer, E. & Manica, R. Theory of non-equilibrium force measurements involving deformable drops and bubbles. *Advances in Colloid and Interface Science* vol. 165 70–90 (2011).
39. Shi, C., Chan, D. Y. C., Liu, Q. & Zeng, H. Probing the hydrophobic interaction between

air bubbles and partially hydrophobic surfaces using atomic force microscopy. *J. Phys. Chem. C* **118**, 25000–25008 (2014).

40. Shi, C., Xie, L., Zhang, L., Lu, X. & Zeng, H. Probing the interaction mechanism between oil droplets with asphaltenes and solid surfaces using AFM. *J. Colloid Interface Sci.* **558**, 173–181 (2019).
41. Tabor, R. F., Grieser, F., Dagastine, R. R. & Chan, D. Y. C. Measurement and analysis of forces in bubble and droplet systems using AFM. *J. Colloid Interface Sci.* **371**, 1–14 (2012).
42. Shi, C. *et al.* Measuring forces and spatiotemporal evolution of thin water films between an air bubble and solid surfaces of different hydrophobicity. *ACS Nano* **9**, 95–104 (2015).
43. Zhang, L., Xie, L., Cui, X., Chen, J. & Zeng, H. Intermolecular and surface forces at solid/oil/water/gas interfaces in petroleum production. *J. Colloid Interface Sci.* **537**, 505–519 (2019).
44. Yang, K., Peng, H., Wen, Y. & Li, N. Re-examination of characteristic FTIR spectrum of secondary layer in bilayer oleic acid-coated Fe 3 O 4 nanoparticles. *Appl. Surf. Sci.* **256**, 3093–3097 (2010).
45. Shi, C. *et al.* Interaction Mechanism of Oil-in-Water Emulsions with Asphaltenes Determined Using Droplet Probe AFM. *Langmuir* **32**, 2302–2310 (2016).
46. Shi, C. *et al.* Interaction Mechanism of Oil-in-Water Emulsions with Asphaltenes Determined Using Droplet Probe AFM. *Langmuir* **32**, 2302–2310 (2016).
47. Dagastine, R. R., Prieve, D. C. & White, L. R. Forces between a rigid probe particle and a liquid interface: III. Extraction of the planar half-space interaction energy E(D). *J. Colloid Interface Sci.* **269**, 84–96 (2004).
48. Hutter, J. L. & Bechhoefer, J. Calibration of atomic-force microscope tips. *Rev. Sci. Instrum.* **64**, 1868–1873 (1993).
49. Xie, L. *et al.* Probing the Interaction Mechanism between Air Bubbles and Bitumen Surfaces in Aqueous Media Using Bubble Probe Atomic Force Microscopy. *Langmuir* **34**, 729–738 (2018).
50. Xie, L. *et al.* Interaction Mechanisms between Air Bubble and Molybdenite Surface: Impact of Solution Salinity and Polymer Adsorption. *Langmuir* **33**, 2353–2361 (2017).
51. Israelachvili, J. N. *Intermolecular and surface forces*. (Academic Press, 2011).
52. Tabor, R. F., Manica, R., Chan, D. Y. C., Grieser, F. & Dagastine, R. R. Repulsive Van der

Waals forces in soft matter: Why bubbles do not stick to walls. *Phys. Rev. Lett.* **106**, (2011).

53. Tabor, R. F., Wu, C., Grieser, F., Dagastine, R. R. & Chan, D. Y. C. Measurement of the hydrophobic force in a soft matter system. *J. Phys. Chem. Lett.* **4**, 3872–3877 (2013).
54. Zavareh, S., Behrouzi, Z. & Avanes, A. Cu (II) binded chitosan/Fe3O4 nanocomomposite as a new biosorbent for efficient and selective removal of phosphate. *Int. J. Biol. Macromol.* **101**, 40–50 (2017).
55. Wu, N. *et al.* Interaction of Fatty Acid Monolayers with Cobalt Nanoparticles. *Nano Lett.* **4**, 383–386 (2004).
56. Zhang, L., He, R. & Gu, H.-C. Oleic acid coating on the monodisperse magnetite nanoparticles. *Appl. Surf. Sci.* **253**, 2611–2617 (2006).
57. Korolev, V. V., Ramazanova, A. G. & Blinov, A. V. Adsorption of surfactants on superfine magnetite. *Russ. Chem. Bull.* **51**, 2044–2049 (2002).
58. Shi, C. *et al.* Surface Interaction of Water-in-Oil Emulsion Droplets with Interfacially Active Asphaltenes. *Langmuir* **33**, 1265–1274 (2017).
59. Shi, C. *et al.* Interaction Mechanism of Oil-in-Water Emulsions with Asphaltenes Determined Using Droplet Probe AFM. *Langmuir* **32**, 2302–2310 (2016).
60. Cao, L., Chen, X. & Peng, Y. The effect of aliphatic alcohol frothers on the dispersion of oily collector. *Miner. Eng.* **157**, 106552 (2020).
61. Liu, A., Fan, M. qiang, Li, Z. hong & Fan, J. chuan. Non-polar oil assisted DDA flotation of quartz I: Interfacial interaction between dodecane oil drop and mineral particle. *Int. J. Miner. Process.* **168**, 1–8 (2017).
62. Helm, C. A., Israelachvili, J. N. & McGuiggan, P. Role of Hydrophobic Forces in Bilayer Adhesion and Fusion. *Biochemistry* **31**, 1794–1805 (1992).
63. Helm, C. A., Israelachvili, J. N. & McGuiggan, P. M. Molecular mechanisms and forces involved in the adhesion and fusion of amphiphilic bilayers. *Science (80-.).* **246**, 919–922 (1989).
64. Zeng, H., Zhao, B., Israelachvili, J. N. & Tirrell, M. Liquid- to solid-like failure mechanism of thin polymer films at micro- and nanoscales. *Macromolecules* **43**, 538–542 (2010).
65. Zeng, H. *et al.* Adhesion and Detachment Mechanisms between Polymer and Solid Substrate Surfaces: Using Polystyrene-Mica as a Model System. *Macromolecules* **49**, 5223–5231 (2016).

66. Zeng, H., Tirrell, M. & Israelachvili, J. Limit cycles in dynamic adhesion and friction processes: A discussion. *J. Adhes.* **82**, 933–943 (2006).
67. Rapacchietta, A. V. & Neumann, A. W. Force and free-energy analyses of small particles at fluid interfaces. II. Spheres. *J. Colloid Interface Sci.* **59**, 555–567 (1977).
68. Binks, B. P. & Kirkland, M. Interfacial structure of solid-stabilised emulsions studied by scanning electron microscopy. *Phys. Chem. Chem. Phys.* **4**, 3727–3733 (2002).

Chapter 6 Novel Multifunctional Solid Slippery Surfaces with Self-Assembled Fluorine-Free Small Molecules

6.1 Introduction

The transport and interactions of gas bubbles or liquid drops, as important phenomena related to solid/gas/liquid interfaces, play an important role in numerous engineering processes, which have also been widely discovered in nature. For example, the desert beetle can survive in very dry areas by harvesting water from fog-laden wind, while the water beetle can survive in river by clinging air bubbles to its hydrophobic body[1,2]. Inspired by these natural phenomena, materials and methods for facile bubble/drop transport have been developed and adopted in various engineering applications, including water harvesting[3,4], photocatalysis[5–8], wastewater treatment[9–12] and food industry[13]. For example, air bubbles in pipelines need to be transported and expelled via air vent to prevent serious erosion and blockage[14]. Automatic transport of testing drops in microfluidic devices could greatly simplify the detection of pathogens[15]. The facile transport of gas bubbles and liquid drops have been realized based on a variety of functional substrates, mainly including superhydrophobic and slippery surfaces[16–20].

Superhydrophobic surfaces, inspired by natural surfaces such as lotus leaf and butterfly wing, are usually constructed with hydrophobic micro/nano structures. These superhydrophobic surfaces generally exhibit a water contact angle larger than 150°, allowing the injected water drops to rebound with almost no residue[21]. Superhydrophobic surfaces could transport water drops as well as gas bubbles[22]. For example, Yu et al. designed a cone-shaped superhydrophobic surface which allowed bubbles to move spontaneously and directionally along the cone due to the Laplace pressure gradient[23]. On the other hand, superhydrophobic surface was found to hinder the buoyancy-driven bubble transport because of the strong adhesion between the bubble and

superhydrophobic surface[24]. To resolve this challenge, researchers have designed lubricant oil-infused slippery (LIS) surfaces, which are inspired by the Pitcher plant[16,25,26]. The LIS surfaces can be fabricated by infusing a polymer lubricant oil (e.g., FC-70, silicon oil) into either nano/micro-textured substrates or porous substrates[27,28]. The selection of lubricant oils generally needs to meet the following requirements: (1) the lubricant oils should spread and fully cover the substrate; (2) the substrate prefers the lubricant oils instead of the testing liquids; (3) the lubricant oils are immiscible with the testing liquids[17]. The properties of lubricant oils such as surface tension and viscosity have a great impact on the behavior of bubble/drop transport on LIS surfaces. The commonly used substrates for fabricating the LIS surfaces are composed of fluorinated polymers or silicone polymers such as polydimethylsiloxane (PDMS)[24,29–33]. The fluorinated polymers perform better than PDMS due to lower surface tension and viscosity, but the fluorinated materials are generally not environmentally friendly. In addition, the impregnated lubricant on LIS surface may be pulled up and cloak the droplet which would contaminate the droplet and cause the loss of lubricant[34,35]. The fabrication of superhydrophobic surfaces requires preparation of complex surface nano/micro structures, while the LIS surfaces always require infused liquids which could be unstable and may cause potential environmental concerns [36]. Besides superhydrophobic and LIS surface, some other smooth non-fluorine slippery surfaces were prepared by grafting polymers such as PDMS, trimethylsiloxyterminated polymethylhydrosiloxanes (PMHSs), and coating paraffin wax to the porous polymer surface. Though these previously reported smooth slippery surfaces can transport liquid drop in air with low contact angle hysteresis and tilting angle, the ability of transporting gas bubbles in liquid media was not demonstrated[37–43]. Despite the considerable effort on developing slippery surfaces, a facile fabrication of slippery surfaces using small molecule without the preparation of complex

nano/micro structures or infused liquids has been rarely reported yet. Thus, it is of fundamental and practical importance to design a novel type of environment-friendly slippery surfaces without the need of lubricant oil infusion. It is known that self-assembled monolayers (SAMs) consisting of short-chain alkanethiols exhibit some liquid-like property[44–47], while the silane derivatives are a commonly used class of lubricants due to their low friction behavior[48–50]. Inspired by the interesting characteristics of short-chain SAMs and silane lubricants, the self-assembly of short-chain thiols terminated with multiple silane tail groups is expected to produce a monolayer coating with promising slippery properties.

In this work, for the *first* time, we report a novel type of slippery surfaces via the self-assembly of a synthesized non-fluorine small molecule, γ-mercaptopropyldi(trimethylsiloxy)methylsilane (MD(SH)M), instead of polymers commonly used in traditional superhydrophobic or LIS surfaces. The MD(SH)M molecules could be readily grafted on gold substrates in different solvents. Due to the slippery characteristic of silane groups and the liquid-like property of short-chain thiols, the as-prepared slippery surfaces can transport air bubbles underwater as well as water drops in oil media without the aid of engineering nano/micro structures or infused lubricant liquids. Interestingly, the slippery surfaces can not only immobilize air bubbles against the buoyance force but also show low friction of three-phase contact line movement, which allows air bubbles to attach to the surfaces while also move freely. The new slippery surfaces have also been applied to facilitate the assembly of nanoparticles suspended in water drops. The developed strategy paves a way towards facilely fabricating multifunctional slippery solid surfaces using chemically bonded small molecules without engineering complex nano/micro structures or infused lubricant liquids.

6.2 Experimental section

6.2.1 Materials

Ethanol (ACS reagent, ≥99.8%), n-hexane (ACS reagent, ≥98.5%), 2-propanol (ACS reagent, ≥99.5%), isopropanol 70% (v/v water) and hydrochloric acid (36%) were purchased from Fisher Scientific, Canada. Silica (SiO_2) nano-powders (~12 nm diameter), Glycerol (≥99.5%), (3-mercaptopropyl)methyldimethoxysilane and hexamethyldisiloxane were purchased from Sigma Aldrich. Gold wafer was purchased from Angstrom Engineering Inc. All materials were used as received. The γ-mercaptopropyldi(trimethylsiloxy)methylsilane (MD(SH)M) was synthesized by stirring the mixture of hexamethyldisiloxane (81.19 g), (3-mercaptopropyl)methyldimethoxysilane (18.04 g), and hydrochloric acid (0.21 g) at 343 K for 4 h under nitrogen atmosphere. After reaction, a suitable amount of Milli-Q water was added to the resultant mixture to facilitate the removal of acid from the organic phase, and the organic phase was separated from the aqueous phase using a separatory funnel. The collected organic phase was mixed with Milli-Q water again for further removal of the acid residues. This process was repeated several times till the pH of the separated phase barely changed. The organic phase was then distilled under reduced pressure to obtain the product MD(SH)M. The structure of MD(SH)M was characterized using proton nuclear magnetic resonance (1H NMR, Bruker AV 500 NMR spectrometer) in chloroform-d ($CDCl_3$).

6.2.2 Self-assembly of MD(SH)M on gold surface in different solvents

The gold wafer was treated under UV ozone for 30 min before immersing into n-hexane, ethanol, 2-propanol and isopropanol 70% solutions with 1 mM MD(SH)M at room temperature (21.5 °C), respectively. After 24 h of deposition, the gold wafer was thoroughly rinsed with a large amount of ethanol to wash away the unbonded MD(SH)M. The MD(SH)M-coated gold surfaces were

denoted as n-hexane-immersed surface (HS), ethanol-immersed surface (ES), 2-propanol-immersed surface (PS) and isopropanol 70%-immersed surface (IS), respectively, according to the type of immersing solvents.

6.2.3 Self-transport of bubble/drop

The MD(SH)M-coated gold surfaces were immersed in a desired liquid in a rectangular transparent cell. A bubble/drop was injected using an automated dispensing system (Ramé-hart instrument company, USA) to approach and contact with the MD(SH)M surface. By controlling the inclined angle of the cell and the size of bubble/drop, the bubble/drop would slide along the MD(SH)M surface spontaneously. The motion video of bubble/drop was recorded by a digital camera. Average velocity was used to represent the overall transport performance since the transport length was almost the same for all the surfaces prepared in this work [16]. Average velocity (v) was calculated by dividing transport distance by transport time, where the transport distance was defined as the distance between the front edge of bubble/drop on starting point and ending point. Several typical frames were taken from the motion video to represent the transport process. The moment that the bubble/drop fully contacted with the sample surface at a certain inclined angle was considered as the starting point, while the moment that the bubble/drop ceased the movement on the sample surface was considered as the ending point. The transport time is the time from the starting point to ending point.

6.2.4 Assembly of nanoparticles facilitated by using as-prepared slippery surfaces

In a typical experiment, a 2 μL SiO_2 (~12 nm diameter) suspension in water (15 mg/mL) was dropped on HS, ES, PS, IS and bare gold surfaces, respectively. The shape changes of the drops with time and the shape of assembled aggregate of SiO_2 nanoparticles at room temperature were recorded by an optical microscope.

6.2.5 Surface characterization

The morphologies of MD(SH)M surfaces and bare gold surface were characterized using atomic force microscope (AFM) imaging (Dimension Icon AFM, Bruker, Santa Barbara, CA) and filed emission scanning electron microscope (FE-SEM) (Zeiss Sigma). A contact angle goniometer (Ramé-hart instrument company, USA) was employed to measure the static water contact angle in air using sessile drop method and the static air contact angle in water using captive bubble method. The sliding angles of water drop (20 μL) and glycerol drop (20 μL) on HS, ES, PS, IS and bare gold surface in air were measured using an Attention Theta tensiometer (Biolin Scientific, Finland) with tilting cradle. The tilted angle was tested from 0° to 20°. The thickness of MD(SH)M layer deposited on gold substrates was measured using a spectroscopic ellipsometer (Sopra GESP-5, France).

6.3 Results and discussion

6.3.1 Characterization of MD(SH)M surfaces

The ^{1}H NMR spectrum of the synthesized molecule is shown in Figure 6.1a, which provides the structural information on the synthesized molecule, demonstrating the successful synthesis of MD(SH)M. The slippery surfaces were fabricated by immersing gold surfaces in four types of solvents (i.e., n-hexane, ethanol, 2-propanol and iso-propanol 70%) with 1 mM MD(SH)M, respectively. The AFM images in Figure 6.1b show the morphologies of HS, ES, PS and IS surfaces, where HS surface exhibits many small aggregates while ES, PS and IS surfaces are smooth and uniform. The root-mean-square roughness (Rq) of HS, ES, PS and IS are 0.95 nm, 0.55 nm, 0.52 nm, and 0.51 nm, respectively. The morphology of bare gold surface before coating MD(SH)M was also characterized using AFM imaging (Figure B.1a) where no aggregation could be observed with Rq ~ 0.49 nm. The topographic AFM image of bare gold surface is similar to

that of ES, PS and IS. The morphology of four as-prepared surfaces (Figure 6.1c) and bare gold surface (Figure B.1b) is also characterized by FE-SEM. ES, PS and IS surfaces are smooth and flat, which are similar to bare gold surface. The SEM image of HS shows some aggregates, agreeing with the result from AFM imaging. The static water contact angles in air (WCA-A), air contact angles in water (ACA-W) and water contact angles in dodecane oil (WCA-O) of the four surfaces, HS, ES, PS and IS, are shown in Figure 6.1d. The WCA-A of ES, PS and IS are close to each other with the value of 102°, 103° and 101°, respectively, revealing the MD(SH)M coatings deposited in alcohol solvents (i.e., ethanol, 2-propanol and iso-propanol 70%) are hydrophobic. However, the WCA-A value of HS is around 75°, indicating the relatively hydrophilic property of HS surface. For the ACA-W measurements, HS (ACA-W ~133°) also exhibits different wettability from other three surfaces (ACA-W ~82°±3°). Besides, compared with ES, PS and IS, HS shows smallest WCA-O due to relatively higher hydrophilicity. For a smooth surface, the WCA-A, θ_W, is correlated to the surface tension of water γ_W and the interfacial energy of water/solid interface γ_{SW} according to the Young's equation (Equation 6.1).

$$\cos\theta_W = (\gamma_S - \gamma_{SW}) / \gamma_W \tag{6.1}$$

Similarly, the ACA-W θ_A is correlated to γ_W and γ_{SW} by Equation 6.2.

$$\cos\theta_A = (\gamma_{SW} - \gamma_S) / \gamma_W \tag{6.2}$$

The sum of θ_W and θ_A for HS, ES, PS and IS was calculated as 208°, 187°, 185° and 180°, respectively. If the surface is atomically smooth, the sum of θ_W and θ_A should be exactly 180° according to Equation 6.1 and 6.2. It is noticed that the sum of θ_W and θ_A for IS is around to 180° while that for HS, ES, and PS exceeds 180°, the derivation of which is mainly caused by the surface roughness (Rq), as the Young's equation is strictly applicable to smooth surfaces. As discussed

above, the Rq of HS is 0.95 nm that is much greater than the Rq of ES (0.55 nm), PS (0.52 nm) and IS (0.51 nm). The higher roughness caused the sum of θ_W and θ_A for HS to deviate more significantly from 180° than other three surfaces. The topographic AFM image and WCA-A of PS surface after heated at 35° and frozen at -20° for 1h are shown in Figure B.2. The WCA-A and Rq of PS after heating treatment (Rq 0.50 nm) and freezing treatment (Rq 0.52 nm) are almost the same as original PS, indicating good chemical stability of the coated MD(SH)M. Figure 6.1e shows that the average coating thicknesses of HS, ES, PS and IS are 1.78, 0.78, 0.70 and 0.85 nm, respectively. The average coating thicknesses of ES, PS and IS are almost the same with the standard deviation considered. However, the coating thickness of HS is more than twice of the other three surface cases, which may indicate the different adsorption behaviors of MD(SH)M on gold substrate in heptane and alcohol solvents. It was reported that the thickness of alkanethiol monolayer on gold surface was about 0.5 nm for 1-propanethiol, 1.1 nm for 1-octanethiol and 1.3 nm for 1-undecanethiol [51]. The backbone of MD(SH)M has five atoms including four carbon atoms and one silicon atom, and thus the thickness is expected to be in the range of 0.5-1.1 nm for monolayer adsorption. The above surface morphology and coating thickness results indicate that MD(SH)M molecules assembled as a monolayer on gold surfaces for ES, PS and IS while it was not the case for HS.

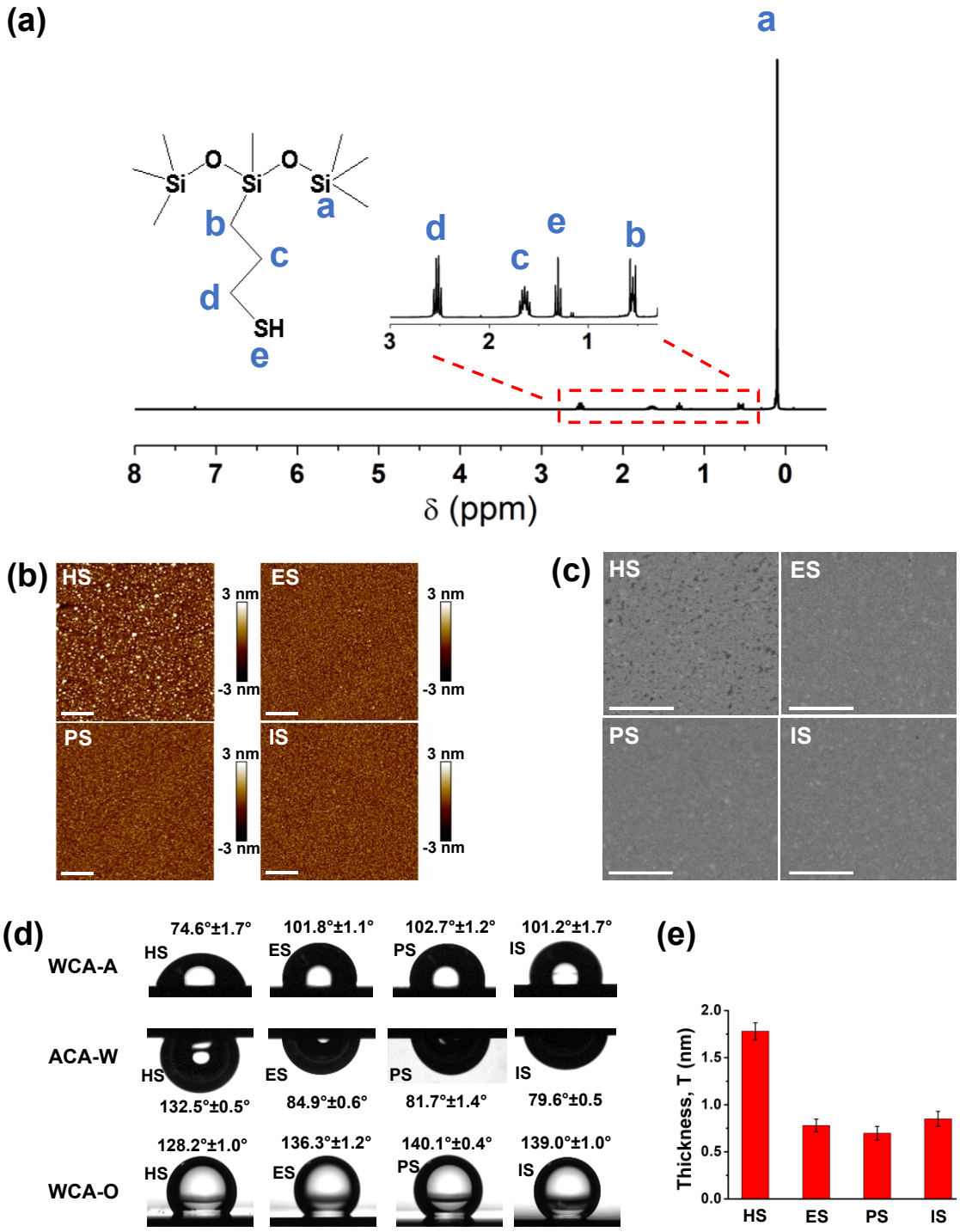

Figure 6.1 (a) The chemical structure and 1H NMR spectrum of MD(SH)M. (b) Topographic AFM images of n-hexane-immersed surface (HS), ethanol-immersed surface (ES), 2-propanol-immersed surface (PS) and isopropanol 70%-immersed surface (IS), (image size: 5×5 μm^2, scale

bar: 1 μm). (c) SEM images of HS, ES, PS and IS (scale bar: 1 μm). (d) Water contact angle in air (WCA-A), air contact angle in water (ACA-W) and water contact angle in oil (WCA-O) for HS, ES, PS and IS. (e) Measured thickness of the MD(SH)M coating on HS, ES, PS and IS.

6.3.2 Adsorption of MD(SH)M on gold surfaces

To further investigate the adsorption behavior of MD(SH)M on gold surface, the CV experiments have been conducted and the results are shown in Figure 6.2. The CV curves of ES, PS and IS commonly show a reduction peak at around -0.95 V, which is attributed to the desorption of MD(SH)M molecules from the gold surface through the de-bonding of Au-S. The area under this reduction peak is used to calculate the adsorption density of MD(SH)M. It is noted that the difference in the peak area of CV curves in Figure 6.2a-c is mainly due to the distinct surface areas of the samples exposed in aqueous media for CV test. Based on the reduction peak and Equation B.4, the density of adsorbed MD(SH)M for ES, PS and IS is calculated to be 2.15, 2.50 and 1.91 chains/nm^2, respectively. The adsorbed MD(SH)M molecules on ES, PS and IS are considered to form a monolayer, which agrees well with the results from AFM imaging (Figure 6.1b) and coating thickness measurements (Figure 6.1e).

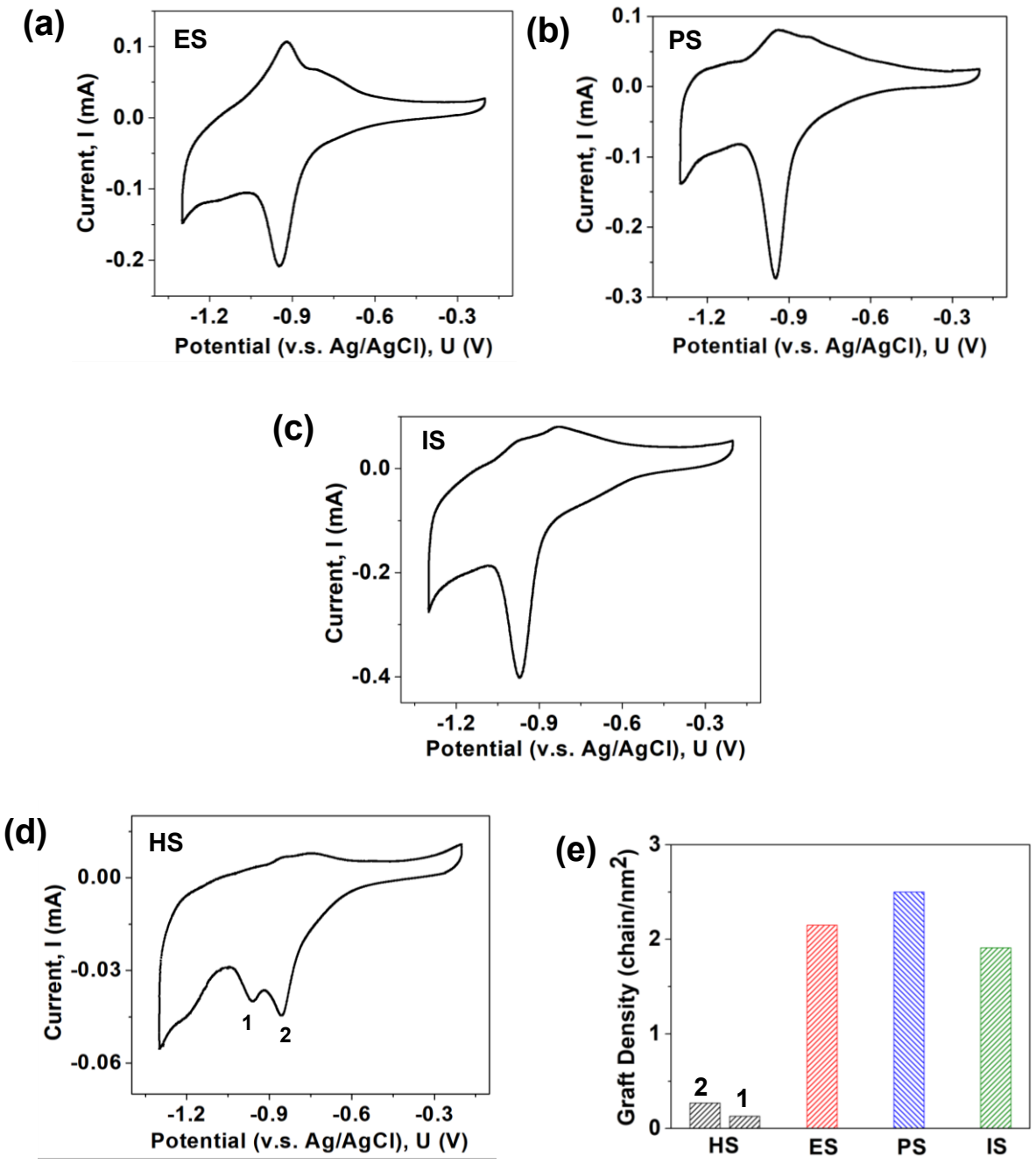

Figure 6.2 CV curves of (a) ES, (b) PS, (c) IS, and (d) HS in 0.5 M KOH and 3.3 M KCl solution, and (e) the surface graft density of MD(SH)M determined on HS, ES, PS and IS.

Unlike ES, PS and IS, the CV curve of HS shows two peaks at -0.95 V (peak 1) and -0.85 V (peak 2) (Figure 6.2d), suggesting two different adsorption forms of MD(SH)M, which require different energies (or potentials) for desorption. Peak 1 has the same peak potential as those reduction peaks for Au-S breaking found in the cases of ES, PS, and IS. The potential of peak 2 is more positive than that of peak 1, indicating that some of the adsorbed MD(SH)M molecules require less energy for desorption. It is reported that the poorly packed alkythiols tend to desorb at more positive potentials compared to the well oriented monolayer, because the poorly packed layers facilitate the permeation of electrolyte ions, which allows the generation of a sufficient potential gradient from hydrocarbon to headgroup of alkythiols to initiate the desorption at a relatively positive potential [52,53]. Therefore, the additional peak 2 in Figure 6.2d is likely to arise from the desorption of disorderly packed MD(SH)M molecules. Based on the peak 1 of CV curve in Figure 6.2d, the graft density of HS is calculated as 0.13 chains/nm^2, much less than that of monolayer on ES, PS and IS, which further suggests that there would be some defects on the HS surface where the disorderly packed MD(SH)M may exist. Besides, the total graft density of peak 1 and 2 on HS was less than that of ES, PS or IS (Figure 6.2e). However, the coating on HS is much thicker than that of ES, PS and IS due to the physical aggregation of MD(SH)M, as also indicated by AFM imaging of HS (Figure 6.1b). The reported graft density of densely packed alkanethiol on gold surface is about 4.92 molecules/nm^2, which is twice or more than the graft density of as-prepared surfaces in this work [42]. The steric effect from the two side groups of MD(SH)M could lower the graft density. Besides, MD(SH)M is a polar small molecule which may aggregate in non-polar solvent (i.e., hexane), resulting in low graft density and large physical aggregation. PS has higher graft density than ES as the configuration of 2-propanol is closer to that of MD(SH)M. Because MD(SH)M is

insoluble in water, its solubility in isopropanol (70%) would be smaller than that in ethanol and 2-propanol which lowers the graft density.

The surface energies of HS, ES, PS and IS are calculated using three-probe-liquid method. The surface energy parameters of three probe liquids (i.e., diiodomethane, water and ethylene glycerol) are listed in Table B.1. The contact angles of the three probe liquids on the four surfaces are measured by sessile drop method (Table B.2). The γ_S values of HS, ES, PS and IS are calculated to be 43.83, 31.08, 28.55, and 37.30 mJ/m^2 , respectively (Table B.3). The difference of surface energy is related to graft density as HS, ES, PS and IS are prepared by self-assembly of MD(SH)M on gold wafer with the same headgroup exposed. The MD(SH)M, containing three silane head groups per molecule, is expected to have relatively low surface energy like other silane derivatives. Thus, the surface with higher graft density (i.e., PS) tends to have lower surface energy. HS has the highest surface energy due to very low graft density and aggregations.

6.3.3 Bubble affinity on MD(SH)M-coated surfaces

Prior to the bubble transport experiments for demonstrating slippery surface property, the affinity of air bubbles on the MD(SH)M surfaces in water was investigated. The air bubble profiles of different volumes on HS, ES, PS and IS surfaces are recorded and shown in Figure 6.3a, where all the bubbles were aligned to the left edge (blue dash line) according to three-phase contact line. The right edges of three-phase contact line are marked by grey, red, yellow and green dash lines, according to the bubble size. For HS, the right edge of 5 μL bubble is marked by grey dash line, while the right edge of the 10, 15 and 20 μL bubbles are vertically on the same position which is marked by red dash line. When the size increases to 25 μL, the bubble is dragged upwards by buoyancy force, leading to the left shift of right edge, and the bubble ultimately detaches from HS when the bubble volume is 30 μL. For ES, PS and IS, the right edges of bubbles keep moving to

the right side with the increase of bubble volume, which are marked by grey, red, yellow, and green for 10, 20, 30, and 40 μL bubbles, respectively. As all the bubbles are aligned to the left, the movement of bubble's right edge reveals the change of bubble-surface contact area, or the change of three-phase contact line. Figure 6.3a shows that with increasing the bubble volume, the three-phase contact line only moves slightly on the HS but expands freely on the ES, PS and IS surfaces. Figure 6.3a also shows that the critical bubble volume that can be immobilized on the HS is only half of that on ES, PS and IS, indicating weaker bubble affinity and stronger three-phase contact line friction for the HS case.

The schematic analysis of a bubble on flat substrate surface in water is shown in Figure 6.3b. The buoyancy (F_b) of the bubble can be expressed as $F_b = \rho g V$, where ρ is the density of water, g is the acceleration of gravity and V is the volume of bubble. The adhesion force (F_a) can be expressed as $F_a = \gamma_W L_{TCL} \sin\alpha$, where L_{TCL} is the length of three-phase contact line and α is the contact angle of bubble on the surface (Figure 6.3c)[54]. When F_b exceeds F_a, the bubble would detach from the surface. F_a was determined assuming three-phase contact line is a round circle shape. The diameter of three-phase contact line was measured from the captured images of the sessile drop or sessile bubble, by assuming the three-phase contact line is a round shape circle.

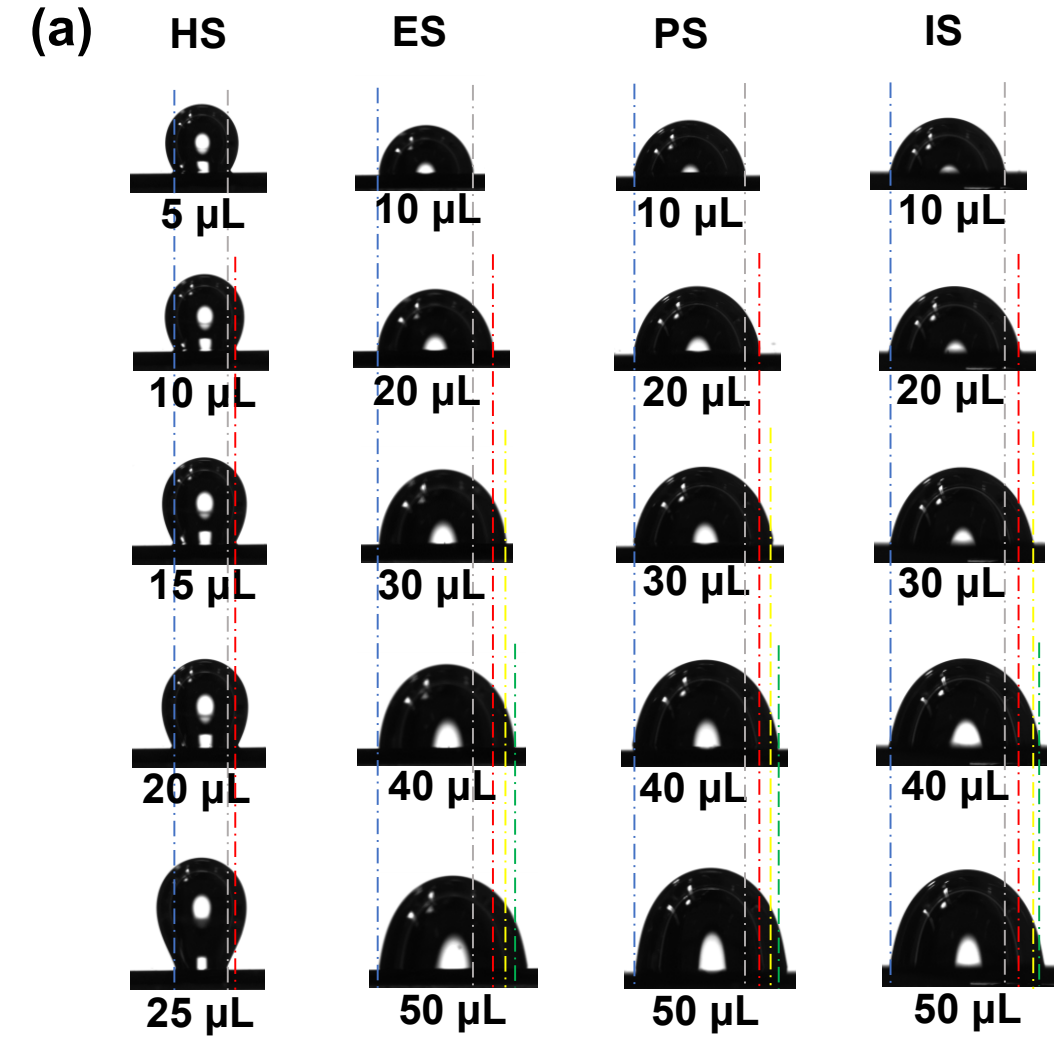
(a)
HS
ES
PS
IS
5 μL
10 μL
10 μL
10 μL
10 μL
20 μL
20 μL
20 μL
15 μL
30 μL
30 μL
30 μL
20 μL
40 μL
40 μL
40 μL
25 μL
50 μL
50 μL
50 μL

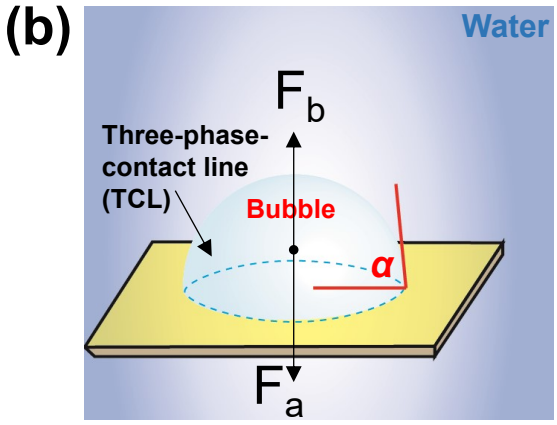
(b)
Water
F b
Three-phase-
contact line
(TCL)
Bubble
α
F a

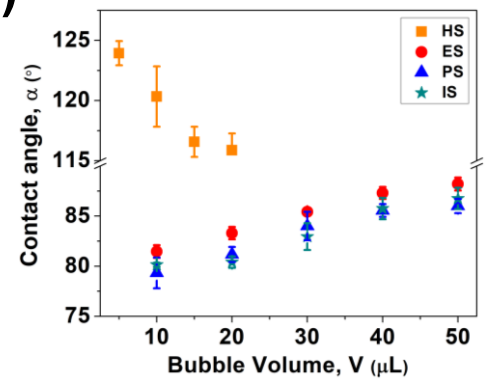
(c)
HS
ES
PS
IS
Contact angle, α (°)
125
120
115
85
80
75
10
20
30
40
50
Bubble Volume, V (μL)

Figure 6.3 (a) Air bubbles of different sizes in contact with HS, ES, PS and IS under water. The dash lines are used to define the edge of three-phase contact line; (b) the schematic analysis of a bubble on substrate surface under water; (c) the contact angle of bubbles of different volumes on HS, ES, PS and IS.

Table 6.1 shows that the F_a values for the ES, PS and IS cases are greater than the F_b values when the bubble size is 10, 20, 30, 40 and 50 μL, respectively. Thus, bubbles would attach to the substrate surfaces, which is consistent with the experiment results. For HS, F_a is greater than F_b for bubbles from 5 to 25 μL, indicating the bubbles would stay on the surfaces. It is noticed that F_a is 0.389 mN for 20 μL bubble and decreases to 0.308 mN for 25 μL bubble due to the shrinkage of three-phase contact line. The F_a of 30 μL bubble becomes less than 0.308 mN because of the further shrinkage of three-phase contact line. Therefore, the 30 μL bubble could not attach on HS surface anymore.

Table 6.1 The buoyancy and adhesion forces (Fb and Fa) calculated for bubbles with different volumes on HS, ES, PS and IS surfaces.

Bubble Volume, V (μL)	Buoyancy, F_b (mN)	Adhesion Force, F_a (mN)			
		HS	ES	PS	IS
5	0.0490	0.278			
10	0.0980	0.334	0.698	0.829	0.852
15	0.147	0.389			
20	0.196	0.389	0.852	0.924	0.988

25	0.245	0.308			
30	0.294		1.01	1.02	1.07
40	0.392		1.02	1.10	1.17
50	0.490		1.19	1.19	1.19

6.3.4 Bubble transport underwater

When the bubble moves along a tilted surface with an inclined angle β, the related forces involved are illustrated in Figure 6.4a. The adhesion force F_a balances with the y-axis (normal direction) component of the buoyancy to ensure the bubble remains on the surface. The x-axis component of buoyancy ($F_b \sin\beta$) provides the driving force for bubble self-transport. The resistant force consists of two parts, one due to the contact angle hysteresis (CAH) and the other arising from the drag force. The resistance of CAH can be expressed as $F_{CAH} = \gamma_W L(\cos\theta_R - \cos\theta_A)$, where L is the line length along the axis-direction between bubble and surface, θ_R is the receding contact angle and θ_A is the advancing contact angle of the bubble [55,56]. The drag force is mainly determined by the velocity of bubble [57]. When the driving force exceeds the resistance force, the bubble would slide along the surface. It is found that the bubble would transport on ES, PS and IS but not HS, and this phenomenon may be due to the strong attraction between water and HS thus leading to strong static friction (resistance force) that has to be overcome before bubble moves. Bare gold surface before coating MD(SH)M is also tested for the bubble transport. However, the bubble releases from bare gold surface before reaching 30 μL volume (Figure B.3). As the bubble self-transport behaviors on ES, PS and IS are quite similar, the transport on ES is shown as an example (Figure 6.4b). Figure 4c and 4d show the effect of inclined angle β on the average velocity of

transport of a 50 μL bubble (Figure 6.4c) and the effect of bubble volume on the average velocity at 20° inclined angle, respectively. The transport velocity of bubble shows the relationship as PS>ES>IS under the same testing condition. The average receding and advancing contact angles during bubble transport are calculated in Table 6.2, where the IS surface shows the largest hysteresis, followed by ES and PS. The $(\cos\theta_R - \cos\theta_A)$ values are calculated as 0.33, 0.32 and 0.36 for ES, PS and IS, respectively. A greater $(\cos\theta_R - \cos\theta_A)$ value would contribute to a larger resistance force F_{CAH}. As the driving force from buoyancy is constant for a certain volume of bubble on a fixed inclined angle, the increase of F_{CAH} would cause a decrease of the net driving force, which could lower the average velocity. Increasing the inclined angle β and bubble volume raises the driving force $F_b \sin\beta$, and thus the average velocity becomes higher. For example, the velocity *v* of 50 μL bubble is 0.46 cm/s on PS with an inclined angle of β =10°, which increases to 1.70 cm/s and 5.06 cm/s when the β increases to 15° and 20°, respectively. At β = 20°, the velocity of 30 μL bubble is $v \sim 0.31$ cm/s on ES, which significantly increases to 4.43 cm/s when the bubble volume is 50 μL.

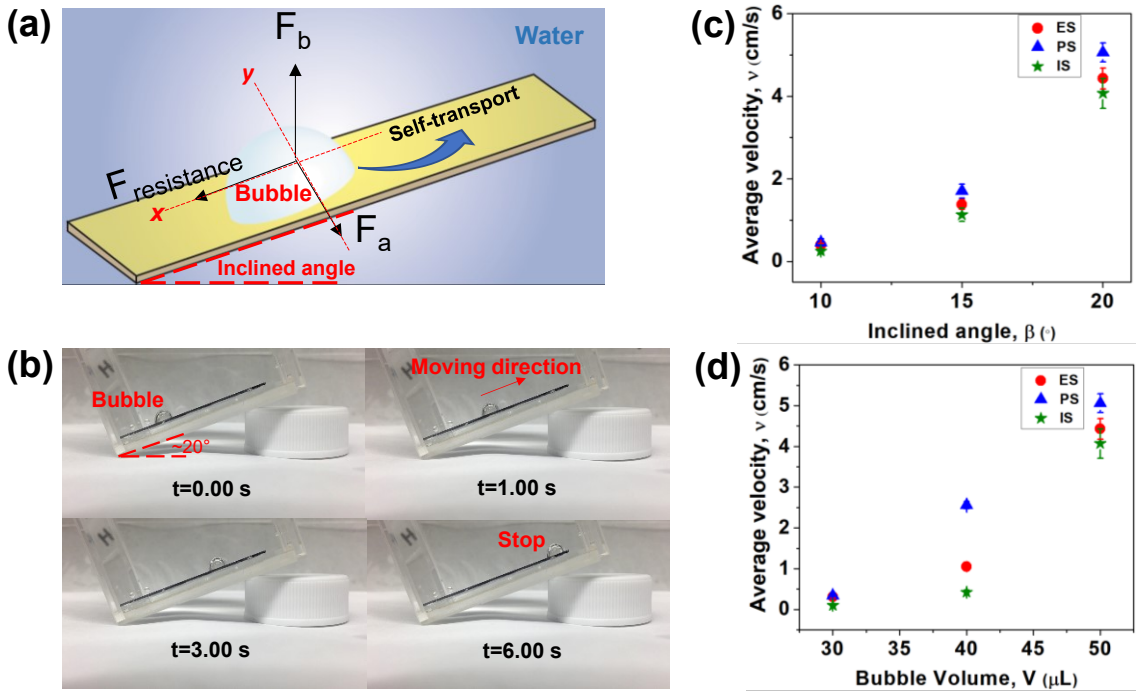

Figure 6.4 (a) Schematic force analysis of a bubble when it moves along an inclined surface. (b) Selected snapshots for the side-view of the transportation process of 30 μL bubble on ES. (c) Influence of the surface inclined angle β on average velocity *v*. (d) Influence of bubble volume V on average velocity *v*.

Table 6.2 Receding and advancing contact angles of bubble transport on ES, PS, and IS

	Receding contact angle (θ_R)	Advancing contact angle (θ_A)
ES	79.3°±1.5°	98.3°±2.1°
PS	84.3°±2.5°	103±2.6°
IS	72.3°±2.1°	93.3°±0.6°

6.3.5 Water drop transport

Besides the transport of air bubbles, the slippery surfaces can also realize the transport of water drops in oil (i.e., dodecane), as shown in Figure 6.5. Similar to bubble transport, the driving force and resistant force involved in the transport of water drop in oil is illustrated in Figure 6.5a. The driving force of water drop transport is the x-axis component of the net force of gravity and buoyancy $(\rho - \rho_O) gV$, where ρ and ρ_O are the density of water and oil, respectively. As an example, Figure 6.5b shows the typical snapshots captured during the water transport on PS, where the water drop slides smoothly from the top to the bottom. Similar to the bubble transport phenomena, the water drop can slide along the ES, PS and IS, but cannot slide on the HS and bare gold surface. As shown in Figure 6.5c, the average transport velocities of a 20 μL drop on an inclined ES, PS and IS (β=20°) are 0.27±0.08, 0.37±0.04 and 0.25±0.06 cm/s, respectively. Same as the bubble transport under water, PS shows the highest transport speed among all the surfaces.

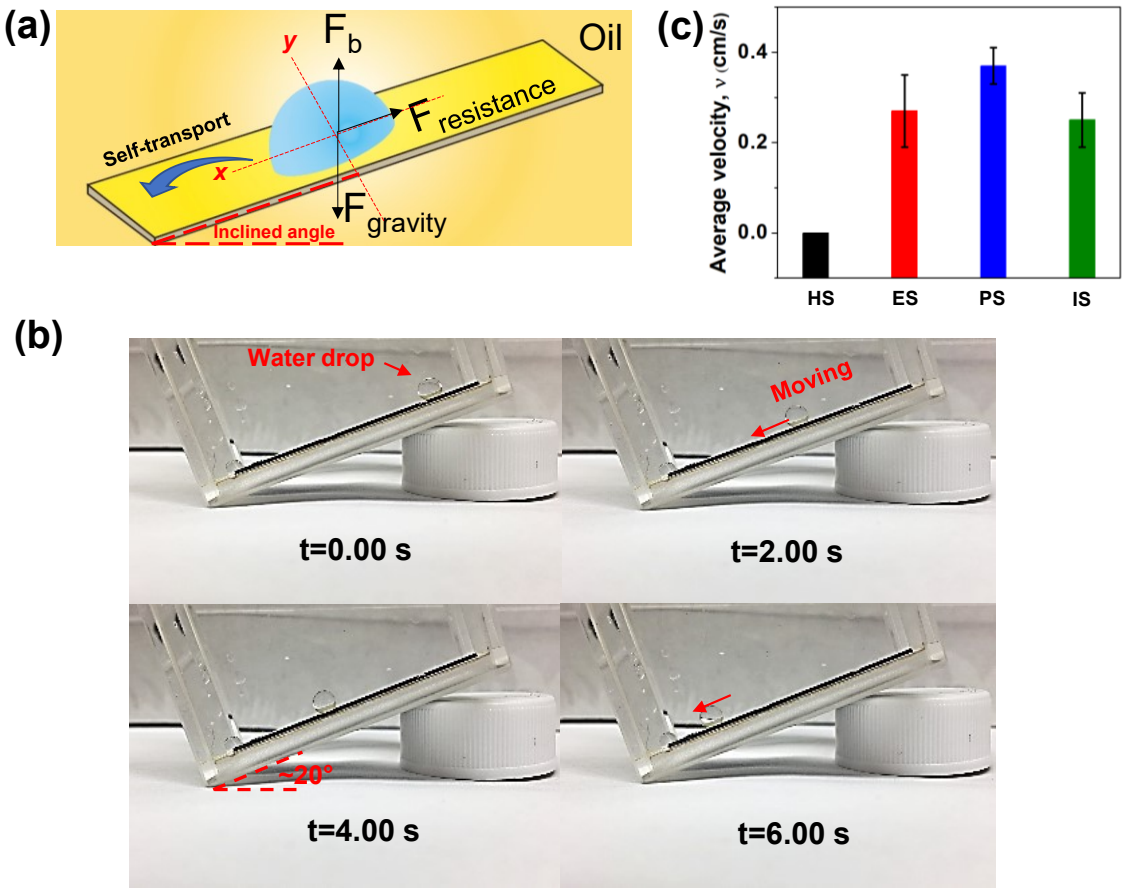

Figure 6.5 (a) Schematic force analysis of a water drop when it moves along an inclined surface in oil (i.e., dodecane). (b) Selected snapshots for the side-view of the transportation process of 20 μL water drop on PS in dodecane. (c) Average velocity of 20 μL water drop moving along tilted HS, ES, PS and IS with inclined angle 20° in dodecane.

The sliding angles of 20 μL water drops on HS, ES, PS, IS and bare gold surface in air were measured (Table 6.3). PS shows the smallest sliding angle, followed by ES and IS. Similar to bubble/water transport, the water drop cannot slide on HS and bare gold surface. The sliding angles of 20 μL glycerol drops are also measured in Table 6.3 where PS shows the best sliding performance among the three slippery surfaces. Compared with water, the sliding angle of glycerol slightly increases due to its higher viscosity.

Table 6.3 Sliding angle of water drop and glycerol drop on HS, ES, PS, IS and bare gold surface in air

	HS	ES	PS	IS	Bare gold surface
Water drop	Cannot slide	13.8°±0.5°	11.0°±0.7°	14.7°±0.4°	Cannot slide
Glycerol drop	Cannot slide	16.5°±1.5°	13.6°±0.5°	18.5°±0.5°	Cannot slide

6.3.6 Self-assembly of nanoparticles

Besides the transport of bubbles/drops, the pinning and depinning of droplets is also an important phenomenon associated with slippery surfaces, which is related to the hindrance of three-phase contact line movement[58,59]. Previous study reported that the edge of the droplet could be strongly pinned on conventional lubricant-infused slippery surface to leave a typical coffee ring [60]. To investigate the possible coffee ring phenomena on HS, ES, PS, IS and bare gold surfaces, 2 μL drops of SiO_2 (diameter~12 nm) suspension in water (15 mg/mL) was dropped on these surfaces and then evaporated in air. The top view of the evaporation process was monitored and recorded using a microscope (Figure 6.6). For suspension droplets on HS and bare gold surface (Figure 6.6a and 6.6e), the three-phase contact line moves slightly in the first 5 min, with the suspension droplet changing from a round shape to an irregular shape, after which the three-phase contact line strongly pins on the substrate surface until the suspension droplet is completely dried. The dried SiO_2 flakes exhibit many cracks and break into pieces due to the strong hinderance of three-phase contact line movement. In contrast, for the ES, PS and IS cases, the suspension drops maintain a spherical shape until they are fully dried, showing their low friction at the three-phase contact line (Figure 6.6b, 6.6c and 6.6d). After the suspension drops were fully dried, the SiO_2 flakes maintain their integrity. It is noted that the dried SiO_2 flake on the PS surface (Figure 6.6c) shows the best

integrity as compared to the ES (Figure 6.6b) and IS (Figure 6.6d) cases, indicating PS has the lowest three-phase contact line friction, which is consistent with the results that PS is the most "slippery" surface for the transport of air bubbles and water drops as discussed above.

Another interesting phenomenon observed during the evaporation process in Figure 6.6 is that the SiO_2 flakes on ES, PS and IS could freely stand from the substrate surface after completely dried. The SiO_2 flakes on the ES and IS could be easily moved with a tweezer by gently touching the edge of SiO_2 flake due to the low friction between the substrate surfaces and SiO_2 flakes. Interestingly, the SiO_2 flake on the PS was found to spontaneously sweep across the PS surface by itself at the end of evaporation process. The SiO_2 flake suddenly disappeared from focused region under the optical microscope at the end of evaporation process, which was found at the edge of the PS substrate. The above results indicate the low friction behaviors between the SiO_2 flakes and the ES, PS and IS surfaces, with the ultralow resistance friction for the PS case. Compared with previously reported lubricant oil-infused slippery surface, the as-prepared slippery surfaces (e.g., PS) in this work show much lower resistance to three-phase contact line movement, which provides a new method to concentrate nanoparticles by self-assembling [60,61].

Figure 6.7 shows the schematic of the evaporation process discussed above, in both top view and corresponding side view. Figure 6.7a represents the case for non-slippery surfaces, such as HS and bare gold surfaces. The edge of hemisphere-shaped droplet changes to an irregular shape and then strongly pins on the substrate surface during evaporation. In this case, the suspension drop dries to from broken flake pieces. Figure 6.7b represents the case for slippery surfaces such as ES, PS and IS. The hemispherical droplet gradually shrinks to a smaller hemispherical droplet during evaporation and dries to from a round and integrate flake.

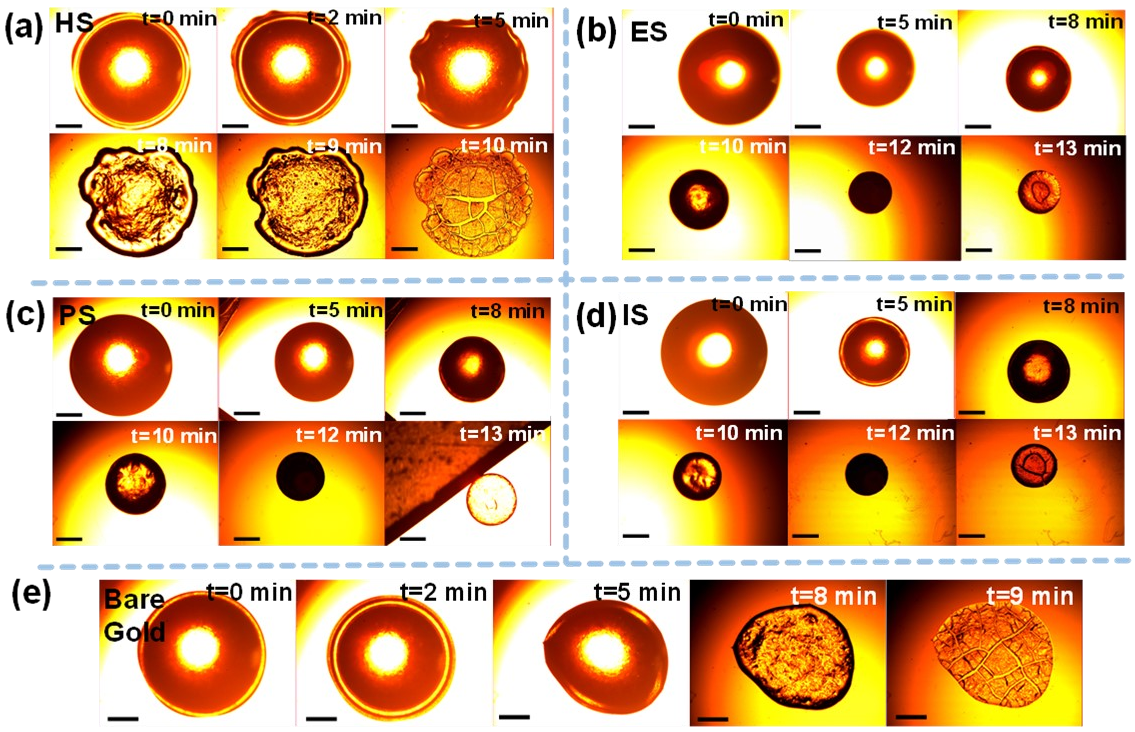

Figure 6.6 Snapshots for the shape change of aqueous silica suspension drops with evaporation time on (a) HS, (b) ES, (c) PS, (d) IS and (e) bare gold surface. The scale bar (400 μm) is the same for all the pictures.

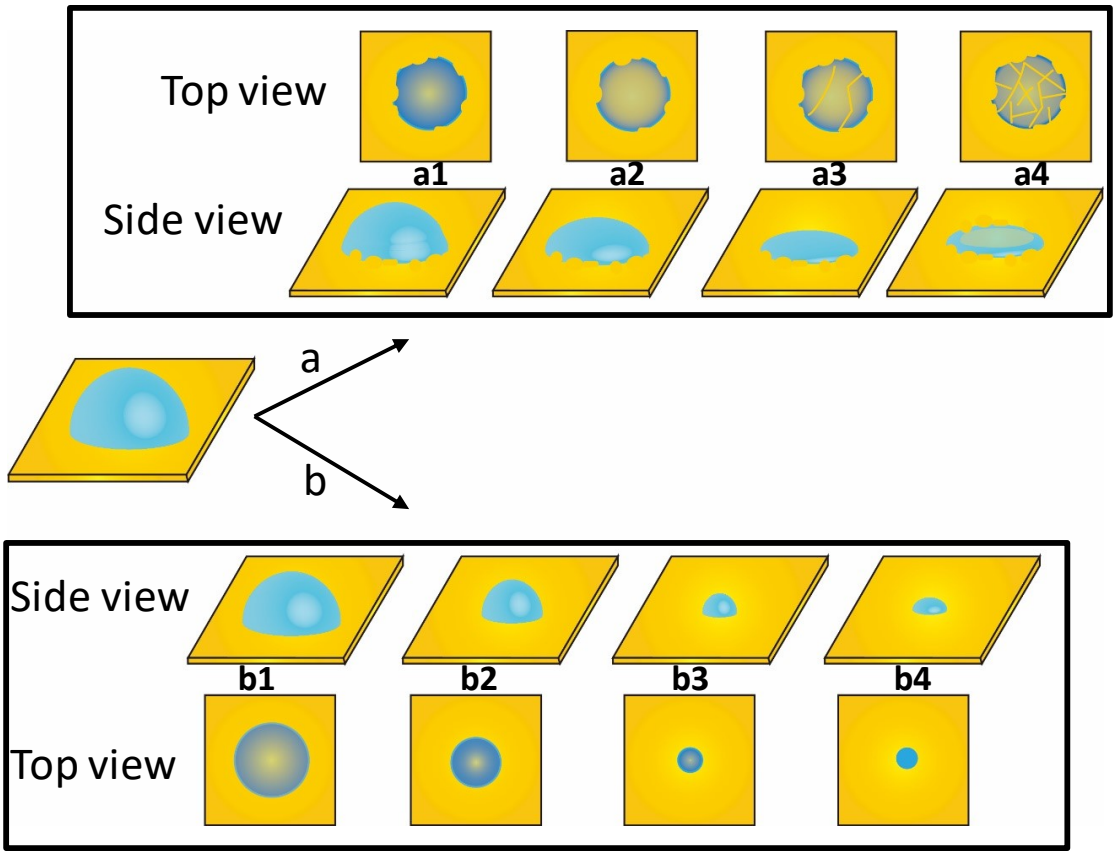

Figure 6.7 Schematic of the evaporation process of an aqueous nanoparticle suspension drop on (a) non-slippery and (b) slippery surfaces.

6.4 Conclusions

In this work, for the *first* time, we have designed and developed novel slippery solid surfaces by one-step self-assembly of a non-fluorine small molecule MD(SH)M. Interestingly, the as-prepared MD(SH)M coatings possess liquid-like slippery properties, which have been applied for directional transport of air bubbles in water and water drops in oil, as well as for self-assembly of nanoparticles from aqueous suspensions. The solvent used for coating deposition was found to significantly influence the graft density and adsorption form of MD(SH)M on gold substrate,

which further affects the surface energy, morphology as well as the slippery property of the MD(SH)M coating obtained. AFM imaging, cyclic voltammetry tests and film thickness measurements demonstrate that MD(SH)M coatings prepared via immersion in ethanol (ES), 2-propanol (ES) and 70% isopropanol (IS) are monolayers, with graft density much higher than that prepared by immersion in n-hexane (HS). PS displays the highest graft density as compared with ES and IS, resulting in the lowest surface energy among the four cases. It is found that air bubbles in water and water drops in oil can be facilely and directionally transported by the PS, ES and IS surfaces, while not on the HS surface. The bubble/drop size and inclined angle of substrate surface play an important role in the bubble/drop transport behavior (e.g., velocity). A larger bubble/drop size or higher inclined angle enhances the driving force (buoyancy or gravity force), leading to a higher average transport velocity. The as-prepared slippery MD(SH)M surfaces can facilitate the self-assembly of SiO_2 nanoparticles associated with the evaporation process of sessile drops of aqueous nanoparticle suspensions on PS, ES and IS, due to the low three-phase contact line resistance. Among the 4 substrates (PS, ES, IS and HS), PS shows the lowest resistance force (or friction) in bubble/drop transport and self-assembling of nanoparticles during drying aqueous suspension drops, which is mainly due to its relatively low surface energy and contact angle hysteresis. This work provides a novel strategy to facilely fabricate solid slippery coatings by using small non-fluorine molecules with lubricative functional groups, which possesses liquid-like slippery properties. This new strategy avoids the fabrication of complex nano/micro structures or using infused lubricant oils as widely used in preparing conventional slippery surfaces. Besides gold surface, this type of small molecule can be coated on other metals (e.g., Cu, Ag) or various surfaces pre-coated with polydopamine via Michael addition/Schiff base reaction. The new

strategy and as-prepared slippery solid surfaces have great potential in a wide range of engineering and bioengineering applications where low friction is desired.

References

1. Stride, G. O. The respiratory bubble of the aquatic beetle, potamodytes tuberosus, hinton. *Nature* **171**, 885–886 (1953).
2. Parker, A. R. & Lawrence, C. R. Water capture by a desert beetle. *Nature* **414**, 33–34 (2001).
3. Dai, X. *et al.* Hydrophilic directional slippery rough surfaces for water harvesting. *Sci. Adv.* **4**, eaaq0919 (2018).
4. Xu, W. *et al.* A droplet-based electricity generator with high instantaneous power density. *Nature* **578**, 392–396 (2020).
5. Chu, S. *et al.* Tunable Syngas Production from CO2and H2O in an Aqueous Photoelectrochemical Cell. *Angew. Chemie - Int. Ed.* **55**, 14262–14266 (2016).
6. Gwizdz, P., Lyson-Sypien, B., Radecka, M., Rekas, M. & Zakrzewska, K. Response modeling of temperature modulated array of chromium doped nanostructured TiO2 gas sensors. in *Procedia Engineering* vol. 120 1054–1057 (2015).
7. Yang, J. *et al.* Light-concentrating plasmonic au superstructures with significantly visible-light-enhanced catalytic performance. *ACS Appl. Mater. Interfaces* **7**, 8200–8208 (2015).
8. Zhang, L., Du, J., Ran, T., Gao, H. & Liao, Y. Preparation and application of poly(zwitterionic ionic liquid) to enhance the photocatalytic activity of TiO2. *J. Mater. Sci.* **51**, 7186–7198 (2016).
9. Von Gunten, U. Ozonation of drinking water: Part II. Disinfection and by-product formation in presence of bromide, iodide or chlorine. *Water Research* vol. 37 1469–1487 (2003).
10. Ternes, T. A. *et al.* Removal of pharmaceuticals during drinking water treatment. *Environ. Sci. Technol.* **36**, 3855–3863 (2002).
11. Zhang, J. *et al.* Unraveling the molecular interaction mechanism between graphene oxide and aromatic organic compounds with implications on wastewater treatment. *Chem. Eng. J.* **358**, 842–849 (2019).
12. Cheng, Y. *et al.* Zwitterionic Polymer-Grafted Superhydrophilic and Superoleophobic Silk Fabrics for Anti-Oil Applications. *Macromol. Rapid Commun.* 2000162 (2020)

doi:10.1002/marc.202000162.

13. Xu, Q., Nakajima, M., Ichikawa, S., Nakamura, N. & Shiina, T. A comparative study of microbubble generation by mechanical agitation and sonication. *Innov. Food Sci. Emerg. Technol.* **9**, 489–494 (2008).

14. Reynolds, C. & Yitayew, M. Low-head bubbler irrigation systems. Part II. Air lock problems. *Agric. Water Manag.* **29**, 25–35 (1995).

15. Tachibana, H. *et al.* Self-propelled continuous-flow PCR in capillary-driven microfluidic device: Microfluidic behavior and DNA amplification. *Sensors Actuators, B Chem.* **206**, 303–310 (2015).

16. Yu, C., Zhu, X., Li, K., Cao, M. & Jiang, L. Manipulating Bubbles in Aqueous Environment via a Lubricant-Infused Slippery Surface. *Adv. Funct. Mater.* **27**, (2017).

17. Wong, T.-S. *et al.* Bioinspired self-repairing slippery surfaces with pressure-stable omniphobicity. *Nature* **477**, 443–7 (2011).

18. Yu, C. *et al.* Spontaneous and Directional Transportation of Gas Bubbles on Superhydrophobic Cones. *Adv. Funct. Mater.* **26**, 3236–3243 (2016).

19. Zhang, C. *et al.* Bioinspired Pressure-Tolerant Asymmetric Slippery Surface for Continuous Self-Transport of Gas Bubbles in Aqueous Environment. *ACS Nano* **12**, 2048–2055 (2018).

20. Xie, L., Cui, X., Gong, L., Chen, J. & Zeng, H. Recent Advances in the Quantification and Modulation of Hydrophobic Interactions for Interfacial Applications. *Langmuir* (2020) doi:10.1021/acs.langmuir.9b03573.

21. Cao, M. *et al.* Water-Repellent Properties of Superhydrophobic and Lubricant-Infused 'slippery' Surfaces: A Brief Study on the Functions and Applications. *ACS Appl. Mater. Interfaces* **8**, 3615–3623 (2016).

22. Roach, P., Shirtcliffe, N. J. & Newton, M. I. Progess in superhydrophobic surface development. *Soft Matter* **4**, 224–240 (2008).

23. Yu, C. *et al.* Spontaneous and Directional Transportation of Gas Bubbles on Superhydrophobic Cones. *Adv. Funct. Mater.* **26**, 3236–3243 (2016).

24. Jiao, Y. *et al.* Pitcher plant-bioinspired bubble slippery surface fabricated by femtosecond laser for buoyancy-driven bubble self-transport and efficient gas capture. *Nanoscale* **11**, 1370–1378 (2019).

25. Zhou, S., Yu, C., Li, C., Dong, Z. & Jiang, L. Programmable unidirectional liquid transport on peristome-mimetic surfaces under liquid environments †. *J. Mater. Chem. A J. Mater. Chem. A Commun.* **2**, 2 (2019).

26. Jiang, J. *et al.* Directional pumping of water and oil microdroplets on slippery surface. *Proc. Natl. Acad. Sci.* **116**, 2482–2487 (2019).

27. Liu, M., Hou, Y., Li, J., Tie, L. & Guo, Z. Transparent slippery liquid-infused nanoparticulate coatings. *Chem. Eng. J.* **337**, 462–470 (2018).

28. Ma, W., Higaki, Y., Otsuka, H. & Takahara, A. Perfluoropolyether-infused nano-texture: a versatile approach to omniphobic coatings with low hysteresis and high transparency. *Chem. Commun.* **49**, 597–599 (2013).

29. Zhang, P. *et al.* Grooved organogel surfaces towards anisotropic sliding of water droplets. *Adv. Mater.* **26**, 3131–3135 (2014).

30. Liu, Y. *et al.* Design and preparation of biomimetic polydimethylsiloxane (PDMS) films with superhydrophobic, self-healing and drag reduction properties via replication of shark skin and SI-ATRP. *Chem. Eng. J.* **356**, 318–328 (2019).

31. Li, X., Cao, M., Shan, H., Handan Tezel, F. & Li, B. Facile and scalable fabrication of superhydrophobic and superoleophilic PDMS-co-PMHS coating on porous substrates for highly effective oil/water separation. *Chem. Eng. J.* **358**, 1101–1113 (2019).

32. Liu, Y., Wang, X. & Feng, S. Nonflammable and Magnetic Sponge Decorated with Polydimethylsiloxane Brush for Multitasking and Highly Efficient Oil–Water Separation. *Adv. Funct. Mater.* **29**, 1902488 (2019).

33. Huang, G. *et al.* Fluorinated Candle Soot as the Lubricant Additive of Perfluoropolyether. *Tribol. Lett.* **65**, 1–11 (2017).

34. Smith, J. D. *et al.* Droplet mobility on lubricant-impregnated surfaces. *Soft Matter* **9**, 1772–1780

(2013).

35. Ozbay, S., Yuceel, C. & Erbil, H. Y. Improved Icephobic Properties on Surfaces with a Hydrophilic Lubricating Liquid. *ACS Appl. Mater. Interfaces* **7**, 22067–22077 (2015).

36. Wang, X., Wang, Z., Heng, L. & Jiang, L. Stable Omniphobic Anisotropic Covalently Grafted Slippery Surfaces for Directional Transportation of Drops and Bubbles. *Adv. Funct. Mater.* **30**, 1902686 (2020).

37. Wooh, S. & Vollmer, D. Silicone Brushes: Omniphobic Surfaces with Low Sliding Angles. *Angew. Chemie Int. Ed.* **55**, 6822–6824 (2016).

38. Cheng, D. F., Urata, C., Yagihashi, M. & Hozumi, A. A Statically Oleophilic but Dynamically Oleophobic Smooth Nonperfluorinated Surface. *Angew. Chemie* **124**, 3010–3013 (2012).

39. Wang, L. & McCarthy, T. J. Covalently Attached Liquids: Instant Omniphobic Surfaces with Unprecedented Repellency. *Angew. Chemie - Int. Ed.* **55**, 244–248 (2016).

40. Liu, P. *et al.* Development of 'liquid-like' Copolymer Nanocoatings for Reactive Oil-Repellent Surface. *ACS Nano* **11**, 2248–2256 (2017).

41. Meng, X., Wang, Z., Wang, L., Heng, L. & Jiang, L. A stable solid slippery surface with thermally assisted self-healing ability. *J. Mater. Chem. A* **6**, 16355–16360 (2018).

42. Singh, N. *et al.* Omniphobic Metal Surfaces with Low Contact Angle Hysteresis and Tilt Angles. *Langmuir* **34**, 11405–11413 (2018).

43. Zhao, X., Arifur Rahman Khandoker, M. & Golovin, K. Non-Fluorinated Omniphobic Paper with Ultralow Contact Angle Hysteresis. *Cite This ACS Appl. Mater. Interfaces* **12**, 15748–15756 (2020).

44. Porter, M. D., Bright, T. B., Allara, D. L. & Chidsey, C. E. D. Spontaneously organized molecular assemblies. 4. Structural characterization of n-alkyl thiol monolayers on gold by optical ellipsometry, infrared spectroscopy, and electrochemistry. *J. Am. Chem. Soc.* **109**, 3559–3568 (1987).

45. Chen, J., Wang, Z., Oyola-Reynoso, S. & Thuo, M. M. Properties of Self-Assembled Monolayers Revealed via Inverse Tensiometry. *Langmuir* **33**, 13451–13467 (2017).

46. Yeon, H., Wang, C., Van Lehn, R. C. & Abbott, N. L. Influence of Order within Nonpolar Monolayers on Hydrophobic Interactions. *Langmuir* **33**, 4628–4637 (2017).

47. Chen, J., Chang, B., Oyola-Reynoso, S., Wang, Z. & Thuo, M. Quantifying Gauche Defects and Phase Evolution in Self-Assembled Monolayers through Sessile Drops. *ACS Omega* **2**, 2072–2084 (2017).

48. Barrena, E., Kopta, S., Ogletree, D. F., Charych, D. H. & Salmeron, M. Relationship between Friction and Molecular Structure: Alkylsilane Lubricant Films under Pressure. *Phys. Rev. Lett.* **82**, 2880–2883 (1999).

49. Ando, E., Goto, Y., Morimoto, K., Ariga, K. & Okahata, Y. Frictional properties of monomolecular layers of silane compounds. *Thin Solid Films* **180**, 287–291 (1989).

50. Siriviriyanun, A. & Imae, T. Anti-fingerprint properties of non-fluorinated organosiloxane self-assembled monolayer-coated glass surfaces. *Chem. Eng. J.* **246**, 254–259 (2014).

51. Cui, X. *et al.* Modulation of Hydrophobic Interaction by Mediating Surface Nanoscale Structure and Chemistry, not Monotonically by Hydrophobicity. *Angew. Chemie Int. Ed.* **57**, 11903–11908 (2018).

52. Widrig, C. A., Chung, C. & Porter, M. D. The electrochemical desorption of n-alkanethiol monolayers from polycrystalline Au and Ag electrodes. *J. Electroanal. Chem.* **310**, 335–359 (1991).

53. Lee, L. Y. S. & Lennox, R. B. Electrochemical desorption of n-alkylthiol SAMs on polycrystalline gold: Studies using a ferrocenylalkylthiol probe. *Langmuir* **23**, 292–296 (2007).

54. Jones, S. F., Evans, G. M. & Galvin, K. P. Bubble nucleation from gas cavities - A review. *Adv. Colloid Interface Sci.* **80**, 27–50 (1999).

55. Olsen, D. A., Joyner, P. A. & Olson, M. D. The sliding of liquid drops on solid surfaces. *J. Phys. Chem.* **66**, 883–886 (1962).

56. Belman, N., Jin, K., Golan, Y., Israelachvili, J. N. & Pesika, N. S. Origin of the contact angle hysteresis of water on chemisorbed and physisorbed self-assembled monolayers. *Langmuir* **28**, 14609–14617 (2012).

57. Yu, C., Zhu, X., Li, K., Cao, M. & Jiang, L. Manipulating Bubbles in Aqueous Environment via a Lubricant-Infused Slippery Surface. *Adv. Funct. Mater.* **27**, 1701605 (2017).

58. Li, Y., Yang, Q., Li, M. & Song, Y. Rate-dependent interface capture beyond the coffee-ring effect. *Sci. Rep.* **6**, 24628 (2016).

59. Xu, W. & Choi, C. H. From sticky to slippery droplets: Dynamics of contact line depinning on superhydrophobic surfaces. *Phys. Rev. Lett.* **109**, 024504 (2012).

60. Cao, M. *et al.* Water-Repellent Properties of Superhydrophobic and Lubricant-Infused "Slippery" Surfaces: A Brief Study on the Functions and Applications. *ACS Appl. Mater. Interfaces* **8**, 3615–3623 (2016).

61. Liu, W., Midya, J., Kappl, M., Butt, H.-J. & Nikoubashman, A. Segregation in Drying Binary Colloidal Droplets. *ACS Nano* **13**, 4972–4979 (2019).

Chapter 7 Conclusion and Future Work

7.1 Major conclusion

The research in this project aims at developing novel functional materials to solve oil contamination problems (i.e., oil/water mixture, oil spill and oil/water emulsion), and elucidating the underlying interfacial interactions in emulsions at nanoscale. This project points out new ways of designing functional materials and provides insights into fundamental understanding of interactions in oil/water emulsions, which has great importance and applications in many engineering and bioengineering processes.

The first work develops novel magnetic microspheres functionalized with superhydrophilic polyelectrolyte, which can effectively break the asphaltenes stabilized W/O emulsion to release the emulsified water. The mechanism of destabilization is studied using AFM force measurement, QCMD and IFT. The AFM force measurement shows that there is strong attraction between the superhydrophilic polyelectrolyte and water droplets in oil with asphaltenes. This strong attraction would allow the as-prepared microsphere to attach to the emulsified water droplets in the bulk emulsion. Besides, the asphaltenes adsorbs to the polyelectrolyte in QCMD experiment which indicates the asphaltenes layer around emulsified water droplets could be broken by superhydrophilic microsphere to facilitate the coalescence of water droplets. An increased water/oil IFT value is observed after adding the microsphere in oil droplet with asphaltenes, suggesting the emulsion becomes unstable with the addition of microsphere. As compared with the control experiment without external magnetic field, it is revealed that the external magnetic force plays an important role in accelerating the demulsification. In all, the destabilization of asphaltenes stabilized W/O emulsion is attributed to the synergic effect from the attraction between

water and polyelectrolyte, the increase of interfacial tension and additional external magnetic force.

The second work aims at developing functional materials with small molecules for oil absorption, oil/water separation and demulsification via a simple and scalable method. The functional materials are prepared using commercially available fiber-based substrates (i.e., cotton fiber, stainless steel mesh) with polydopamine as intermediate layer and the small molecule MD(SH)M as outer layer. The substrates are simply immersed in dopamine dissolved solution to generate the polydopamine layer and then immersed in 2-propanol with MD(SH)M to prepare the functional materials, which has the hydrophobic and oleophilic (oil contact angle ~0°) property in air. The contact angle of water on functionalized cotton fibers (CF@PM) can reach up to ~160°. In the oil/water separation experiment, the functionalized stainless steel mesh (SSM@PM) can effectively separate the water mixture with high-/low-density oil and the separation mechanism is revealed by studying the interaction between a water droplet and SSM@PM in oil as well as between an oil droplet and SSM@PM in water using ITFDA. Strong attraction is found between oil droplet and SSM@PM in water and repulsion is observed between water droplet and SSM@PM in oil. In the measurement of hydrophobic interaction between an air bubble and MD(SH)M in water, the decay length is determined to be 1.5 nm. This strong hydrophobic interaction also contributes to strong affinity of functional materials to oil under water. The CF@PM can absorb five types of oil spills from water, as well as break the span80 stabilized emulsion to decrease the water content from 1% to a few hundred ppm. The demulsification efficiency is maintained above 95% after ten runs. Besides, the CF@PM can break the asphaltenes stabilized W/O emulsion to obtain a clear organic solution without emulsified water droplets.

In the third work, the stabilization mechanisms of W/O and O/W Pickering emulsions with pH-responsive Fe_3O_4@2OA NPs are studied using AFM force measurement, IFT tests and microscope imaging. The forces between two water droplets in oil and two oil droplets in water without interfacially active Fe_3O_4@2OA NPs are measured first as control experiment. The two water droplets coalesced in oil due to VDW attraction while two oil droplets in water are stable against each other and no adhesion is measured because of strong EDL repulsion. The force curves without Fe_3O_4@2OA NPs can be well fitted to a theoretical model based on Reynolds lubrication theory and augmented Young-Laplace equation. In the force measurements with Fe_3O_4@2OA NPs, water droplets are stable against each other in oil under acidic condition (i.e., pH 2 and pH 4) with adhesion detected during separation and no adhesion is detected between two oil droplets under basic condition (i.e., pH 9 and pH 11). By analyzing the IFT results and microscope imaging, it is proposed that particles are confined to form a steric barrier in acidic condition to prevent droplet coalescence and the attractions during the separation of droplets arise from bridging of confined particles and aggregates. Under basic condition the oil droplets are mainly stabilized due to relatively lower IFT, strong electrostatic repulsion from negatively charged carboxyl groups, and steric repulsion from the confined particles and their aggregates. The effect from maximum loading force and dwelling time on interactions of emulsion droplets are studied by AFM force measurement. It is found that the increase of maximum loading force and dwelling time enhance the confinement of particles and particle aggregates at oil/water interface.

In the fourth work, the small molecule MD(SH)M (same small molecule in the second work) is assembled on gold wafer to prepare slippery surfaces. The slippery surface can transport air bubble in water, and transport water droplets in oil/air. This slippery behavior is related to the liquid-like property of small molecule and the low surface tension after coating MD(SH)M. With the study

of solvent effect, it is found that the gold surface modified in 2-propanol with MD(SH)M has the highest coating density and lowest surface tension which contributes to the highest transport speed of air bubble/droplet, as compared with those modified in ethanol, hexane and 2-propanol/water mixture. The as-prepared slippery surfaces show low resistance to the three-phase-contact line movement which allows the SiO_2 nanoparticles suspending in water to self-assembly a round shape solid SiO_2 flake.

In summary, novel functional materials for destabilizing emulsions, oil/water separation and oil absorption have been developed and the relative interfacial interactions have been studied at nanoscale using AFM force measurement. The developed magnetic microsphere points out a new way in the demulsification of asphaltenes stabilized emulsion using superhydrophilic material instead of traditional amphiphilic materials. The external magnetic field greatly facilitates the demulsification process which can be extended to the application of breaking other types of emulsions. The developed fiber-based functional materials for oil absorption, oil/water separation and demulsification sheds novel lights on the use of suitable small molecule, rather than traditional polymers, to solve the oil related problems. The interactions between droplets with immobilized nanoparticles in W/O and O/W emulsion have been studied and the models of particle arrangement at oil/water interface are proposed, which contributes to the study of stabilizing mechanism of Pickering emulsion. A novel non-fluorine slippery surface without micro/nano structure and infused liquid has been prepared by small molecules.

7.2 Suggestions for future work

(1) Considering the excellent demulsification performance of superhydrophilic polyelectrolyte in breaking the asphaltenes-stabilized emulsions, it is worth to explore the demulsification capability of other superhydrophilic polyelectrolytes, such as cationic polyelectrolyte and anionic

polyelectrolyte. The charge of polyelectrolyte may interact with the charged asphaltenes in aqueous phase to alter the emulsion stability. Therefore, the comparison of cationic, anionic and zwitterionic polyelectrolyte has significance in understanding the influence arising from ionic interactions on stability of asphaltenes-stabilized emulsions.

(2) As the aqueous phase of emulsions in many engineering and bioengineering processes contains salts and acidic/basic components, it is important to include the effect from salinity and pH in the study of demulsification. The demulsification work (i.e., first and second work) in this project uses pure water to prepare the emulsion. Hence, it is suggested to study the salinity and pH effect in the future work.

(3) As shown in the second and fourth work, the silicon based small molecules can be used to prepare materials for oil/water separation, oil absorption and bubble/droplets transportation under liquid, which indicates the small molecules are good candidates to solve the oil contamination issues. However, the study of small molecules, specifically the novel silicon based small molecules is very rare in the interactions with oil/water and interfacially active components (e.g., asphaltenes, particles). In the future work, it is suggested to synthesize several novel silicon based small molecules by changing a certain functional group of MD(SH)M, for example, changing the alkane chain length of MD(SH)M, and substituting the $–CH_3$ with $-SiR_3$ to change the number of Si in MD(SH)M. In this case, the effect from chain length and Si content will be studied, which provides the guidance in designing suitable small molecules for oil decontamination processes.

Bibliography

1. Adewunmi, A. A., Kamal, M. S. & Solling, T. I. Application of magnetic nanoparticles in demulsification: A review on synthesis, performance, recyclability, and challenges. Journal of Petroleum Science and Engineering vol. 196 107680 (2021).
2. Ali, M. F. & Alqam, M. H. Role of asphaltenes, resins and other solids in the stabilization of water in oil emulsions and its effects on oil production in Saudi oil fields. Fuel 79, 1309–1316 (2000).
3. Al-Sabagh, A. M., Nasser, N. M., El-Sukkary, M. M. A., Eissa, A. M. F. & Abd El-Hamid, T. M. Demulsification Efficiency of Some New Stearate Esters of Ethoxylated and Propoxylated 1,8-Diamino-Octane for Water in Crude Oil Emulsions. J. Dispers. Sci. Technol. 34, 1409–1420 (2013).
4. Alvarez, G., Jestin, J., Argillier, J. F. & Langevin, D. Small-angle neutron scattering study of crude oil emulsions: Structure of the oil - Water interfaces. Langmuir 25, 3985–3990 (2009).
5. An, Q. et al. A facile method to fabricate functionally integrated devices for oil/water separation. Nanoscale 7, 4553–4558 (2015).
6. Ando, E., Goto, Y., Morimoto, K., Ariga, K. & Okahata, Y. Frictional properties of monomolecular layers of silane compounds. Thin Solid Films 180, 287–291 (1989).
7. Asatekin, A. & Mayes, A. M. Oil industry wastewater treatment with fouling resistant membranes containing amphiphilic comb copolymers. Environ. Sci. Technol. 43, 4487–4492 (2009).

8. Asnaashari, M., Farhoosh, R. & Sharif, A. Antioxidant activity of gallic acid and methyl gallate in triacylglycerols of Kilka fish oil and its oil-in-water emulsion. Food Chem. 159, 439–444 (2014).

9. Atarian, M., Rajaei, A., Tabatabaei, M., Mohsenifar, A. & Bodaghi, H. Formulation of Pickering sunflower oil-in-water emulsion stabilized by chitosan-stearic acid nanogel and studying its oxidative stability. Carbohydr. Polym. 210, 47–55 (2019).

10. Aurell, J. & Gullett, B. K. Aerostat sampling of PCDD/PCDF emissions from the Gulf oil spill in situ burns. Environ. Sci. Technol. 44, 9431–9437 (2010).

11. Barnes, T. J. & Prestidge, C. A. PEO-PPO-PEO block copolymers at the emulsion droplet-water interface. Langmuir 16, 4116–4121 (2000).

12. Barrena, E., Kopta, S., Ogletree, D. F., Charych, D. H. & Salmeron, M. Relationship between Friction and Molecular Structure: Alkylsilane Lubricant Films under Pressure. Phys. Rev. Lett. 82, 2880–2883 (1999).

13. Barrera-Díaz, C., Roa-Morales, G., Ávila-Córdoba, L., Pavón-Silva, T. & Bilyeu, B. Electrochemical Treatment Applied to Food-Processing Industrial Wastewater. Ind. Eng. Chem. Res. 45, 34–38 (2006).

14. Belman, N., Jin, K., Golan, Y., Israelachvili, J. N. & Pesika, N. S. Origin of the contact angle hysteresis of water on chemisorbed and physisorbed self-assembled monolayers. Langmuir 28, 14609–14617 (2012).

15. Bhattacharyya, B. R., Nikolov, A. D. & Wasan, D. T. Demulsification of Water in Oil Emulsions Using Water Soluble Demulsifiers. J. Dispers. Sci. Technol. 13, 121–133 (1992).

16. Binks, B. P. & Clint, J. H. Solid wettability from surface energy components: Relevance to pickering emulsions. Langmuir 18, 1270–1273 (2002).

17. Binks, B. P. & Kirkland, M. Interfacial structure of solid-stabilised emulsions studied by scanning electron microscopy. Phys. Chem. Chem. Phys. 4, 3727–3733 (2002).

18. Binks, B. P. & Lumsdon, S. O. Stability of oil-in-water emulsions stabilised by silica particles. Phys. Chem. Chem. Phys. 1, 3007–3016 (1999).

19. Binks, B. P. Particles as surfactants - Similarities and differences. Curr. Opin. Colloid Interface Sci. 7, 21–41 (2002).

20. Borges, B., Rondón, M., Sereno, O. & Asuaje, J. Breaking of water-in-crude-oil emulsions. 3. influence of salinity and water-oil ratio on demulsifier action. in Energy and Fuels vol. 23 1568–1574 (2009).

21. Boyd, J., Parkinson, C. & Sherman, P. Factors affecting emulsion stability, and the HLB concept. J. Colloid Interface Sci. 41, 359–370 (1972).

22. Cai, Y. et al. A facile method to fabricate a double-layer stainless steel mesh for effective separation of water-in-oil emulsions with high flux. J. Mater. Chem. A 4, 18815–18821 (2016).

23. Cammarota, M. C. & Freire, D. M. G. A review on hydrolytic enzymes in the treatment of wastewater with high oil and grease content. Bioresource Technology vol. 97 2195–2210 (2006).

24. Cao, L., Chen, X. & Peng, Y. The effect of aliphatic alcohol frothers on the dispersion of oily collector. Miner. Eng. 157, 106552 (2020).

25. Cao, M. et al. Water-Repellent Properties of Superhydrophobic and Lubricant-Infused “Slippery” Surfaces: A Brief Study on the Functions and Applications. ACS Appl. Mater. Interfaces 8, 3615–3623 (2016).

26. Chan, D. Y. C., Klaseboer, E. & Manica, R. Theory of non-equilibrium force measurements involving deformable drops and bubbles. Advances in Colloid and Interface Science vol. 165 70–90 (2011).

27. Chaverot, P., Cagna, A., Glita, S. & Rondelez, F. Interfacial tension of bitumen - Water interfaces. Part 1: Influence of endogenous surfactants at acidic pH. Energy and Fuels 22, 790–798 (2008).

28. Chen, J., Chang, B., Oyola-Reynoso, S., Wang, Z. & Thuo, M. Quantifying Gauche Defects and Phase Evolution in Self-Assembled Monolayers through Sessile Drops. ACS Omega 2, 2072–2084 (2017).

29. Chen, J., Wang, Z., Oyola-Reynoso, S. & Thuo, M. M. Properties of Self-Assembled Monolayers Revealed via Inverse Tensiometry. Langmuir 33, 13451–13467 (2017).

30. Chen, T., Colver, P. J. & Bon, S. A. F. Organic–Inorganic Hybrid Hollow Spheres Prepared from TiO2-Stabilized Pickering Emulsion Polymerization. Adv. Mater. 19, 2286–2289 (2007).

31. Cheng, D. F., Urata, C., Yagihashi, M. & Hozumi, A. A Statically Oleophilic but Dynamically Oleophobic Smooth Nonperfluorinated Surface. Angew. Chemie 124, 3010–3013 (2012).

32. Cheng, M. et al. A functionally integrated device for effective and facile oil spill cleanup. Langmuir 27, 7371–7375 (2011).

33. Cheng, M., Ju, G., Jiang, C., Zhang, Y. & Shi, F. Magnetically directed clean-up of underwater oil spills through a functionally integrated device. J. Mater. Chem. A 1, 13411 (2013).

34. Cheng, Y. et al. Zwitterionic Polymer-Grafted Superhydrophilic and Superoleophobic Silk Fabrics for Anti-Oil Applications. Macromol. Rapid Commun. 2000162 (2020) doi:10.1002/marc.202000162.

35. Chevalier, Y. & Bolzinger, M. A. Emulsions stabilized with solid nanoparticles: Pickering emulsions. Colloids Surfaces A Physicochem. Eng. Asp. 439, 23–34 (2013).

36. Chu, S. et al. Tunable Syngas Production from CO2and H2O in an Aqueous Photoelectrochemical Cell. Angew. Chemie - Int. Ed. 55, 14262–14266 (2016).

37. Crispin, X. et al. Conductivity, morphology, interfacial chemistry, and stability of poly(3,4-ethylene dioxythiophene)-poly(styrene sulfonate): A photoelectron spectroscopy study. J. Polym. Sci. Part B Polym. Phys. 41, 2561–2583 (2003).

38. Cui, X. et al. Modulation of Hydrophobic Interaction by Mediating Surface Nanoscale Structure and Chemistry, not Monotonically by Hydrophobicity. Angew. Chemie Int. Ed. 57, 11903–11908 (2018).

39. Cui, X., Shi, C., Xie, L., Liu, J. & Zeng, H. Probing Interactions between Air Bubble and Hydrophobic Polymer Surface: Impact of Solution Salinity and Interfacial Nanobubbles. Langmuir 32, 11236–11244 (2016).

40. Da Rocha, S. R. P., Harrison, K. L. & Johnston, K. P. Effect of Surfactants on the Interfacial Tension and Emulsion Formation between Water and Carbon Dioxide. Langmuir 15, 419–428 (1999).

41. Dagastine, R. R., Prieve, D. C. & White, L. R. Forces between a rigid probe particle and a liquid interface: III. Extraction of the planar half-space interaction energy E(D). J. Colloid Interface Sci. 269, 84–96 (2004).

42. Dai, X. et al. Hydrophilic directional slippery rough surfaces for water harvesting. Sci. Adv. 4, eaaq0919 (2018).

43. Daksa Ejeta, D. et al. Preparation of superhydrophobic and superoleophilic cotton-based material for extremely high flux water-in-oil emulsion separation. Chem. Eng. J. 402, 126289 (2020).

44. Daniel-David, D. et al. Elastic properties of crude oil/water interface in presence of polymeric emulsion breakers. Colloids Surfaces A Physicochem. Eng. Asp. 270–271, 257–262 (2005).

45. Deng, W., Fan, T. & Li, Y. In situ biomineralization-constructed superhydrophilic and underwater superoleophobic PVDF-TiO2 membranes for superior antifouling separation of oil-in-water emulsions. J. Memb. Sci. 622, 119030 (2021).

46. Deng, Y. et al. Facile one-step preparation of robust hydrophobic cotton fabrics by covalent bonding polyhedral oligomeric silsesquioxane for ultrafast oil/water separation. Chem. Eng. J. 379, 122391 (2020).

47. Dickinson, E. Stabilising emulsion-based colloidal structures with mixed food ingredients. J. Sci. Food Agric. 93, 710–721 (2013).

48. Donovan, M. S., Sumerlin, B. S., Lowe, A. B. & McCormick, C. L. Controlled/“Living” Polymerization of Sulfobetaine Monomers Directly in Aqueous Media via RAFT †. Macromolecules 35, 8663–8666 (2002).

49. Eyssautier, J. et al. Insight into asphaltene nanoaggregate structure inferred by small angle neutron and X-ray scattering. J. Phys. Chem. B 115, 6827–6837 (2011).

50. Fan, Y., Simon, S. & Sjöblom, J. Chemical destabilization of crude oil emulsions: Effect of nonionic surfactants as emulsion inhibitors. Energy and Fuels 23, 4575–4583 (2009).

51. Feng, L. et al. A Super-Hydrophobic and Super-Oleophilic Coating Mesh Film for the Separation of Oil and Water. Angew. Chemie 116, 2046–2048 (2004).

52. Feng, S., Zhong, Z., Zhang, F., Wang, Y. & Xing, W. Amphiphobic Polytetrafluoroethylene Membranes for Efficient Organic Aerosol Removal. ACS Appl. Mater. Interfaces 8, 8773–8781 (2016).

53. Feng, X. et al. Effect of hydroxyl content and molecular weight of biodegradable ethylcellulose on demulsification of water-in-diluted bitumen emulsions. Ind. Eng. Chem. Res. 50, 6347–6354 (2011).

54. Feng, X., Xu, Z. & Masliyah, J. Biodegradable Polymer for Demulsification of Water-in-Bitumen Emulsions. Energy & Fuels 23, 451–456 (2009).

55. Feng, X., Zhai, J. & Jiang, L. The fabrication and switchable superhydrophobicity of TiO2 nanorod films. Angew. Chemie - Int. Ed. 44, 5115–5118 (2005).

56. Fenistein, D. et al. Viscosimetric and neutron scattering study of asphaltene aggregates in mixed toluene/heptane solvents. Langmuir 14, 1013–1020 (1998).

57. Fortuny, M. et al. Effect of Salinity, Temperature, Water Content, and pH on the Microwave Demulsification of Crude Oil Emulsions †. Energy & Fuels 21, 1358–1364 (2007).

58. Freer, E. M. & Radke, C. J. Relaxation of asphaltenes at the toluene/water interface: Diffusion exchange and surface rearrangement. J. Adhes. 80, 481–496 (2004).

59. French, D. J. et al. The secret life of Pickering emulsions: particle exchange revealed using two colours of particle. Sci. Rep. 6, 1–9 (2016).

60. French, D. J., Taylor, P., Fowler, J. & Clegg, P. S. Making and breaking bridges in a Pickering emulsion. J. Colloid Interface Sci. 441, 30–38 (2015).

61. Gafonova, O. V. & Yarranton, H. W. The stabilization of water-in-hydrocarbon emulsions by asphaltenes and resins. J. Colloid Interface Sci. 241, 469–478 (2001).

62. Gawrys, K. L. & Kilpatrick, P. K. Asphaltenic aggregates are polydisperse oblate cylinders. J. Colloid Interface Sci. 288, 325–334 (2005).

63. Gong, L. et al. Interaction Mechanisms of Zwitterions with Opposite Dipoles in Aqueous Solutions. Langmuir 35, 2842–2853 (2019).

64. Goubault, C. et al. Shear rupturing of complex fluids: Application to the preparation of quasi-monodisperse water-in-oil-in-water double emulsions. Langmuir 17, 5184–5188 (2001).

65. Gwizdz, P., Lyson-Sypien, B., Radecka, M., Rekas, M. & Zakrzewska, K. Response modeling of temperature modulated array of chromium doped nanostructured TiO2 gas sensors. in Procedia Engineering vol. 120 1054–1057 (2015).

66. Hachem, C., Bocquillon, F., Zahraa, O. & Bouchy, M. Decolourization of textile industry wastewater by the photocatalytic degradation process. Dye. Pigment. 49, 117–125 (2001).

67. Han, L. et al. Universal Mussel-Inspired Ultrastable Surface-Anchoring Strategy via Adaptive Synergy of Catechol and Cations. ACS Appl. Mater. Interfaces 10, 2166–2173 (2018).

68. He, K. et al. Cleaning of Oil Fouling with Water Enabled by Zwitterionic Polyelectrolyte Coatings: Overcoming the Imperative Challenge of Oil-Water Separation Membranes. ACS Nano 9, 9188–9198 (2015).

69. Hearn, M. Contesting 'the Ballarat cry': Interpreting the unstable narrative of trade and race in the 1903 federal election. Hist. Aust. 15, 693–710 (2018).

70. Helm, C. A., Israelachvili, J. N. & McGuiggan, P. M. Molecular mechanisms and forces involved in the adhesion and fusion of amphiphilic bilayers. Science (80-.). 246, 919–922 (1989).

71. Helm, C. A., Israelachvili, J. N. & McGuiggan, P. Role of Hydrophobic Forces in Bilayer Adhesion and Fusion. Biochemistry 31, 1794–1805 (1992).

72. Higaki, Y. et al. Adsorption and Desorption Behavior of Asphaltene on Polymer-Brush-Immobilized Surfaces. ACS Appl. Mater. Interfaces 6, 20385–20389 (2014).

73. Honda, T. et al. Polymer coating glass to improve the protein antifouling effect. Polym. J. 50, 381–388 (2018).

74. Hong, L., Sun, G., Cai, J. & Ngai, T. One-Step Formation of W/O/W Multiple Emulsions Stabilized by Single Amphiphilic Block Copolymers. Langmuir 28, 2332–2336 (2012).

75. Horozov, T. S. & Binks, B. P. Particle-Stabilized Emulsions: A Bilayer or a Bridging Monolayer? Angew. Chemie 118, 787–790 (2006).

76. Hu, Z., Marway, H. S., Kasem, H., Pelton, R. & Cranston, E. D. Dried and Redispersible Cellulose Nanocrystal Pickering Emulsions. ACS Macro Lett. 5, 185–189 (2016).

77. Huang, C. et al. Preparation of a reversed-phase/anion-exchange mixed-mode spherical sorbent by Pickering emulsion polymerization for highly selective solid-phase extraction of acidic pharmaceuticals from wastewater. J. Chromatogr. A 1521, 1–9 (2017).

78. Huang, G. et al. Fluorinated Candle Soot as the Lubricant Additive of Perfluoropolyether. Tribol. Lett. 65, 1–11 (2017).

79. Hutter, J. L. & Bechhoefer, J. Calibration of atomic-force microscope tips. Rev. Sci. Instrum. 64, 1868–1873 (1993).

80. Ingram, D. R. et al. Superparamagnetic nanoclusters coated with oleic acid bilayers for stabilization of emulsions of water and oil at low concentration. J. Colloid Interface Sci. 351, 225–232 (2010).

81. Israelachvili, J. N. Intermolecular and surface forces. (Academic Press, 2011).

82. J. Ekott, E. & J. Akpabio, E. A Review of Water-in-Crude Oil Emulsion Stability, Destabilization and Interfacial Rheology. J. Eng. Appl. Sci. 5, 447–452 (2010).

83. Jamaly, S., Giwa, A. & Hasan, S. W. Recent improvements in oily wastewater treatment: Progress, challenges, and future opportunities. Journal of Environmental Sciences (China) vol. 37 15–30 (2015).

84. Jeong, S. et al. Erratum to: Comparison of the Efficacy of Atopalm(®) Multi-Lamellar Emulsion Cream and Physiogel(®) Intensive Cream in Improving

Epidermal Permeability Barrier in Sensitive Skin. Dermatol. Ther. (Heidelb). 6, 57 (2016).

85. Jestin, J., Simon, S., Zupancic, L. & Barré, L. A small angle neutron scattering study of the adsorbed asphaltene layer in water-in-hydrocarbon emulsions: Structural description related to stability. Langmuir 23, 10471–10478 (2007).

86. Jian, C. et al. Reduction of Water/Oil Interfacial Tension by Model Asphaltenes: The Governing Role of Surface Concentration. J. Phys. Chem. B 120, 5646–5654 (2016).

87. Jian, C., Liu, Q., Zeng, H. & Tang, T. A Molecular Dynamics Study of the Effect of Asphaltenes on Toluene/Water Interfacial Tension: Surfactant or Solute? Energy and Fuels 32, 3225–3231 (2018).

88. Jiang, J. et al. Directional pumping of water and oil microdroplets on slippery surface. Proc. Natl. Acad. Sci. 116, 2482–2487 (2019).

89. Jiang, L., Tang, Z., Park-Lee, K. J., Hess, D. W. & Breedveld, V. Fabrication of non-fluorinated hydrophilic-oleophobic stainless steel mesh for oil-water separation. Sep. Purif. Technol. 184, 394–403 (2017).

90. Jiao, Y. et al. Pitcher plant-bioinspired bubble slippery surface fabricated by femtosecond laser for buoyancy-driven bubble self-transport and efficient gas capture. Nanoscale 11, 1370–1378 (2019).

91. Jin, Y. et al. Superhydrophobic and superoleophilic polydimethylsiloxane-coated cotton for oil-water separation process: An evidence of the relationship between its loading capacity and oil absorption ability. J. Hazard. Mater. 300, 175–181 (2015).

92. Jones, S. F., Evans, G. M. & Galvin, K. P. Bubble nucleation from gas cavities - A review. Adv. Colloid Interface Sci. 80, 27–50 (1999).

93. Ju, G., Cheng, M. & Shi, F. A pH-responsive smart surface for the continuous separation of oil/water/oil ternary mixtures. NPG Asia Mater. 6, (2014).

94. Khan, B. A. et al. Basics of pharmaceutical emulsions: A review. African Journal of Pharmacy and Pharmacology vol. 5 2715–2725 (2011).

95. Kim, J. W., Lee, D., Shum, H. C. & Weitz, D. A. Colloid surfactants for emulsion stabilization. Adv. Mater. 20, 3239–3243 (2008).

96. Kim, Y. et al. Robust superhydrophilic/hydrophobic surface based on self-aggregated Al 2O 3 nanowires by single-step anodization and self-assembly method. ACS Appl. Mater. Interfaces 4, 5074–5078 (2012).

97. Kobayashi, M. et al. Wettability and Antifouling Behavior on the Surfaces of Superhydrophilic Polymer Brushes. Langmuir 28, 7212–7222 (2012).

98. Korolev, V. V., Ramazanova, A. G. & Blinov, A. V. Adsorption of surfactants on superfine magnetite. Russ. Chem. Bull. 51, 2044–2049 (2002).

99. Kristiansen, K., McGuiggan, P., Carver, G., Meinhart, C. & Israelachvili, J. 3D force and displacement sensor for SFA and AFM measurements. Langmuir 24, 1541–1549 (2008).

100. Kumar, N. & Mandal, A. Surfactant Stabilized Oil-in-Water Nanoemulsion: Stability, Interfacial Tension, and Rheology Study for Enhanced Oil Recovery Application. Energy and Fuels 32, 6452–6466 (2018).

101. Lam, S., Blanco, E., Smoukov, S. K., Velikov, K. P. & Velev, O. D. Magnetically responsive pickering foams. J. Am. Chem. Soc. 133, 13856–13859 (2011).

102. Lan, Q. et al. Synthesis of bilayer oleic acid-coated Fe3O4nanoparticles and their application in pH-responsive Pickering emulsions. J. Colloid Interface Sci. 310, 260–269 (2007).

103. Langevin, D. & Argillier, J. F. Interfacial behavior of asphaltenes. Advances in Colloid and Interface Science vol. 233 83–93 (2016).

104. Lee, L. Y. S. & Lennox, R. B. Electrochemical desorption of n-alkylthiol SAMs on polycrystalline gold: Studies using a ferrocenylalkylthiol probe. Langmuir 23, 292–296 (2007).

105. Lee, M. N., Chan, H. K. & Mohraz, A. Characteristics of pickering emulsion gels formed by droplet bridging. Langmuir 28, 3085–3091 (2012).

106. Li, J. & Stöver, H. D. H. Doubly pH-responsive pickering emulsion. Langmuir 24, 13237–13240 (2008).

107. Li, J. J., Zhou, Y. N. & Luo, Z. H. Smart Fiber Membrane for pH-Induced Oil/Water Separation. ACS Appl. Mater. Interfaces 7, 19643–19650 (2015).

108. Li, M. F. et al. The formation of zein-chitosan complex coacervated particles: Relationship to encapsulation and controlled release properties. Int. J. Biol. Macromol. 116, 1232–1239 (2018).

109. Li, X., Cao, M., Shan, H., Handan Tezel, F. & Li, B. Facile and scalable fabrication of superhydrophobic and superoleophilic PDMS-co-PMHS coating on porous substrates for highly effective oil/water separation. Chem. Eng. J. 358, 1101–1113 (2019).

110. Li, Y., Yang, Q., Li, M. & Song, Y. Rate-dependent interface capture beyond the coffee-ring effect. Sci. Rep. 6, 24628 (2016).

111. Li, Z., Ming, T., Wang, J. & Ngai, T. High Internal Phase Emulsions Stabilized Solely by Microgel Particles. Angew. Chemie 121, 8642–8645 (2009).

112. Liang, C., He, X., Liu, Q. & Xu, Z. Adsorption-Based Synthesis of Magnetically Responsive and Interfacially Active Composite Nanoparticles for Dewatering of Water-in-Diluted Bitumen Emulsions. Energy and Fuels 32, 8078–8089 (2018).

113. Liang, C., Liu, Q. & Xu, Z. Dewatering Bitumen Emulsions Using Interfacially Active Organic Composite Absorbent Particles. Energy and Fuels 30, 5253–5258 (2016).

114. Liu, A., Fan, M. qiang, Li, Z. hong & Fan, J. chuan. Non-polar oil assisted DDA flotation of quartz I: Interfacial interaction between dodecane oil drop and mineral particle. Int. J. Miner. Process. 168, 1–8 (2017).

115. Liu, C.-Y. & Huang, C.-J. Functionalization of Polydopamine via the Aza-Michael Reaction for Antimicrobial Interfaces. Langmuir 32, 5019–5028 (2016).

116. Liu, D. et al. Multifunctional Polymer/Porous Boron Nitride Nanosheet Membranes for Superior Trapping Emulsified Oils and Organic Molecules. Adv. Mater. Interfaces 2, 1500228 (2015).

117. Liu, H. et al. Robust translucent superhydrophobic PDMS/PMMA film by facile one-step spray for self-cleaning and efficient emulsion separation. Chem. Eng. J. 330, 26–35 (2017).

118. Liu, J. et al. Destabilization of fine solids suspended in oil media through wettability modification and water-assisted agglomeration. Fuel 254, 115623 (2019).

119. Liu, J. et al. Probing effects of molecular-level heterogeneity of surface hydrophobicity on hydrophobic interactions in air/water/solid systems. J. Colloid Interface Sci. 557, 438–449 (2019).

120. Liu, K., Jiang, J., Cui, Z. & Binks, B. P. PH-Responsive Pickering Emulsions Stabilized by Silica Nanoparticles in Combination with a Conventional Zwitterionic Surfactant. Langmuir 33, 2296–2305 (2017).

121. Liu, M., Hou, Y., Li, J., Tie, L. & Guo, Z. Transparent slippery liquid-infused nanoparticulate coatings. Chem. Eng. J. 337, 462–470 (2018).

122. Liu, M., Wang, S., Wei, Z., Song, Y. & Jiang, L. Bioinspired design of a superoleophobic and low adhesive water/solid interface. Adv. Mater. 21, 665–669 (2009).

123. Liu, P. et al. Development of 'liquid-like' Copolymer Nanocoatings for Reactive Oil-Repellent Surface. ACS Nano 11, 2248–2256 (2017).

124. Liu, W., Midya, J., Kappl, M., Butt, H.-J. & Nikoubashman, A. Segregation in Drying Binary Colloidal Droplets. ACS Nano 13, 4972–4979 (2019).

125. Liu, Y. et al. Design and preparation of biomimetic polydimethylsiloxane (PDMS) films with superhydrophobic, self-healing and drag reduction properties via replication of shark skin and SI-ATRP. Chem. Eng. J. 356, 318–328 (2019).

126. Liu, Y., Wang, X. & Feng, S. Nonflammable and Magnetic Sponge Decorated with Polydimethylsiloxane Brush for Multitasking and Highly Efficient Oil–Water Separation. Adv. Funct. Mater. 29, 1902488 (2019).

127. Luo, Z. Y. et al. Superhydrophilic Nickel Nanoparticles with Core-Shell Structure to Decorate Copper Mesh for Efficient Oil/Water Separation. J. Phys. Chem. C 120, 12685–12692 (2016).

128. Lv, N., Wang, X., Peng, S., Luo, L. & Zhou, R. Superhydrophobic/superoleophilic cotton-oil absorbent: Preparation and its application in oil/water separation. RSC Adv. 8, 30257–30264 (2018).

129. Ma, Q. et al. Zeolitic imidazolate framework-8 film coated stainless steel meshes for highly efficient oil/water separation. Chem. Commun. 54, 5530–5533 (2018).

130. Ma, T. et al. Fabrication of electro-neutral nanofiltration membranes at neutral pH with antifouling surface via interfacial polymerization from a novel zwitterionic amine monomer. J. Memb. Sci. 503, 101–109 (2016).

131. Ma, W., Higaki, Y., Otsuka, H. & Takahara, A. Perfluoropolyether-infused nano-texture: a versatile approach to omniphobic coatings with low hysteresis and high transparency. Chem. Commun. 49, 597–599 (2013).

132. Malollari, K. G. et al. Mechanical Enhancement of Bioinspired Polydopamine Nanocoatings. (2019) doi:10.1021/acsami.9b15740.

133. Mansur, C. R. E., Barboza, S. P., González, G. & Lucas, E. F. PLURONIC x TETRONIC polyols: Study of their properties and performance in the destabilization of emulsions formed in the petroleum industry. J. Colloid Interface Sci. 271, 232–240 (2004).

134. Mansur, C. R. E., Lechuga, F. C., Mauro, A. C., González, G. & Lucas, E. F. Behavior of mixtures of nonionic polyoxide-based surfactants and their application in the destabilization of oil emulsions. J. Appl. Polym. Sci. 106, 2947–2954 (2007).

135. Mao, X. et al. Novel Fe3O4 based superhydrophilic core-shell microspheres for breaking asphaltenes-stabilized water-in-oil emulsion. Chem. Eng. J. 358, 869–877 (2019).

136. Mao, X., Tan, J., Xie, L., Wang, J. & Zeng, H. Novel multifunctional solid slippery surfaces with self-assembled fluorine-free small molecules. Chem. Eng. J. 404, 127064 (2021).

137. Meneghetti, P. & Qutubuddin, S. Synthesis of Poly(methyl methacrylate) Nanocomposites via Emulsion Polymerization Using a Zwitterionic Surfactant. Langmuir 20, 3424–3430 (2004).

138. Meng, Q. Rethink potential risks of toxic emissions from natural gas and oil mining. Environ. Pollut. 240, 848–857 (2018).

139. Meng, X., Wang, Z., Wang, L., Heng, L. & Jiang, L. A stable solid slippery surface with thermally assisted self-healing ability. J. Mater. Chem. A 6, 16355–16360 (2018).

140. Moradi, M., Alvarado, V. & Huzurbazar, S. Effect of salinity on water-in-crude oil emulsion: Evaluation through drop-size distribution proxy. Energy and Fuels 25, 260–268 (2011).

141. Mullins, O. C. The asphaltenes. Annu. Rev. Anal. Chem. 4, 393–418 (2011).

142. Murakami, D., Jinnai, H. & Takahara, A. Wetting transition from the cassie-baxter state to the wenzel state on textured polymer surfaces. Langmuir 30, 2061–2067 (2014).

143. Natarajan, A. et al. Understanding molecular interactions of asphaltenes in organic solvents using a surface force apparatus. J. Phys. Chem. C 115, 16043–16051 (2011).

144. Ngai, T., Behrens, S. H. & Auweter, H. Novel emulsions stabilized by pH and temperature sensitive microgels. Chem. Commun. 331–333 (2005) doi:10.1039/b412330a.

145. Niu, Z. et al. Interfacial properties pertinent to W/O and O/W emulsion systems prepared using polyaromatic compounds. Colloids Surfaces A Physicochem. Eng. Asp. 575, 283–291 (2019).

146. Nordvik, A. B., Simmons, J. L., Bitting, K. R., Lewis, A. & Strøm-Kristiansen, T. Oil and water separation in marine oil spill clean-up operations. Spill Sci. Technol. Bull. 3, 107–122 (1996).

147. Olsen, D. A., Joyner, P. A. & Olson, M. D. The sliding of liquid drops on solid surfaces. J. Phys. Chem. 66, 883–886 (1962).

148. Opawale, F. O. & Burgess, D. J. Influence of interfacial properties of lipophilic surfactants on water- in-oil emulsion stability. J. Colloid Interface Sci. 197, 142–150 (1998).

149. Ortiz, D. P., Baydak, E. N. & Yarranton, H. W. Effect of surfactants on interfacial films and stability of water-in-oil emulsions stabilized by asphaltenes. J. Colloid Interface Sci. 351, 542–555 (2010).

150. Ozbay, S., Yuceel, C. & Erbil, H. Y. Improved Icephobic Properties on Surfaces with a Hydrophilic Lubricating Liquid. ACS Appl. Mater. Interfaces 7, 22067–22077 (2015).

151. Parker, A. R. & Lawrence, C. R. Water capture by a desert beetle. Nature 414, 33–34 (2001).

152. Pensini, E. et al. Demulsification mechanism of asphaltene-stabilized water-in-oil emulsions by a polymeric ethylene oxide-propylene oxide demulsifier. Energy and Fuels 28, 6760–6771 (2014).

153. Pérez-Hernández, R. et al. Microstructural study of asphaltene precipitated with methylene chloride and n-hexane☆. Fuel 82, 977–982 (2003).

154. Pickering, S. U. CXCVI-Emulsions. J. Chem. Soc. Trans. 91, 2001–2021 (1907).

155. Porte, G., Zhou, H. & Lazzeri, V. Reversible description of asphaltene colloidal association and precipitation. Langmuir 19, 40–47 (2003).

156. Porter, M. D., Bright, T. B., Allara, D. L. & Chidsey, C. E. D. Spontaneously organized molecular assemblies. 4. Structural characterization of n-alkyl thiol monolayers on gold by optical ellipsometry, infrared spectroscopy, and electrochemistry. J. Am. Chem. Soc. 109, 3559–3568 (1987).

157. Poteau, S., Argillier, J. F., Langevin, D., Pincet, F. & Perez, E. Influence of pH on stability and dynamic properties of asphaltenes and other amphiphilic molecules at the oil-water interface. Energy and Fuels 19, 1337–1341 (2005).

158. Pradilla, D., Simon, S. & Sjöblom, J. Mixed interfaces of asphaltenes and model demulsifiers part I: Adsorption and desorption of single components. Colloids Surfaces A Physicochem. Eng. Asp. 466, 45–56 (2015).

159. Prystupa, J. Fluorine - A current literature review. An NRC and ATSDR based review of safety standards for exposure to fluorine and fluorides. Toxicology Mechanisms and Methods vol. 21 103–170 (2011).

160. Rapacchietta, A. V. & Neumann, A. W. Force and free-energy analyses of small particles at fluid interfaces. II. Spheres. J. Colloid Interface Sci. 59, 555–567 (1977).

161. Razi, M., Rahimpour, M. R., Jahanmiri, A. & Azad, F. Effect of a Different Formulation of Demulsifiers on the Efficiency of Chemical Demulsification of Heavy Crude Oil. J. Chem. Eng. Data 56, 2936–2945 (2011).

162. Reynolds, C. & Yitayew, M. Low-head bubbler irrigation systems. Part II. Air lock problems. Agric. Water Manag. 29, 25–35 (1995).

163. Roach, P., Shirtcliffe, N. J. & Newton, M. I. Progess in superhydrophobic surface development. Soft Matter 4, 224–240 (2008).

164. Rocha, J. A. et al. Role of Aqueous Phase Chemistry, Interfacial Film Properties, and Surface Coverage in Stabilizing Water-in-Bitumen Emulsions. Energy & Fuels 30, 5240–5252 (2016).

165. Rohrbach, K. et al. A cellulose based hydrophilic, oleophobic hydrated filter for water/oil separation. Chem. Commun. 50, 13296–13299 (2014).

166. Rondón, M. et al. Breaking of water-in-crude-oil emulsions. 2. Influence of asphaltene concentration and diluent nature on demulsifier action. Energy and Fuels 22, 702–707 (2008).

167. Roux, J. N., Broseta, D. & Demé, B. SANS study of asphaltene aggregation: Concentration and solvent quality effects. Langmuir 17, 5085–5092 (2001).

168. Sadeghpour, A., Pirolt, F. & Glatter, O. Submicrometer-Sized Pickering Emulsions Stabilized by Silica Nanoparticles with Adsorbed Oleic Acid. Langmuir 29, 6004–6012 (2013).

169. Saigal, T., Dong, H., Matyjaszewski, K. & Tilton, R. D. Pickering emulsions stabilized by nanoparticles with thermally responsive grafted polymer brushes. Langmuir 26, 15200–15209 (2010).

170. Schrope, M. Oil spill: Deep wounds. Nature vol. 472 152–154 (2011).

171. Serhan, M. et al. Total iron measurement in human serum with a smartphone. in AIChE Annual Meeting, Conference Proceedings vols 2019-Novem 1–3 (2019).

172. Shang, B., Wang, Y., Peng, B. & Deng, Z. Bioinspired polydopamine particles-assisted construction of superhydrophobic surfaces for oil/water separation. J. Colloid Interface Sci. 482, 240–251 (2016).

173. Shao, K. et al. Emulsion PCR: A High Efficient Way of PCR Amplification of Random DNA Libraries in Aptamer Selection. PLoS One 6, e24910 (2011).

174. Sharkawy, A., Barreiro, M. F. & Rodrigues, A. E. Chitosan-based Pickering emulsions and their applications: A review. Carbohydrate Polymers vol. 250 116885 (2020).

175. Shi, C. et al. Interaction between Air Bubbles and Superhydrophobic Surfaces in Aqueous Solutions. Langmuir 31, 7317–7327 (2015).

176. Shi, C. et al. Interaction Mechanism of Oil-in-Water Emulsions with Asphaltenes Determined Using Droplet Probe AFM. Langmuir 32, 2302–2310 (2016).

177. Shi, C. et al. Long-Range Hydrophilic Attraction between Water and Polyelectrolyte Surfaces in Oil. Angew. Chemie - Int. Ed. 55, 15017–15021 (2016).

178. Shi, C. et al. Measuring forces and spatiotemporal evolution of thin water films between an air bubble and solid surfaces of different hydrophobicity. ACS Nano 9, 95–104 (2015).

179. Shi, C. et al. Surface Interaction of Water-in-Oil Emulsion Droplets with Interfacially Active Asphaltenes. Langmuir 33, 1265–1274 (2017).

180. Shi, C., Chan, D. Y. C., Liu, Q. & Zeng, H. Probing the hydrophobic interaction between air bubbles and partially hydrophobic surfaces using atomic force microscopy. J. Phys. Chem. C 118, 25000–25008 (2014).

181. Shi, C., Xie, L., Zhang, L., Lu, X. & Zeng, H. Probing the interaction mechanism between oil droplets with asphaltenes and solid surfaces using AFM. J. Colloid Interface Sci. 558, 173–181 (2019).

182. Shi, Z. et al. Ultrafast Separation of Emulsified Oil/Water Mixtures by Ultrathin Free-Standing Single-Walled Carbon Nanotube Network Films. Adv. Mater. 25, 2422–2427 (2013).

183. Singh, N. et al. Omniphobic Metal Surfaces with Low Contact Angle Hysteresis and Tilt Angles. Langmuir 34, 11405–11413 (2018).

184. Siriviriyanun, A. & Imae, T. Anti-fingerprint properties of non-fluorinated organosiloxane self-assembled monolayer-coated glass surfaces. Chem. Eng. J. 246, 254–259 (2014).

185. Sivaram, N. M., Gopal, P. M. & Barik, D. Toxic waste from textile industries. in Energy from Toxic Organic Waste for Heat and Power Generation 43–54 (Elsevier, 2018). doi:10.1016/B978-0-08-102528-4.00004-3.

186. Smith, J. D. et al. Droplet mobility on lubricant-impregnated surfaces. Soft Matter 9, 1772–1780 (2013).

187. Song, P., Mao, X., Ren, Y., Zeng, H. & Lu, Q. Buckling Effect of Sole Zeolitic Imidazolate Framework-8 Nanoparticles Adsorbed at the Water/Oil Interface. Langmuir 36, 2322–2329 (2020).

188. Song, Y. et al. Hydrophilic/Oleophilic Magnetic Janus Particles for the Rapid and Efficient Oil–Water Separation. Adv. Funct. Mater. 28, 1802493 (2018).

189. Strassner, J. E. Effect of pH on Interfacial Films and Stability of Crude Oil-Water Emulsions. J. Pet. Technol. 20, 303–312 (1968).

190. Stride, G. O. The respiratory bubble of the aquatic beetle, potamodytes tuberosus, hinton. Nature 171, 885–886 (1953).

191. Sundar, S. et al. Efficacy and Safety of Amphotericin B Emulsion versus Liposomal Formulation in Indian Patients with Visceral Leishmaniasis: A Randomized, Open-Label Study. PLoS Negl. Trop. Dis. 8, e3169 (2014).

192. Suzuki, D., Tsuji, S. & Kawaguchi, H. Janus microgels prepared by surfactant-free pickering emulsion-based modification and their self-assembly. J. Am. Chem. Soc. 129, 8088–8089 (2007).

193. Tabor, R. F., Grieser, F., Dagastine, R. R. & Chan, D. Y. C. Measurement and analysis of forces in bubble and droplet systems using AFM. J. Colloid Interface Sci. 371, 1–14 (2012).

194. Tabor, R. F., Manica, R., Chan, D. Y. C., Grieser, F. & Dagastine, R. R. Repulsive Van der Waals forces in soft matter: Why bubbles do not stick to walls. Phys. Rev. Lett. 106, (2011).

195. Tabor, R. F., Wu, C., Grieser, F., Dagastine, R. R. & Chan, D. Y. C. Measurement of the hydrophobic force in a soft matter system. J. Phys. Chem. Lett. 4, 3872–3877 (2013).

196. Tachibana, H. et al. Self-propelled continuous-flow PCR in capillary-driven microfluidic device: Microfluidic behavior and DNA amplification. Sensors Actuators, B Chem. 206, 303–310 (2015).

197. Tadros, T. F. Emulsion Formation and Stability. Emulsion Formation and Stability vol. 13 (2013).

198. Tavernier, I., Wijaya, W., Van der Meeren, P., Dewettinck, K. & Patel, A. R. Food-grade particles for emulsion stabilization. Trends in Food Science and Technology vol. 50 159–174 (2016).

199. Tchoukov, P. et al. Role of asphaltenes in stabilizing thin liquid emulsion films. Langmuir 30, 3024–3033 (2014).

200. Ternes, T. A. et al. Removal of pharmaceuticals during drinking water treatment. Environ. Sci. Technol. 36, 3855–3863 (2002).

201. Vakarelski, I. U. et al. Dynamic interactions between microbubbles in water. Proc. Natl. Acad. Sci. U. S. A. 107, 11177–11182 (2010).

202. Vignati, E., Piazza, R. & Lockhart, T. P. Pickering emulsions: Interfacial tension, colloidal layer morphology, and trapped-particle motion. Langmuir 19, 6650–6656 (2003).

203. Von Gunten, U. Ozonation of drinking water: Part II. Disinfection and by-product formation in presence of bromide, iodide or chlorine. Water Research vol. 37 1469–1487 (2003).

204. Wang, D. et al. Stabilization mechanism and chemical demulsification of water-in-oil and oil-in-water emulsions in petroleum industry: A review. Fuel vol. 286 119390 (2021).

205. Wang, J., Liu, Q. & Zeng, H. Understanding Copper Activation and Xanthate Adsorption on Sphalerite by Time-of-Flight Secondary Ion Mass Spectrometry, X-ray Photoelectron Spectroscopy, and in Situ Scanning Electrochemical Microscopy. J. Phys. Chem. C 117, 20089–20097 (2013).

206. Wang, L. & McCarthy, T. J. Covalently Attached Liquids: Instant Omniphobic Surfaces with Unprecedented Repellency. Angew. Chemie - Int. Ed. 55, 244–248 (2016).

207. Wang, X., Shi, Y., Graff, R. W., Lee, D. & Gao, H. Developing recyclable pH-responsive magnetic nanoparticles for oil-water separation. Polymer (Guildf). 72, 361–367 (2015).

208. Wang, X., Wang, Z., Heng, L. & Jiang, L. Stable Omniphobic Anisotropic Covalently Grafted Slippery Surfaces for Directional Transportation of Drops and Bubbles. Adv. Funct. Mater. 30, 1902686 (2020).

209. Wei, Y., Xie, Y., Cai, Z., Guo, Y. & Zhang, H. Interfacial rheology, emulsifying property and emulsion stability of glyceryl monooleate-modified corn fiber gum. Food Chem. 343, 128416 (2021).

210. Widrig, C. A., Chung, C. & Porter, M. D. The electrochemical desorption of n-alkanethiol monolayers from polycrystalline Au and Ag electrodes. J. Electroanal. Chem. 310, 335–359 (1991).

211. Wong, T.-S. et al. Bioinspired self-repairing slippery surfaces with pressure-stable omniphobicity. Nature 477, 443–7 (2011).

212. Wooh, S. & Vollmer, D. Silicone Brushes: Omniphobic Surfaces with Low Sliding Angles. Angew. Chemie Int. Ed. 55, 6822–6824 (2016).

213. Wu, J., Xu, Y., Dabros, T. & Hamza, H. Effect of Demulsifier Properties on Destabilization of Water-in-Oil Emulsion. Energy and Fuels 17, 1554–1559 (2003).

214. Wu, J., Xu, Y., Dabros, T. & Hamza, H. Effect of Demulsifier Properties on Destabilization of Water-in-Oil Emulsion. Energy and Fuels 17, 1554–1559 (2003).

215. Wu, J., Xu, Y., Dabros, T. & Hamza, H. Effect of EO and PO positions in nonionic surfactants on surfactant properties and demulsification performance. Colloids Surfaces A Physicochem. Eng. Asp. 252, 79–85 (2005).

216. Wu, N. et al. Interaction of Fatty Acid Monolayers with Cobalt Nanoparticles. Nano Lett. 4, 383–386 (2004).

217. Wu, Z., Lee, D., Rubner, M. F. & Cohen, R. E. Structural color in porous, superhydrophilic, and self-cleaning SiO 2/TiO2́ bragg stacks. Small 3, 1445–1451 (2007).

218. Xie, C. Y. et al. Light and Magnetic Dual-Responsive Pickering Emulsion Micro-Reactors. Langmuir 33, 14139–14148 (2017).

219. Xie, L. et al. A wet adhesion strategy via synergistic cation-π and hydrogen bonding interactions of antifouling zwitterions and mussel-inspired binding moieties. J. Mater. Chem. A 7, 21944–21952 (2019).

220. Xie, L. et al. Interaction Mechanisms between Air Bubble and Molybdenite Surface: Impact of Solution Salinity and Polymer Adsorption. Langmuir 33, 2353–2361 (2017).

221. Xie, L. et al. Interfacial behavior and interaction mechanism of pentol/water interface stabilized with asphaltenes. J. Colloid Interface Sci. 553, 341–349 (2019).

222. Xie, L. et al. Mapping the Nanoscale Heterogeneity of Surface Hydrophobicity on the Sphalerite Mineral. J. Phys. Chem. C 121, 5620–5628 (2017).

223. Xie, L. et al. Probing the Interaction Mechanism between Air Bubbles and Bitumen Surfaces in Aqueous Media Using Bubble Probe Atomic Force Microscopy. Langmuir 34, 729–738 (2018).

224. Xie, L., Cui, X., Gong, L., Chen, J. & Zeng, H. Recent Advances in the Quantification and Modulation of Hydrophobic Interactions for Interfacial Applications. Langmuir (2020) doi:10.1021/acs.langmuir.9b03573.

225. Xie, L., Cui, X., Gong, L., Chen, J. & Zeng, H. Recent Advances in the Quantification and Modulation of Hydrophobic Interactions for Interfacial Applications. Langmuir 36, 2985–3003 (2020).

226. Xie, Y. et al. Highly Regenerable Mussel-Inspired Fe 3 O 4 @Polydopamine-Ag Core–Shell Microspheres as Catalyst and Adsorbent for Methylene Blue Removal. ACS Appl. Mater. Interfaces 6, 8845–8852 (2014).

227. Xin, X. et al. Influence of CTAB and SDS on the properties of oil-in-water nano-emulsion with paraffin and span 20/Tween 20. Colloids Surfaces A Physicochem. Eng. Asp. 418, 60–67 (2013).

228. Xu, C. et al. Dopamine as a robust anchor to immobilize functional molecules on the iron oxide shell of magnetic nanoparticles. J. Am. Chem. Soc. 126, 9938–9939 (2004).

229. Xu, D. et al. Influence of whey protein–beet pectin conjugate on the properties and digestibility of β-carotene emulsion during in vitro digestion. Food Chem. 156, 374–379 (2014).

230. Xu, Q., Nakajima, M., Ichikawa, S., Nakamura, N. & Shiina, T. A comparative study of microbubble generation by mechanical agitation and sonication. Innov. Food Sci. Emerg. Technol. 9, 489–494 (2008).

231. Xu, W. & Choi, C. H. From sticky to slippery droplets: Dynamics of contact line depinning on superhydrophobic surfaces. Phys. Rev. Lett. 109, 024504 (2012).

232. Xu, W. et al. A droplet-based electricity generator with high instantaneous power density. Nature 578, 392–396 (2020).

233. Xu, Y. et al. Breaking water-in-bitumen emulsions using polyoxyalkylated DETA demulsifier. Can. J. Chem. Eng. 82, 829–835 (2004).

234. Xu, Y., Dabros, T., Hamza, H. & Shefantook, W. Destabilization of water in bitumen emulsion by washing with water. Pet. Sci. Technol. 17, 1051–1070 (1999).

235. Xue, Z., Cao, Y., Liu, N., Feng, L. & Jiang, L. Special wettable materials for oil/water separation. Journal of Materials Chemistry A vol. 2 2445–2460 (2014).

236. Yan, B. et al. Rapid Dewatering and Consolidation of Concentrated Colloidal Suspensions: Mature Fine Tailings via Self-Healing Composite Hydrogel. ACS Appl. Mater. Interfaces 11, 21610–21618 (2019).

237. Yan, Z., Elliott, J. A. W. & Masliyah, J. H. Roles of Various Bitumen Components in the Stability of Water-in-Diluted-Bitumen Emulsions. J. Colloid Interface Sci. 220, 329–337 (1999).

238. Yang, D. et al. Probing Anisotropic Surface Properties and Interaction Forces of Chrysotile Rods by Atomic Force Microscopy and Rheology. Langmuir 30, 10809–10817 (2014).

239. Yang, F. et al. Asphaltene subfractions responsible for stabilizing water-in-crude oil emulsions. Part 1: Interfacial behaviors. Energy and Fuels 28, 6897–6904 (2014).

240. Yang, F. et al. Asphaltene Subfractions Responsible for Stabilizing Water-in-Crude Oil Emulsions. Part 2: Molecular Representations and Molecular Dynamics Simulations. Energy & Fuels 29, 4783–4794 (2015).

241. Yang, H. & Deng, Y. Preparation and physical properties of superhydrophobic papers. J. Colloid Interface Sci. 325, 588–593 (2008).

242. Yang, H.-C. et al. Mussel-inspired modification of a polymer membrane for ultra-high water permeability and oil-in-water emulsion separation. J. Mater. Chem. A 2, 10225–10230 (2014).

243. Yang, H.-C. et al. Mussel-inspired Modification of Polymer Membrane for Ultrahigh Water Permeability and Oil-in-Water Emulsion Separation. J. Name 00, (2013).

244. Yang, J. et al. Light-concentrating plasmonic au superstructures with significantly visible-light-enhanced catalytic performance. ACS Appl. Mater. Interfaces 7, 8200–8208 (2015).

245. Yang, K., Peng, H., Wen, Y. & Li, N. Re-examination of characteristic FTIR spectrum of secondary layer in bilayer oleic acid-coated Fe3O4 nanoparticles. Appl. Surf. Sci. 256, 3093–3097 (2010).

246. Yang, X. et al. Bio-inspired method for preparation of multiwall carbon nanotubes decorated superhydrophilic poly(vinylidene fluoride) membrane for oil/water emulsion separation. Chem. Eng. J. 321, 245–256 (2017).

247. Yang, Y. et al. An overview of pickering emulsions: Solid-particle materials, classification, morphology, and applications. Frontiers in Pharmacology vol. 8 287 (2017).

248. Yarranton, H. W. Asphaltene Self-Association. J. Dispers. Sci. Technol. 26, 5–8 (2005).

249. Yarranton, H. W., Sztukowski, D. M. & Urrutia, P. Effect of interfacial rheology on model emulsion coalescence. I. Interfacial rheology. J. Colloid Interface Sci. 310, 246–252 (2007).

250. Yeon, H., Wang, C., Van Lehn, R. C. & Abbott, N. L. Influence of Order within Nonpolar Monolayers on Hydrophobic Interactions. Langmuir 33, 4628–4637 (2017).

251. Yeung, A., Moran, K., Masliyah, J. & Czarnecki, J. Shear-induced coalescence of emulsified oil drops. J. Colloid Interface Sci. 265, 439–443 (2003).

252. Yu, C. et al. Spontaneous and Directional Transportation of Gas Bubbles on Superhydrophobic Cones. Adv. Funct. Mater. 26, 3236–3243 (2016).

253. Yu, C. et al. Spontaneous and Directional Transportation of Gas Bubbles on Superhydrophobic Cones. Adv. Funct. Mater. 26, 3236–3243 (2016).

254. Yu, C., Zhu, X., Li, K., Cao, M. & Jiang, L. Manipulating Bubbles in Aqueous Environment via a Lubricant-Infused Slippery Surface. Adv. Funct. Mater. 27, (2017).

255. Yu, C., Zhu, X., Li, K., Cao, M. & Jiang, L. Manipulating Bubbles in Aqueous Environment via a Lubricant-Infused Slippery Surface. Adv. Funct. Mater. 27, 1701605 (2017).

256. Yu, Y., Shapter, J. G., Popelka-Filcoff, R., Bennett, J. W. & Ellis, A. V. Copper removal using bio-inspired polydopamine coated natural zeolites. J. Hazard. Mater. 273, 174–182 (2014).

257. Yuan, T., Meng, J., Hao, T., Wang, Z. & Zhang, Y. A scalable method toward superhydrophilic and underwater superoleophobic PVDF membranes for effective oil/water emulsion separation. ACS Appl. Mater. Interfaces 7, 14896–14904 (2015).

258. Yue, X., Li, Z., Zhang, T., Yang, D. & Qiu, F. Design and fabrication of superwetting fiber-based membranes for oil/water separation applications. Chemical Engineering Journal vol. 364 292–309 (2019).

259. Zavareh, S., Behrouzi, Z. & Avanes, A. Cu (II) binded chitosan/Fe3O4 nanocomomposite as a new biosorbent for efficient and selective removal of phosphate. Int. J. Biol. Macromol. 101, 40–50 (2017).

260. Zeng, H. et al. Adhesion and Detachment Mechanisms between Polymer and Solid Substrate Surfaces: Using Polystyrene-Mica as a Model System. Macromolecules 49, 5223–5231 (2016).

261. Zeng, H., Tirrell, M. & Israelachvili, J. Limit cycles in dynamic adhesion and friction processes: A discussion. J. Adhes. 82, 933–943 (2006).

262. Zeng, H., Zhao, B., Israelachvili, J. N. & Tirrell, M. Liquid- to solid-like failure mechanism of thin polymer films at micro- and nanoscales. Macromolecules 43, 538–542 (2010).

263. Zhang, C. et al. Bioinspired Pressure-Tolerant Asymmetric Slippery Surface for Continuous Self-Transport of Gas Bubbles in Aqueous Environment. ACS Nano 12, 2048–2055 (2018).

264. Zhang, C. et al. CuSO4/H2O2-Induced Rapid Deposition of Polydopamine Coatings with High Uniformity and Enhanced Stability. Angew. Chemie - Int. Ed. 55, 3054–3057 (2016).

265. Zhang, J. et al. Scalable polyzwitterion-polydopamine coating for regenerable oil/water separation and underwater self-cleaning of stubborn heavy oil fouling without pre-hydration. Chem. Commun. 54, 9734–9737 (2018).

266. Zhang, J. et al. Unraveling the molecular interaction mechanism between graphene oxide and aromatic organic compounds with implications on wastewater treatment. Chem. Eng. J. 358, 842–849 (2019).

267. Zhang, L. Y., Lawrence, S., Xu, Z. & Masliyah, J. H. Studies of Athabasca asphaltene Langmuir films at air-water interface. J. Colloid Interface Sci. 264, 128–140 (2003).

268. Zhang, L., Du, J., Ran, T., Gao, H. & Liao, Y. Preparation and application of poly(zwitterionic ionic liquid) to enhance the photocatalytic activity of TiO2. J. Mater. Sci. 51, 7186–7198 (2016).

269. Zhang, L., He, R. & Gu, H.-C. Oleic acid coating on the monodisperse magnetite nanoparticles. Appl. Surf. Sci. 253, 2611–2617 (2006).

270. Zhang, L., Li, L. & Dang, Z. M. Bio-inspired durable, superhydrophobic magnetic particles for oil/water separation. J. Colloid Interface Sci. 463, 266–271 (2016).

271. Zhang, L., Shi, C., Lu, Q., Liu, Q. & Zeng, H. Probing Molecular Interactions of Asphaltenes in Heptol Using a Surface Forces Apparatus: Implications on Stability of Water-in-Oil Emulsions. Langmuir 32, 4886–4895 (2016).

272. Zhang, L., Xie, L., Cui, X., Chen, J. & Zeng, H. Intermolecular and surface forces at solid/oil/water/gas interfaces in petroleum production. J. Colloid Interface Sci. 537, 505–519 (2019).

273. Zhang, P. et al. Grooved organogel surfaces towards anisotropic sliding of water droplets. Adv. Mater. 26, 3131–3135 (2014).

274. Zhang, W. et al. A Solvothermal Route Decorated on Different Substrates: Controllable Separation of an Oil/Water Mixture to a Stabilized Nanoscale Emulsion. Adv. Mater. 27, 7349–7355 (2015).

275. Zhang, Z., Xu, G., Wang, F., Dong, S. & Chen, Y. Demulsification by amphiphilic dendrimer copolymers. J. Colloid Interface Sci. 282, 1–4 (2005).

276. Zhao, X., Arifur Rahman Khandoker, M. & Golovin, K. Non-Fluorinated Omniphobic Paper with Ultralow Contact Angle Hysteresis. Cite This ACS Appl. Mater. Interfaces 12, 15748–15756 (2020).

277. Zhou, J. E., Chang, Q., Wang, Y., Wang, J. & Meng, G. Separation of stable oil-water emulsion by the hydrophilic nano-sized ZrO2 modified Al2O3 microfiltration membrane. Sep. Purif. Technol. 75, 243–248 (2010).

278. Zhou, S., Yu, C., Li, C., Dong, Z. & Jiang, L. Programmable unidirectional liquid transport on peristome-mimetic surfaces under liquid environments †. J. Mater. Chem. A J. Mater. Chem. A Commun. 2, 2 (2019).

279. Zhou, X. et al. Robust and durable superhydrophobic cotton fabrics for oil/water separation. ACS Appl. Mater. Interfaces 5, 7208–7214 (2013).

280. Zhu, Y. et al. A novel zwitterionic polyelectrolyte grafted PVDF membrane for thoroughly separating oil from water with ultrahigh efficiency. J. Mater. Chem. A 1, 5758–5765 (2013).

Appendix A Supporting Information for Chapter 3

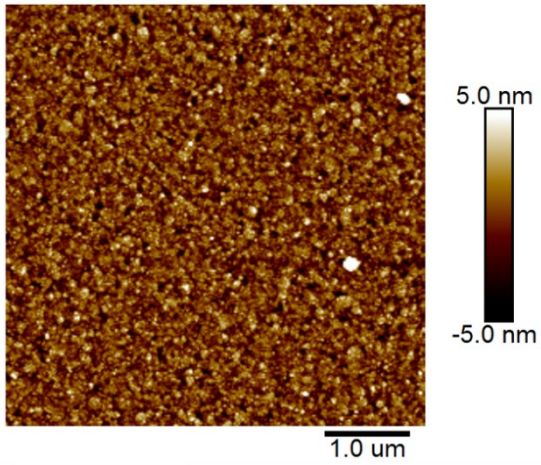

Figure A.1 AFM topographic image of PMAPS coated on gold in air.

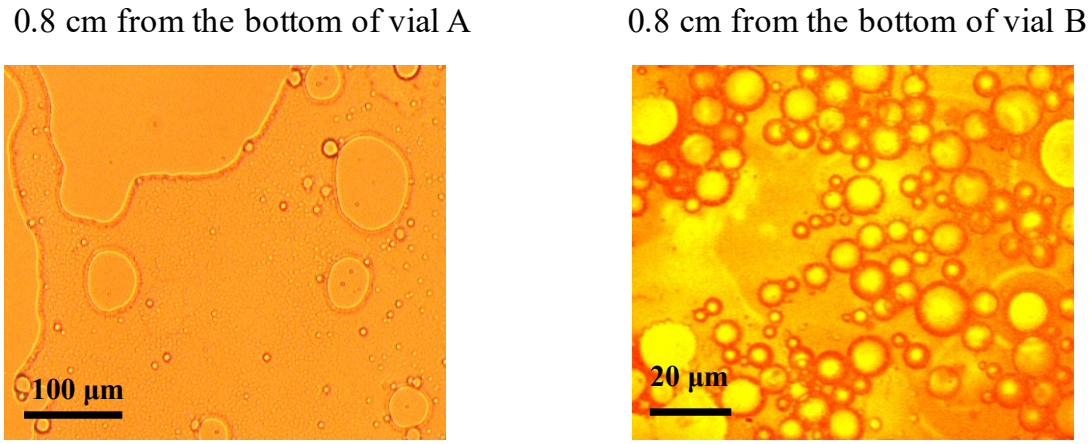

Figure A.2 Optical microscopic image of emulsion stabilized by asphaltenes. The emulsions for imaging were taken at 0.8 cm height from the bottom of vial A and vial B in Figure 3.7.

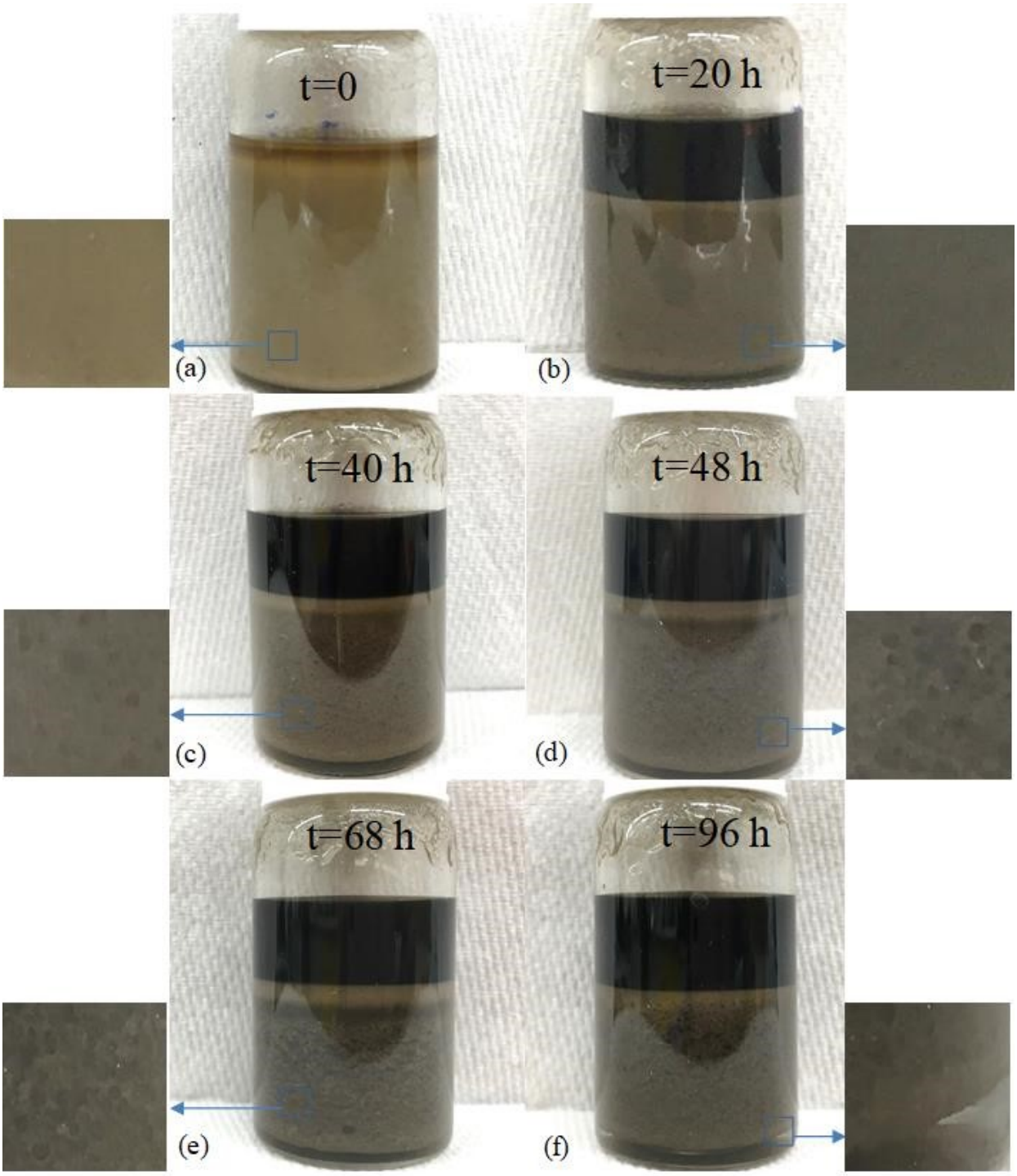

Figure A.3 (a) Prepared water-in-oil emulsions in the presence of asphaltenes. After adding 1 mL 3mg/mL FPPM in toluene solution the emulsion was settled without external magnetic force for (b) 20 h (c) 40 h (d) 48 h (e) 68 h and (f) 96 h, respectively.

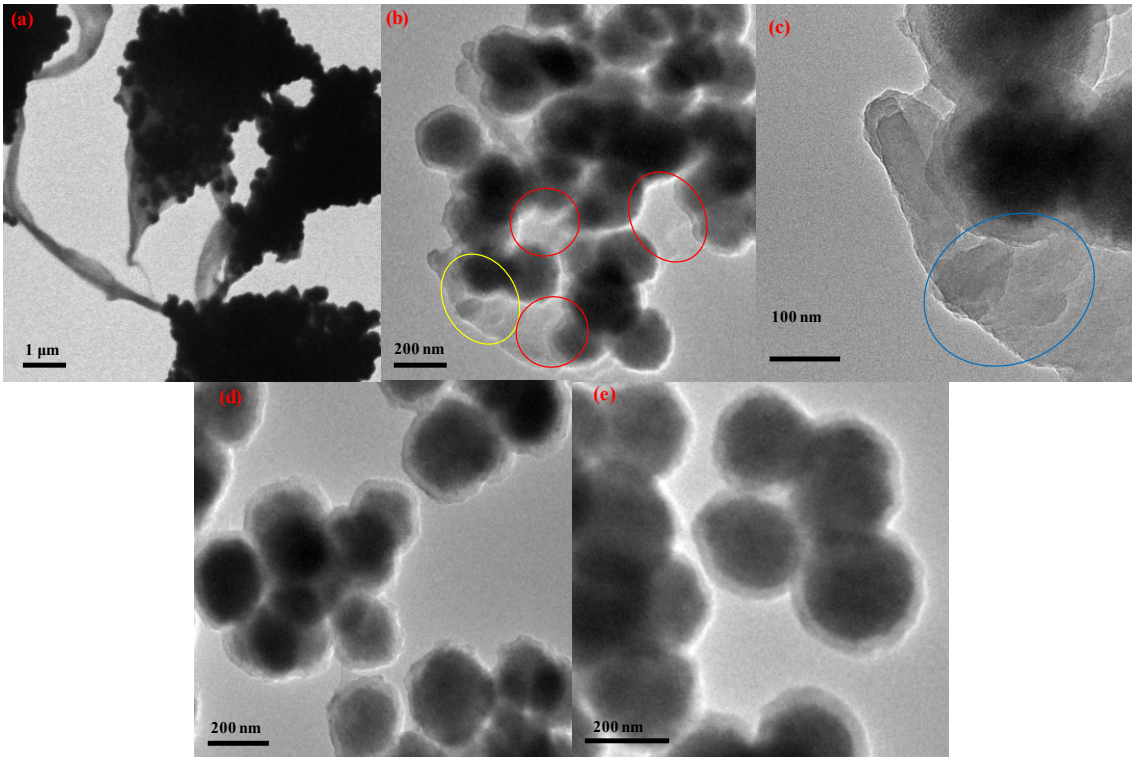

Figure A.4 TEM images of (a), (b) FPPM after treatment in asphaltenes-in-toluene solution; (c) magnified view of the region circled in yellow in (b); (d), (e) FPPM after sonication in water.

Appendix B Supporting Information for Chapter 6

B.1 Experimental section

B.1.1 Surface energy measurement

The surface energies of MD(SH)M-coated gold surfaces were measured using a three-probe-liquid method [1,2]. The contact angles of three probe liquids, including one non-polar liquid (i.e., diiodomethane) and two polar liquids (i.e., water and ethylene glycol), on the MD(SH)M-coated gold surfaces were measured by sessile drop method. The surface energy (γ) consists of Lifshitz-van der Waals component (γ^{LW}) and Lewis acid-base component (γ^+ and γ^-) according to the Good and Van Oss model (Equation B.1).

$$\gamma = \gamma^{LW} + 2\sqrt{\gamma^+\gamma^-} \tag{B.1}$$

The relationship between liquid contact angle (θ) and the surface energy components is shown in Equation B.2, where the subscript S or L represents MD(SH)M-coated gold surface or liquid, respectively.

$$\gamma_L(\cos\theta + 1) = 2(\sqrt{\gamma_S^{LW}\gamma_L^{LW}} + \sqrt{\gamma_S^+\gamma_L^-} + \sqrt{\gamma_S^-\gamma_L^+}) \tag{B.2}$$

To determine the surface energy of MD(SH)M-coated gold surface (γ_S) using Equation B.1, three surface energy components, γ_S^{LW}, γ_S^+ and γ_S^-, need to be determined based on Equation B.2 by using three probe liquids with known surface energies. The correlation can be rearranged as Equation B.3, where L_1, L_2 and L_3 represent three different probe liquids, respectively.

$$\begin{pmatrix} \gamma_S^{LW} \\ \gamma_S^+ \\ \gamma_S^- \end{pmatrix} = \left\{ \left[2 \begin{pmatrix} \sqrt{\gamma_{L1}^{LW}} & \sqrt{\gamma_{L1}^-} & \sqrt{\gamma_{L1}^+} \\ \sqrt{\gamma_{L2}^{LW}} & \sqrt{\gamma_{L2}^-} & \sqrt{\gamma_{L2}^+} \\ \sqrt{\gamma_{L3}^{LW}} & \sqrt{\gamma_{L3}^-} & \sqrt{\gamma_{L3}^+} \end{pmatrix} \right]^{-1} \begin{pmatrix} \gamma_{L1}(\cos\theta_1 + 1) \\ \gamma_{L2}(\cos\theta_2 + 1) \\ \gamma_{L3}(\cos\theta_3 + 1) \end{pmatrix} \right\} \tag{B.3}$$

B.1.2 Cyclic voltammetry (CV) measurement

The number density of MD(SH)M molecules grafted on gold substrate was characterized by CV measurement using a CHI 920c electrochemical workstation (CH Instruments Inc.) [3–5]. During a typical CV measurement, a platinum wire was used as counter electrode, a Ag/AgCl (1 M KCl) microelectrode worked as reference electrode (0.222 V vs standard hydrogen electrode (SHE)), and the MD(SH)M-coated gold surface was set as working electrode. All potentials quoted were referred to the Ag/AgCl (1 M KCl) reference electrode. The experimental solution consisted of 0.5 M KOH and 3.3 M KCl, which was purged with nitrogen for 30 min before each experiment. The potential swept between -0.2 V and -1.3 V at a rate of 0.5 V/s. One electron was transferred from the working electrode to the adsorbed MD(SH)M to break the Au-S covalent bond, which led to the desorption of MD(SH)M, showing a reduction peak between -0.8 V and -1.0 V. The reduction reaction is presented as $Au\text{-}S\text{-}R + 1e^- = Au + R\text{-}S^-$. The number density σ of MD(SH)M grafted on gold substrate can be calculated by Equation B.4.

$$\sigma = \frac{Q \times N_A}{F} \tag{B.4}$$

Where Q is the total charge density on the surface as calculated based on the area of reduction peak, the area of substrate surface and the scan rate, N_A is the Avogadro constant and F is the Faraday constant.

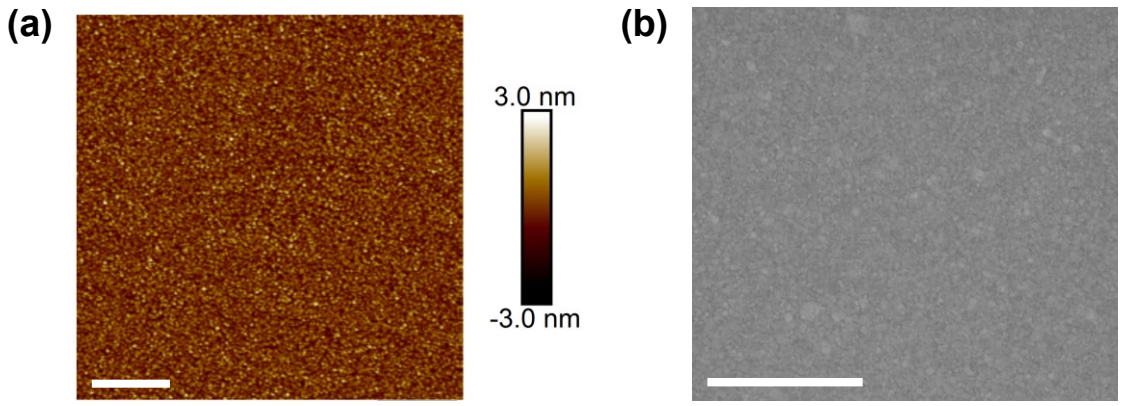

Figure B.1 (a) Topographic AFM image and (b) SEM image of bare gold surface before coating MD(SH)M, the scale bar is 1 μm.

Table B.1 Surface energy parameters of three probe liquids

Surface Energy (mJ/m^2)	γ_L^{LW}	γ_L^+	γ_L^-	γ_L
Diiodomethane	50.80	0.00	0.00	50.80
Water	21.80	25.50	25.50	72.80
Ethylene Glycerol	29.00	1.92	47.00	48.00

Table B.2 Contact angles of three probe liquids on HS, ES, PS and IS

	Water	diiodomethane	Ethylene glycol
HS	74.6°±1.7°	43.2°±1.8°	72.3°±0.4°
ES	101.8°±1.1°	55.8°±2.0°	79.6°±1.5°

PS	102.7°±1.2°	61.0°±1.0°	80.4°±0.9°
IS	101.2°±1.7°	48.1°±1.9°	80.9°±0.1°

Table B.3 Calculated surface energies of HS, ES, PS and IS

Surface Energy (mJ/m^2)	γ_S^{LW}	γ_S^+	γ_S^-	γ_S
HS	37.96	3.05	2.82	43.83
ES	30.99	0.01	0.24	31.08
PS	28.00	0.08	1.01	28.55
IS	35.33	0.72	1.35	37.30

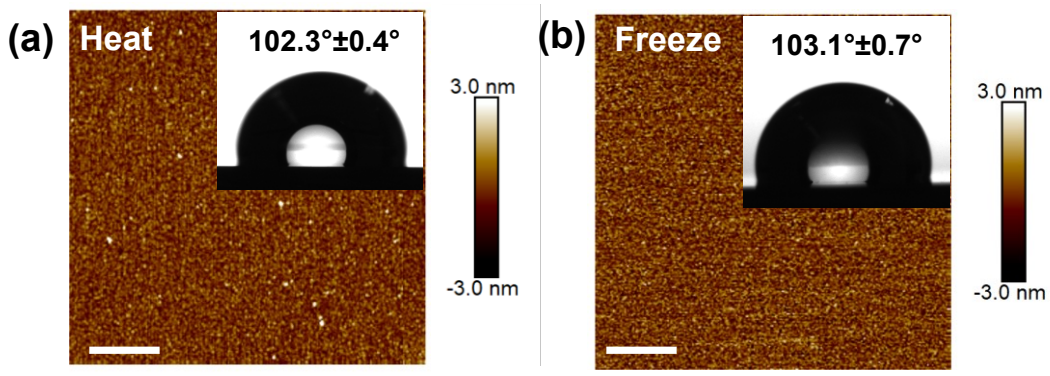

Figure B.2 Topographic AFM images of PS surface after (a) being heated at 35° and (b) being frozen at -20° for 1h (scale bar: 1 μm). The inset is water contact angle on the corresponding surface.

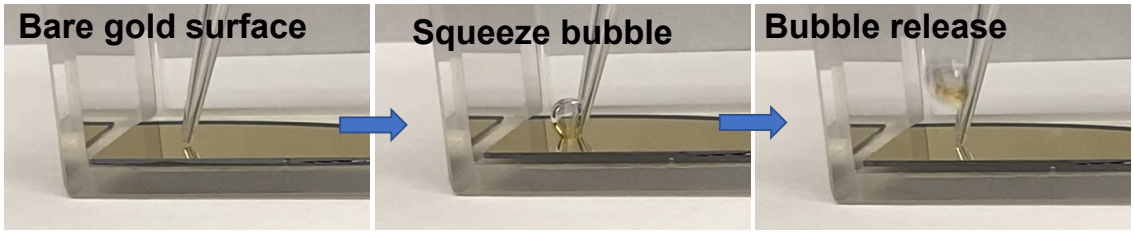

Figure B.3 Bubble on bare gold surface under water.

References

1. Xie, L. *et al.* Mapping the Nanoscale Heterogeneity of Surface Hydrophobicity on the Sphalerite Mineral. *J. Phys. Chem. C* **121**, 5620–5628 (2017).

2. Xie, L. *et al.* Probing the Interaction Mechanism between Air Bubbles and Bitumen Surfaces in Aqueous Media Using Bubble Probe Atomic Force Microscopy. *Langmuir* **34**, 729–738 (2018).

3. Xie, L. *et al.* A wet adhesion strategy via synergistic cation-π and hydrogen bonding interactions of antifouling zwitterions and mussel-inspired binding moieties. *J. Mater. Chem. A* **7**, 21944–21952 (2019).

4. Wang, J., Liu, Q. & Zeng, H. Understanding Copper Activation and Xanthate Adsorption on Sphalerite by Time-of-Flight Secondary Ion Mass Spectrometry, X-ray Photoelectron Spectroscopy, and in Situ Scanning Electrochemical Microscopy. *J. Phys. Chem. C* **117**, 20089–20097 (2013).

5. Gong, L. *et al.* Interaction Mechanisms of Zwitterions with Opposite Dipoles in Aqueous Solutions. *Langmuir* **35**, 2842–2853 (2019).